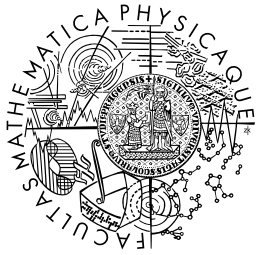

FACULTY
OF MATHEMATICS
AND PHYSICS
Charles University

DOCTORAL THESIS

Ina Carli

Angular analysis of the $B^0 \to K^* \mu^+ \mu^-$ decay with the ATLAS detector

Institute of Particle and Nuclear Physics

Supervisor of the doctoral thesis:	doc. RNDr. Zdeněk Doležal, Dr.
Study programme:	Physics
Study branch:	Subnuclear Physics

Prague 2018

I declare that I carried out this doctoral thesis independently, and only with the cited sources, literature and other professional sources.

I understand that my work relates to the rights and obligations under the Act No. 121/2000 Sb., the Copyright Act, as amended, in particular the fact that the Charles University has the right to conclude a license agreement on the use of this work as a school work pursuant to Section 60 subsection 1 of the Copyright Act.

In Prague, 12th October 2018 Ina Carli

Title: Angular analysis of the $B^0 \to K^*\mu^+\mu^-$ decay with the ATLAS detector

Author: Ina Carli

Institute: Institute of Particle and Nuclear Physics

Supervisor: doc. RNDr. Zdeněk Doležal, Dr., Institute of Particle and Nuclear Physics

Abstract: An angular analysis of the rare decay $B^0 \to K^*(K^+\pi^-)\mu^+\mu^-$ is presented. The study is based on a data sample from pp collisions at centre-of-mass energy of 8 TeV recorded by the ATLAS detector at the Large Hadron Collider which corresponds to an integrated luminosity of $20.3\,\mathrm{fb}^{-1}$. An extended unbinned maximum-likelihood fit of the decay angular distribution is used to measure the CP-averaged angular observables F_L, S_3, S_4, S_5, S_7 and S_8 and the corresponding form-factor independent observables P_1, P_4', P_5', P_6' and P_8'. The measurements are performed in the region $0.04\,\mathrm{GeV}^2 < q^2 < 6\,\mathrm{GeV}^2$, where q is the dimuon invariant mass.
The results are in agreement with the Standard Model predictions and compatible with measurements published by other experiments. The most significant deviations are observed for parameters P_4', P_5' at the level of 2.7 standard deviations and for P_8' which is 1.9 standard deviations away from one of the predictions. The P_5' deviation in bin $4\,\mathrm{GeV}^2 < q^2 < 6\,\mathrm{GeV}^2$ is consistent with the one reported by the LHCb collaboration.
The second part of this work shortly summarises the operation of the ATLAS Semiconductor Tracker, testing of the prototype module for the Inner Tracker strip upgrade, and the monitoring of non-collision background which was developed as a part of this thesis.

Keywords: CERN LHC, ATLAS, B-physics, rare decay, angular distribution

"I think that curiosity and the need to do research is a part of our humanity... So there will certainly be a future. "

Maria Fidecaro

Acknowledgements

I was lucky to be based at CERN for most of the duration of my PhD studies and meet many people who made this experience so valuable and enjoyable. I cannot name all of them but I would like to name a few.

First and foremost, I am very grateful to my supervisor Zdeněk Doležal who gave me the opportunity to work on various topics and always supported me. Thank you for your advice, experience and for being patient with me when often I have been doing what I love instead of what I should.

I would also like to thank my consultant, Pavel Řezníček, for his help with B-physics, technical problems and paper writing. The $B^0 \to K^*\mu^+\mu^-$ analysis was finished thanks to him, Adrian Bevan, Tamsin Nooney and Anna Usanova.

A big thank you goes to all colleagues and friends who made my stay at CERN enriching, motivated me, kept me sane, helped me so much or were simply there as role models. Thanks to the SCT community (Steve, Dave, Pat, Sandra, Ewa, Per, Kathrin, Koichi, Saverio, Kyle, Hide and many more) for welcoming me to the operations team and introducing me to the world of detector physics and readout, to ITk folks (Carlos, Ingrid, Susanne, Peter, Jiří and Marcela) for giving me a chance to put my hands on some hardware and to the members of the ATLAS operations and data quality teams for being helpful and collaborative during all my shifts - there is no way to name them all.

Thanks to Markus Joos for giving me a chance to join the Beamline for Schools team and to Bane, Theo, Sarah and Jorgen for being such great colleagues. I learned so much and it was an unforgettable experience.

Thanks to colleagues from IPNP in Prague, CERN library and outreach people and to my friends who were there, close or far.

And a big thank you to my family and especially Samuele for all their support over the years. It would not be possible without you. Ďakujem.

Contents

Introduction

The Standard Model (SM) of particle physics describes all known elementary particles and three of the four fundamental forces in the Universe. Although it is well tested and it can interpret most of the experimental observations, it fails to fully explain some of the observed phenomena and it has a few theoretical shortcomings. Many new theories were proposed as extensions or replacements of the SM but direct experimental evidence for any of these models is still missing.

The Large Hadron Collider (LHC) at CERN and its detectors were built to precisely measure the parameters of the SM and to search for signs of the Beyond Standard Model (BSM) physics. New particles might be discovered directly, by detecting their signal and decay products, or indirectly, via measurements of the known processes. The flavour physics is one of the promising directions for precision measurements because many SM parameters related to the flavour sector are known with an impressive precision thanks to the improvements in theoretical and experimental techniques. Although there is not a single golden parameter, combining information from various types of decays increases the discovery potential and the correlations between measurements can distinguish among new theories.

Few anomalies in the quark flavour sector were observed recently, especially in the decays of B mesons which are mediated by flavour-changing neutral currents. These include measurements of decay rates ratios of B-meson decays to final states with different leptons that test the lepton flavour universality (parameters R_K, R_{K^*}, R_D, R_{D^*} and $R_{J/\psi}$ [1–4]), differential branching fractions of decays $B_s^0 \to \phi\mu^+\mu^-$ [5], $B^+ \to K^+\mu^+\mu^-$ and $\Lambda_b \to \Lambda(pK^-)\mu^+\mu^-$ [1] or angular parameters of the $B^0 \to K^*\mu^+\mu^-$ decay, particularly P_5' [6–13]. Even though none of these measurement has a high statistical significance alone, they are consistent among different experiments and it is difficult to explain all these deviations in the SM. Some groups performing global fits claim that the model-independent BSM hypothesis is preferred over the SM with a significance as high as 5 standard deviations [14,15]. However, discussions about the used techniques and attempts to account for all anomalies at once are ongoing in the theory community. The angular analysis of one these decays, $B^0 \to K^*\mu^+\mu^-$, is presented in this thesis. The study uses data from proton-proton collisions collected by the ATLAS detector at the LHC in 2012 and the results were published in the Journal of High Energy Physics [16].

The LHC started physics data taking in pp collisions in 2010 at centre-of-mass energy of 7 TeV. Thanks to the improvements and gained experience, the instantaneous luminosity and availability of the machine improve over the years. The energy was raised to 8 TeV in 2012 and in total an integrated luminosity of nearly $30\,\text{fb}^{-1}$ was delivered to the ATLAS experiment during the whole Run 1 period. Since 2015, the data taking continues with a centre-of-mass energy of 13 TeV. Operation of the ATLAS detector and all steps of data processing and analysis are highly collaborative. The author of this thesis contributed to the smooth operation of detector as a member of the SCT operations team (in 2011-2013, DAQ&DCS and online monitoring on-call expert), by taking Shift Leader shifts in the ATLAS control room (since 2013) and by reviewing the

SCT data quality (as shifter and expert, since 2012). As a part of activities for the upgrade of the ATLAS strip detector, the author took part in setting up the prototype tests in laboratory of IPNP in Prague and in stavelet testing and module irradiation campaign at CERN. Furthermore, a tool for monitoring of the non-collision backgrounds for the ATLAS Non-collision Background Task Force was developed as a part of this work.

This dissertation consists of six chapters. The theoretical basis of physics of rare B-meson decays and the motivation for the analysis of the $B^0 \to K^*\mu^+\mu^-$ angular distribution are presented in Chapter 1. A short overview of the LHC accelerator is given in Chapter 2 and the ATLAS detector is described in Chapter 3. This section contains also short overviews of performance parameters important for B-physics analyses and of the planned ATLAS upgrade projects. Chapter 4 contains the main topic of this thesis, angular analysis of the $B^0 \to K^*\mu^+\mu^-$ decay. The last two chapters contain more technical topics: the operation and performance of the ATLAS silicon strip tracker and testing of prototypes for the tracker upgrade are discussed in Chapter 5 and the monitoring of non-collision background is shortly outlined in Chapter 6.

1. Theory overview

The Standard Model (SM) is a theory of elementary particles and their interactions that represents our current understanding of the strong and electroweak interactions. Since it was formulated in the present form in the mid-70s, it was extremely successful in describing almost all known phenomena over a wide range of energies. However, the model fails to describe some experimental results such as neutrino oscillations or dark matter and has a few theoretical shortcomings, for example the missing incorporation of gravity, hierarchy and naturalness problems. This motivates the development of further theoretical concepts and many ongoing experimental searches for new particles.

The present chapter provides a brief introduction of the flavour physics in SM with emphasis on rare decays of B mesons and decay $B^0 \to K^*\mu^+\mu^-$. The text is largely based on books [17–19] and review [20].

Throughout this thesis, natural units are used, i.e. $\hbar = c = 1$ and the names of particles also represent their antiparticles, unless specified otherwise.

1.1 The Standard Model

The SM describes all matter in the universe in terms of two classes of fundamental particles: fermions (particles with half-odd spin) and bosons (spin-1 particles) that mediate the forces. Fermions are further divided into two categories, leptons and quarks, and come in at least three generations. The leptons are electron, muon and tau-lepton and their neutrinos. There are six types of quarks: **u**p, **d**own, **c**harm, **s**trange, **t**op and **b**ottom. For historic reasons, t and b are also referred to as **t**rue and **b**eauty.

Selected properties of fermions are summarised in Table 1.1. Leptons have integer electric charge and the charge of quarks is fractional. Baryons are described as bound states of three quarks, while mesons are composed of quark and antiquark. All baryons observed until now have integer charge. In addition to the particles listed in the table, each fermion has its own antiparticle.

Table 1.1: Properties of leptons and their quantum numbers: charge Q, lepton number L and baryon number B. The antiparticles are not listed here. [20]

Group	**I**	**II**	**III**	$\boldsymbol{Q}$ $[e]$	$\boldsymbol{L}$	$\boldsymbol{B}$
Leptons	e	μ	τ	-1	1	0
	ν_e	ν_μ	ν_τ	0	1	0
Quarks	u	c	t	$+2/3$	0	$1/3$
	d	s	b	-1/3	0	$1/3$

The SM is a gauge quantum field theory with an internal symmetry group $\mathrm{SU}(3)_c \times \mathrm{SU}(2)_L \times \mathrm{U}(1)_Y$. Three of the four fundamental forces are included: the $\mathrm{SU}(3)_c$ describes the strong interaction and $\mathrm{SU}(2)_L \times \mathrm{U}(1)_Y$ describes the electroweak interaction, unification of the electromagnetic and weak nuclear forces.

The index c refers to colour, L to the left-handed chiral nature of the SU(2) coupling and Y to the weak hypercharge.

The theory of strong interactions or Quantum Chromodynamics (QCD) is a non-Abelian $\mathrm{SU}(3)_c$ gauge theory which describes interactions between quarks that carry colour charge with gluons, massless spin-1 bosons. Leptons do not have a colour charge, therefore they do not interact strongly. The QCD describes the asymptotic freedom and colour confinement observed experimentally and explains why quarks cannot be observed in isolation and are always forming hadrons which are colour singlets.

The electroweak interaction is a unification of the weak and electromagnetic forces into a single theory where their coupling constants g and e are related via the weak mixing angle θ_{W} as

$$g \sin \theta_{\mathrm{W}} = e.$$

The $\mathrm{SU}(2)_L \times \mathrm{U}(1)_Y$ symmetry group is broken by the Brout-Englert-Higgs mechanism such that a subgroup U(1) generates one photon, the boson of the electromagnetic force. The other three intermediate vector bosons, W^+, W^- and Z, become massive. The mechanism generates also the spin-0 Higgs boson.

1.2 Flavour and the CKM matrix

Flavour is a term used in particle physics to refer to the type of quarks or leptons. Flavour physics studies the interactions of heavy quarks s, c, b and t. The conservation of lepton flavour numbers L_ℓ for each $\ell \in \{e, \mu, \tau\}$ is experimentally well established and explains for example why some kinematically allowed decays, such as $\mu^- \to e^- \gamma$, have never been observed.

In the quark sector, each quark has an additive quantum number to define its type and composite particles carry flavour quantum numbers according to their valence quark content. Because of an approximate symmetry observed historically in hadron interactions, up and down quark were assigned in a doublet with isospin 1/2. Up quark has a value of the third component $I_3 = 1/2$ and down quark $I_3 = -1/2$. All other quarks have their own quantum numbers, e.g. strangeness $S = -[n(s) - n(\bar{s})]$ and similarly charm, bottomness and topness.[1] The quark flavour numbers are conserved by the strong and electromagnetic interaction and only weak interaction mediated by $W^\pm$ violates it in the SM.

The interactions and masses of quarks in the SM can be derived by defining the quark fields and studying their interactions while conserving the local gauge invariance and renormalizability of the theory. The quark masses can be derived from Yukawa coupling

$$\mathscr{L}^q_{\mathrm{Yukawa}} = \sum_{\substack{q=d,s,b \\ q\prime=d,s,b}} h_{qq\prime} \overline{L^q} \Phi q'_R + h.c. + \sum_{\substack{q=d,s,b \\ q\prime=u,c,t}} \widetilde{h}_{qq\prime} \overline{L^q} \widetilde{\Phi} q'_R + h.c. \ ,$$

where $h_{qq\prime}$ and $\widetilde{h}_{qq\prime}$ are coupling constants, L^q are the left-handed SU(2) doublets, q'_R are right-handed singlets and $\Phi(\widetilde{\Phi})$ is the (conjugate) scalar doublet of the Higgs field.

[1] For historic reasons, the quantum numbers of upper quarks are defined positive (charm of c is +1) and of lower quarks negative (bottomness of b is –1).

However, quark fields q' defined in this way are not necessarily mass eigenstates, i.e. the mass matrices M_u and M_d are general complex matrices. They can be diagonalised by biunitary transformations as $M_q = V_{qL}^{\dagger} m_q V_{qR}$, where $V_{L,R}$ is unitary and m_q is a diagonal real matrix. The transformed fields are then mass eigenstates with masses proportional to their coupling to the Higgs field.

The Lagrangian of charged-current interactions between quarks and $W^{\pm}$ after diagonalization becomes

$$\mathscr{L}_{W^{\pm}} = \frac{g}{\sqrt{2}} \left[\overline{U_L^i} \gamma^{\mu} \left(V_{\mathrm{CKM}}\right)_{ij} D_L^j W_{\mu}^{+} + \overline{D_L^j} \gamma^{\mu} \left(V_{\mathrm{CKM}}\right)_{ij} U_L^i W_{\mu}^{-} \right], \tag{1.1}$$

where g is the electroweak coupling constant, vectors $U_L = (u_L, c_L, t_L)^{\mathrm{T}}$ and $D_L = (d_L, s_L, b_L)^{\mathrm{T}}$ represent quark fields and V_{CKM} is the unitary Cabibbo-Kobayashi-Maskawa (CKM) matrix [21, 22]

$$V_{\mathrm{CKM}} = V_{uL}^{\dagger} V_{dL} = \begin{pmatrix} V_{ud} & V_{us} & V_{ub} \\ V_{cd} & V_{cs} & V_{cb} \\ V_{td} & V_{ts} & V_{tb} \end{pmatrix}.$$

Elements of the V_{CKM} matrix represent couplings between up- and down-type quarks. Because of the unitarity conditions and the possibility to redefine the relative phases of quark fields, the number of real parameters can be reduced from eighteen to three and one phase. The presence of a complex phase gives a possibility for CP violation because the CP conjugated process corresponds to interaction via Hermitian conjugation of the Lagrangian (1.1). This was not possible in a model with four quarks where the V_{CKM} was a real 2×2 matrix with one real parameter, the Cabibbo angle.

Experimental measurements show that the structure of the V_{CKM} matrix is hierarchical and elements on the diagonal corresponding to transitions between quarks in the same family are approximately 1, while transitions between generations that are further from the diagonal are suppressed [23]. This can be emphasised by writing V_{CKM} using the Wolfenstein parameterization [20], which uses expansion in powers with respect to the parameter λ as

$$\begin{aligned} V_{\mathrm{CKM}} &= \begin{pmatrix} 0.97434^{+0.00011}_{-0.00012} & 0.22506 \pm 0.00050 & 0.00357 \pm 0.00015 \\ 0.22492 \pm 0.00050 & 0.97351 \pm 0.00013 & 0.0411 \pm 0.0013 \\ 0.00875^{+0.00032}_{-0.00033} & 0.0403 \pm 0.0013 & 0.99915 \pm 0.00005 \end{pmatrix} = \\ &= \begin{pmatrix} 1 - \lambda^2/2 & \lambda & A\lambda^3 \left(\bar{\rho} - i\bar{\eta}\right) \\ -\lambda & 1 - \lambda^2/2 & A\lambda^2 \\ A\lambda^3 \left[1 - \left(\bar{\rho} + i\bar{\eta}\right)\right] & -A\lambda^2 & 1 \end{pmatrix} + \mathcal{O}(\lambda^4), \end{aligned}$$

where parameters $\lambda, A, \bar{\rho}$ and $\bar{\eta}$ are defined as

$$\lambda^2 = \frac{|V_{us}|^2}{|V_{ud}|^2 + |V_{us}|^2}, \qquad A^2\lambda^4 = \frac{|V_{cb}|^2}{|V_{ud}|^2 + |V_{us}|^2}, \qquad \bar{\rho} + i\bar{\eta} = -\frac{V_{ud}V_{ub}^*}{V_{cd}V_{cb}^*}.$$

The unitarity condition of the CKM matrix $V_{\mathrm{CKM}} V_{\mathrm{CKM}}^{\dagger} = \mathbb{I}$ corresponds to a set of 12 equations between its components. In particular, equations for the off-diagonal terms can be represented as triangles in the complex plane. The most commonly used unitarity triangle arises from equation

$$V_{ud}V_{ub}^* + V_{cd}V_{cb}^* + V_{td}V_{tb}^* = 0,$$

rescaled by a factor $V_{cd}V_{cb}^*$. Figure 1.1 shows a plot summarising the up-to-date experimental constraints to its parameters.

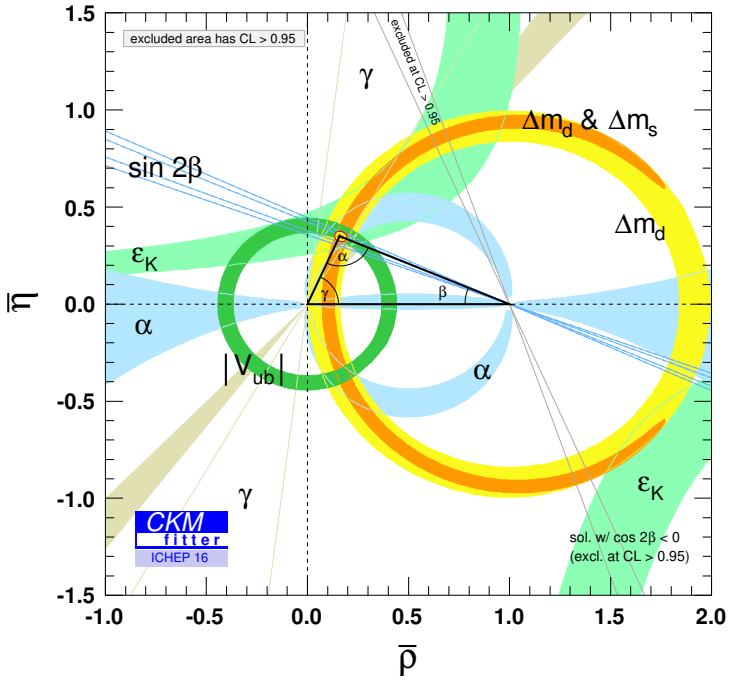

Figure 1.1: Status of recent CKM unitarity triangle fit in $(\overline{\rho}, \overline{\eta})$ plane [23].

1.3 Rare b-hadron decays

The study of b hadrons is an important part of experimental tests of the SM and searches for new physics. The b quark is the heaviest quark that is forming composite particles and its large mass might increase the coupling to new particles predicted by the Beyond Standard Model (BSM) theories. Furthermore, the B mesons have a relatively long lifetime and their displaced decay vertices provide a useful experimental signature.

The decays of b hadrons can be described on quark level as $b \to q$ transitions with q being one of the lighter quarks. Processes $b \to u/c$ are mediated by the W^- boson and are allowed at tree level in the SM. Transitions $b \to d$ and $b \to s$ are Flavour-Changing Neutral Currents (FCNC) processes and are forbidden at tree level: they can only occur at higher orders through loop diagrams. For example, two SM-allowed Feynman diagrams for $b \to s$ with photon of dilepton in the final state are penguin and box diagrams shown in Figure 1.2.

The FCNC decays are suppressed because they involve at least two charged flavour-changing currents and the mediating $W^\pm$ boson is virtual. Moreover, one of the two currents is running between two quark families and is suppressed by the corresponding element of the CKM matrix. As a result, branching fractions of FCNC decays are typically at the order of 10^{-4} or smaller and are therefore called rare decays.[2] FCNC decays are sensitive to new physics because even small

[2]The FCNC decays are sometimes described as semi-rare if they have branching fractions of $10^{-6} - 10^{-4}$ or rare for branching fractions smaller than $\sim 10^{-6}$.

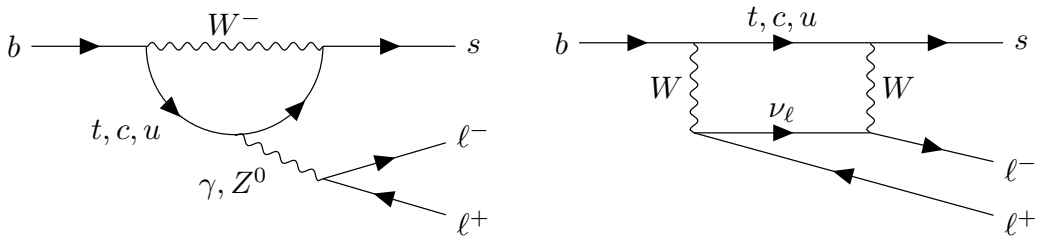

Figure 1.2: Feynman diagrams of FCNC $b \to s$ process via penguin (left) and box diagram.

contributions from new virtual particles, too heavy to be produced directly (up to hundreds of TeV, depending on coupling), might lead to measurable deviations from the SM predictions. Furthermore, the interference of known and new-physics decay channels might manifest itself as a change of angular distributions of the final products, CP asymmetries or other observables.

Effective Hamiltonian

The description of flavour decays requires an understanding of weak interactions but it has to also include the strong dynamics of hadronisation by the QCD. The electroweak scale describing the decay on quark level is defined by the mass of W boson. On the other hand, strong interactions taking place at lower energy scales (few hundred MeV to few GeV) are non-perturbative and cannot be calculated analytically. A solution for this problem is a construction of a low energy effective field theory, where the short-range interactions with heavy fields such as $W^{\pm}$, Z or t approximately correspond to point interactions.

Construction of the effective Hamiltonian follows the Operator Product Expansion technique [24, 25]. The method implements a summation over all contributing local operators $\mathcal{O}_i$ weighted by the corresponding effective coupling constants, Wilson coefficients C_i. For the $b \to s$ transition the effective Hamiltonian can be written as [26]

$$\mathcal{H}_{\text{eff}} = -\frac{4\,G_F}{\sqrt{2}} V_{tb} V_{ts}^* \frac{\alpha}{4\pi} \sum_i C_i(\mu_s)\mathcal{O}_i(\mu_s)\,, \tag{1.2}$$

where G_F is the Fermi constant, V_{ij} are CKM matrix elements, α is the fine structure constant and μ_s is the renormalisation scale. Additional terms $\propto V_{ub}V_{us}^*$ are doubly Cabibbo-suppressed and have been neglected. The long-distance contributions are described by the operators, while short-distance physics at higher energy scales is encoded in the Wilson coefficients. The operators and their Wilson coefficients are evaluated at one renormalisation scale μ_s. The effects of particles with a mass greater than μ_s (typically $W^{\pm}$, Z and t) are effectively removed by integrating them out and each of them contributes to at least one Wilson coefficient.

The effective theory is matched with the SM at a matching scale (e.g. the electroweak scale μ_W) and renormalisation group equations are derived for the Wilson coefficients, using the scale-independence of the effective Hamiltonian. Amplitudes of exclusive hadronic decays with initial state I and final state F can

be calculated as expectation values of the effective Hamiltonian

$$A(I \to F) = \langle F|\mathcal{H}_{\text{eff}}|I\rangle = -\frac{G_F}{\sqrt{2}} \sum_i V_{\text{CKM}}\, C_i(\mu_s)\, \langle F|\mathcal{O}_i(\mu_s)|I\rangle\,,$$

where V_{CKM} represents the appropriate terms of the CKM matrix. Calculations of the matrix elements for processes with hadrons in the final state such as $B^0 \to K^*\mu^+\mu^-$ are difficult and the decay has to be described in terms of form factors and decay constants, including corrections from charm loops and other effects. While some parameters can be extracted from data, others have to be calculated using non-perturbative methods, e.g. lattice QCD [27] or QCD light-cone sum rules [28].

Operators

The operators in effective Hamiltonian (1.2) can be separated into the left- and right-handed components as following:

$$\mathcal{H}_{\text{eff}} = -\frac{4\,G_F}{\sqrt{2}} V_{tb}V_{ts}^* \frac{\alpha}{4\pi} \sum_i^{10} [C_i\mathcal{O}_i + C_i'\mathcal{O}_i']\,.$$

A complete operator basis for $\Delta B = -\Delta S = 1$ processes can be defined by 10 local operators of dimension ≤ 6 [26]. Operators $\mathcal{O}_1$ and $\mathcal{O}_2$ are four-quark operators arising predominantly from the tree-level $W^\pm$ exchanges, $\mathcal{O}_{3-6}$ and $\mathcal{O}_8$ are penguin diagrams mediated by gluons. The last three operators are the most relevant for rare radiative, leptonic and semileptonic b hadron decays: operator $\mathcal{O}_7$ describes the penguin diagram mediated by photon and operators $\mathcal{O}_9$ and $\mathcal{O}_{10}$ represent the vector and axial currents in $b \to q\ell\ell$.[3] They have a form

$$\begin{aligned}
\mathcal{O}_7 &= \tfrac{m_b}{e}(\bar{s}\sigma^{\mu\nu}P_R b)F_{\mu\nu}\,, & \mathcal{O}_7' &= \tfrac{m_b}{e}(\bar{s}\sigma^{\mu\nu}P_L b)F_{\mu\nu}\,,\\
\mathcal{O}_9 &= (\bar{s}\gamma_\mu P_L b)\,(\bar{\ell}\gamma^\mu \ell)\,, & \mathcal{O}_9' &= (\bar{s}\gamma_\mu P_R b)\,(\bar{\ell}\gamma^\mu \ell)\,,\\
\mathcal{O}_{10} &= (\bar{s}\gamma_\mu P_L b)\,(\bar{\ell}\gamma^\mu\gamma_5 \ell)\,, & \mathcal{O}_{10}' &= (\bar{s}\gamma_\mu P_R b)\,(\bar{\ell}\gamma^\mu\gamma_5 \ell)\,.
\end{aligned}$$

The terms $P_{L/R} = (1\mp\gamma_5)/2$ denote the left- or right-handed chiral projection and $F_{\mu\nu}$ is the electromagnetic field strength tensor. Operators $\mathcal{O}_i'$ correspond to the right-handed couplings obtained by swapping P_L and P_R. The left-handedness of charged currents in the SM means that the Wilson coefficients C_i' are suppressed by $\mathcal{O}(m_s/m_b)$.

Because the effective Hamiltonian (1.2) describes a set of similar processes, it is possible to perform global fits to Wilson coefficients and study the self-consistency of the SM. Some processes are dominated by a single operator and measuring their branching fractions provides direct constraints, e.g. in case of $b \to s\gamma$ which is dominated by the $\mathcal{O}_7$ operator.

Contributions from new heavy particles (such as flavour-changing Z' bosons) might be expressed in a model-independent way as additive factors in Wilson coefficients $C_i = C_i^{\text{SM}} + \delta C_i$. BSM models with sources of lepton universality lead to splitting of some operators and coefficients depending on the interacting lepton, $\mathcal{O}_i \to \mathcal{O}_i^e, \mathcal{O}_i^\mu, \mathcal{O}_i^\tau$, and $C_i \to C_i^e, C_i^\mu, C_i^\tau$.

[3] Some authors use a more explicit notation $\mathcal{O}_{7\gamma}$, $\mathcal{O}_{9V}$ and $\mathcal{O}_{10A}$.

Observables

Semileptonic decays with one vector meson in the final state such as $B^0 \to K^*\mu^+\mu^-$ offer a number of observables potentially sensitive to BSM effects. The most direct is a measurement of the decay rates which can be enhanced by new particles generating additional tree-level diagrams or FCNC loops. A rich set of observables can be accessed via angular distributions of the end-state particles, such as forward-backward asymmetry or polarisation. However, their theoretical predictions have relatively high uncertainties originating from form factor, hence the need to construct new, form-factor independent observables.

One of the possible solutions is to measure ratios of branching fractions for similar decays to cancel out the uncertainties due to hadronisation, e.g. decays with electrons and muons in the final state (e.g. measurement of $R_{K^*} = \mathcal{B}(B^0 \to K^*\mu^+\mu^-)/\mathcal{B}(B^0 \to K^*e^+e^-)$). Another approach is to measure the weak isospin asymmetry, a normalised difference of branching fractions, for decays which proceed via the same fundamental process but where the spectator quark has a different flavour. For example, decays $B^0 \to K^*\mu^+\mu^-$ and $B^+ \to K^{*+}\mu^+\mu^-$ have the same $b \to s\mu^+\mu^-$ transition but the spectator quarks are d and u, respectively.

1.4 $B^0 \to K^*\mu^+\mu^-$ decay

The $B^0 \to K^*(892)\mu^+\mu^-$ is a semileptonic decay mediated by FCNC with a branching fraction of $(1.03 \pm 0.06) \times 10^{-6}$ [20].[4] The B^0 meson has a relatively long lifetime of 1.52×10^{-14} s, translating to a decay length of $c\tau = 456\,\mu$m. Taking into account the Lorentz boost, many B^0 mesons decay few millimetres away from their production vertex. In contrast, the lifetime of the K^* resonance is so short ($\tau \simeq 10^{-23}$ s) that it decays practically instantly to K^+ and π^- (with branching ratio of 99.9 %). As a result, a fully reconstructed $B^0 \to K^*\mu^+\mu^-$ manifests itself as a four-prong decay with a secondary vertex displaced from the production vertex.

The decay was first observed in 2003 by the BaBar collaboration [29] and since then it was further studied by other experiments: BaBar, Belle, CDF, LHCb and CMS. The related decay $B^0 \to K^*e^+e^-$ is also studied experimentally but is more difficult to reconstruct, while $B^0 \to K^*\tau^+\tau^-$ was not observed yet. There exists a large amount of literature about $B^0 \to K^*\mu^+\mu^-$ and $B^0 \to V\ell\ell$ processes. The following description is based on [26, 30] and references cited therein.

The leading-order SM Feynman diagrams are shown in Figure 1.3. The largest contributions come from diagrams with t quark but the loop with c quark cannot be neglected either. The phenomenology of $B^0 \to K^*\mu^+\mu^-$ is complicated because its theoretical description depends on the kinematics of decay, often expressed as a function of the dimuon invariant mass squared, $q^2 = (p_{\mu^+} + p_{\mu^-})^2$. As an example, a dependence of the differential decay rate on q^2 is schematically illustrated in Figure 1.4. For very low q^2, near maximal kinetic energy of K^* (large recoil), the decay behaves as $B^0 \to K^*\gamma$ with a slightly off-shell photon

[4] Throughout this thesis, $K^*(892)$ will be denoted simply K^* and CP-conjugated decays will be implied for all decays unless stated otherwise.

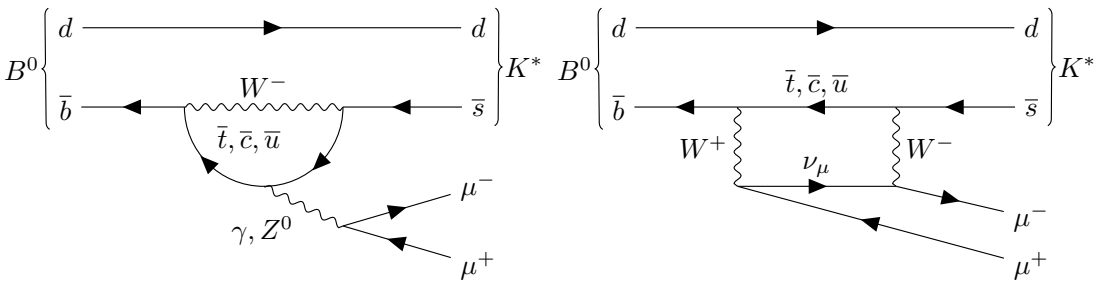

Figure 1.3: Lowest order Feynman diagrams of the $B^0 \to K^*\mu^+\mu^-$ decay in the Standard model: electroweak penguin (left) and box (right).

decaying to two leptons. Therefore, the virtual photon contribution associated with C_7 dominates. In the region of $1 < q^2 < 6\,\mathrm{GeV}^2$ where the emitted hadron is energetic, QCD factorisation applies and the theoretical predictions are cleanest [31]. The interference between C_7 and C_9 is large in this region giving excellent sensitivity to new physics in C_9.

The intermediate q^2 region is dominated by the narrow J/ψ and $\psi(2S)$ charmonia produced on tree level via $b \to c\bar{c}s$ and the calculations are complicated due to the interference of all allowed decay modes. Moreover, these regions have to be removed in experimental analyses, including tails from radiative charmonium decays. In the high q^2 region with low K^* recoil, $q^2 > 15\,\mathrm{GeV}^2$, the Operator Product Expansion can be applied and C_9 and C_{10} dominate. However, the calculation of form factors in the $1/m_b$ expansion breaks down for very high q^2 and some modelling is necessary to fully describe the phenomenology [32]. It also has to include contributions from broad charmonium resonances such as those observed in $B^+ \to K^+\mu^+\mu^-$ by the LHCb collaboration [33].

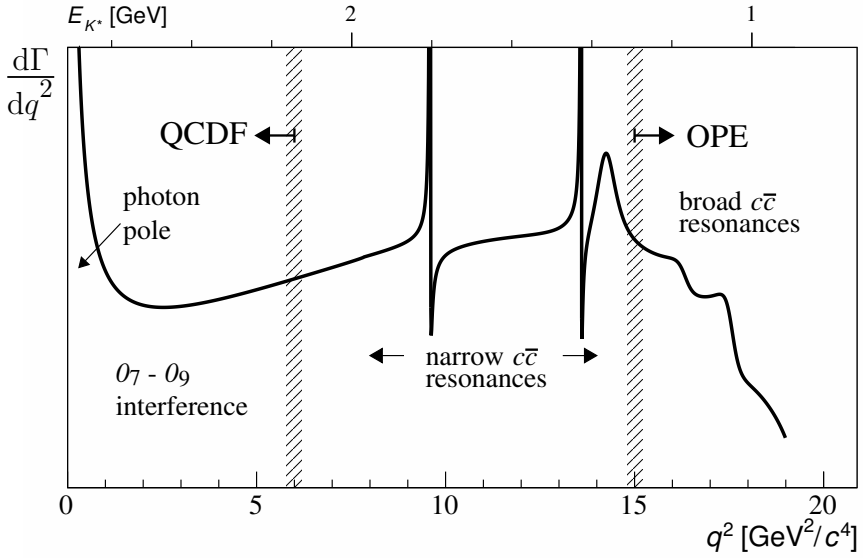

Figure 1.4: Scatch of $B^0 \to K^*\mu^+\mu^-$ decay rate dependence on dimuon invariant mass squared q^2 [26].

1.4.1 Angular observables

There is a certain amount of freedom in the definition of the decay angles describing the four final-state particles of $B^0 \to K^*\mu^+\mu^-$ and its CP conjugate. Different conventions were chosen by the theory community and for experimental measurements. The following text will focus on two of them: the *experimental convention* for the ATLAS measurement described in this thesis, which follows the definition used by the LHCb collaboration for analyses [12, 34, 35], and the *theoretical convention* adopted for example by [30]. Other definitions used in literature are similar to the theoretical convention, often with opposite sign of one of the angles, resulting in inverted sign of some angular parameters. This will be noted explicitly when citing such references.

In the following, notation $p_a^{(f)}$ means the momentum 4-vector of particle a in the rest frame of f, $p_{ab}^{(f)} = p_a^{(f)} + p_b^{(f)}$ and the normal vector to plane is defined as

$$n_{ab}^{(f)} = \frac{p_a^{(f)} \times p_b^{(f)}}{|p_a^{(f)} \times p_b^{(f)}|} .$$

In the experimental convention, the angles are shown in Figures 1.5 and 1.6 and defined as following:

- θ_K is the angle between the kaon in the K^* ($\overline{K}^*$) and the direction of the K^* ($\overline{K}^*$) in the B^0 ($\overline{B}^0$) rest frame. The later is equivalent to the direction opposite to the B^0 in the K^* rest frame. Explicitly that means

$$\cos\theta_K = \frac{p_K^{(K\pi)} \cdot p_{K\pi}^{(B)}}{|p_K^{(K\pi)}||p_{K\pi}^{(B)}|} = \frac{p_K^{(K\pi)} \cdot (-p_B^{(K\pi)})}{|p_K^{(K\pi)}||p_B^{(K\pi)}|} .$$

- θ_L is the angle between the μ^+ (μ^-) in the dimuon rest frame and the direction of the dimuon in the B^0 ($\overline{B}^0$) rest frame. The later is equivalent to the direction opposite to the B^0 ($\overline{B}^0$) in the dimuon rest frame. Explicitly for B^0 it means

$$\cos\theta_L = \frac{p_{\mu^+}^{(\mu\mu)} \cdot p_{\mu\mu}^{(B)}}{|p_{\mu^+}^{(\mu\mu)}||p_{\mu\mu}^{(B)}|} = \frac{p_{\mu^+}^{(\mu\mu)} \cdot (-p_B^{(\mu\mu)})}{|p_{\mu^+}^{(\mu\mu)}||p_B^{(\mu\mu)}|}$$

  and for $\overline{B}^0$

$$\cos\theta_L = \frac{p_{\mu^-}^{(\mu\mu)} \cdot p_{\mu\mu}^{(B)}}{|p_{\mu^-}^{(\mu\mu)}||p_{\mu\mu}^{(B)}|} = \frac{p_{\mu^-}^{(\mu\mu)} \cdot (-p_B^{(\mu\mu)})}{|p_{\mu^-}^{(\mu\mu)}||p_B^{(\mu\mu)}|} .$$

- ϕ is the angle between the two decay planes formed by the K^* ($\overline{K}^*$) and the dimuon systems in the B^0 ($\overline{B}^0$) rest frame. For B^0 decays, it can be computed from relations

$$\cos\phi = n_{\mu^+\mu^-}^{(B)} \cdot n_{K^+\pi^-}^{(B)}$$
$$\sin\phi = \left(n_{\mu^+\mu^-}^{(B)} \times n_{K^+\pi^-}^{(B)}\right) \cdot \frac{p_{K^*}^{(B)}}{|p_{K^*}^{(B)}|} ,$$

while for $\overline{B}^0$ decays it is

$$\cos\phi = n^{(B)}_{\mu^-\mu^+} \cdot n^{(B)}_{K^-\pi^+} = -n^{(B)}_{\mu^+\mu^-} \cdot n^{(B)}_{K^-\pi^+}$$
$$\sin\phi = \left(n^{(B)}_{\mu^+\mu^-} \times n^{(B)}_{K^-\pi^+}\right) \cdot \frac{p^{(B)}_{K^*}}{|p^{(B)}_{K^*}|} \,.$$

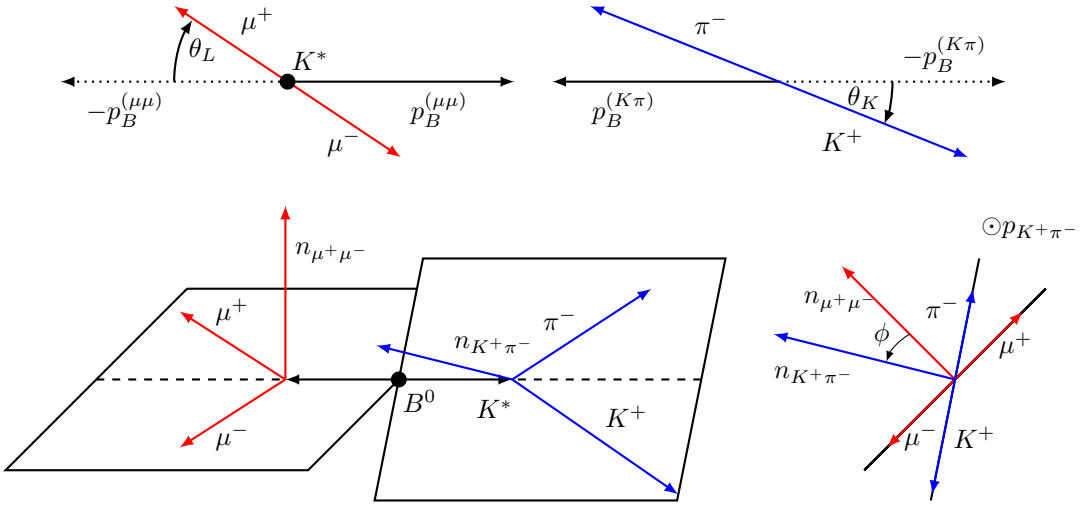

Figure 1.5: Definition of helicity angles θ_L, θ_K and ϕ for $B^0 \to K^*\mu^+\mu^-$ decay in the experimental convention (consistent with LHCb publications [12, 34, 35].

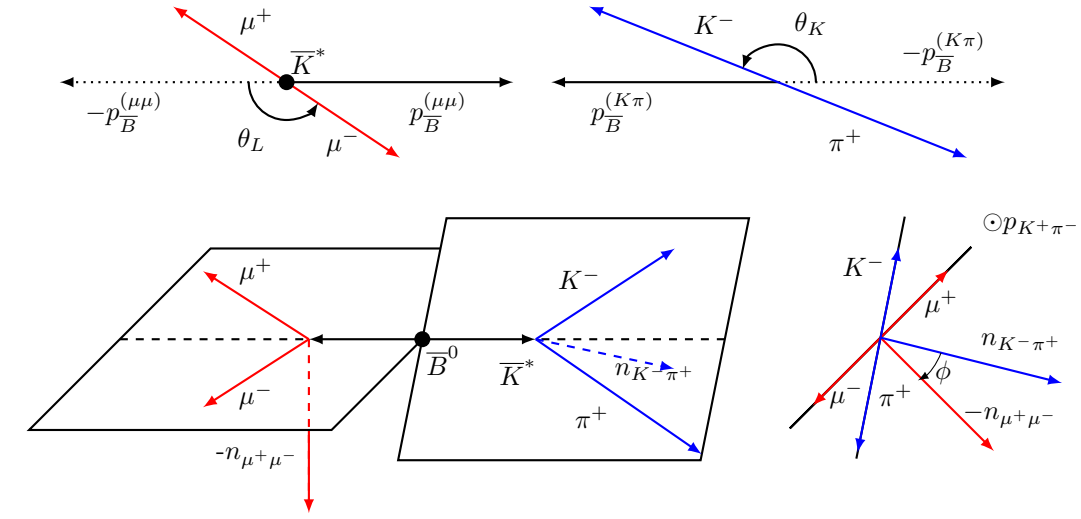

Figure 1.6: Definition of helicity angles θ_L, θ_K and ϕ for $\overline{B}^0 \to \overline{K}^*\mu^+\mu^-$ decay in the experimental convention.

In this convention, the CP-conjugated decay $\overline{B}^0 \to \overline{K}^* \mu^+ \mu^-$ with the same angular parameters has the same values of $\cos\theta_K$, $\cos\theta_L$ and ϕ. In case of wrong flavour tag (K/π track swap resulting in reconstructing B^0 candidate as $\overline{B}^0$ and vice versa), the measured angles are

$$\begin{aligned} \theta_K &\to \pi - \theta_K \\ \theta_L &\to \pi - \theta_L \\ \phi &\to -\phi\,, \end{aligned} \tag{1.3}$$

what results in translations of the observables listed in Table 1.2.

Table 1.2: Mistag translations of trigonometric functions found in the angular distribution of the signal mode.

Correct tag	**Incorrect tag**	**Correct tag**	**Incorrect tag**
$\theta_{K,L}$	$\pi - \theta_{K,L}$	ϕ	$-\phi$
$\cos\theta$	$\cos(\pi-\theta) = -\cos\theta$	$\cos\phi$	$\cos -\phi = \cos\phi$
$\sin\theta$	$\sin(\pi-\theta) = \sin\theta$	$\sin\phi$	$\sin -\phi = -\sin\phi$
$\cos 2\theta$	$\cos(2\pi-2\theta) = \cos 2\theta$	$\cos 2\phi$	$\cos -2\phi = \cos 2\phi$
$\sin 2\theta$	$\sin(2\pi-2\theta) = -\sin 2\theta$	$\sin 2\phi$	$\sin -2\phi = -\sin 2\phi$
$\cos^2\theta$	$\cos^2(\pi-\theta) = \cos^2\theta$	-	-
$\sin^2\theta$	$\sin^2(\pi-\theta) = \sin^2\theta$	-	-

Additionally, the wrong mass hypotheses for kaon and pion tracks result in different reconstructed K^* momentum. This influences most significantly the measurement of angle θ_K as will be shown in Section 4.3.

1.4.2 Differential decay rate

The differential decay rate distribution of $B^0 \to K^* \mu^+ \mu^-$ as a function of θ_K, θ_L, ϕ and q^2 can be derived in many ways, one of which is described in [30]. Squaring the decay matrix element, summing over spins of the final state particles and neglecting lepton masses one gets the full angular distribution as a sum of products of trigonometric functions of angles (originating from spherical harmonics) and angular observables I_i as

$$\frac{\mathrm{d}^4\Gamma}{\mathrm{d}q^2\,\mathrm{d}\overrightarrow{\Omega}} = \frac{9}{32\pi} I(q^2, \theta_K, \theta_L, \phi)\,,$$

where $\overrightarrow{\Omega} = (\cos\theta_K, \cos\theta_L, \phi)$ and

$$\begin{aligned} I(q^2, \theta_K, \theta_L, \phi) = {} & I_1^s \sin^2\theta_K + I_1^c \cos^2\theta_K + (I_2^s \sin^2\theta_K + I_2^c \cos^2\theta_K)\cos 2\theta_L \\ & + I_3 \sin^2\theta_K \sin^2\theta_L \cos 2\phi + I_4 \sin 2\theta_K \sin 2\theta_L \cos\phi + I_5 \sin 2\theta_K \sin\theta_L \cos\phi \\ & + (I_6^s \sin^2\theta_K + I_6^c \cos^2\theta_K)\cos\theta_L + I_7 \sin 2\theta_K \sin\theta_L \sin\phi \\ & + I_8 \sin 2\theta_K \sin 2\theta_L \sin\phi + I_9 \sin^2\theta_K \sin^2\theta_L \sin 2\phi \end{aligned}$$

Angular parameters I_i are functions of q^2 only and depend on complex amplitudes $\mathcal{A}_{0,\parallel,\perp}^{\mathrm{L,R}}$ of the K^* decay in the transversity basis and chirality of the lepton current. Explicit formulae and coefficients can be found in [30].[5]

The decay rate of the CP-conjugated decay $\overline{B}^0 \to \overline{K}^* \mu^+ \mu^-$ can be expressed similarly as a function of the parameters $\overline{I}_i$. Because of the definition of angles in the theoretical convention, some coefficients have an opposite sign for the decay of $\overline{B}^0$ ($I^{(a)}_{5,6,8,9} \to -\overline{I}^{(a)}_{5,6,8,9}$, $I^{(a)}_{1,2,3,4,7} \to \overline{I}^{(a)}_{1,2,3,4,7}$) but this is not the case for the experimental convention.

To separate the CP-conserving and CP-violating effects, it is convenient to define CP-averaged angular coefficients

$$S_i^{(a)} = \left(I_i^{(a)} + \bar{I}_i^{(a)}\right) \Big/ \frac{\mathrm{d}(\Gamma + \bar{\Gamma})}{\mathrm{d}q^2}$$

and CP asymmetries

$$A_i^{(a)} = \left(I_i^{(a)} - \bar{I}_i^{(a)}\right) \Big/ \frac{\mathrm{d}(\Gamma + \bar{\Gamma})}{\mathrm{d}q^2}\,.$$

which depend only on q^2. The $S_i^{(a)}$ observables offer a clean way to describe the decay phenomenology because the CP-violating effects are washed out. For the experiments this also means fitting one distribution to a dataset containing candidates for decays of both B^0 and $\overline{B}^0$, resulting in smaller statistical uncertainties. Parameters $A_i^{(a)}$ are expected to be small in the Standard Model so any new physics enhancing the CP violation can be easily identified.

As is shown in Ref. [30], due to small lepton masses compared to q^2, the S_6^c parameter is suppressed and the following relations can be derived

$$S_1^s = 3S_2^s, \quad S_1^c = -S_2^c, \quad 4S_2^s + S_1^c = 1.$$

This reduces the number of CP-averaged observables from twelve to eight. By definition, parameter S_1^c corresponds to the fraction of longitudinal polarisation of the K^* meson F_L. It is also conventional to replace S_6^s by the forward-backward asymmetry of the dimuon system as

$$A_{FB} = \frac{3}{4} S_6.$$

The resulting differential decay rate is

$$\begin{aligned}
\frac{1}{\mathrm{d}(\Gamma + \overline{\Gamma})/\mathrm{d}q^2} \frac{\mathrm{d}^4(\Gamma + \overline{\Gamma})}{\mathrm{d}q^2 \mathrm{d}\overrightarrow{\Omega}} = \qquad (1.4)\\
\frac{9}{32\pi} \Bigg[\frac{3}{4}(1 - F_L)\sin^2\theta_K + F_L \cos^2\theta_K + \frac{1}{4}(1 - F_L)\sin^2\theta_K \cos 2\theta_L \\
- F_L \cos^2\theta_K \cos 2\theta_L + S_3 \sin^2\theta_K \sin^2\theta_L \cos 2\phi \\
+ S_4 \sin 2\theta_K \sin 2\theta_L \cos\phi + S_5 \sin 2\theta_K \sin\theta_L \cos\phi \\
+ S_6 \sin^2\theta_K \cos\theta_L + S_7 \sin 2\theta_K \sin\theta_L \sin\phi \\
+ S_8 \sin 2\theta_K \sin 2\theta_L \sin\phi + S_9 \sin^2\theta_K \sin^2\theta_L \sin 2\phi \Bigg].
\end{aligned}$$

[5] In the literature, term with I_6^c is sometimes omitted because it is suppressed by small lepton mass and I_6^s is denoted as I_6.

Additional observables can be built from F_L and S_i in a way that the form-factor uncertainties cancel. As is shown in [36], a set of eight observables can fully describe the decay in an approximation of massless leptons. The proposed set of observables is $\{\mathrm{d}\Gamma/\mathrm{d}q^2, F_L, P_1, ..., P_6\}$, where parameters P_i are form-factor independent but $\mathrm{d}\Gamma/\mathrm{d}q^2$ and F_L suffer from form-factor uncertainties. It is advantageous to slightly redefine the last three parameters and measure P_4', P_5' and P_6', because these new quantities depend less on averaging of observables over the bin sizes [37]. The resulting set of optimised observables is then

$$P_1 = \frac{2S_3}{(1-F_L)} = A_{\mathrm{T}}^{(2)} \tag{1.5}$$

$$P_2 = \frac{S_6}{2(1-F_L)} = \frac{2A_{FB}}{3(1-F_L)} \tag{1.6}$$

$$P_3 = \frac{-S_9}{1-F_L} \tag{1.7}$$

$$P'_{4,5,8} = \frac{S_{4,5,8}}{\sqrt{F_L(1-F_L)}} \tag{1.8}$$

$$P_6' = \frac{S_7}{\sqrt{F_L(1-F_L)}}. \tag{1.9}$$

Here $A_{\mathrm{T}}^{(2)}$ is the transverse polarisation asymmetry. While observables $P_{1-6}^{(\prime)}$ are independent observables, P_8' is not as it can be constructed from a combination of other $P_i^{(\prime)}$, F_L and $\mathrm{d}\Gamma/\mathrm{d}q^2$. Its measurement is still an important check of the consistency with other observables.

1.4.3 Reducing the number of observables

Because of a limited number of candidates in the dataset available for analysis described in this thesis (dataset collected in 2012 by the ATLAS experiment), fitting the full angular distribution (1.4) would result in an unstable fit and big systematic uncertainties. It is, however, possible to apply transformations which use symmetries of trigonometric functions and reduce the number of parameters in the fit without losing experimental sensitivity. This is referred to as *folding*. [6]

The analysis described here uses a set of four transformations proposed by the LHCb collaboration in [35] and described in detail in [38]. Each transformation preserves the first five terms and the corresponding S_i term in (1.4) while cancelling the remaining of angular terms. The resulting distributions depend only on three variables: F_L, S_3 and one of $S_{4,5,7,8}$. Sensitivity to other angular parameters is lost, i.e S_6, S_9 and the related parameters A_{FB}, P_2 and P_3 cannot be measured.

Transformations for S_4: The following transformations are applied to (1.4) to obtain differential decay rate as a function of F_L, S_3 and S_4:

$$S_4, P_4^{'}: \begin{cases} \phi \to -\phi & \text{for } \phi < 0 \\ \phi \to \pi - \phi & \text{for } \theta_L > \frac{\pi}{2} \\ \theta_L \to \pi - \theta_L & \text{for } \theta_L > \frac{\pi}{2}. \end{cases} \tag{1.10}$$

[6] Other folding schemes are sensitive to different parameters of angular distributions, e.g. to *CP*-asymmetries A_i. This analysis was focused on measurement of the P_5'.

The angular ranges are then

$$\begin{aligned} \theta_K \in [0,\pi], \qquad & \theta_L \in [0,\pi/2], \qquad & \phi \in [0,\pi], \\ \cos\theta_K \in [-1,1], \qquad & \cos\theta_L \in [0,1] \end{aligned} \tag{1.11}$$

and the differential decay rate is

$$\begin{aligned} \frac{1}{\mathrm{d}(\Gamma+\overline{\Gamma})/\mathrm{d}q^2}\frac{\mathrm{d}^4(\Gamma+\overline{\Gamma})}{\mathrm{d}q^2\mathrm{d}\overrightarrow{\Omega}} =& \frac{9}{8\pi}\Bigg[\frac{3}{4}(1-F_L)\sin^2\theta_K + F_L\cos^2\theta_K \\ &+ \frac{1}{4}(1-F_L)\sin^2\theta_K\cos 2\theta_L - F_L\cos^2\theta_K\cos 2\theta_L \\ &+ S_3\sin^2\theta_K\sin^2\theta_L\cos 2\phi + S_4\sin 2\theta_K\sin 2\theta_L\cos\phi\Bigg]. \end{aligned} \tag{1.12}$$

Transformations for S_5:

$$S_5, P_5^{'}: \begin{cases} \phi \to -\phi & \text{for } \phi < 0 \\ \theta_L \to \pi - \theta_L & \text{for } \theta_L > \frac{\pi}{2}, \end{cases} \tag{1.13}$$

with angular ranges

$$\begin{aligned} \theta_K \in [0,\pi], \qquad & \theta_L \in [0,\pi/2], \qquad & \phi \in [0,\pi], \\ \cos\theta_K \in [-1,1], \qquad & \cos\theta_L \in [0,1] \end{aligned} \tag{1.14}$$

and differential decay rate

$$\begin{aligned} \frac{1}{\mathrm{d}(\Gamma+\overline{\Gamma})/\mathrm{d}q^2}\frac{\mathrm{d}^4(\Gamma+\overline{\Gamma})}{\mathrm{d}q^2\mathrm{d}\overrightarrow{\Omega}} =& \frac{9}{8\pi}\Bigg[\frac{3}{4}(1-F_L)\sin^2\theta_K + F_L\cos^2\theta_K \\ &+ \frac{1}{4}(1-F_L)\sin^2\theta_K\cos 2\theta_L - F_L\cos^2\theta_K\cos 2\theta_L \\ &+ S_3\sin^2\theta_K\sin^2\theta_L\cos 2\phi + S_5\sin 2\theta_K\sin\theta_L\cos\phi\Bigg]. \end{aligned} \tag{1.15}$$

Transformations for S_7:

$$S_7, P_6^{'}: \begin{cases} \phi \to \pi - \phi & \text{for } \phi > \frac{\pi}{2} \\ \phi \to -\pi - \phi & \text{for } \phi < -\frac{\pi}{2} \\ \theta_L \to \pi - \theta_L & \text{for } \theta_L > \frac{\pi}{2}, \end{cases} \tag{1.16}$$

with angular ranges

$$\begin{aligned} \theta_K \in [0,\pi], \qquad & \theta_L \in [0,\pi/2], \qquad & \phi \in [-\pi/2,\pi/2], \\ \cos\theta_K \in [-1,1], \qquad & \cos\theta_L \in [0,1] \end{aligned} \tag{1.17}$$

and the differential decay rate

$$\begin{aligned} \frac{1}{\mathrm{d}(\Gamma+\overline{\Gamma})/\mathrm{d}q^2}\frac{\mathrm{d}^4(\Gamma+\overline{\Gamma})}{\mathrm{d}q^2\mathrm{d}\overrightarrow{\Omega}} =& \frac{9}{8\pi}\Bigg[\frac{3}{4}(1-F_L)\sin^2\theta_K + F_L\cos^2\theta_K \\ &+ \frac{1}{4}(1-F_L)\sin^2\theta_K\cos 2\theta_L - F_L\cos^2\theta_K\cos 2\theta_L \\ &+ S_3\sin^2\theta_K\sin^2\theta_L\cos 2\phi + S_7\sin 2\theta_K\sin\theta_L\sin\phi\Bigg]. \end{aligned} \tag{1.18}$$

Transformations for S_8:

$$S_8, P_8^{'}: \begin{cases} \phi \to \pi - \phi & \text{for } \phi > \frac{\pi}{2} \\ \phi \to -\pi - \phi & \text{for } \phi < -\frac{\pi}{2} \\ \theta_L \to \pi - \theta_L & \text{for } \theta_L > \frac{\pi}{2} \\ \theta_K \to \pi - \theta_K & \text{for } \theta_L > \frac{\pi}{2}, \end{cases} \tag{1.19}$$

with angular ranges

$$\begin{aligned} \theta_K \in [0, \pi], \qquad & \theta_L \in [0, \pi/2], \qquad \phi \in [-\pi/2, \pi/2], \\ \cos\theta_K \in [-1, 1], \qquad & \cos\theta_L \in [0, 1] \end{aligned} \tag{1.20}$$

and differential decay rate

$$\begin{aligned} \frac{1}{\mathrm{d}(\Gamma + \overline{\Gamma})/\mathrm{d}q^2} \frac{\mathrm{d}^4(\Gamma + \overline{\Gamma})}{\mathrm{d}q^2 \mathrm{d}\overrightarrow{\Omega}} = & \frac{9}{8\pi} \Bigg[\frac{3}{4}(1 - F_L)\sin^2\theta_K + F_L \cos^2\theta_K \\ & + \frac{1}{4}(1 - F_L)\sin^2\theta_K \cos 2\theta_L - F_L \cos^2\theta_K \cos 2\theta_L \\ & + S_3 \sin^2\theta_K \sin^2\theta_L \cos 2\phi + S_8 \sin 2\theta_K \sin 2\theta_L \sin\phi \Bigg]. \end{aligned} \tag{1.21}$$

1.4.4 Experimental status

The first experiments to measure angular parameters A_{FB} and F_L of decay $B^0 \to K^*\mu^+\mu^-$ were BaBar and Belle in 2008 and 2009 respectively [6, 7]. In 2011 the CDF collaboration published their measurements, adding two new observables $A_{\mathrm{T}}^{(2)}$ and A_{Im} [8]. However, these analyses respectively observed only about 60, 230 and 164 events in their datasets. All three experiments used projections in one of the angles to extract the observables because a fit in more than one angle was not possible with such a small number of candidates. The BaBar and Belle measurements of A_{FB} in the low-q^2 region seemed to hint a deviation from the SM, while the CDF results could not confirm nor exclude this conclusion.

In 2013 the LHCb collaboration published the first measurements of angular observables F_L, A_{FB}, S_3, S_9, A_9 , $A_{\mathrm{T}}^{(2)}$ and $A_{\mathrm{T}}^{\mathrm{Re}}$ [34] and soon after a measurement of form-factor independent observables P_i [35]. Both measurements used $1\,\mathrm{fb}^{-1}$ of pp collision data collected in 2011. All measurements agreed with the SM within uncertainties, except the P_5' which showed a discrepancy of 3.7 standard deviations from predictions in one q^2 bin.

Since then, the CMS [9,39] and Belle collaborations [10,11] published measurements of F_L, A_{FB} (CMS only) and of optimised variables P_4' and P_5'. The BaBar collaboration measured the values of F_L, A_{FB} and P_2 in a dataset containing $B^0 \to K^*\mu^+\mu^-$ and $B^0 \to K^*e^+e^-$ candidates [40].

The most precise measurements come from the analysis of the whole LHC Run 1 dataset by the LHCb collaboration [12] (integrated luminosity of $3\,\mathrm{fb}^{-1}$). Thanks to a larger number of observed decay candidates, the analysis could be performed in smaller q^2 bins and fitting of the full angular distribution became possible without folding. The results of CP asymmetries $A_{3,4,5,6,7,8,9}$ and parameters F_L, A_{FB}, S_i and P_i were consistent with the theoretical predictions for

SM, except of P_5' which confirmed a discrepancy of 2.9 standard deviations from the SM predictions in q^2 bins of 4–6 and 6–8 GeV^2. A χ^2 fit of measured values of the CP-averaged observables F_L, A_{FB} and S_3-S_9 was also performed. Assuming that the discrepancies with respect to the SM can be accounted for by modifying only the real part of the Wilson coefficient C_9, the fitted value of $Re(C_9)$ is shifted from the SM prediction by $\Delta Re(C_9) = -1.04 \pm 0.25$, corresponding to 3.4 standard deviations. The obtained values of P_5' parameter and χ^2 fit of $Re(C_9)$ are shown in Figure 1.7. The latest results of angular analyses come from the CMS collaboration [13] and from the ATLAS collaboration [16] which are presented in this thesis.

The most recent hints of deviations from the SM are the measurements of lepton flavour universality in $B \to K^{(*)}\ell\ell$ for $\ell = e$ and μ, published by the LHCb collaboration [2, 3]. The measured ratios of branching fractions $R_{K^{(*)}} = \mathcal{B}_\mu/\mathcal{B}_e$ are shown in Figure 1.8, together with the predictions of SM and some BSM scenarios. The single deviations are at the level of $\sim 2.5\sigma$ but the global fits of $b \to s\ell\ell$ observables show a tension with the SM that needs to be studied both experimentally and theoretically.

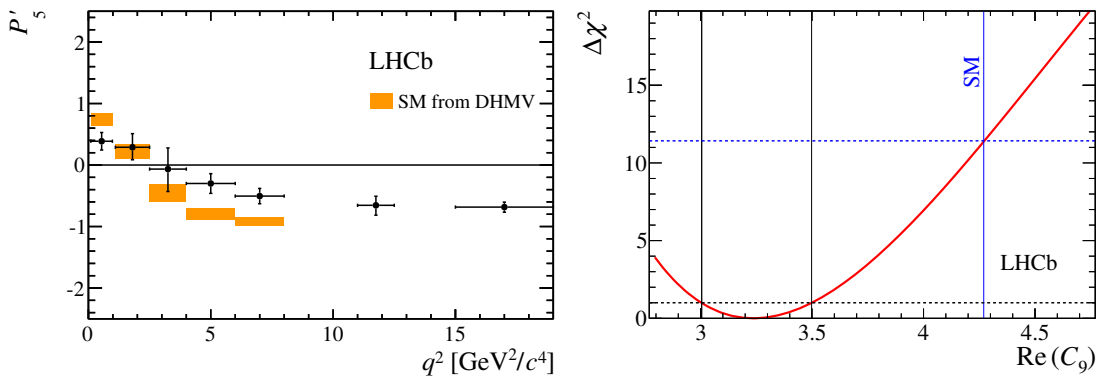

Figure 1.7: LHCb measurement of the $B^0 \to K^*\mu^+\mu^-$ parameter P_5' in bins of q^2 (left) and the χ^2 fit of the real part of C_9 Wilson coefficient computed from the measured values of F_L, A_{FB} and S_3-S_9 (right) [12].

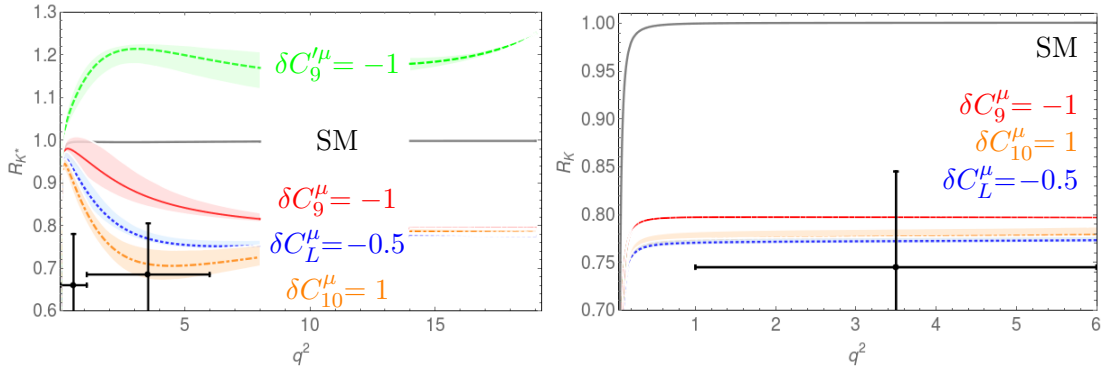

Figure 1.8: $R_{K^{(*)}}$ parameters measured by LHCb (crosses), together with predictions of various BSM scenarios with alternated values of Wilson coefficients [41].

2. The Large Hadron Collider

The Large Hadron Collider (LHC) [42] at the European Laboratory for Particle Physics (CERN)[1] in Geneva, Switzerland, is a hadron collider designed to provide significantly higher energies and luminosities than achieved before. Among the main motivations for the LHC and its experiments are precision measurements of the SM and search for the Higgs boson, candidates for dark matter and other phenomena beyond the SM.

CERN accelerator complex

The LHC is supplied with protons from a duoplasmatron source using ionisation of hydrogen gas. Protons are accelerated by the injector chain Linac2 — Proton Synchrotron Booster (PSB) — Proton Synchrotron (PS) — Super Proton Synchrotron (SPS). The energy is increased in steps from 50 MeV after Linac2 to 1.4 GeV, 25 GeV and 450 GeV, which is the injection energy into the LHC. The injectors existed before the proposal of LHC but had to be upgraded to provide the beam quality needed for LHC design goals.

The collider is installed in the 26.7 km long tunnel previously used by CERN's Large Electron-Positron Collider (LEP), which lies between 45 and 170 m below the surface. As is shown in Figure 2.1, there are eight arcs with dipole magnets bending the particle trajectory and eight straight sections with caverns, access shafts and possible collision points (usually denoted as Point 1 to Point 8 or P1-P8). Big detectors are installed at four interaction points: ATLAS at P1, ALICE at P2, CMS at P5 and LHCb at P8. The other points are used for radio-frequency accelerating cavities (P4), beam dump (P6) and momentum and betatron beam cleaning (P3 and P7). There are two transfer lines from SPS to LHC, each approximately 2.5 km long, injecting the clockwise beam before P2 and anticlockwise before P8.

The magnetic field in the arcs is provided by 1232 superconducting twin-bore dipole magnets, producing opposite magnetic field of 8.33 T (for the nominal energy of 7 TeV) in two vacuum chambers with a horizontal separation of 194 mm. The beams share a common beam pipe for approximately 130 m before and after each experiment. In addition, there are focusing and correcting magnets around the ring.

The LHC beam structure

The majority of the physics programme on LHC is based on proton-proton collisions with centre-of-mass energy of up to 14 TeV and design luminosity of $10^{34}\,\mathrm{cm}^{-2}\mathrm{s}^{-1}$. The accelerator also provides a possibility to accelerate and collide lead ions at energy of 2.8 TeV per nucleon and luminosity of $10^{27}\,\mathrm{cm}^{-2}\mathrm{s}^{-1}$ ($^{208}_{82}$Pb isotope). Additionally, proton-lead collisions are possible and running with other nuclei is considered (e.g. $^{129}_{54}$Xe collisions tests in 2017).

The LHC beam is composed of proton bunches with typically $1 - 2 \times 10^{11}$ protons per bunch (design value is 1.15×10^{11}). The radio-frequency cavities

[1] Acronym retained from French *Conseil Européen pour la Recherche Nucléaire* or European Council for Nuclear Research which established the laboratory.

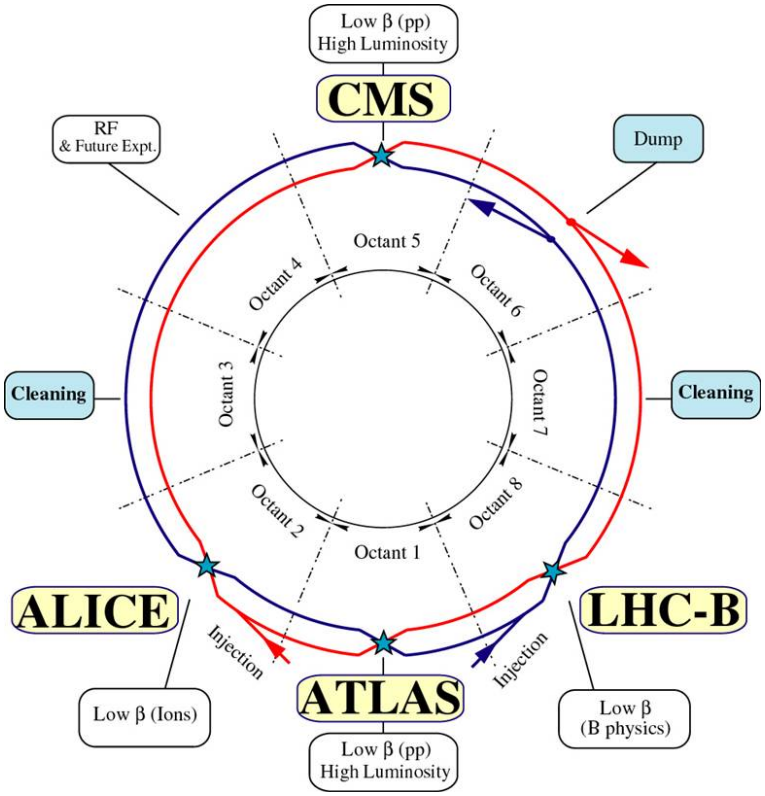

Figure 2.1: The schematic layout of LHC [42].

providing the acceleration of beams operate at a frequency of 400 MHz. This corresponds to a possible bunch position (bucket) every 2.5 ns, of which nominally every tenth can contain a proton bunch. To describe the filling patterns, groups of ten buckets are assigned the same Bunch Crossing IDentifier (BCID) of which there are 3564 in total. Due to limitations of the injector chain and injection process, the bunches are injected in trains with gaps between them. In addition, a 3 µs long gap is left in the end of the cycle, corresponding to the rise-time of the kicker magnets in the beam abort system, bringing the maximum number of bunches down to the design value of 2808. The first BCID after the abort gap is numbered as 1.

Typically, about 95 % of proton bunches are colliding in ATLAS. The pattern includes also empty bunches and a small fraction of non-colliding, unpaired bunches. Empty bunches are important for monitoring of detector noise, while the unpaired bunches (in trains or isolated) are used for monitoring of beam-induced background.

LHC performance and perspectives

The LHC operation is planned in data-taking runs, interleaved with shorter or longer technical stops for maintenance and upgrades. The Run 1 started in 2009 and from the machine point of view, the period 2009-10 was still a commissioning phase, used to gain experience in operational procedures and to reach the design parameters. Years 2011-12 were devoted to collection of a large datasets of pp collisions. The total integrated luminosity delivered to ATLAS and CMS in 2011 at $\sqrt{s}$ =7 TeV was about 6.1 fb^{-1} and in 2012 at $\sqrt{s}$ =8 TeV about 23.1 fb^{-1} [43].

Table 2.1: The LHC operating parameters: the design parameters are from [42], 2012 values are from [43], LHC Run 2 parameters reached in 2017 were presented at the LHC Evian workshop [44] and HL-LHC parameters are taken from [45].

Parameter	**Design**	**Run 1 (2012)**	**Run 2 (2017)**	**HL-LHC (2026)**
Total beam energy [TeV]	14	8	13	14
Average p/bunch [10^{11}]	1.15	1.65	2.06	2.2
Bunches	2808	1380	2556	2748
Bunch spacing [ns]	25	50	25	25
β^* [cm]	55	60	40–30	20
Peak luminosity[$\mathrm{cm}^{-2}\mathrm{s}^{-1}$]	10^{34}	7.7×10^{33}	2×10^{34}	$5 - 7.5 \times 10^{34}$
Maximum pile-up	19	40	70[a]	140-200[b]

[a] Peak luminosity and pile-up in physics fills, without levelling. [b] Levelled luminosity.

The nominal bunch spacing in proton runs in the 2009-2012 run period was 50 ns, i.e. every second BCID was filled.

Run 1 was followed by the Long Shutdown 1 (LS1) in 2013-14 which was used for improvements of many LHC and detector systems. Among the most important interventions were consolidations of the electrical connections between the LHC superconducting magnets, which allowed to increase the centre-of-mass energy in Run 2 to 13 TeV. Since 2015 LHC has operated with 25 ns bunch spacing and the number of bunches and the peak instantaneous luminosity were increased progressively. The beam emittance from injectors was also reduced and the β^* value reached 40 and 30 cm in 2016 and 2017, respectively (the design value is 55 cm).[2] In 2017 the instantaneous luminosity in the beginning of fills often reached twice the design value and a luminosity levelling to about $1.5 \times 10^{34}\,\mathrm{cm}^{-2}\mathrm{s}^{-1}$ had to be implemented so the detectors could deal with the increased pile-up.[3] These improvements and high availability of the accelerator complex allowed ATLAS and CMS to collect datasets with integrated luminosity of $50\,\mathrm{fb}^{-1}$ in 2017 alone [44].

The LHC performance achieved in Run 1 (2012) and Run 2 (2017) is summarised in Table 2.1, together with design and proposed upgrade parameters.

The preliminary LHC plans for the next few years are described in Ref. [45] and shown in Figure 2.2. Year 2018 will be the last year of data taking in Run 2. Next two years of LS2 will be used for injector upgrades (replacement of Linac2 by Linac4, increase of PS Booster energy), consolidation of the LHC infrastructure and training of the superconducting magnets to reach the current needed for acceleration of protons beams to energy of 7 TeV during LHC Run 3. The goal is to deliver a total of about $300\,\mathrm{fb}^{-1}$ until the end of Run 3 in 2023.

A major LHC upgrade is planned during LS3, referred to as High-Luminosity Large Hadron Collider (HL-LHC). The proposed nominal (ultimate) instantan-

[2] β^* is the value of beam amplitude function β at the interaction point. Lower β^* value means smaller beam size and higher achievable instantaneous luminosity.

[3] Pile-up refers to the number of inelastic pp collisions per one bunch crossing.

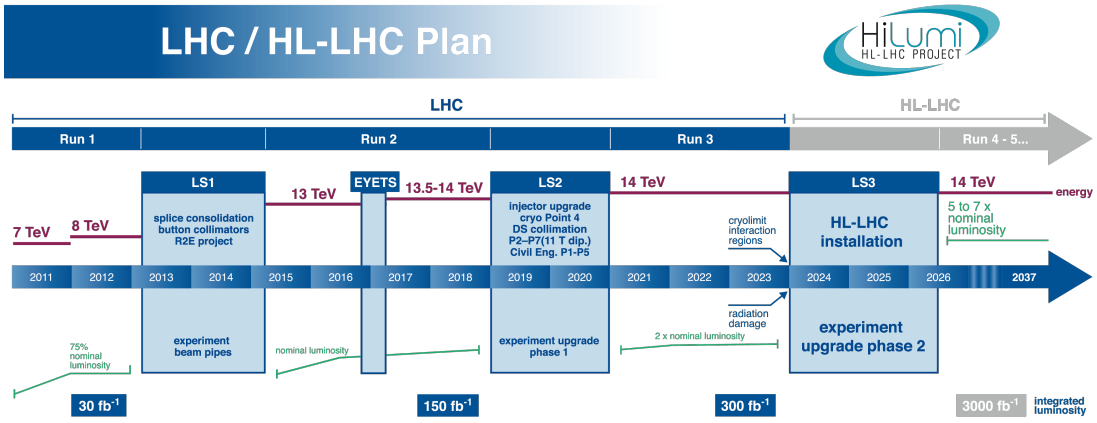

Figure 2.2: LHC and HL-LHC preliminary plans [45].

eous luminosity of $5(7.5) \times 10^{34}\,\mathrm{cm}^{-2}\mathrm{s}^{-1}$ translates to about 140 (200) proton-proton collisions per bunch crossing and the projected integrated luminosity delivered until 2037 is about $3000\,\mathrm{fb}^{-1}$. This presents a challenging environment for the ATLAS detector, well beyond the conditions for which it was designed. The upgrade projects planned by the ATLAS collaboration will be shortly described in Section 3.8.

3. The ATLAS experiment

ATLAS (A Toroidal LHC ApparatuS) [46] is one of the four big experiments at the LHC. It was designed as a general-purpose particle detector capable of detecting a wide range of final states expected at the TeV energy scale. To enable precision measurements of SM processes with small cross-sections and search for new physics phenomena, the LHC collides beams with the highest energy and interaction rate achievable today. The resulting events contain the collisions of interest accompanied by tens of inelastic scattering collisions per bunch crossing. This presents serious experimental difficulties and requires reconstruction and identification of particles in a large kinematic range with very high resolution and large angular acceptance. Moreover, the high collision frequency and high energy of LHC result in high particle fluxes which require fast, radiation-hard detectors and readout electronics with high granularity.

The overall layout of the ATLAS detector is illustrated in Figure 3.1 and its required performance parameters are listed in Table 3.1. Particles produced in the Interaction Point (IP) in the middle of the detector pass through a thin beryllium beam pipe and the tracking system, the Inner Detector (ID) which is immersed in a 2 T solenoidal magnetic field. Their energy is then measured in the electromagnetic and hadronic calorimeters. Finally, the escaping muons are identified in the outermost layer, the Muon Spectrometer (MS), which also measures their momenta. The choice of technology, performance requirements and layout of subdetectors was guided by simulation studies of selected processes from the experimental programme of ATLAS.

ATLAS uses a right-handed coordinate system which has its origin in the nominal interaction point and the beam direction defines the z-axis. The positive x-axis points to the centre of the LHC ring, and the positive y-axis points upwards. The azimuthal angle ϕ is measured around the z-axis with $\phi = 0$ on the positive x-axis and the polar angle θ is the angle from the positive z-axis. The pseudorapidity η is defined as $\eta = -\ln\tan(\theta/2)$. The side A of the detector is defined as that with positive z (toward the LHC Point 8) and side C that with negative z coordinates.

The detector, magnets, trigger and data acquisition systems will be described

Table 3.1: Performance requirements of the ATLAS detector. Energy E and transverse momentum p_{T} are in units of GeV [46].

Detector system	**Resolution**	**Measurement**	**Trigger**
Tracking	$\sigma_{p_{\mathrm{T}}}/p_{\mathrm{T}} = 0.05\% p_{\mathrm{T}} \oplus 1\%$	$\lvert\eta\rvert < 2.5$	–
EM calorimeter	$\sigma_E/E = 10\%/\sqrt{E} \oplus 0.7\%$	$\lvert\eta\rvert < 3.2$	$\lvert\eta\rvert < 2.5$
Hadronic calorimeter			
- barrel and endcap	$\sigma_E/E = 50\%/\sqrt{E} \oplus 3\%$	$\lvert\eta\rvert < 3.2$	
- forward	$\sigma_E/E = 100\%/\sqrt{E} \oplus 10\%$	$3.1 < \lvert\eta\rvert < 4.9$	
Muon spectrometer	$\sigma_{p_{\mathrm{T}}}/p_{\mathrm{T}} = 10\%$ at 1 TeV	$\lvert\eta\rvert < 2.7$	$\lvert\eta\rvert < 2.4$

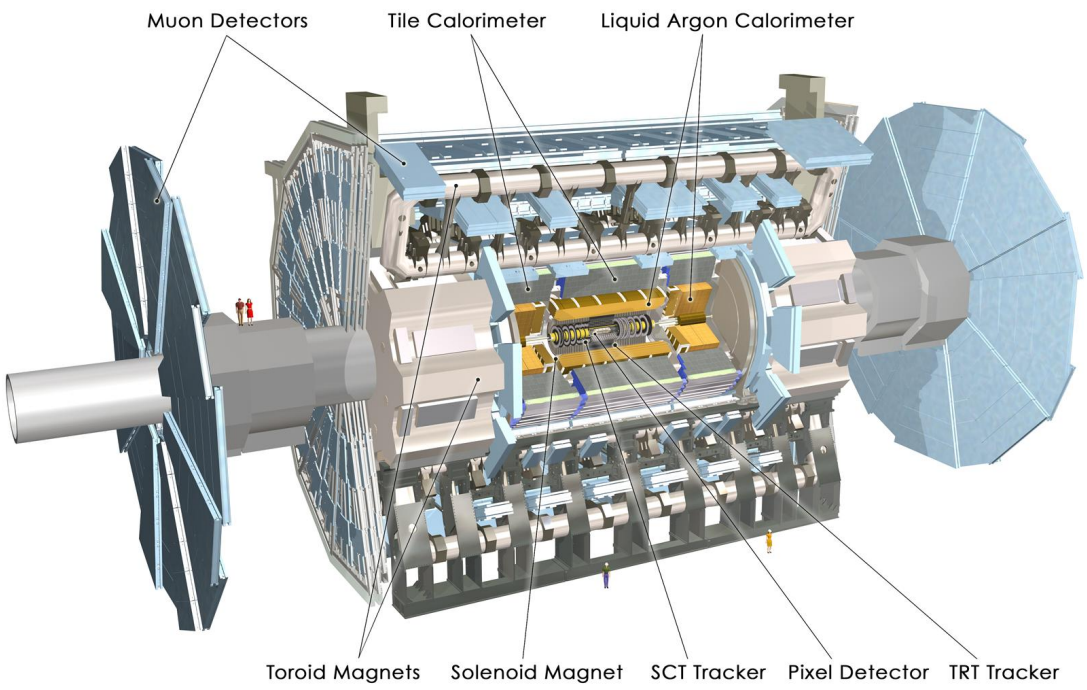

Figure 3.1: Schematic view of the ATLAS detector [46].

in the following sections using mostly information given in Ref. [46]. The emphasis will be given to the aspects that are needed to understand the subsequent analysis chapters (e.g. tracking, muon detectors and triggering). The detector status and performance will be quoted as of 2012 (end of Run 1 of LHC). Section 3.8 will outline improvements implemented since then and the upgrade projects in preparation.

3.1 Inner Detector

The ID provides track reconstruction and high-resolution momentum measurements for charged particles in the pseudorapidity range $|\eta| < 2.5$. It is also used for electron identification in the $|\eta| < 2.0$ region. This is achieved by a combination of three independent subsystems: semiconductor Pixel and microstrip SemiConductor Tracker (SCT) detectors in the inner part and straw-tube Transition Radiation Tracker (TRT) in the outer part of the tracking volume.

The ID surrounds the beam pipe and is enclosed inside a solenoid magnet in a cylindrical volume of radius 1.15 m and length of 7 m. The elements of the silicon detectors are arranged in concentric layers at the central section (barrel) and in disks perpendicular to the beam axis in the forward sections (endcaps). The layout of barrel and endcap sections of ID is shown in Figure 3.2. The granularity is maximum close to the IP to cope with high particle fluxes. Pixel sensors are segmented in $(R - \phi)$ and z direction and particle tracks cross typically three layers. For the SCT, eight strip layers give four additional space points. In the $|\eta| < 2.0$ region a large number of hits (typically 36) from TRT contribute to momentum measurement. The lower precision per single point is compensated by a higher number of hits over the longer track path.

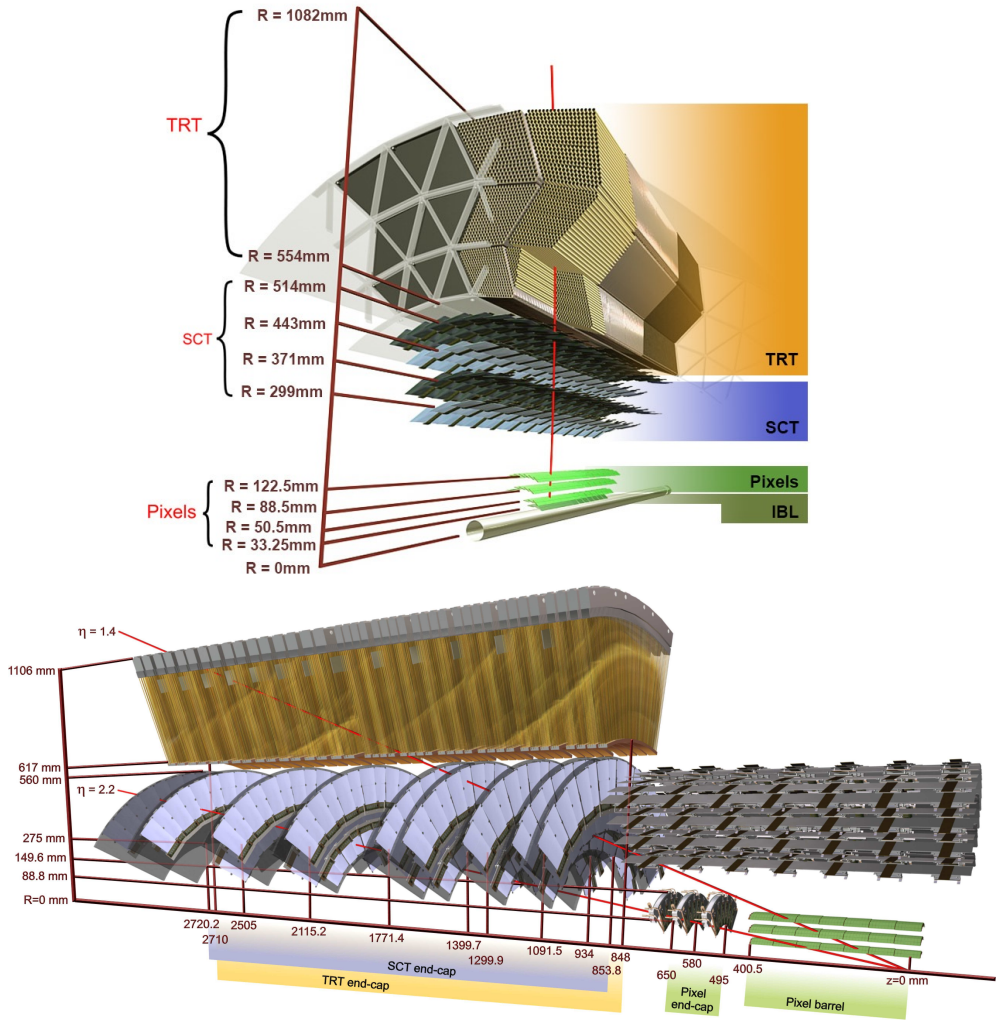

Figure 3.2: Layout of the ATLAS Inner Detector barrel and endcap regions. Figures include a simulated particle track with p_{T} =10 GeV. [46, 47]

Pixel detector

The Pixel detector consists of three layers in the barrel region and four disks in each endcap. The sensors are 250 µm thick oxygenated n-type wafers with pixels on the n^+-doped side and an active area of $16.4 \times 60.8\,\mathrm{mm}^2$. The n^+-in-n design gives high radiation tolerance and improved charge collection after type inversion even below depletion voltage, because the depletion zone grows from the pixel side.

A schematic view of a barrel pixel module is shown in Figure 3.3. Each sensor is read out by 16 chips that are bump-bonded to pixels. A flexible Printed-Circuit Board (PCB) glued to flex-hybrid provides power, readout and module control. Each detector layer has a thickness of about 2.5 % of radiation length at normal incidence. Digital readout provides a measurement of charge deposited in the pixel by charged particles in the silicon, allowing a limited identification of particles with low momenta.

In total, there are 1744 sensors with 47232 pixels each, yielding approximately 80.4 million readout channels and a total area of about $1.7\,\mathrm{m}^2$. Pixels have a nominal size of 50 µm × 400 µm what translates to intrinsic accuracy of 10 µm ×

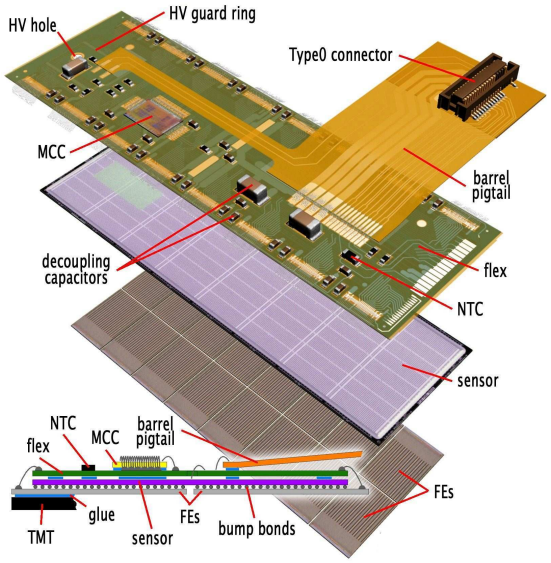

Figure 3.3: Components of a barrel pixel module: the front-end chips (FEs) are bump-bonded onto the silicon sensor. The supporting flex PCB carries the module-control chip (MCC), the NTC thermistors and the high-voltage (HV) elements [46].

115 µm in $(R-\phi)\times z$ in barrel and 10 µm × 115 µm in $(R-\phi)\times R$ in endcaps. Special long pixels (50 µm × 600 µm) and ganged pixels cover areas between front-end chips.

Semiconductor Tracker

The SCT is a silicon microstrip detector consisting of four barrel layers and nine forward disks in each endcap. The system is designed to contribute to momentum and track parameter measurements with a smaller number of readout channels than Pixel detector. This is achieved by using single-sided p^+-in-n sensors that are daisy-chained in pairs and form 768 strips with length of 12.8 cm. The sensor thickness is 285 µm.

Barrel modules are built from two pairs of rectangular sensors with strip pitch of 80 µm, glued back-to-back such that strips of one side are parallel with the beam axis and the second side is rotated by 40 mrad. This results in an intrinsic resolution of 17 µm × 580 µm in $(R-\phi)\times z$. Endcap modules are arranged in wheels and built from five types of sensors that have various shapes and strip pitches ranging from 56.9 µm to 94.2 µm. In total there are 4088 modules with 6.3 millions readout channels, covering a sensitive area of $\sim$63 m^2. More details about the readout electronics, operations and performance of the SCT during Run 1 of the LHC will be given in Section 5.2.

The radiation damage to Pixel and SCT sensors can be partially mitigated by cooling to low temperatures (approximately −5 °C to −15 °C, implying the C_2F_6/C_3F_8 coolant temperatures down to −25 °C). In contrast, the TRT is operated at room temperature.

Transition Radiation Tracker

The TRT is a gaseous drift detector used for track measurements and electron identification via the detection of transition radiation. The detector consists of 351.000 straw tubes with a diameter of 4 mm interleaved with polypropylene fibres (barrel) or foils (endcaps) acting as radiators. Each tube's wall (cathode) is made of 70 µm thick multi-layer foil, which is made of polyimide coated with thin films of aluminium, graphite-polyimide and polyurethane to achieve good electrical and mechanical properties with minimal wall thickness. The anodes are 31 µm thick gold-plated tungsten wires. Cathodes are typically operated at -1530 V to give a gain of 2.5×10^4 for gas mixture of 70 % Xe, 27 % CO_2 and 3 % O_2.

The straws in the barrel are 144 cm long and are arranged in 73 planes parallel with the beam direction. The anode wires are read out from both ends but electrically split in half by a glass capillary to reduce the occupancy. In this configuration, hit positions are measured only in the $(R - \phi)$ plane and the hit accuracy of about 130 µm is given by the uncertainty of drift time measurement. In the endcaps, 37 cm long straws form 160 planes with straws installed radially and anode wires read out from the outer side only.

The electron identification is possible thanks to the fact that the energy irradiated by transition radiation is proportional to particles Lorentz factor γ. Low-energy photons from transition radiation are absorbed in the xenon-based gas mixture and yield much larger signal amplitudes than minimum-ionising particles. The distinction between transition radiation and tracking signal can be then obtained on a straw-by-straw basis by setting two different thresholds in the front-end electronics. Typically 7 to 10 high-threshold hits provide a sufficient e/π separation for energies above 2 GeV.

Central solenoid

The solenoid magnet surrounds the ID and provides the magnetic field for measurement of momenta of charged particles. It is composed of a cylinder with a diameter of 2.56 m, length of 5.8 m and a 10 cm thick wall. The 2 T magnetic field is induced by a current of 7730 A in 1154 turns of Al-stabilised NbTi superconducting cable. The design and materials were optimised to keep the amount of material in front of the calorimeters as low as possible, resulting in a total of 0.66 radiation lengths. As a consequence, the central solenoid and barrel of the electromagnetic calorimeter share a common cryostat. The magnetic flux is returned by the steel of the hadronic calorimeter and its girder structure.

Beam Conditions Monitor

The ID region contains the Beam Conditions Monitor (BCM) that is designed to detect events when the primary LHC beam gets unstable or hits the collimators close to ATLAS and produces a high number of secondary particles. BCM can trigger a beam dump to prevent serious detector damage by high instantaneous radiation dose in such cases. It also provides bunch-by-bunch luminosity measurement and a minimum-bias trigger input.

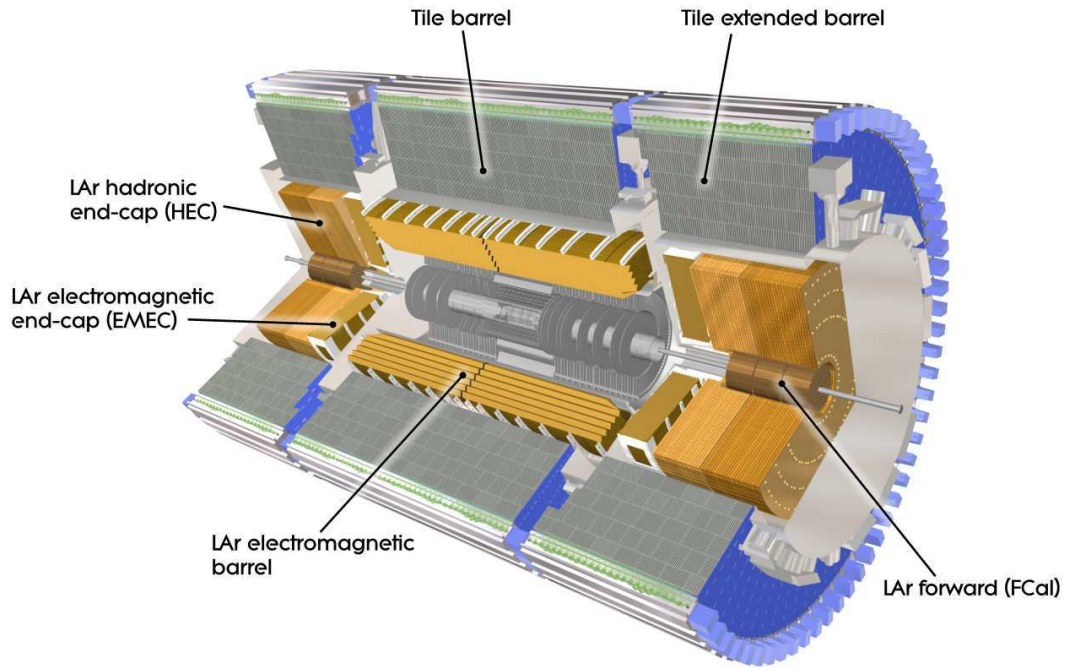

Figure 3.4: Layout of the ATLAS calorimeter system and its subsystems [46].

The detector consists of two stations, each with four modules installed symmetrically around the interaction point at $z = \pm 184\,\text{cm}$ and $R = 5.5\,\text{cm}$ (equivalent to $|\eta| = 4.2$). Each module has two $1 \times 1\,\text{cm}^2$ sensors (500 mm thick polycrystalline vapour-deposited diamond) with high radiation hardness and fast signal formation. The sensors have a bias of 1000 V and are read out in parallel by radiation-tolerant electronics. The difference in time of flight between stations can distinguish particles from collision point (time difference of 0, 25, 50 ns) and beam or beam-induced background particles (12.5, 37.5 ns, etc.).

3.2 Calorimeters

The ATLAS calorimeter system covers the range of $|\eta| < 4.9$ and consists of electromagnetic, hadronic and forward calorimeters. Different techniques and granularity are used based on requirements for resolution and radiation conditions. All subsystems are constructed as sampling calorimeters, combining a high-density absorber (lead, iron, copper or tungsten) with liquid argon or plastic scintillator as detecting medium.

A schematic view of the calorimeter system is shown in Figure 3.4. The electromagnetic Liquid Argon Calorimeter (LAr) is divided into a barrel (referred to as EMB) and two endcap components (EMEC). The EMB shares a common vacuum vessel with the central solenoid. Each of the two endcap cryostats contains EMEC, two coaxial wheels of Hadronic Endcap Calorimeter (HEC) and a Forward Calorimeter (FCal) closest to the beam pipe. The liquid argon technology was chosen for these regions of high ionising dose because of its intrinsically high radiation hardness. The outer hadronic calorimeter, the Tile calorimeter, is composed of a central barrel and two extended barrels. It is exposed to a lower ionising dose so plastic scintillator can be used as a sampling medium.

In the central region, covering the pseudorapidity of the ID, the electromagnetic calorimeter has a fine granularity to allow for identification and precision measurements of electrons and photons. The remaining parts of the calorimeter are used for jet reconstruction and measurements of the total missing transverse energy, where coarser granularity is sufficient to satisfy the physics requirements.

The total thickness of the electromagnetic calorimeter is 22–33 radiation lengths (X_0) in the barrel and 24–38 X_0 in the endcaps. In terms of interaction length λ, the total depth of electromagnetic and hadronic calorimeters combined is about 9.7 λ in the barrel and 10 λ in the endcap. This was found to be sufficient to reduce punch-through into the muon system and to measure high-energy jets with good resolution.

Liquid argon electromagnetic calorimeter

The LAr is a segmented electromagnetic calorimeter with liquid argon as the active medium and lead plates covered with stainless-steel sheets as absorbers. Multi-layer copper electrodes are fixed in the middle of the liquid-argon gaps by honeycomb spacers. At the nominal operating voltage of 2 kV and 2.1 mm gap width, the total drift time in the barrel is about 450 ns. The gap width in EMEC varies as a function of the radius from 0.9 mm to 3.1 mm so the high voltage is modified in steps between 1 kV and 2.5 kV to achieve a better uniformity in response.

A sketch of an EMB module is shown in Figure 3.5. The module readout is longitudinally segmented into three layers. The first layer has fine granularity in η and provides precise position measurements of photon clusters, even in cases where two photons originate from a decay of a particle with high momentum and are close together. Most of the energy of a typical electromagnetic shower is collected in the second layer. The combination of information from the first and second layer allows for a precise measurement of photon direction. The third layer collects the tail of the shower, therefore a coarser granularity is sufficient. Thanks to the accordion-shape of the electrodes, the detector coverage is perfectly symmetric in ϕ without any azimuthal gaps. EMEC modules are similar to EMB with absorber waves parallel to the radial direction and running axially.

In the $|\eta| < 1.8$ region a presampler detector is used to correct for energy loss of electrons and photons before they enter the calorimeter. It consists of a 1.1 cm (0.5 cm) thick layer of liquid argon in the barrel (endcap) region.

Including the presampler, there are about 173 000 channels in EMB and EMEC together. The design energy resolution is $\sigma_E/E = 10\%/\sqrt{E[\text{GeV}]} \oplus 0.7\,\%$, however the first (sampling) term is worse at higher η because of the increased amount of material in front of the calorimeter.

Tile calorimeter

The Tile calorimeter is a sampling calorimeter constructed from steel absorber plates interleaved with scintillating tiles. It is subdivided into a central barrel and two extended barrels, each consisting of 64 wedge-shaped modules.

The geometry of a module is shown in Figure 3.6. The absorber structure is formed by 5 mm thick plates onto which 4 mm spacers are glued forming the pockets for insertion of scintillator tiles. The trapezoidal tiles are fabricated from

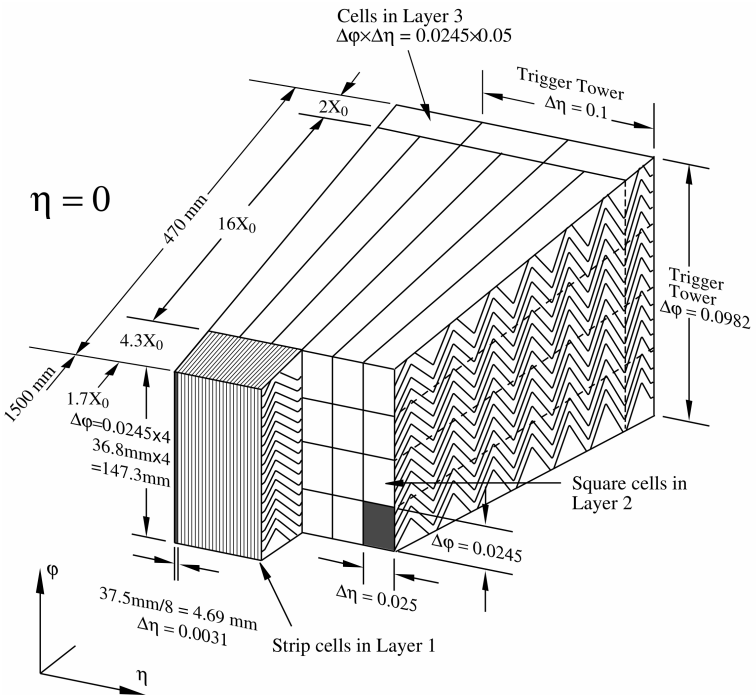

Figure 3.5: Schema of a LAr barrel module with three layers together with η and ϕ sizes of trigger and readout cells [46].

fluorine-doped polystyrene and are wrapped in a plastic sleeve with a printed mask to improve the light yield and optical uniformity. Plastic channels with 3 or 4 wavelength-shifting optic fibres are placed on both edges of the tiles to collect light, convert it to a longer wavelength and transfer it to a photomultiplier tube (PMT) located in a girder at the top of the module. The channels are opaque and have slots that allow fibres to read out different depths in the calorimeter. The fibre grouping defines a readout structure with cells of dimensions $\Delta\eta \times \Delta\phi = 0.1 \times 0.1$ in the first two layers and 0.2×0.1 in the last layer, corresponding to layers of thickness 1.5, 4.1 and 1.8 λ at $\eta = 0$. The design resolution is $\sigma_E/E = 50\,\%/\sqrt{E[\mathrm{GeV}]} \oplus 3\,\%$.

Additional detector components such as smaller modules of Intermediate Tile and thin scintillator counters are located in between the barrel and extended barrel structures.

Hadronic endcap calorimeter

The Hadronic Endcap Calorimeter (HEC) consists of two wheels on each side. Absorber plates (25 mm thick copper plates in the inner wheel, 50 mm in the outher) run perpendicular to the beam axis and form gaps for liquid argon in between them. Kapton electrodes at a voltage of 1.8 kV provide readout of the 1.8 mm thick drift zone. The total thickness of HEC together with endcaps of the electromagnetic calorimeter is 10 λ.

Forward calorimeters

Each of the two Forward Calorimeter (FCal) endcaps is composed of one electromagnetic (FCal1) and two hadronic modules (FCal2 and FCal3). FCal1 is built

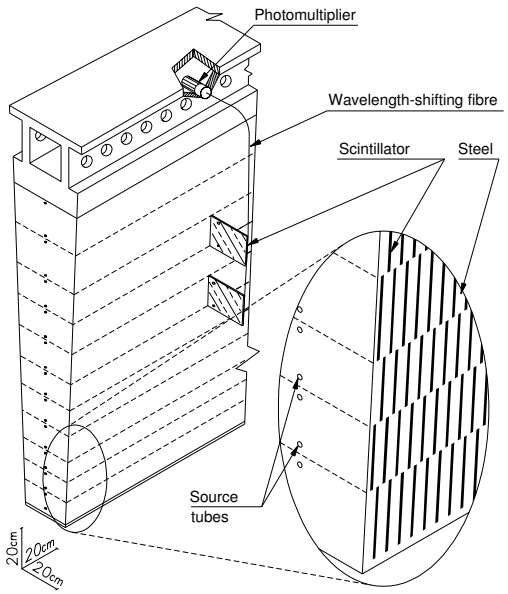

Figure 3.6: Sketch of a tile calorimeter module with optic fibres and photomultipliers [46].

from a copper matrix with regularly spaced longitudinal electrodes consisting of coaxial copper tubes and copper rods. A thin plastic fibre wound around the rod holds it in the middle of the tube and creates a gap for liquid argon. Similarly, hadronic modules consist of tungsten matrix, copper pipes filled with liquid argon and tungsten rods. The total thickness of FCal modules is equivalent to $10\,\lambda$ or $208\,\mathrm{X}_0$ and the design energy resolution is $\sigma_E/E = 100\,\%/\sqrt{E[\mathrm{GeV}]} \oplus 10\,\%$.

3.3 Muon Spectrometer

The MS is the outermost layer of the ATLAS detector and is designed to detect and measure momenta of charged particles that pass through calorimeters in a pseudorapidity range $|\eta| < 2.7$. It also provides fast trigger signals up to $|\eta| = 2.4$. The measurement of muon momenta is based on deflection in a magnetic field and track position measurement in at least three layers of high-precision chambers. The LHC collision energy and physics programme of ATLAS require a long lever arm, high magnetic field and high position resolution to reach high p_T resolution up to $\sim$3 TeV. Additional requirement to minimise multiple scattering, which is the dominant source of uncertainty for low-p_T muons, motivated the choice of three large air-core toroids.

The chambers in the barrel are arranged in three concentric layers at radii of approximately 5, 7.5 and 10 m. Each endcap is composed of four wheels perpendicular to the beam direction, located at 7.4, 10.8, 14 and 21.5 m from the IP. The configuration is schematically drawn in Figure 3.7. Each layer has both triggering and precision chambers.

The detector technologies were chosen for their ability to provide accurate space-point measurements and a fast response, while cost-effectively covering a large surface. Precision measurement of the muon track coordinates is provided by Monitored Drift Tubes (MDT) over most of the η range, while Cathode Strip

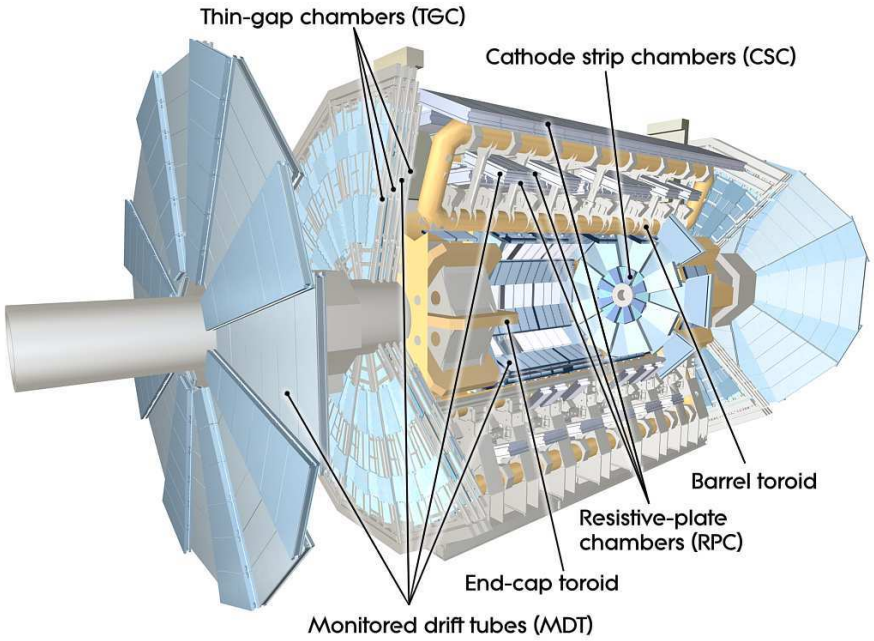

Figure 3.7: Layout of the ATLAS Muon Spectrometer [46].

Table 3.2: Subsystems of the Muon Spectrometer [46].

Type	Function	Coverage	Chambers	Channels
MDT	tracking	$\|\eta\| < 2.7$	1150	354 000
CSC	tracking	$2.0 < \|\eta\| < 2.7$	32	31 000
RPC	trigger	$\|\eta\| < 1.05$	606	373 000
TGC	trigger	$1.05 < \|\eta\| < 2.7$	3588	318 000

Chambers (CSC) are used in the innermost layer of endcaps. Resistive Plate Chambers (RPC) are used for triggering in barrel and Thin Gap Chambers (TGC) in endcaps. The triggering chambers also provide a hit coordinate in the direction orthogonal to the direction measured by precision chambers. The main parameters of the MS are listed in Table 3.2 and the four technologies are described in the following subsections.

An important part of the MS is the optical alignment system which allows to measure the deformation, planarity and relative positions of precision chambers needed to reach a high-resolution sagitta measurement. Additional track-based alignment, which uses cosmic data without magnetic field, is applied during data processing.

Monitored Drift Tubes

The MDT chambers provide precision track coordinates up to $|\eta| = 2.7$ (up to $|\eta| = 2.0$ in the innermost endcap). The basic elements of a drift tube are aluminium cylinder with a diameter of 30 mm and a 50 µm thick tungsten-rhenium

wire placed in its centre. Tubes are filled with a gas mixture containing 93 % Ar, 7 % CO_2 and a small admixture of water vapour and are operated in proportional mode at voltage of 3080 V.

Rectangular and trapezoidal chambers (in barrel and endcap, respectively) are built from 3 to 8 layers of tubes with direction along ϕ, hence providing only a measurement in the bending plane $(R - z)$. The spatial resolution is about 80 µm per tube and 35 µm per chamber. After matching the η of muon hit in MDT and in the neighbouring trigger chamber, the ϕ measured by the trigger chamber is assigned as the second hit coordinate.

The MDT layout is projective with chamber dimensions increasing with their distance from the IP. Eighteen types of chambers in various shapes were used to cover a total area of 5000 m^2, including special shapes installed around coils and support structures. The tube lengths vary between 1.7 and 6.5 m.

Cathode Strip Chambers

The CSC are used in the innermost tracking layer in the forward region ($2 < |\eta| < 2.7$) because of their capability to detect particles at high-rates with better spatial, temporal and double-track resolution than MDT. The chambers are arranged in two disks in each endcap region, about 7 m from the IP. Each chamber contains four CSC planes that provide four independent measurements of hits per track.

The CSCs are large multiwire proportional chambers with 80 % Ar + 20 % CO_2 gas mixture and two cathodes, one segmented in the radial direction and the second one perpendicularly. A charged particle passing through gas produces primary ionisation and an avalanche is induced by an electric potential of 1900 V on wires running in the radial direction. The hit positions are interpolated from charge induced in clusters of cathode strips, while wires are not read out. With a readout pitch of 5.31 and 5.56 mm (there are two shapes of chambers) in the bending direction, the CSCs reach a spatial resolution of 60 µm per plane. A coarser cathode segmentation of 12 and 21 cm in the other plane translates into a resolution of about 5 mm. The chamber thickness of 5 mm with drift times of less than 40 ns translate to a timing resolution of about 7 ns per plane.

Resistive Plate Chambers

The layout of muon chambers used for triggering is shown in Figure 3.8. The RPC are positioned in barrel in three stations: two around the middle layer of MDT and one mounted on the outermost layer. Each of three layers has two independent chambers, both measuring η and ϕ coordinate, hence providing 6 measurements in total. Coincidence of signals in the reference (pivot) plane and in the closer or further plane is then used for tagging of low- or high-p_T muons. The redundant measurements are used to improve trigger efficiency and suppress noise. Coincidence required separately in η and ϕ coordinate increases robustness against converted photon background.

RPC provide fast trigger signals and bunch-crossing identification in the barrel regions ($|\eta| < 1.05$). These gaseous detectors are built from two parallel plates of resistive plastic with an electric field between them. After a passage of ionising particle, an avalanche is formed in the gas and a signal is induced via capacitive

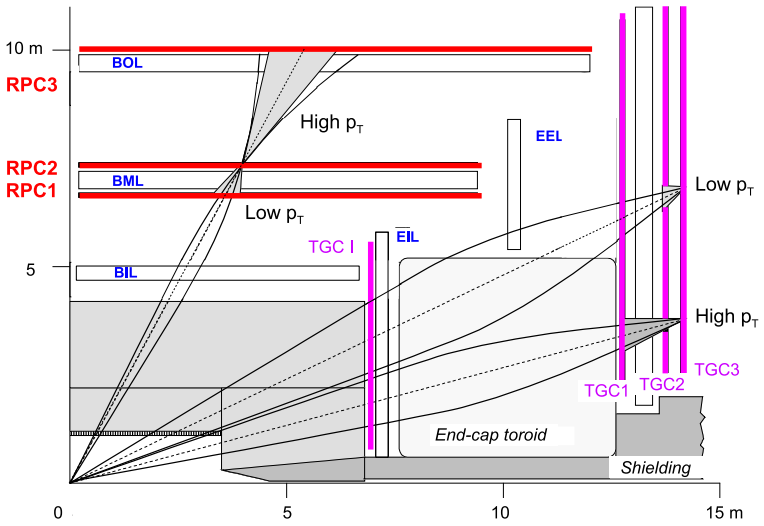

Figure 3.8: Layout of the muon trigger system. Detector stations labelled RPC2 and TGC3 are the pivot planes for muon trigger algorithms [46].

coupling on metal strips on the outer sides of the plates (the strip pitch is 23-35 mm). The 2 mm thin gap filled with gas mixture of $C_2H_2F_4$/Iso-C_4H_{10}/SF_6 and electric field of 4.9 kV/mm produce signals with a width of about 5 ns and a time jitter of less than 10 ns, including strip propagation time.

Thin Gap Chambers

The TGC were selected for triggering in the endcap regions because of good time resolution, high rate capability and robustness in high-radiation environments. A special characteristics of these multiwire chambers is that the wire-to-cathode distance of 1.4 mm is smaller than the distance between wires which is 1.8 mm. Together with a gas mixture of carbon dioxide and n-pentane (55/45) this prevents the occurrence of streamers, while preserving good time resolution thanks to high electric field around wires. Chambers have wires running in the η direction to measure the bending coordinate (R) and radial strips etched on one of two cathodes for ϕ measurement.

Modules are formed from two or three TGC layers and combined with precision chambers as shown in Figure 3.8. Chambers located in the small wheel in front of the endcap toroid measure the track ϕ. One layer of TGCs before and two layers after the middle MS station (big wheel) measure the slope of track segments with a precision of 2–3 mrad. The deviation from a straight line between the IP and a hit in the reference plane (labelled TGC3 in Figure 3.8) can be translated to curvature in the magnetic field. Coincidence patterns can then be implemented to evaluate if the track passed a given momentum threshold.

Toroid magnets

The magnet system of the Muon Spectrometer consists of three toroids, each containing eight superconducting coils with Al-stabilised NbTi/Cu conductor. A sketch of the configuration is shown in Figure 3.9. The large barrel toroid covers region of $|\eta| < 1.4$ and its coils are enclosed in individual stainless-steel vacuum

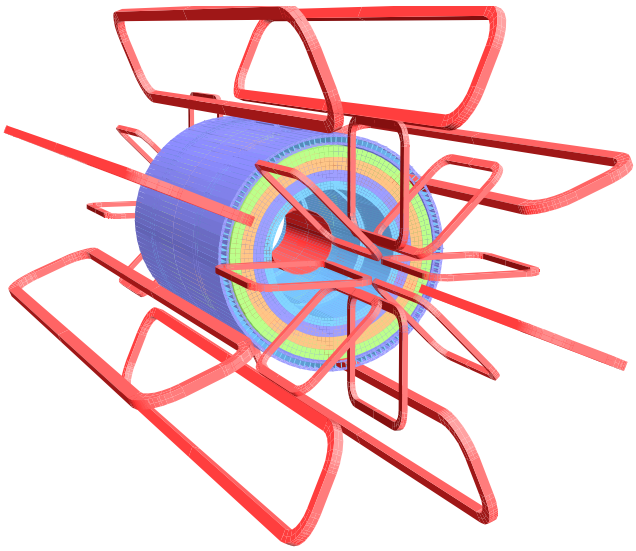

Figure 3.9: ATLAS magnet systems: the barrel and endcap toroid coils are red, the central solenoid is light blue. The steel of tile calorimeter is modelled as four layers with different magnetic properties and acts as the return yoke [46].

vessels. Coils of each endcap toroid are placed in one common cryostat; they are inserted into the central toroid and rotated by an angle of 22.5° to provide a radial overlap and to optimise the bending power in transition region.

With 120 turns per coil and a nominal current of 20.5 kA, the magnets provide approximately 0.5 T in the central and 1 T in the endcap region, with a peak field of about 3.9 T. The magnetic field integral seen by particles ranges from 1.5 to 5.5 Tm in barrel and between 1 and 7.5 Tm in the endcaps, with lower bending power in the overlap regions ($1.4 < |\eta| < 1.6$).

3.4 Forward and luminosity detectors

The forward region of ATLAS is instrumented with additional detector systems, three of them are schematically shown in Figure 3.10.

The LUminosity Cerenkov Integrating Detector (LUCID) is a dedicated luminosity detector installed around the beam pipe 17 m on either side of the IP. The aim is to detect inelastic pp scattering and measure the instantaneous luminosity assuming that the number of particles passing through the tubes scales with the number of interactions per bunch crossing. Each detector consists of 20 1.5 m-long aluminium tubes with a diameter of 15 mm which contain C_4F_{10}. The Cherenkov light produced by charged particles in gas is reflected on the inside of tubes and detected by radiation-hard PMTs on their end. The fast response provides measurements on bunch-by-bunch basis. However, the gas was removed during 2011 because os signal saturation on all channels and only the quartz window of PMT is used as a Cherenkov medium since [48].

Zero Degree Calorimeter (ZDC) is located 140 m from the IP, where beams pass from two beam pipes into one straight-section pipe. Its primary purpose is to measure the number of forward neutrons with $|\eta| > 8.2$ which is correlated with the centrality of heavy-ion collisions. During Run 1 of the LHC it was also

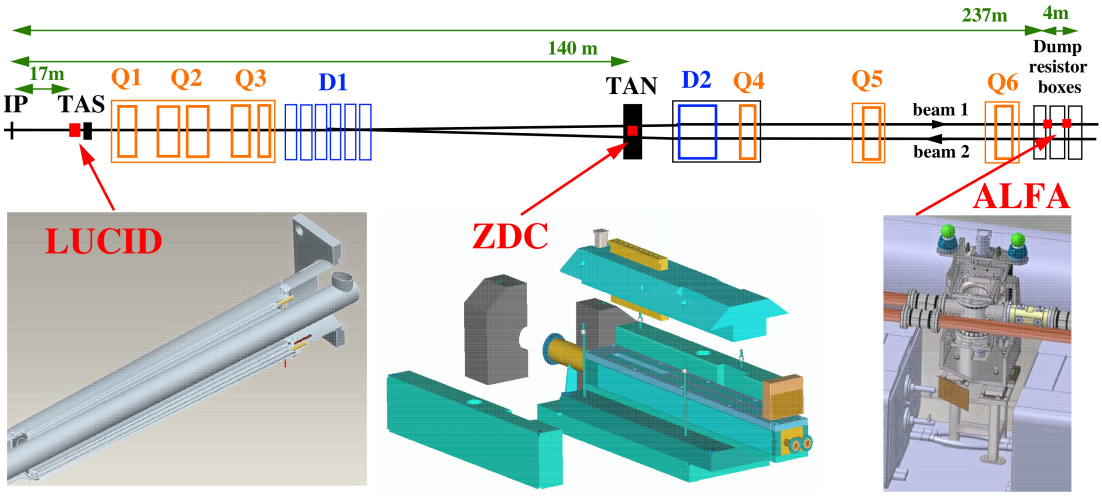

Figure 3.10: ATLAS forward detectors and their placement with respect to the IP. Elements Q1–Q6 are LHC quadrupoles, D1–D2 dipoles and TAS and TAN are absorbers [46].

used during *pp* data taking to measure diffractive processes. The detector is built as a sampling calorimeter composed of tungsten plates, quartz rods and multi-anode PMTs that detect the Cherenkov light produced in quartz. Sets of rods run parallel and perpendicular to the beam direction, allowing measurement of position and energy of the incident particles. To limit the radiation damage, ZDC modules were removed after 2009 for *pp* operation and are reinstalled only for the heavy-ion data taking.

The Absolute Luminosity For ATLAS (ALFA) detector system is a tracking detector placed 240 m from the IP which was installed in the winter shutdown 2010-2011. It is used to determine the absolute luminosity by measuring the elastic-scattering of protons in dedicated LHC runs with special conditions (runs with low β^*). The system consists of two stations on both sides of ATLAS, each of them housing a bottom and a top tracking module. Because of the need for radiation-hard detector placed very close to the beam, a design with scintillating-fibre tracker placed in Roman pots (vessels separated from the LHC ultra-high vacuum by 200 µm thin window) was chosen. Aluminium-coated fibres with a width of 0.5 mm are arranged in 10 diagonal layers and staggered in depth with an offset of 50 µm between planes to reach a resolution of ∼30 µm. Additional layer of fibres is used to align the upper and lower parts of each station. The signals are read out by multi-anode PMTs and can provide trigger.

The Minimum Bias Trigger Scintillators (MBTS) consists of 32 scintillator counters installed in two wheels around the beam pipe at $z = \pm 3.56$ m from the IP (in front of the calorimeter endcaps). It is used to tag charged particles in the forward region ($2.12 < |\eta| < 3.85$) and during Run 1 it provided an input to Level 1 trigger. Its readout is integrated into the Tile calorimeter system because of their proximity and because they share the same detector technology. Due a large accumulated dose during LHC Run 1, it was replaced by a new system during LS1.

3.5 Trigger and data acquisition

The LHC design luminosity of $10^{34}\text{cm}^{-2}\,\text{s}^{-1}$ translates to about 25 interactions per bunch crossing at 40 MHz rate. The readout of nearly 100 million channels of the ATLAS detector at such rate would require a computing infrastructure which is not yet feasible. Therefore, fast and highly efficient trigger with sufficient background rejection is needed to select potentially interesting collisions. Additional challenges are a correct application of zero suppression, as well as compression and readout of the data fragments from all subdetectors.

The data acquisition is intertwined with the trigger system and together they are referred to as Trigger and Data AcQuisition, TDAQ. The system receives and buffers event data from subdetectors, assembles event fragments to complete events and moves the selected ones to a storage. It also takes care of configuration, control and timing of the subsystems. The detector hardware is supervised by the Detector Control System which controls gas systems, power supplies and safety interlocks. It also reads collision timing (clock) and machine states of LHC via machine interfaces.

Trigger

The trigger system has three distinct levels and the rate reduction is performed in three steps as is shown schematically in Figure 3.11. At the Level 1 trigger (L1), a limited set of detector channels is read out to take a decision within 2.5 ns and with an output rate of about 75 kHz. The two higher levels, Level 2 trigger (L2) and the Event Filter (EF), referred to as High-Level Trigger (HLT), decrease the rate further to about 200 Hz, corresponding to a writing rate of about 300 MB/s [49]. Thanks to algorithm and hardware improvements during Run 1, the recording rate was increased up to 700 Hz by the end of 2012, with peaks of about 1 kHz [50]. Before the LHC Run 2, the L2 and EF were merged into one level.

The first trigger level is a configurable hardware-based trigger using fast custom-built electronics and searching for candidate physics objects (signatures) such as high-p_{T} muons, electrons, photons, jets or evaluating the total transverse energy of the event, missing transverse energy $E_{\text{T}}^{\text{miss}}$ etc. The Central Trigger Processor (CTP) combines the low-granularity data from calorimeters and muon triggers and provides a trigger decision (the L1 accept, L1A). Data from other subdetectors such as ID are not read out at this stage and are stored in on-detector buffers for about 3.2 µs until the L1A signal arrives from L1. In consequence, the L1 latency is about 2.5 ns and its output rate is limited by the detector readout bandwidth to ∼75 kHz. If an event is accepted at L1, the Region of Interest (RoI) information is passed to the second trigger level and data fragments from all ATLAS subsystems are read out to Readout Buffers, pending the L2 decision. The RoI is defined by $\eta - \phi$ coordinates of the part of detector where the selection process identified some of the predefined signatures.

The L2 requests data in the RoI region from all subdetectors with full granularity (about 12 % of total data volume) and uses software algorithms which are simplified versions of the full event reconstruction to make a decision in 40 ms on average. Improved selection criteria are applied in this step, such as e/γ discrimination, refined computation of $E_{\text{T}}^{\text{miss}}$ and invariant mass of pairs of L1 objects

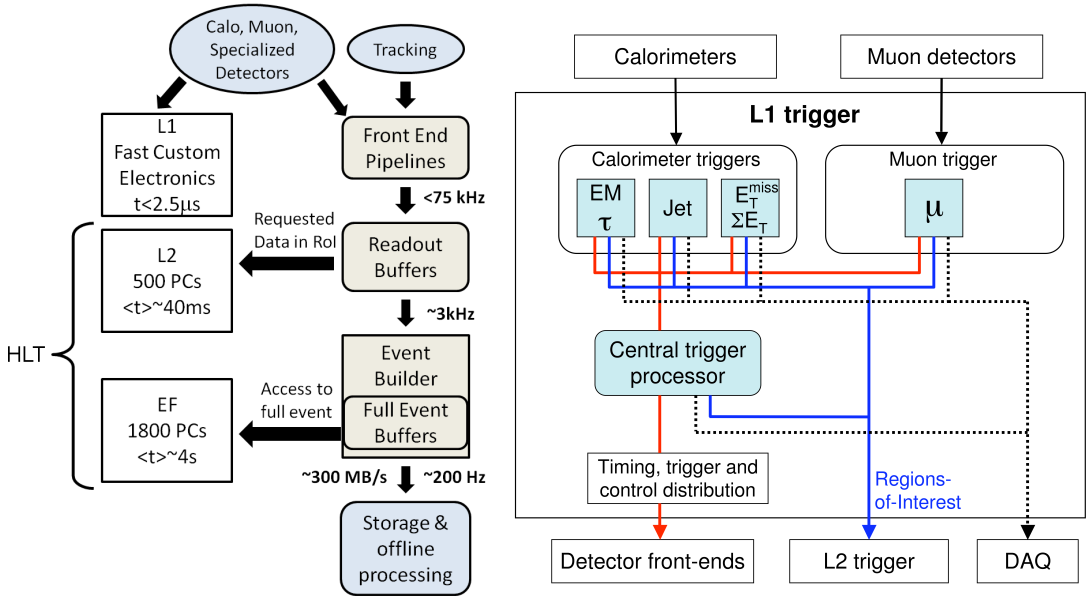

Figure 3.11: Schema of the ATLAS trigger system (left) and diagram of the Level 1 trigger [46, 49].

(dimuon, dielectron), identification of jets with b-flavour tagging, etc. The output rate of L2 is limited to few kHz, depending on running conditions like luminosity or background conditions.

In the last step, the EF combines data fragments from all detectors and reduces the rate to about 200 Hz. The processing time is on average 4 s/event. The HLT algorithms also provide information about physics objects such as track/muon/calorimeter cluster coordinates, kinetic variables, invariant masses of J/ψ, Z and τ candidates, etc. for online monitoring and data quality checks during data taking.

The trigger configuration is prepared in a form of *trigger menu* which defines a list of trigger chains with thresholds and objects defined at each level. Trigger chains[1] might be configured for single objects (e.g. at least one muon with p_{T} >6 GeV, referred to as mu6), multiple objects (at least two muons with p_{T} >6 GeV, 2mu6), combined (electron and missing transverse energy) or topological triggers, which require information from more RoIs (a pair of muons with invariant mass consistent with J/ψ). Additional cuts can be applied during object selection (represented as loose, medium or tight cuts in trigger menu) and variables such as isolation are computed (e.g. energy deposited in calorimeter in a cone around muon direction). Special triggers also provide randomly seeded minimum-bias sample, data for detector monitoring and calibration, background monitoring or testing.

Typically, the configuration contains about 500 triggers. Some items, e.g. low-p_{T} triggers, must be prescaled by a factor N because of very high rates, meaning that the chain accepts only one in N events that pass the selection. In this way a single trigger menu provides flexibility and full usage of processing power and bandwidth even during long runs when luminosity varies significantly.

[1] Trigger chains are often referred to simply as triggers.

Calorimeter trigger algorithms

The L1 Calorimeter trigger (L1Calo) is a system designed to evaluate an input from about 7200 analog trigger towers, regions of electromagnetic and hadronic calorimeters with reduced granularity of about 0.1×0.1 in $\Delta\eta \times \Delta\phi$ in the central part (larger in the forward region).

The analog input signals are digitised by a pre-processor, the value of transverse energy deposited in each tower is calculated using look-up tables and the information is sent to the cluster and jet/energy-sum processors in parallel. The cluster processor identifies e/γ and τ-lepton candidates as small isolated clusters with E_{T} in the electromagnetic calorimeter above a given threshold. It receives energy sums deposited in tower pairs in η or ϕ and with a sliding window of 4×4 cells searches for clusters for which at least one of the sums is above a threshold. If required, isolation is implemented by checking the energy deposited in 12 cells around the 2×2 tower core.

The jet/energy-sum processor receives data in the form of E_{T} sums in 2×2 trigger towers, from both the electromagnetic and hadronic calorimeters up to $|\eta| < 3.2$ (4.9) for jet ($E_{\mathrm{T}}^{\mathrm{miss}}$) triggers. The jet trigger algorithms can be defined to use sum of E_{T} in a window of 2×2, 6×6 or 8×8 trigger towers.

For both processors, the multiplicities of the objects which are above defined the thresholds are sent to the CTP and in case of an L1 accept, the positions and types of candidates are sent to the to L2. Here, custom algorithms are used to confirm the results of L1, compute cluster variables with higher precision and add ID track information. Finally, at the EF, algorithms similar to the offline ones are used to reconstruct trigger signatures and their more complicated combinations. They use additional information such as shower shape variables, leakage parameters (from electromagnetic to hadronic calorimeter) and corrections for energy loss or muons are applied.

Muon trigger algorithms

To search for muon candidates, the L1 muon trigger uses information from the RPC and TGC systems. It requires spatial and temporal coincidence in trigger stations within one geometrical road, which is defined as the envelope of paths from the IP through detector for muons with p_{T} above a defined threshold). Therefore, the width of this region depends on the threshold applied. There are six programmable thresholds, during 2012 the thresholds were 4, 6, 10, 11, 15 and 20 GeV [50]. The information from barrel and endcap regions is combined, duplicates are removed and the output is sent to the CTP in a form of observed muon multiplicity per p_{T} threshold. A formatted information about RoI of candidate muon is sent to L2. Typical dimensions of RoIs in $\Delta\eta \times \Delta\phi$ are 0.1×0.1 in RPC and 0.03×0.03 in TGC, giving approximately 7200 trigger cells.

At L2, muon track in RoI is reconstructed by adding more precise information from MDT to form a standalone L2 muon. Information from the ID is added and several pattern recognition algorithms are used to search for tracks. The track closest to a muon in η and ϕ is selected as the best matching track. The p_{T} of combined muon is computed as a weighted average of measurements from the MS and ID.

The RoI-based muons are refined at EF level and a degree of isolation of

combined muons is computed as a sum of p_{T} of ID tracks in a cone around the muon track. A full scan for additional muons is also performed, searching for muon segments in the MS, reconstructing tracks in the ID and forming combined muons from pairs of them.

Data acquisition and processing

The third level of trigger, EF, assigns accepted events to different data streams according to the detected trigger signature, e.g. Muons, L1Calo, Egamma. Monitoring streams are used during data taking for online data quality and detector checks. Express stream provides mixed signatures for prompt calibration and data quality evaluation. Additional streams include events for subdetector calibrations.

Collision data is collected in runs (usually one LHC fill) and subdivided in so called luminosity blocks, fundamental units of time with the same readout and trigger settings which typically last 1 min. Files are transferred to the Tier0 centre located at CERN, the central node of the LHC Computing Grid, and the full offline event reconstruction of express steam is started promptly. The first pass provides calibration constants for detectors and other inputs data for reconstruction such as flagging of problematic or noisy readout channels. The output is also used for data quality assessment and the luminosity blocks can be flagged according to different data quality criteria. The resulting good run lists are used as inputs for physics analysis.

ATLAS is using a software framework called Athena [51] for the reconstruction of collision data. Athena components are implemented in object-oriented C++ and dynamically loaded by Python configuration scripts. The processing happens in several steps and the intermediate files have different level of information. Reconstruction algorithms process the data in byte-stream format (called also RAW data) and produce the Event Summary Data (ESD) which contain all event information in a form of detector level objects (ID hits and tracks, calorimeter cells and clusters, muon segments, etc.). One event is typically about 1 MB at this stage, only a bit less than 1.6 MB for RAW format. This is reduced in the next step that produces the Analysis Object Data (AOD) files containing reconstructed physics objects like electrons, muons, jets. Trigger information is also saved in AODs. Datasets which will be used for physics analysis are then derived by analysis subgroups and typically contain only the information needed for given final state in the form of n-tuples or trees that can be processed by ROOT [52]. This brings the size of input files for analysis down to TB range, instead of PB.

To avoid large data transfers and to save computing power, the reconstruction up to AOD is usually done on the Worldwide LHC Computing Grid [53] (often referred to simply as Grid) by the ATLAS Distributed Computing team. The data is then available on Grid sites for user analysis.

The datasets used for the analysis presented in this work were in the AOD format for both collision data and simulated samples. Reconstruction of the $B^0 \to K^*\mu^+\mu^-$ candidates was implemented by the author in Athena and submitted with Panda [54] to Grid. Output files were skimmed by applying cuts, slimmed (keeping only variables used for fitting) and merged as will be described in Section 4.2.

3.6 Monte Carlo simulations

Simulation of the physics processes and detector response is needed for understanding of detector effects and comparison of data with theory predictions. The ATLAS simulation [55] proceeds in several steps. First, the particle collision is simulated using one of Monte Carlo (MC) event generators. Various requirements on the final-state particles can be placed to generate a given decay, inclusive samples or to improve statistics by applying generator-level cuts.

Decays of b-hadrons are usually generated on ATLAS by Pythia [56].[2] However, a general pp collision simulation would result in large amount of background without a $b\bar{b}$ quark pair and high computational time requirements. A wrapper called PythiaB [57] was developed to overcome this problem. It speeds up the generation by using one parton-level simulation as an input for multiple hadronisation processes. It also checks the presence of $b\bar{b}$ pair and implements a mechanism to enforce a concrete exclusive b-hadron decay while allowing other b-hadrons to decay freely. While Pythia can simulate decays according to the phase-space, EvtGen package [58] contains detailed models that describe semileptonic decays of b-hadrons and correctly reproduce angular distributions of sequential decays.

A passage of final-state particles through magnetic field and detectors is simulated using the GEANT4 toolkit [59]. This is followed by adding a modelling of pile-up and digitisation which is converting the energy deposits in simulated detector components into voltages and currents and adding detector effects such as noise or inefficiency. Trigger response is also simulated.

3.7 Tracking performance during LHC Run 1

ATLAS has been successfully operating during LHC Run 1 and recorded data with an integrated luminosity of $\sim$25 fb^{-1}. The peak instantaneous luminosity reached 7.7×10^{33}cm^{-2}s^{-1} [43] what means up to $\sim$40 collisions per bunch crossing.

The performance of track and vertex reconstruction plays an important role in flavour physics as it has a direct impact on full reconstruction of B-meson decays, b-tagging and identification of signal and background candidates. The primary vertex resolution after alignment as measured in 2012 dataset collected by minimum-bias triggers is shown in Figure 3.12. The achieved transverse position resolution is better than 20 µm and is dominated by the uncertainty of the luminous-region size. The longitudinal resolution is about 30 µm for events with high multiplicity of tracks. The resolution remains stable with increasing pile-up [60].

The performance of muon reconstruction was estimated using the J/ψ, $\Upsilon(1S)$ and $Z \to \mu^+\mu^-$ decays. The efficiency measured in 2012 data is above 99 % over most of phase space (muon $|\eta|$ <2.7 and $5 < p_{\mathrm{T}} < 100$ GeV). The momentum resolution varies from 1.7 % at central rapidity and $p_{\mathrm{T}} \simeq$10 GeV to 4 % at large rapidity and $p_{\mathrm{T}} \simeq$100 GeV [61]. The muon reconstruction efficiency as a function of p_{T} and the invariant mass resolution of dimuons are shown in Figure 3.13.

[2] Samples used for analysis presented in this thesis were generated by Pythia 8 and EvtGen.

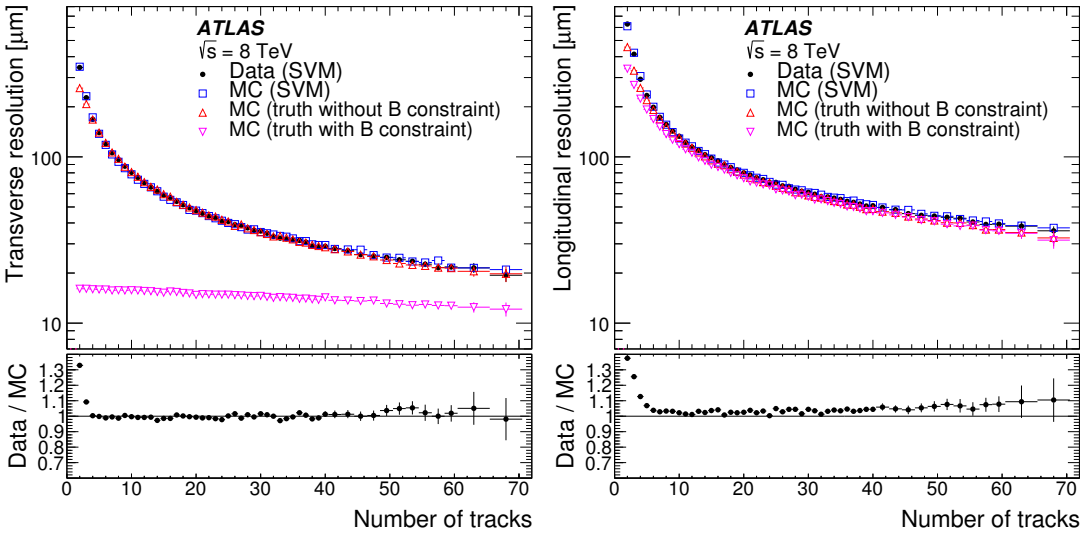

Figure 3.12: Resolution of the primary vertex position in x (left) and z as function of the number of fitted tracks in 2012 data (points) and MC simulation (squares). Resolution computed as the difference between the generated and reconstructed primary vertex position in MC simulation with and without the beam-spot constraint is also shown (triangles) [60].

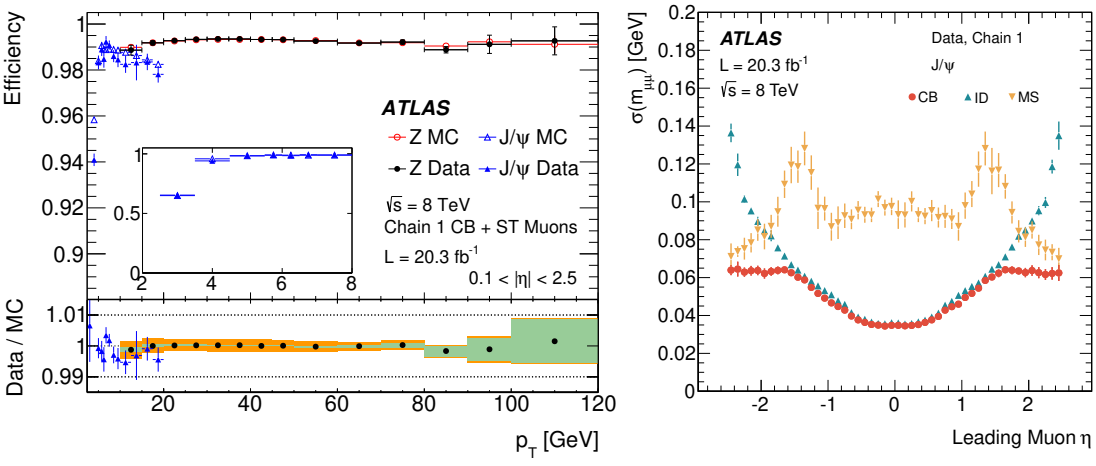

Figure 3.13: Reconstruction efficiency for combined and standalone muons as a function of the muon p_{T} (left) and the dimuon invariant mass resolution in $J/\psi \to \mu^+\mu^-$ events as a function of the pseudorapidity η of the highest-p_{T} muon for combined (CB), MS and ID muon reconstruction [61].

3.8 Upgrade projects

The ATLAS collaboration is constantly trying to improve the detector, readout and trigger systems to extend and improve its physics programme. Some changes are also necessary because of unprecedented conditions reached in LHC collisions and its planned upgrades. The increased instantaneous and integrated luminosity will result in higher detector occupancy and radiation damage and will require improving or replacing most of subdetectors, especially those at low radii. In the following, the main ideas and concepts will be described, the Phase 2 Inner Tracker will be described in more detail in Section 5.3. More details about the ATLAS upgrade plans can be found in Letters of intent [62, 63].

Phase 0

ATLAS used the LHC LS1 period (2013-14) for detector consolidation including installation of new Diamond Beam Monitor (DBM), new ID cooling system, replacement of Pixel on-detector service electronics, new calorimeter power supplies and addition of muon chambers between the barrel and endcap regions of MS. A new forward detector, ATLAS Forward Protons (AFP), was also installed in the LHC tunnel 200 meters from the interaction point. The AFP is based on layers of 3D pixel sensors for tracking and quartz Cherenkov detectors for time-of-flight measurement. It is used for proton tagging and diffractive physics, since 2015 in single-arm configuration and since 2017 with detectors installed on both sides of the interaction point.

However, the main activity was an installation of the fourth layer of Pixel detector, the Insertable B-Layer (IBL). It was placed between the existing Pixel detector and a new, smaller-radius beam-pipe, with a sensor average radius of 33 mm. The IBL consists of 14 staves, each carrying 32 pixel sensors. To cope with the high occupancy and radiation doses, two new sensor technologies with smaller pixels (planar and 3D) and a new read-out chip were developed. The flavour-physics analyses benefit from IBL thanks to improved vertex position resolution which improves for example the impact parameter resolution, as is shown in Figure 3.14.

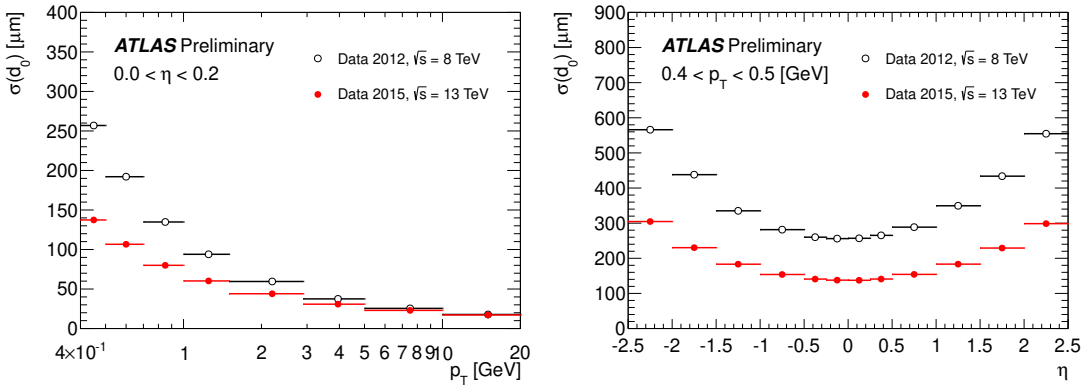

Figure 3.14: Transverse impact parameter resolution as a function of p_{T} (left) and pseudorapidity η measured in data collected in 2015 with the IBL installed. It is compared to data collected in 2012 [64].

Phase 1

For the Phase 1 upgrades in 2019-2020, an installation of New Small Wheels (NSW) in the Muon Spectrometer and several changes in the trigger and data acquisition systems are proposed [62].

Replacement of the innermost muon detectors in endcap regions (called small wheels) is necessary to maintain a high performance of muon tracking and trigger even at high occupancy. Moreover, the L1 muon trigger in endcap regions uses only segments in chambers located after the endcap toroid (as shown in Figure 3.8 on page 36). In case of high cavern background rates, this results in a high fraction of fake muon triggers (e.g. for `L1MU20` trigger chain searching for muons above 20 GeV, the fraction of high-quality muons is only 10 % even after the fake removal cuts are applied [62]). The NSW which will ensure efficient tracking with better resolution than current chambers and will be included in the L1 trigger logic. Two technologies will be used: the small-strip Thin Gap Chambers (sTGC) for triggering and MicroMegas chambers for precision tracking.

The LAr electronics will be upgraded to provide 10 times higher granularity, higher resolution and longitudinal shower information from the calorimeter to the L1 trigger processors. It will improve trigger energy resolution and increase the efficiency of electron, photon, tau and jet selection while suppressing backgrounds and fake triggers.

The Fast Track Trigger (FTK) is a hardware trigger system which will provide track finding and fitting after each L1 trigger in whole detector, as opposed to existing tracking in RoIs. FTK will use hits from the Pixel and SCT detectors to perform a fast pattern recognition implemented as Associative memory on FPGA. After processing, the track parameters, associated hits and goodness of fit can be requested by the L2 processors in a RoI or whole detector.

Additional changes are also proposed for the TDAQ, such as a topological L1 trigger processor which will take inputs from calorimeters and muon detectors. The glshlt farm will be also upgraded to allow the processing of full calorimetry and FTK information.

Phase 2

ATLAS is planning major upgrades of its subsystems during the LS3 (2024-26) to cope with the expected conditions at HL-LHC (instantaneous luminosity reaching $5-7\times10^{34}$, up to 200 interactions per bunch crossing and total integrated luminosity of 3000 fb^{-1}) [63].

The present ID performance would be severely deteriorated due to radiation damage and high occupancy (especially for the gas-based TRT). Therefore, the ID will be replaced by a new, all-silicon Inner Tracker (ITk) [65,66]. The ITk layout is similar as the current tracker: the barrel region is composed of 5 cylinders of pixel detectors with inclined modules at higher η followed by 4 layers of strip sensors. In the endcap regions, both pixel and strip sensors will be placed on disk support structures as shown in Figure 3.15.[3] The design requirements are: pseudorapidity coverage up to $|\eta| = 4$, robust tracking with at least 11 hits/track, readout channel occupancy below 1 % for pile-up of 200 and reduced material with respect to

[3] The design, performance and testing of the ITk strip modules will be described in Section 5.3.

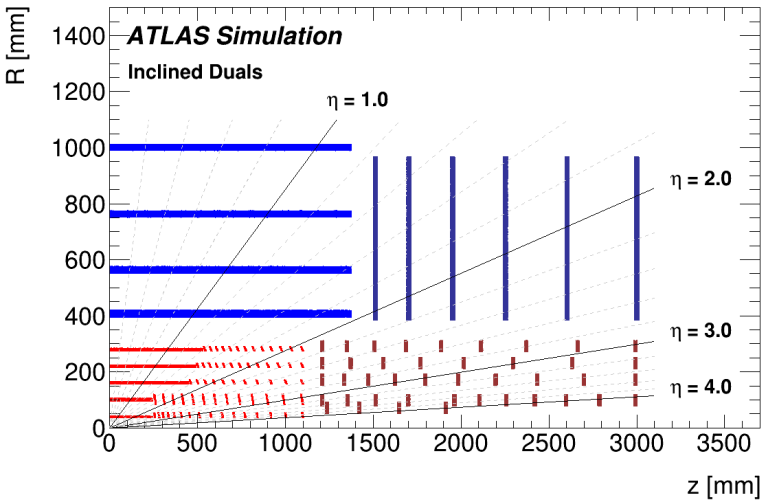

Figure 3.15: Schematic layout of the ITk. Only active elements in one quadrant are shown [66].

current ID. With the proposed pixel and strip sensors, the track vertex position resolution will improve thanks to smaller pixels and the momentum resolution will be about two times better than the current detector. Figure 3.16 shows examples of the expected resolution of some B-physics observables with ITk.

A new architecture of the trigger system shown schematically in Figure 3.17 is also proposed. The first level of trigger will be split into two: the hardware Level-0 will have the same functionality as the Phase 1 L1 system, based on inputs from calorimeters and muon detectors. The Level-1 will further reduce the rate using track and calorimeter information from the RoIs and will refine the muon selection using inputs from MDT. The front-end readout electronics of calorimeters and muon chambers will be upgraded to allow higher readout rates (40 MHz without buffering from calorimeters) and higher trigger latency (bigger on-detector buffers are needed).

To mitigate the effects of pile-up, an installation of the High-Granularity Timing Detector (HGTD) on the front face of the electromagnetic calorimeter endcap was proposed recently [67]. The detector will be based on low gain avalanche technology with a timing resolution of 30 ps for minimum-ionising particles and cover a pseudorapidity range of $2.4 < |\eta| < 4.0$. It will significantly improve the track-to-vertex association and the performance of jet and lepton track reconstruction will be similar to the central region.

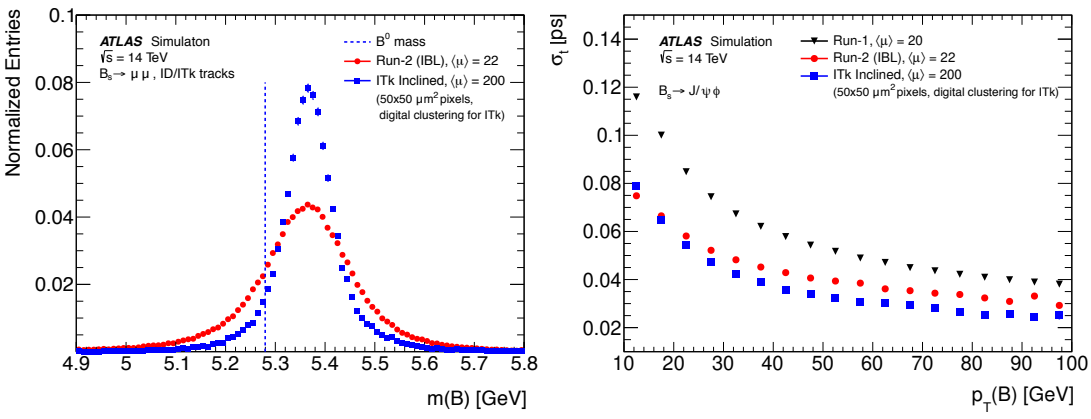

Figure 3.16: Expected performance after Phase 2 upgrade (ITk inclined geometry): reconstructed $B_s^0 \rightarrow \mu^+\mu^-$ mass spectrum for muons with $|\eta| < 2.5$ (left) and the average B_s^0 proper decay time resolution as a function of the B_s^0 p_{T} (right). Values obtained during Run 2 (and Run 1) configuration are also shown for comparison [66].

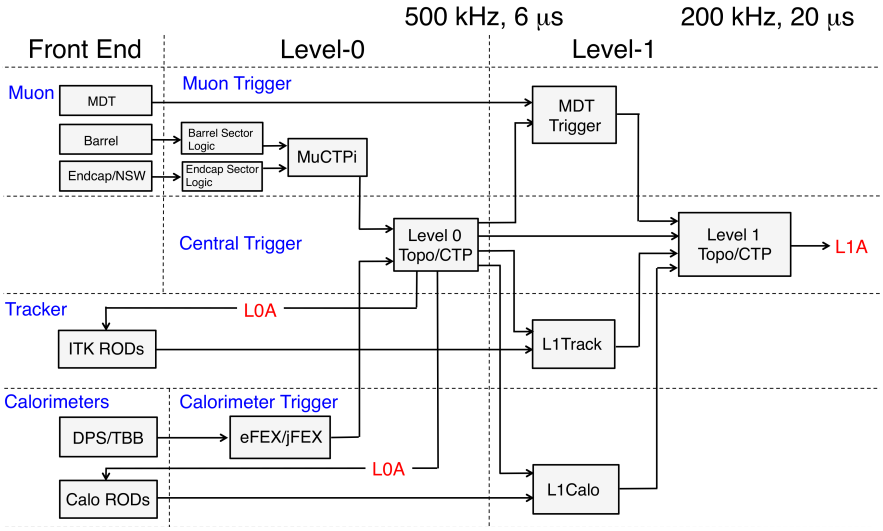

Figure 3.17: Hardware trigger architecture proposed for the Phase 2 upgrade [63].

4. Angular analysis of the $B^0 \to K^*\mu^+\mu^-$ decay

This chapter describes the main part of the author's work - the angular analysis of the $B^0 \to K^*\mu^+\mu^-$ decay with a dataset collected by the ATLAS experiment in 2012 in pp collisions at the centre-of-mass energy of $\sqrt{s}$ =8 TeV.

The study was approved by the ATLAS collaboration, preliminary results were published as a public note in 2017 and the paper was published in the Journal of High Energy Physics in 2018 [16]. Like many measurements in high-energy physics nowadays, this result is a work of the whole ATLAS collaboration, from detector design, construction, operations to data processing, reconstruction and finally physics analysis in a small group. The author of this thesis prepared data and simulated samples and worked on event reconstruction, signal candidate selection, fit validation, acceptance maps fits, background studies and extraction of the final results. Many tasks were done by other members of the team or in a close collaboration with them and they will be included for completeness. Additional validations, studies and checks were also performed but will not be included in this thesis, part of them is documented in internal notes [68–70].

The analysis strategy is to select the $B^0 \to K^*\mu^+\mu^-$ and $\overline{B}^0 \to \overline{K}^*\mu^+\mu^-$ decay candidates using cut-based criteria and to extract angular parameters S_i and F_L by unbinned maximum-likelihood fits of B^0 candidate mass and decay angles.[1] The measurements are performed in six bins of q^2 in the range 0.04 to 6 GeV^2, where three of these bins overlap. The tree-level decays $B^0 \to J/\psi K^*$ and $B^0 \to \psi(2S)K^*$ are used as control samples to validate the fit procedure and to extract the nuisance parameters.

4.1 Data and simulated samples

The dataset analysed here was recorded in 2012 in pp collisions at centre-of-mass energy of $\sqrt{s}$ =8 TeV. Only luminosity blocks which were recorded with stable beam conditions and which pass basic data quality criteria are used, as recommended by the detector and combined performance working groups. The resulting integrated luminosity corresponds to 20.3 fb^{-1} measured with a relative uncertainty of 1.9 % [71]. The good run list and processed data containers are listed in Appendix A.

Several signal and background MC datasets were prepared. The signal-like samples were generated by PythiaB (interface to Pythia 8 [56, 57]) using the ATLAS A14 tune with CTEQ6L1 parton distribution functions and underlying event tune AU2, both documented in Ref. [72]. The output from Pythia 8 was then passed to EvtGen [58] which simulated the b-hadron decays and the final-state radiation (using PHOTOS [73]). The samples include:

- $B^0 \to K^*\mu^+\mu^-$ decays with SM values of F_L and A_{FB}. EvtGen decay mode was set to BTOSLLBALL for SM-like decays of B^0 as modelled in [32] and

[1] Definition of decay angles in the experimental convention described Section 1.4.1 allows extraction of angular parameters from a combined sample with B^0 and $\overline{B}^0$ decays.

to VSS for the K^* decay.

- $\overline{B}^0 \to \overline{K}^* \mu^+ \mu^-$ decays generated according to SM.
- $B^0 \to K^* \mu^+ \mu^-$ generated according to phase space. EvtGen mode PHSP was used to generate signal decay with flat angular distributions of $\cos\theta_K$, $\cos\theta_L$ and ϕ (i.e. $F_L = 1/3$). This sample is used to model the detector and selection acceptance effects as will be described in Section 4.4.2.
- $B^0 \to K^+ \pi^- \mu^+ \mu^-$ was used for S-wave studies and systematic uncertainty.

The exclusive background samples include processes which have a similar final state as the $B^0 \to K^* \mu^+ \mu^-$ decay or which can be misreconstructed as a signal. For example, $B^+ \to K^+ \mu^+ \mu^-$ with additional π^- or fake track can mimic the signal decay and pass all selection cuts. About half of samples were simulated by Pythia and EvtGen with appropriate decay mode settings. The rest of the samples were produced by Pythia only. The following decays were studied:

- $B^+ \to K^{*+}(K^0 \pi^+)\ \mu^+ \mu^-$ (EvtGen)
- $B_s \to \phi\ \mu^+ \mu^-$ (EvtGen)
- $B^0 \to J/\psi K^*$ (EvtGen)
- $B^0 \to \psi(2S) K^*$ (EvtGen)
- $B^+ \to K^+ \mu^+ \mu^-$ (EvtGen)
- $B_s \to J/\psi\ K^*$ (EvtGen)
- $B^0 \to \phi\ K^*$ (EvtGen)
- $\Lambda_b \to \Lambda(pK^-)\ \mu^+ \mu^-$ (EvtGen)
- $\Lambda_b \to pK^- \mu^+ \mu^-$ (EvtGen)
- $B_s \to J/\psi\ \phi$ (Pythia)
- $\Lambda_b \to \Lambda\ J/\psi$ (Pythia)
- $\overline{\Lambda_b} \to \overline{\Lambda}\ J/\psi$ (Pythia)
- $B^0 \to J/\psi\ K^0_S$ (Pythia)
- $B^0 \to \psi(2S) K^0_S$ (Pythia)
- $\Lambda_b \to \Lambda\ \psi(2S)$ (Pythia)
- $\overline{\Lambda_b} \to \overline{\Lambda}\ \psi(2S)$ (Pythia)
- $B^+ \to J/\psi\ K^+$ (Pythia)
- $B^+ \to J/\psi\ \pi^+$ (Pythia)
- $B^- \to J/\psi\ K^-$ (Pythia)

Inclusive background samples $b\bar{b} \to \mu^+ \mu^- X$ were generated with both Pythia and EvtGen for comparison and studies. Additionally, four big samples generated by Pythia for the ATLAS $B^0_{(s)} \to \mu^+ \mu^-$ analysis [74] were used. The AA label of the sample means that none of b and $\bar{b}$ can decay semileptonically, AB and BA prevent either the quark or antiquark semileptonic decays and BB includes semileptonic decays of both. Inclusive background sample containing $c\bar{c} \to \mu^+ \mu^- X$ processes was also simulated.

The number of events generated for all samples and correspondent MC run numbers are listed in in Tables A.1 and A.2 in Appendix A.

4.2 Event reconstruction and candidate selection

All simulated datasets are processed in the same way as the collision data. The output format is the same with an exception of the MC truth information which is present only in the simulated samples. The reconstruction and selection of signal candidates proceeds in the following steps:

- search, reconstruction of candidates and preselection (loose cuts only)
- application of the final selection cuts (variables not used in the next steps are also removed, referred to as slimming)
- selection of the best candidate for events with multiple signal candidates
- merging of files from different trigger streams and removal of duplicates
- trigger reweighting

The event selection is based on studies performed for the $B^0 \to K^*\mu^+\mu^-$ analysis of 2011 dataset with a few minor differences which will be noted explicitly. The 2011 analysis was released as an ATLAS conference note but was withdrawn before publication because of issues related to the definitions of angles that affected the final results. However, the cut-based selection described in [75] is valid and is used for the 2012 analysis.

Reconstruction and preselection

The reconstruction of signal candidates is implemented in the Athena framework. The input AOD files contain event and trigger information, lists of reconstructed physics objects, referred to as containers (muons, tracks, primary vertices) and truth MC information (simulated samples only). The Athena codebase of B-physics subgroup provides classes which are extended versions of track and vertex fitting, histogramming and ntuple handling tools, some of which are described in Ref. [76].

The reconstruction algorithm uses the `JpsiFinder` tool to select muons from the *Staco* muon container and to search for muon pairs with opposite charge and dimuon invariant mass lower than 5500 MeV. Dimuon candidates are accepted if the vertex χ^2 per degree of freedom is lower than 20. Candidates for B^0 are formed from two tracks associated with muons and two other oppositely-charged tracks not identified as muons. These four tracks are fitted into a common vertex with track mass hypotheses set for B^0 or $\overline{B}^0$ (K/π mass hypotheses are assigned to both positively and negatively charged tracks). The secondary B^0 and K^* vertices are refitted by a `TrkVKalVrtFitter` and all primary vertices are refitted excluding the 4 candidate tracks.

No matching to trigger-level muon or track objects is required. The information from the Muon Spectrometer is used only for the identification of muon candidates and the parameters of muon tracks are measured by the Inner Detector. The candidates are retained if they pass all criteria listed in Table 4.1. If more candidates per event pass, they are kept and the choice of one candidate per event is done later.[2]

[2] In majority of events with multiple signal candidate, both B^0 or $\overline{B}^0$ candidates are formed from the same quartet of tracks.

Table 4.1: $B^0 \to K^*\mu^+\mu^-$ preselection criteria. The particle names stand for the system of their corresponding daughter particles, e.g. B^0 cuts are applied to the $K^\pm\ \pi^\mp\ \mu^+\ \mu^-$ system.

Particle	**Variable**	**Value**
μ	collection	Staco
	p_{T}	$> 500\,\mathrm{MeV}$
dimuon	mass	$[0,\ 5500]\,\mathrm{MeV}$
	χ^2/n.d.f.	< 20
π/K track	p_{T}	$> 500\,\mathrm{MeV}$
	Pixel hits	> 0
	SCT hits	> 1
K^*	mass	$[600,\ 1050]\,\mathrm{MeV}$
B^0	mass	$[4600,\ 6000]\,\mathrm{MeV}$
	χ^2/n.d.f.	< 15

Final candidate selection

The final selection follows the approach used in the 2011 analysis and allows to produce files with three levels of selection for various studies.

In the first step, basic quality cuts are applied to muon, pion and kaon tracks. The muon selection is based on performance studies described in [61]. This analysis requires at least one of the muons to be a combined muon[3] and the following tracking criteria for muon ID tracks are applied:

- at least 1 Pixel hit + number of crossed dead Pixel sensors
- more than 4 SCT hits + number of crossed dead SCT sensors
- at most two active Pixel and SCT sensors without hit on track (holes)
- if a track has pseudorapidity $|\eta| < 1.9$, at least 6 hits + outliers on track in TRT and the number of outliers is at most 90 % of sum of hits and outliers

Additionally, at least 1 Pixel and 6 SCT hits are required for tracks associated with pion and kaon.

Next, a set of baseline cuts is applied to select the signal decay candidates:

- all four tracks, as well as the dimuon, K^* and B^0 systems, are required to be in the ID acceptance and have $|\eta| < 2.5$
- dimuon vertex fit quality χ^2/n.d.f. < 10
- $p_{\mathrm{T}}(\mu) > 3500\,\mathrm{MeV}$

[3] A combined muon object is reconstructed from ID and MS tracks, while tagged muons are ID tracks extrapolated to the MS and matched to hits which were not sufficient to form a standalone MS track. The last type, standalone muon, does not have an ID track associated with it.

- $p_{\mathrm{T}}(\pi/K) > 500\,\mathrm{MeV}$
- K^* candidate mass in range [846, 946] MeV
- B^0 candidate mass in range [5150, 5700] MeV

The cuts are consistent with the 2011 analysis except of the B^0 candidate mass. The mass window was originally [4900, 5700] MeV but the lower bound was increased to remove the background from misreconstructed B decays.[4]

At last, selection cuts are applied to suppress the contributing backgrounds.

- The long B^0 lifetime is a good tool to remove short-lived hadrons from $b\bar{b} \to \mu^+\mu^- X$ and $c\bar{c} \to \mu^+\mu^- X$ processes. Using the lifetime significance τ/σ_τ instead of lifetime τ allows selection of the B^0 candidate with the smallest uncertainty of measured lifetime. The decay time uncertainty σ_τ is calculated for each candidate from the covariance matrices associated with the secondary four-track vertex and with the primary vertex.
- The B^0 production and decay kinematics can be exploited by a cut on the 3D pointing angle θ_{point}, defined as the angle between the reconstructed direction of flight of the B^0 from the primary to secondary vertex, and its 3-momentum vector. This angle should be zero for real B^0 (within the detector resolution) and $\cos\theta_{\mathrm{point}}$ should be close to 1.
- A requirement on a minimum value of $p_{\mathrm{T}}(K^*)$ selects the K^* candidates which were produced in the B^0 decay and suppresses the combinatorial hadronic background.
- The quality of B^0 candidates is improved by a tighter vertex χ^2/n.d.f. cut.
- The last requirement is applied to suppress radiative charmonium decays originating from $B^0 \to J/\psi K^*$ and $B^0 \to \psi(2S)K^*$ in which the charmonium decays to $\mu^+\mu^-\gamma$. A large fraction of these cases can be removed by computing the difference between the charmonium reconstructed mass and its world average mass $m_{c\bar{c}}$, and similarly for the B^0 with the world average mass m_{B^0}. A cut is applied for both $c\bar{c} = J/\psi$ and $\psi(2S)$ on the mass difference

$$\Delta m_{\mathrm{rad}}(c\bar{c}) = \left|(m_{K\pi\mu\mu} - m_{B^0}) - (m_{\mu\mu} - m_{c\bar{c}})\right|.$$

The thresholds for selection cuts were optimised using the signal and background MC samples and an estimator $\mathcal{P}(N_{\mathrm{sig}}, N_{\mathrm{bck}}) = N_{\mathrm{sig}}/\sqrt{N_{\mathrm{sig}} + N_{\mathrm{bck}}}$. The parameter space was scanned in discrete steps and the highest estimator value corresponds to the following set of cuts [75]:

- $\tau/\sigma_\tau > 12.75$
- $\cos\theta_{\mathrm{point}} > 0.999$
- $p_{\mathrm{T}}(K^*) > 3000\,\mathrm{MeV}$
- $\chi^2/\mathrm{n.d.f.}(B^0) < 2$
- $\Delta m_{\mathrm{radiative}} > 130\,\mathrm{MeV}$

[4] This will be discussed more in detail in Section 4.5

Table 4.2: $B^0 \to K^*\mu^+\mu^-$ final selection criteria. The meaning of variables in explained in the text above.

Particle	**Variable**	**Value**
μ	$\|\eta\|$	< 2.5
	p_{T}	$> 3500\,\mathrm{MeV}$
	Pixel hits + dead sensors	> 0
	SCT hits + dead sensors	> 4
	holes Pixel + SCT	< 3
	TRT hits + outliers	> 5
	TRT outliers	$< 0.9\times$(hits + outliers)
dimuon	$\|\eta\|$	< 2.5
	χ^2/n.d.f.	< 10
	combined muons	> 0
π/K track	$\|\eta\|$	< 2.5
	p_{T}	$> 500\,\mathrm{MeV}$
	Pixel hits	> 0
	SCT hits	> 5
K^*	$\|\eta\|$	< 2.5
	p_{T}	$> 3000\,\mathrm{MeV}$
	mass	$[846, 946]\,\mathrm{MeV}$
	mass for $\phi \to K^+K^-$	$\notin [1008.5, 1030.5]\,\mathrm{MeV}$
B^0	$\|\eta\|$	< 2.5
	χ^2/n.d.f.	< 2
	mass	$[5150, 5700]\,\mathrm{MeV}$
	τ/σ_τ	> 12.75
	$\cos\theta_{\mathrm{point}}$	> 0.999
	Δm_{rad}	$>130\,\mathrm{MeV}$

An additional criterion was implemented to remove $B_s^0 \to J/\psi\ \phi\,(\to K^+K^-)$ with one of kaons reconstructed as pion. The kaon mass hypotheses are set to both hadron tracks and candidates with an invariant mass in range [1008.5, 1030.5] MeV are removed.

All final selection cuts are listed in Table 4.2.

Best candidate selection

After candidate selection described above, approximately 15 % of the selected events in the collision sample have more than one signal candidate (there are on average 1.123 candidates per event). The number of candidates per event in simulated samples is 1.173 for the signal sample while for background samples it varies between 1.010 and 1.268 candidates/event. The exact values can be found in Tables A.1 and A.2 in Appendix A.

Because of the low branching fraction of the $B^0 \to K^*\mu^+\mu^-$ decay ($\sim 10^{-6}$), the probability of two such decays in one event is negligible. Furthermore, the candidates often share one or more tracks and should not be included in the analysis so a two-step procedure to select only one candidate was implemented. The first step is to pick the candidate with the best fit quality of the reconstructed B^0 vertex, i.e. with the minimal χ^2/n.d.f. This removes about 4 % of multiple candidates.

In the remaining events, the same four-track combination is reconstructed as two candidates with B^0 and $\overline{B}^0$ hypotheses. The ambiguity arises because the ATLAS detector does not have any dedicated particle-identification system which would be able to distinguish pion and kaon tracks. When assigning mass hypotheses to hadron tracks, it is possible that both $K^+\pi^-\mu^+\mu^-$ and $K^-\pi^+\mu^+\mu^-$ combinations pass the selection criteria. Because the primary and secondary vertices are the same, the vertex χ^2/n.d.f. is equal as well and cannot be used for the discrimination. However, the reconstructed K^* and B^0 masses differ and the candidate with a better K^* mass significance $m_{K\pi}/\sigma_{m_{K\pi}}$ can be selected.

A study of simulated signal sample has shown that this approach gives a slightly higher fraction of true B^0 candidates than choosing the candidate with the reconstructed mass $m_{K\pi}$ closer to the world average value of K^* mass [20], as it was done in the 2011 analysis. Additionally, comparing the distribution of B^0 mass uncertainty σ_{m_B} before and after the removal of multiple candidates, there is a smaller error of the reconstructed B^0 mass after the procedure. This is consistent with the hypothesis that it successfully removes the fake four-track combinations. Because the described procedure changes the mass distribution of K^* candidates, it is not straightforward to include the K^* mass in the fit and it is not used as a discriminating variable.

Merging of trigger streams and event yields

During 2012, events which were selected by the triggers relevant for this analysis were saved mainly in the *Muons* trigger stream. Soon after the data taking started, delayed *Bphysics* stream with additional bandwidth was added.[5]

In this analysis, datasets from *Bphysics* and *Muons* streams were processed separately and the samples were combined applying selection cuts and the duplicate events were removed. Typically, about 35–40 % of events were present in both trigger streams, depending on the data taking period.

The number of events passing all selection cuts after merging of trigger streams (before trigger selection) is listed in Table 4.3. The event yield per fb^{-1} is stable during the year, except periods A and B which are missing or partially missing the *Bphysics* stream. The dataset is dominated by the $B^0 \to J/\psi K^*$ and $B^0 \to \psi(2S)K^*$ candidates which are used as control regions. The number of extracted candidates in the $q^2 < 6\,\text{GeV}^2$ region is 1603.

The plots of invariant mass $m_{K\pi\mu\mu}$ and $m_{K\pi}$ versus q^2 for signal candidates in the collision dataset are shown in Figure 4.1 (after full selection but before applying the trigger selection).

[5] The *Bphysics* trigger stream was added during period B at the beginning of May 2012, meaning that period A has only *Muons* stream. Delayed stream means that data reconstruction is not done promptly because of limited computing resources.

Table 4.3: The number of events and the integrated luminosity L_{int} per data-taking periods in 2012. The number of events is quoted after all selection cuts were applied, before trigger selection.

Period	**Trigger stream**	$\boldsymbol{L_{\text{int}}}$ **[fb^{-1}]**	**Events**	**Events/fb^{-1}**
A	Muons	0.794	13390	16864
B	Muons + Bphys	5.095	88335	17338
C	Muons + Bphys	1.406	28550	20306
D	Muons + Bphys	3.288	67671	20581
E	Muons + Bphys	2.526	51251	20289
G	Muons + Bphys	1.275	26009	20399
H	Muons + Bphys	1.445	29411	20354
I	Muons + Bphys	1.016	20822	20494
J	Muons + Bphys	2.596	53378	20562
L	Muons + Bphys	0.840	17460	20786
All	Muons + Bphys	20.281	396277	19539
$q^2 < 6\,\text{GeV}^2$	Muons + Bphys	20.281	1603	79

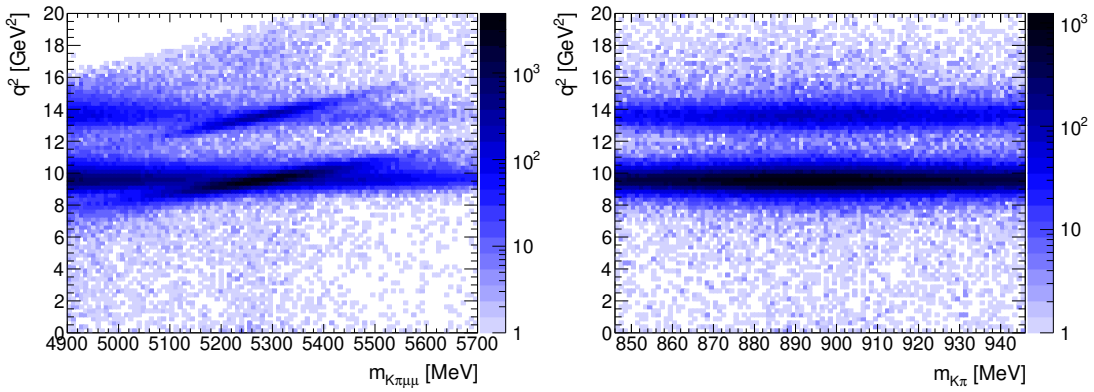

Figure 4.1: $B^0 \to K^*\mu^+\mu^-$ candidates from the collision dataset after selection, in the $m_{K\pi\mu\mu}$–q^2 plane (left) and in the $m_{K\pi}$–q^2 plane. The horizontal regions in the first plot come from combinatorial backgrounds (candidates reconstructed from J/ψ or $\psi(2S)$ and two tracks) and the tilted regions contain mostly the $B^0 \to J/\psi K^*$ and $B^0 \to \psi(2S)K^*$ candidates.

Trigger selection

Even though the analysis described here does not use trigger information explicitly, the trigger composition has to be studied to understand the source of events in the sample. Moreover, the analysis relies upon MC simulated samples and it is necessary to correct for differences between the trigger configuration in simulated and real data that could possibly influence the measurement. For example, the trigger menu varied during 2012 and trigger prescales typically vary during runs, but these effects are not modelled in the simulated datasets. These issues can be fixed by building a possibly large but limited set of trigger chains which are present in both real and simulated datasets and developing a reweighting procedure to reproduce the effect of trigger prescales and trigger overlap.

The sample of 1603 events which passed the selection described above in the $q^2 < 6\,\text{GeV}^2$ region is used to build a list containing the most efficient trigger chains. In an iterative process, the trigger chain collecting the largest number of events is selected and a new event list is created without the selected events. The list of 15 most efficient triggers is shown in Table 4.4. Four additional chains were added to the list because of their related logic. In the end, the 19 trigger chains select a total of 1497 events, i.e. 93 % of the data sample.

The dominant contribution comes from chains searching for $B \to \mu^+\mu^- X$ final states, where X represents one or more hadronic tracks: the `BmumuX\_v2` triggers are seeded by dimuon L1 items and at L2 and EF they select muon pairs with invariant mass $m_{\mu\mu} < 5.5\,\text{GeV}$ and combine them with ID tracks to build $B \to \mu^+\mu^- X$ topologies including $B^0 \to K^*\mu^+\mu^-$. Although suffering from ID track reconstruction inefficiency, these triggers provide a good rejection allowing to extend the q^2 range down to zero and they dominate in the low-q^2 region.

The `Bmumux\_v2\_L2StarB` chains are similar but use another track reconstruction algorithm at L2.[6] The `Barrel` or `BarrelOnly` means that they were seeded from L1 items in the barrel part of the MS.

The remaining events were triggered at L1 by single muon (`mu24, mu36, mu40`), dimuon (`2mu6`) and three muon chains (`3mu4`) with various thresholds and additional requirements. Other events come from combined chains searching for muon and an additional object (e.g. `mu4T\_j65` and `mu24\_j65` chains require a muon and an additional jet). Although the additional objects are not of interest for this analysis, these chains had high rejection (thus had relatively low prescales) and collected events with soft muons.

After selecting a list of triggers, a reweighting procedure is applied to the simulated datasets to account for different trigger content than in collision data. The 19 trigger chains can be divided into three groups:

- Unprescaled triggers which were present during the whole 2012:
  - `EF\_mu4T\_j65\_a4tchad\_xe60\_tclcw\_loose`,
  - `EF\_mu18\_tight\_mu8\_EFFS`,
  - `EF\_2mu8\_EFxe30\_tclcw`,
  - `EF\_mu36\_tight`,

[6] The L2star trigger algorithms [77] were added during 2012 to improve the reconstruction efficiency of tracks with high impact parameter. They were used for many B-physics muon triggers.

Table 4.4: Iterative selection of the 15 most efficient triggers. The last four triggers are also selected because of their related logic.

Run	Trigger chain	Weight	Events	
			found	left
	Total			1603
1	EF_mu4Tmu6_Bmumux_v2	0.68	889	714
2	EF_2mu4T_Bmumux_v2_L2StarB	0.58	182	532
3	EF_mu4T_j65_a4tchad_xe60_tclcw_loose	1.0	120	412
4	EF_mu18_tight_mu8_EFFS	1.0	90	322
5	EF_2mu8_EFxe30_tclcw	1.0	50	272
6	EF_mu36_tight	1.0	40	232
7	EF_2mu4T_Bmumux_v2	0.58	23	209
8	EF_3mu4T	1.0	23	186
9	EF_2mu4T_Bmumux_BarrelOnly_v2_L2StarB	0.69	22	164
10	EF_mu24_j65_a4tchad_EFxe40_tclcw	1.0	20	144
11	EF_mu24_tight_mu6_EFFS	1.0	9	135
12	EF_mu24_tight	0.15	7	128
13	EF_2mu6_Bmumux_v2_L2StarB	0.70	7	121
14	EF_mu40_MSonly_barrel_tight	1.0	7	114
15	EF_2mu6_DiMu_noVtx_noOS	0.15	5	109
	EF_2mu6_Bmumux_v2	0.70	1	108
	EF_mu4Tmu6_Bmumux_v2_L2StarB	0.68	1	107
	EF_2mu4T_Bmumux_Barrel_v2_L2StarB	0.65	1	106
	EF_mu4Tmu6_Bmumux_Barrel_v2_L2StarB	0.65	0	106

  - EF_3mu4T,
  - EF_mu24_j65_a4tchad_EFxe40_tclcw
  - EF_mu24_tight_mu6_EFFS,
  - EF_mu40_MSonly_barrel_tight

  Events passing any of these 8 triggers had a weight $w = 1$ assigned. If none of these was fired, the next group is checked.

- Bmumux_v2 trigger chains including L2StarB versions, which were introduced later in 2012 and thus missed ∼30 % of the collected integrated luminosity. Moreover, some of the dimuon L1 items were switched off at very high instant luminosity because their rates became too high. Events passing these chains had a weight computed according to their collected integrated luminosity, ranging between 0.58 and 0.70.

- The last group contains the two remaining triggers, EF_mu24_tight and EF_2mu6_DiMu_noVtx_noOS, which were operational during whole 2012 but heavily prescaled. They collected data during a period equivalent to

13 % and 5 % of the integrated luminosity, respectively. Given that their prescales were not correlated, the trigger weight was defined as

$$w = 1 - \sum_{i=1}^{n} (1 - L^i_{\text{frac}}) \,,$$

where L^i_{frac} is the integrated luminosity fraction collected by the i-th trigger chain and the product is taken over all triggers which fired. The resulting weight of these triggers was 0.15.

If none of the above chains was passed, the event has a weight $w = 0$ and is rejected from the analysed sample. The weights assigned to events according to trigger fired are listed in Table 4.4.

The trigger efficiency for selecting $B^0 \to K^* \mu^+ \mu^-$ signal candidates is estimated using the sum of weights of the signal MC samples. The efficiencies are (28.0 ± 0.2) %, (29.4 ± 0.1) % and (29.1 ± 0.1) % for the flat, SM B^0 and SM $\overline{B}^0$ sample, respectively.

4.3 Kaon and pion misidentification

In an ideal case, the flavour of the B^0 and $\overline{B}^0$ candidates can be inferred from the sign of the final-state pion and kaon tracks. However, because the ATLAS detector has only a limited ability to identify hadron tracks (which is not used for this analysis), there is an ambiguity in setting the $\pi^{\pm}/K^{\mp}$ mass hypotheses to the reconstructed tracks. The selection applied in this analysis relies on kinematics and results in a fraction of B^0 and $\overline{B}^0$ candidates which have an incorrect flavour tag assigned (i.e. they are mistagged).

If a candidate is mistagged and the observables $\cos\theta_K$, $\cos\theta_L$ and ϕ are measured in the experimental convention defined in Section 1.4.1, they change sign as has been shown in Table 1.2. Moreover, the distributions of $\cos\theta_K$ and ϕ are slightly shaped by the swapped track mass hypothesis because of kinematics.[7] The sign changes of measured angles translate into a change of sign of the terms multiplied by angular coefficients S_5, S_6, S_8 and S_9 in the full angular differential decay rate expressed by Eq. 1.4 (and for the corresponding P_i parameters).[8]

As a result, for a sample containing the same number of B^0 and $\overline{B}^0$ meson candidates with mistag probabilities ω and $\overline{\omega}$, dilution D can be defined as

$$D = 1 - \omega - \overline{\omega} \approx 1 - 2\langle\omega\rangle \,, \tag{4.1}$$

where $\langle\omega\rangle$ is the average mistag probability. The measured value of an angular parameter which changes sign in case of mistag is then the real physical value scaled by a factor D. Hence, the values of S_5 and S_8 (and P'_5, P'_8) obtained from

[7] An opposite mass hypothesis for hadron tracks results in a small difference in the reconstructed K^* invariant mass. Because the angle $\cos\theta_K$ is measured in the K^* rest-frame, there is a slight change in the measured value. The same is true for the ϕ angle, measured in the B^0 centre-of-mass frame.

[8] Because of the folding transformations, parameters S_6 and S_9 are not measured in this analysis.

Table 4.5: Mistag probability ω and $\overline{\omega}$ determined from MC samples over the whole range of q^2.

Mode	$\boldsymbol{\omega}$	$\overline{\boldsymbol{\omega}}$	$\boldsymbol{\Delta\omega = \omega - \overline{\omega}}$
signal (phase space)	0.1092 ± 0.0002	–	–
signal (SM)	0.1097 ± 0.0007	0.1087 ± 0.0007	0.0010 ± 0.0010
signal (SM, p_{T} reweighted)	0.1093 ± 0.0007	–	–
$B^0 \to J/\psi K^*$	0.1041 ± 0.0007	–	–
$B^0 \to \psi(2S) K^*$	0.1102 ± 0.0007	–	–

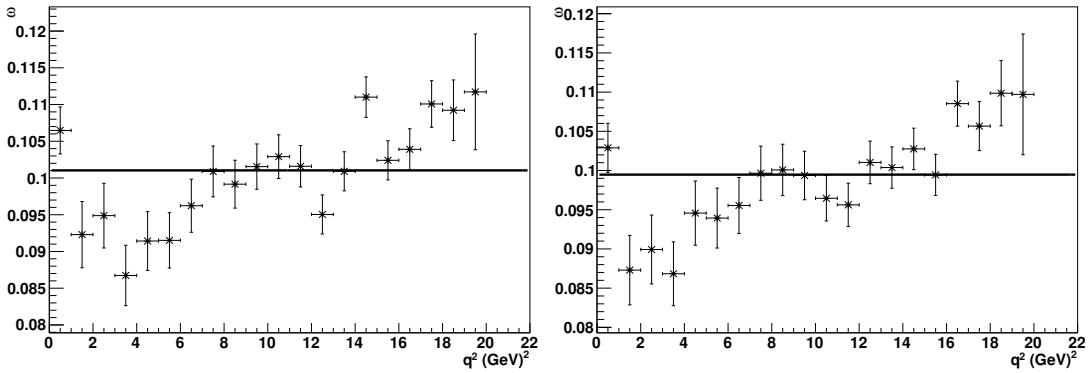

Figure 4.2: Mistag probability as a function of q^2 for SM-like MC simulated datasets of $B^0 \to K^*\mu^+\mu^-$ (left) and $\overline{B}^0 \to \overline{K}^*\mu^+\mu^-$ (right).

fits should be multiplied by $1/D$ and the uncertainties should scale accordingly. No scaling is needed for F_L, S_3, S_4 and S_7 (nor for P_1, P_4' and P_6').

The mistag probability of B^0 ($\overline{B}^0$) meson ω ($\overline{\omega}$) is studied in the MC simulated datasets and the results are listed in Table 4.5. They include $B^0 \to K^*\mu^+\mu^-$ signal samples (phase-space and SM-like decays), SM-like $\overline{B}^0 \to \overline{K}^*\mu^+\mu^-$ and control decays $B^0 \to J/\psi K^*$ and $B^0 \to \psi(2S)K^*$. As an additional check, a reweighting procedure is applied to the SM-like signal sample, to account for a different p_{T} distribution of data and MC simulated samples.

The mistag probability as a function of q^2 for $B^0 \to K^*\mu^+\mu^-$ and $\overline{B}^0 \to \overline{K}^*\mu^+\mu^-$ is shown in Figure 4.2. It varies slightly with q^2 from 9.1 % to 12.4 % because of kinematics but the difference $\Delta\omega = \omega - \overline{\omega}$ in q^2 bins remains consistent with zero (evaluated for 1 and 2 GeV^2 bins). Therefore the average mistag rate in a given bin is computed and applied after fitting.

4.4 Fitting

The aim of this analysis is to extract the parameters of $B^0 \to K^*\mu^+\mu^-$ angular distribution by fitting the differential decay rate expressed by Eq. (1.4) in bins of dimuon invariant mass squared q^2. As described in Section 1.4.3, it is possible to apply a set of transformations which reduce the number of parameters in the fits. The four folded angular distributions (1.12), (1.15), (1.18) and (1.21) each depend on three parameters: F_L, S_3 and one of $S_{4,5,7,8}$. Therefore, four sets of extended unbinned maximum-likelihood fits of the angular distributions were implemented for each q^2 bin.

The discriminating variables are the reconstructed invariant mass of the B^0 candidate $m_{K\pi\mu\mu}$ and the angular observables defined in Section 1.4.1 in the experimental convention: cosines of the helicity angles $\cos\theta_K$ and $\cos\theta_L$, and ϕ. The invariant mass of the K^* candidate cannot be included because the selection of one candidate in multiple-candidate events uses the K^* mass significance and influences the distribution. The resolution of angular variables $\cos\theta_K$, $\cos\theta_L$ and ϕ is considered to have a negligible effect on the results, following the studies performed for the $B_s^0 \to J/\psi\ \phi$ analysis [78, 79].

The likelihood function $\mathcal{L}$ for a given q^2 bin and folding is defined as

$$\mathcal{L} = \frac{\mathrm{e}^{-n}}{N!} \prod_{k=1}^{N} \sum_{l} n_l P_{kl}(m_{K\pi\mu\mu}, \cos\theta_K, \cos\theta_L, \phi; \widehat{p}, \widehat{\theta}) \,, \tag{4.2}$$

where P_{kl} is the probability distribution function (PDF) evaluated for event k and component l, and N is the total number of events. The sum runs over signal and background components with n_l being the fitted yield for the l-th component. Additionally, n is the sum over n_l. The $\widehat{p}$ represents the parameters of interest (F_L and S_i) and $\widehat{\theta}$ are the nuisance parameters. In the nominal fit, l iterates only over one signal and one background component. Additional components such as inclusive backgrounds or the non-resonant component $B^0 \to K^+\pi^-\mu^+\mu^-$ are included in fits of control samples and for evaluation of systematic uncertainties.

Given the limited numbers of candidates in the analysed sample, a two-stage fit strategy was chosen. The first step is a simplified fit of the B^0 mass with the event-by-event uncertainty of the reconstructed mass as a conditional variable. In this fit, the nuisance parameters (mass and the scale parameter of the signal Gaussian PDF) are fixed to parameters obtained by fitting the data control samples. The second step is a simultaneous angular and mass fit which extracts the F_L and S_i parameters together with the nuisance parameters related to the shape of combinatorial background. Some of the nuisance parameters in the second fit are fixed to the results obtained from the first step, as will be described in detail later on.

The fit was implemented using the RooFit toolkit [80] and the minimisation is done by the MINUIT software package. The value of $-\ln\mathcal{L}$ is minimised, which is equivalent to maximising the likelihood $\mathcal{L}$. The uncertainties of extracted parameters can be determined by MINOS (according to $-2\Delta\log\mathcal{L} = 1$ rule) or by HESSE which is using the second derivative matrix.

Binning

Because of the small number of signal candidates in the analysed sample, it is necessary to select a q^2 binning which has a sufficient signal-to-background ratio and where the systematic uncertainties and fit bias are reduced. Moreover, the bin width must be sufficiently large so that the q^2 resolution effects are negligible.

Fit validation studies were done with approximately $1\,\text{GeV}^2$ wide bins and $2\,\text{GeV}^2$ wide bins in q^2, taking into account binning schemes used by the other experiments and by the theory community to allow comparisons. A high number of angular variable fits were failing for the narrow bins for the expected signal yields, which were extrapolated from the ATLAS 2011 analysis [75]. As a result, a $2\,\text{GeV}^2$ binning scheme was adopted, with bins

- $q^2 \in [0.04, 2.0]\,\text{GeV}^2$,
- $q^2 \in [2.0, 4.0]\,\text{GeV}^2$,
- $q^2 \in [4.0, 6.0]\,\text{GeV}^2$.

This binning showed a good fit convergence for the expected signal and background yields. The q^2 uncertainty in the simulated signal sample is about 20 times smaller than the $2\,\text{GeV}^2$ bin width across all range of q^2. Therefore the q^2 resolution has a negligible impact on this measurement.

Three wide bins were added:

- $q^2 \in [0.04, 4.0]\,\text{GeV}^2$ which was used by the Belle collaboration in Ref. [7],
- $q^2 \in [1.1, 6.0]\,\text{GeV}^2$ which was used by the CMS collaboration in Ref. [39] and removes the virtual photon contribution that dominates at very low q^2,
- $q^2 \in [0.04, 6.0]\,\text{GeV}^2$ covering the whole q^2 range of this analysis.

In all bins, the ϕ veto $q^2 \in [0.98, 1.10]\,\text{GeV}^2$ was applied. Lastly, the control sample regions were defined as

- $q^2 \in [8.0, 11.0]\,\text{GeV}^2$ for $B^0 \to J/\psi K^*$ sample and
- $q^2 \in [12.0, 15.0]\,\text{GeV}^2$ for $B^0 \to \psi(2S) K^*$ sample.

4.4.1 Signal and background fit models

Signal fit model

The $B^0 \to K^*\mu^+\mu^-$ mass distribution is modelled by a single Gaussian function with per-candidate error of the reconstructed mass σ_m as

$$P_{\text{sig}}(m) = \frac{1}{S\sigma_m\sqrt{2\pi}} \exp\left(-\frac{(m-m_0)^2}{2S^2\sigma_m^2}\right), \tag{4.3}$$

where m_0 is the mean fitted mass of the B^0 candidate. The dimensionless scale factor $S = \sigma/\sigma_m$ accounts for a possible difference between the fitted width of mass peak σ and the distribution of per-candidate mass errors σ_m, calculated from covariance matrices of the secondary vertex fits. The nuisance parameters m_0 and S are extracted from fit to data in the $B^0 \to J/\psi K^*$ control region described in Section 4.4.3 and fixed to these values in all subsequent fits.

Combinatorial background

The PDF of the combinatorial background, which does not peak in the $m_{K\pi\mu\mu}$ distribution, is assumed to factorise into a product of one-dimensional terms. PDF shapes are motivated by sideband regions in control samples and simulated inclusive background samples. The mass distribution is described by an exponential function and second-order Chebyshev polynomials are used to model the angular distributions in $\cos\theta_K$, $\cos\theta_L$ and ϕ. The resulting function can be expressed as

$$P_{\text{comb}}(m, \cos\theta_K, \cos\theta_L, \phi) = \mathrm{e}^{-\lambda m} \cdot (1 + A_1 T_1(\cos\theta_K) + A_2 T_2(\cos\theta_K)) \cdot \\ \cdot (1 + B_1 T_1(\cos\theta_L) + B_2 T_2(\cos\theta_L)) \cdot (1 + C_1 T_1(\phi) + C_2 T_2(\phi)) \,, \quad (4.4)$$

with Chebyshev polynomial terms $T_1(x) = x$, $T_2(x) = 2x^2 - 1$, and coefficients λ, A_i, B_i and C_i. Because the mass resolution is expected to vary on an event-by-event basis due to different detector resolution in different regions, the PDF depends on both mass and per-event mass error. This requires a correction of the likelihood, such that the PDF sampled from a histogram of the conditional variable σ_m is included to avoid biases from the Punzi effect [81].

All parameters are determined from fits to the data in each q^2 bin so the systematic dependence of the signal parameters on the modelling of combinatorial background shape is included directly in the uncertainties extracted from the fit.

Peaking background

An extensive list of processes with similar topology as $B^0 \to K^*\mu^+\mu^-$ was considered. It included decays with the same particles in the final state, decays that can mimic signal after hadron misidentification (final states $h^+h^-\mu^+\,\mu^-$, where $h^\pm$ are hadrons with track in the ID) and decays with three (five) particles in the final state which can be misreconstructed as signal with addition (removal) of one particle track. The contribution of many B^0, B_s^0, B^+, B_c^+ and Λ_b decays was found negligible because of different mass range or very small branching fraction; hence the generation of these samples was not requested.

Simulated samples of exclusive background modes which might contribute to the signal region are listed in Section 4.1 and the numbers of events which were simulated and passed the selection cuts are listed in Table A.2 in Appendix A. The samples were reconstructed in the same way as data samples and the cut-based and trigger selections were applied. The expected number of events for processes with known cross-section was calculated using the integrated luminosity and decay cross-sections listed in Ref. [20]. For the other decays, the number of expected events was computed from the number of B^0 mesons in data, b-quark fragmentation functions and branching fractions.

Most of the simulated processes have negligible contributions and a threshold of 0.25 event per $1\,\text{GeV}^2$ bin in q^2 is set to consider the decay as significant. Five decays that satisfy this requirement and their expected number of events per bin are listed in Table 4.6. Because these decays have nontrivial angular distributions that is not well measured and relatively low number of expected events, these components are not included in the nominal signal fit. The resulting bias is evaluated by embedded toy MC experiments and included as a systematic uncertainty (described in Section 4.6.1).

Table 4.6: Expected peaking background contributions per q^2 bin. Only decays with more than 0.25 event/bin are included.

Decay mode	**q^2 bin range (GeV^2)**					
	[0.04, 0.98]	**[1.1, 2]**	**[2, 3]**	**[3, 4]**	**[4, 5]**	**[5, 6]**
$B^+ \to K^{*+}(K^0\pi^+)\mu^+\mu^-$	0.17	0.12	0.03	0.25	0.12	0.22
$B_s^0 \to \phi\mu^+\mu^-$	0.40	0.19	0.22	0.23	0.25	0.28
$B^+ \to K^+\mu^+\mu^-$	0.89	0.81	1.00	1.30	1.50	1.90
$\Lambda_b \to \Lambda(pK^-)\mu^+\mu^-$	1.83	1.88	0.61	0.66	0.09	0.08
$\Lambda_b \to pK^-\mu^+\mu^-$	0.99	0.87	0.46	0.48	0.10	0.11
Total	4.28	3.87	2.32	2.92	2.06	2.59

The same procedure is applied for the control regions. Due to the large number of signal events in these bins, the thresholds are set to 0.25 % of the expected yield, corresponding to about 500 events in the J/ψ region and 30 events in the $\psi(2S)$ region. The contributing modes are $B^+ \to J/\psi\ K^+$, $\Lambda_b \to \Lambda\, J/\psi$ and $B_s^0 \to J/\psi\ K^*$ (and the equivalent decays with $\psi(2S)$ in the final state). Double or triple Gaussian PDFs are used to describe the mass distribution of these backgrounds and they are included in the control sample fits which will be described in Section 4.4.3.

After the fit validation and unblinding, additional background was observed. It does not peak in the mass distribution but it accumulates in the left B^0 mass sideband. It is also clearly visible in the $\cos\theta_K$ and $\cos\theta_L$ distributions. Studies of this background and its possible sources will be discussed in Section 4.5. This contribution is not included in the nominal fit to data but it is treated as a systematic uncertainty.

4.4.2 Signal acceptance functions

To describe the signal angular distributions, their sculpting by detector, trigger, reconstruction and selection effects must be understood and accounted for. An acceptance function is defined as the ratio of reconstructed and generated distributions of $\cos\theta_K$, $\cos\theta_L$ and ϕ, meaning that it is compensating for the bias in angular distributions. A large sample of $B^0 \to K^*\mu^+\mu^-$ signal was simulated with decay according to phase space model to extract the acceptance functions. The generator-level angular distributions were validated to be flat in $\cos\theta_K$, $\cos\theta_L$ and ϕ, so any deviation from a constant distribution is due to acceptance effects.

The acceptance function is assumed to be constant across each bin and to factorise for each angular distribution as

$$\varepsilon(\cos\theta_K, \cos\theta_L, \phi) = \varepsilon(\cos\theta_K)\varepsilon(\cos\theta_L)\varepsilon(\phi)\,. \tag{4.5}$$

Sixth order polynomials were found to provide the best fit agreement for the $\cos\theta_K$ and $\cos\theta_L$ distributions during fit validation studies. For ϕ, second order

polynomial function gives a good compromise between the goodness of fit and fit complexity. The acceptance function is thus given by

$$\begin{aligned}\varepsilon(\cos\theta_K, \cos\theta_L, \phi) = N\cdot \\ (1 + K_1\cos\theta_K + K_2\cos^2\theta_K + K_3\cos^3\theta_K + K_4\cos^4\theta_K + K_5\cos^5\theta_K + K_6\cos^6\theta_K)\cdot \\ (1 + L_1\cos\theta_L + L_2\cos^2\theta_L + L_3\cos^3\theta_L + L_4\cos^4\theta_L + L_5\cos^5\theta_L + L_6\cos^6\theta_L)\cdot \\ (1 + P_1\phi + P_2\phi^2)\,, \quad (4.6)\end{aligned}$$

where N is a normalisation constant and K_i, L_i and P_j are polynomial coefficients ($i = 1, 2, ..., 6$; $j = 1, 2$). Because the acceptance functions have a significant q^2 dependence, fits are done for each of six q^2 bins and each angular folding.

The extracted acceptance functions are applied to data such that the signal probability distribution functions are

$$P_{kl} = \varepsilon(\cos\theta_K)\varepsilon(\cos\theta_L)\varepsilon(\phi)g(\cos\theta_K, \cos\theta_L, \phi)\cdot G(m_{K\pi\mu\mu})\,,$$

where $g(\cos\theta_K, \cos\theta_L, \phi)$ is the angular differential decay rate after one of the folding transformations and $G(m_{K\pi\mu\mu})$ is the signal mass distribution. For the background components, the angular acceptance is set to 1.

An example of acceptance functions measured for S4 folding in three bins of q^2 is shown in Figure 4.3.

To verify the procedure, a closure test is performed in which the acceptance functions are applied to the flat-angle MC sample from which they were extracted. The angular distributions are then fitted with parameters F_L and S_i allowed to float. The fit bias is measured as the difference between the input and fitted values and is included in the systematic uncertainty.

4.4.3 Control sample fits

Data and simulated MC samples from the control regions are used to validate the fit models and to extract parameters of the B^0 mass distribution used in the subsequent angular fits. The q^2 bins are defined as $[8.0, 11.0]\,\text{GeV}^2$ for sample dominated by $B^0 \to J/\psi K^*$ and $[12.0, 15.0]\,\text{GeV}^2$ for the $B^0 \to \psi(2S)K^*$ sample.

An extended unbinned maximum-likelihood fit of the reconstructed mass $m_{K\pi\mu\mu}$ is used. The signal PDF is defined by Equation (4.3) as a Gaussian with per-candidate error and the combinatorial background is described by an exponential distribution. In addition, three exclusive background modes, which contribute to the regions according to the background MC studies, are included: $B^+ \to J/\psi\ K^+$, $\Lambda_b \to \Lambda\, J/\psi$ and $B_s^0 \to J/\psi\ K^*$. Similarly, decays with $\psi(2S)$ in the final state are included as component in the $\psi(2S)$ region fit. The mass distributions of inclusive backgrounds are extracted from the corresponding simulated samples and represented by double and triple Gaussian functions. The background components are added sequentially and the largest of the statistical errors of the fitted m_0 and S parameters is taken. The systematic uncertainty is extracted from the fits as half of the total spread of measured values.

The fit results are shown in Figure 4.4 and the fitted parameters are

$$\begin{aligned} m_0 &= (5276.6 \pm 0.3\,(\text{stat.}) \pm 0.5\,(\text{syst.}))\,\text{MeV} \\ S &= 1.219 \pm 0.005\,(\text{stat.}) \pm 0.017\,(\text{syst.}) \end{aligned} \quad (4.7)$$

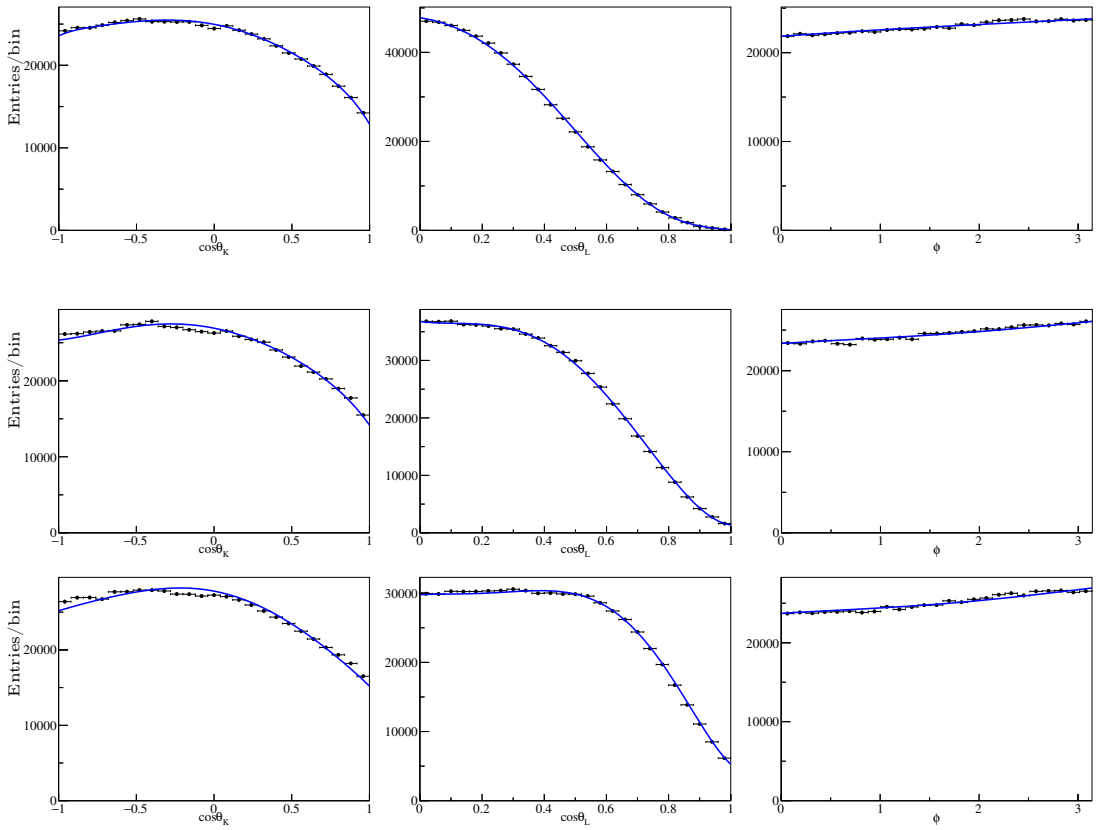

Figure 4.3: Acceptance functions for S4 folding in bin $q^2 \in [0.04, 2.0]\,\mathrm{GeV}^2$ (top), $[2.0, 4.0]\,\mathrm{GeV}^2$ (middle) and $[4.0, 6.0]\,\mathrm{GeV}^2$ (bottom). The black points are the angular distributions of candidates after full selection, blue curves are sixth (second) order polynomial fits of $\cos\theta_K$ and $\cos\theta_L$ (ϕ).

for the $B^0 \to J/\psi K^*$ region and

$$m_0 = (5275.5 \pm 1.2\,(\mathrm{stat.}) \pm 1.7\,(\mathrm{syst.}))\,\mathrm{MeV}$$
$$S = 1.191 \pm 0.020\,(\mathrm{stat.}) \pm 0.006\,(\mathrm{syst.})$$

for the $B^0 \to \psi(2S)K^*$ control sample. The results are consistent with each other but the fitted mean value of B^0 mass is systematically smaller than the world average $m_{\mathrm{PDG}}(B^0) = (5279.55 \pm 0.26)\,\mathrm{MeV}$ [20]. However, the results obtained from the fits of MC simulated samples are consistent with fits of data. This shows that by fitting the control regions it is possible to translate information about the ID momentum and mass scale to the signal region.[9] Moreover, the systematic error of fitted mass after including all effects would be at the order of few MeV. Because the values obtained from the $\psi(2S)$ region have larger uncertainty, the results from the J/ψ region will be used as nuisance parameters in the $B^0 \to K^*\mu^+\mu^-$ fits.

[9] Previous ATLAS studies of processes with $J/\psi \to \mu^+\mu^-$ such as $B_s^0 \to J/\psi\,\phi$ [78] found that the muon momentum reconstructed by ID is influenced by trigger p_{T} cuts and is slightly lower than the world average value from Ref. [20]. It can be corrected by setting the reconstructed mass of dimuon to $m_{\mathrm{pdg}}(J/\psi)$ but this is not possible for the non-resonant $B^0 \to K^*\mu^+\mu^-$.

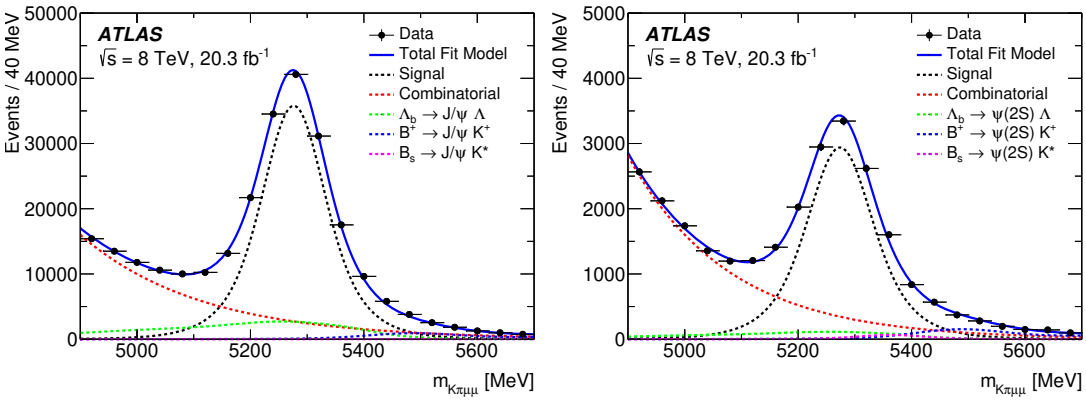

Figure 4.4: Fits to the $K\pi\mu\mu$ invariant mass distributions for the K^*J/ψ (left) and $K^*\psi(2S)$ (right) control region samples. The data are shown as points and the total fit model as the solid lines. The dashed lines represent signal (black), combinatorial background (red) and background from decays of Λ_b (green), B^+ (blue) and B_s^0 (magenta).

4.4.4 Fit validation

Toy MC validation of the fit models

Various checks are performed to evaluate the convergence and bias of mass and angular fits. For mass-only fits, the signal MC samples are fitted and the resulting yields and parameters of the mass distribution m_0 and S are used to determine the difference between the true mass distribution and the PDF.

The validation of angular fits is done by generating sets of pseudo-experiments (toys) with known event yields and angular distributions, and comparing the fitted results with the initial values. The fit performance can be deduced from the pull distribution of a parameter p, where the pull between fitted value x_{fit} with an uncertainty σ_{fit}, and generated value x_{gen} of parameter is defined as

$$p = \frac{x_{\text{fit}} - x_{\text{gen}}}{\sigma_{\text{fit}}} .$$

For an unbiased sample with uncertainties extracted correctly and in a limit of high statistics, the pull distribution is expected to have a Gaussian distribution with a mean of zero and width of one.

Ensembles of toy experiments for evaluation of the intrinsic fit bias are dataset generated with signal and combinatorial background events distributed according to expectations of the likelihood and with known angular distributions of the signal candidates. The event yields used for each ensemble of toys are randomly generated to have a Poisson distribution with a mean equal to the yield extracted from the nominal mass fit. The parameters of the mass distribution are fixed to those extracted from the control sample fits, i.e. $m_0 = (5276.6 \pm 0.6)\,\text{MeV}$ and $S = 1\,219 \pm 0\,018$. The samples are then fitted in the same way as data by a two-step fit and the pull and width of the extracted observables can be measured. The results show that the angular fits for all S_i folds are largely unbiased and with correctly extracted errors (the pull mean value is consistent with zero and pull width with one).

Similarly, sets of embedded toys are studied. These are datasets including signal and combinatorial background components generated as above, with additional events representing the peaking background contributions as listed in Table 4.6. Both mass and angular fits are then performed. An example of results of angular fits from 500 embedded toy experiments using the S_4 folding are shown in Table 4.7.

In general, a sufficiently high fraction of fits was found to converge for the angular fits ($> 80\,\%$) and most of the biases of mass and angular fits are small, meaning that the fit is correctly extracting the signal and background event yields and the angular parameters. The largest bias is measured in F_L, especially in two wide bins $q^2 \in [1.1, 6.0]\,\mathrm{GeV}^2$ and $[0.04, 6.0]\,\mathrm{GeV}^2$.

Additional checks of the fitting procedure and tools included linearity tests, angular fits of the control decay $B^0 \to J/\psi K^*$, fits of the dataset collected in 2011 and fits with altered parameters to assess the systematic uncertainties (e.g. the order of the Gaussian functions used to model the mass distribution of backgrounds). These studies were done by other members of the analysis group and are not be described here.

Table 4.7: Results of angular fits from 500 embedded angular distribution toys using the S_4 folding. The fit model includes signal, combinatorial background and peaking background contributions from Table 4.6.

q^2 bin [GeV^2]	Parameter	Pull mean	Pull width	Bias [σ]
[0.04, 2.00]	F_L	-0.094 ± 0.044	0.887 ± 0.041	-2.133
	S_3	0.004 ± 0.047	0.933 ± 0.041	0.076
	S_4	-0.048 ± 0.041	0.813 ± 0.036	-1.169
[2.00, 4.00]	F_L	-0.155 ± 0.049	0.969 ± 0.044	-3.168
	S_3	-0.015 ± 0.050	0.995 ± 0.046	-0.296
	S_4	-0.023 ± 0.049	0.944 ± 0.045	-0.469
[4.00, 6.00]	F_L	0.008 ± 0.049	0.901 ± 0.042	0.165
	S_3	0.089 ± 0.049	0.909 ± 0.038	1.822
	S_4	0.061 ± 0.047	0.862 ± 0.043	1.297
[0.04, 4.00]	F_L	0.011 ± 0.053	1.029 ± 0.058	0.209
	S_3	-0.042 ± 0.047	0.951 ± 0.050	-0.883
	S_4	-0.012 ± 0.047	0.960 ± 0.043	-0.256
[1.10, 6.00]	F_L	-0.196 ± 0.048	0.956 ± 0.050	-4.045
	S_3	-0.022 ± 0.046	0.924 ± 0.047	-0.477
	S_4	-0.008 ± 0.051	1.031 ± 0.045	-0.163
[0.04, 6.00]	F_L	-0.046 ± 0.049	1.011 ± 0.038	-0.955
	S_3	0.048 ± 0.048	0.943 ± 0.041	0.990
	S_4	-0.068 ± 0.045	0.889 ± 0.041	-1.529

4.5 Background studies

An unexpected background was observed after the validation of the analysis procedure and unblinding of the signal region. The background does not peak in the B^0 nor K^* mass distributions but it seems to peak in both $\cos\theta_K$ and $\cos\theta_L$ distributions and to accumulate in the high q^2 bins. A systematic study of possible sources was performed and the results are shown here. The treatment that was adopted for this background and proposed steps for Run 2 analysis are described in Section 4.5.3.

The plots of $m_{K\pi\mu\mu}$, $\cos\theta_K$, $\cos\theta_L$ and ϕ for signal region in three bins of q^2 are shown in Figure 4.5. The $m_{K\pi\mu\mu}$ range is $[4900, 5700]\,\text{MeV}$, as used in the 2011 analysis. An excess in a few regions of angular distributions are clearly visible and it cannot be easily described by the fit used. The observed features are:

- background peaking at $|\cos\theta_L| \simeq 0.7$
- background peaking at high values of $\cos\theta_K \simeq 1$
- both are more visible in the middle and high q^2 region and at low values of $m_{K\pi\mu\mu}$

The backgrounds are more evident in the 2D distributions of $\cos\theta_K$ and $\cos\theta_L$ versus $m_{K\pi\mu\mu}$ and q^2 shown in Figure 4.6. Events from both regions of $|\cos\theta_L| \simeq 0.7$ and $\cos\theta_K \simeq 1$ accumulate at low $m_{K\pi\mu\mu}$ and at high q^2. In contrast, the distributions of helicity angle ϕ for candidates with low $m_{K\pi\mu\mu}$ and high q^2 is approximately uniform. This observation triggered the hypothesis that these candidates are either from combinatorial background or they come from misreconstructed decays.

In general, the combinatorial background reconstructed from four final-state particles can fall into various categories: the truly combinatorial candidates reconstructed from four random tracks in the event are expected to have smoothly varying distributions of reconstructed masses $m_{K\pi\mu\mu}$, $m_{K\pi}$ and $m_{\mu\mu}$ and helicity angles, while candidates reconstructed by combining two muons from J/ψ decay and two tracks may peak in variables related to the dimuon system, similarly for candidates originating from $X \to K^\pm\pi^\mp$ combined with two muons.

Additional combinatorial candidates may come from quadruplets of tracks for which one or more of the final-state particles were misidentified in the detector. Because of the limited $K^\pm/\pi^\pm$ discrimination capabilities of the ATLAS detector, the mass hypotheses were set to hadron tracks during reconstruction and the signal selection was based on kinematic cuts only. There is, however, also a non-negligible probability that charged hadrons decay in-flight and get matched to the daughter muon's segment in the Muon Spectrometer and identified as muon (often referred to as hadronic punch-through). This contribution was estimated from simulations by the authors of $B_s^0 \to \mu^+\mu^-$ analysis [74] to be at the level of 3 % (8 %) of the total fake kaon (pion) tracks. In addition, the probability that a charged-hadron track in the ID will be misidentified as muon was estimated to be about 0.4 % (0.2 %) for kaon (pion). More complicated cases include double swap, when hadron track (K or π) is identified as muon and muon track as hadron.

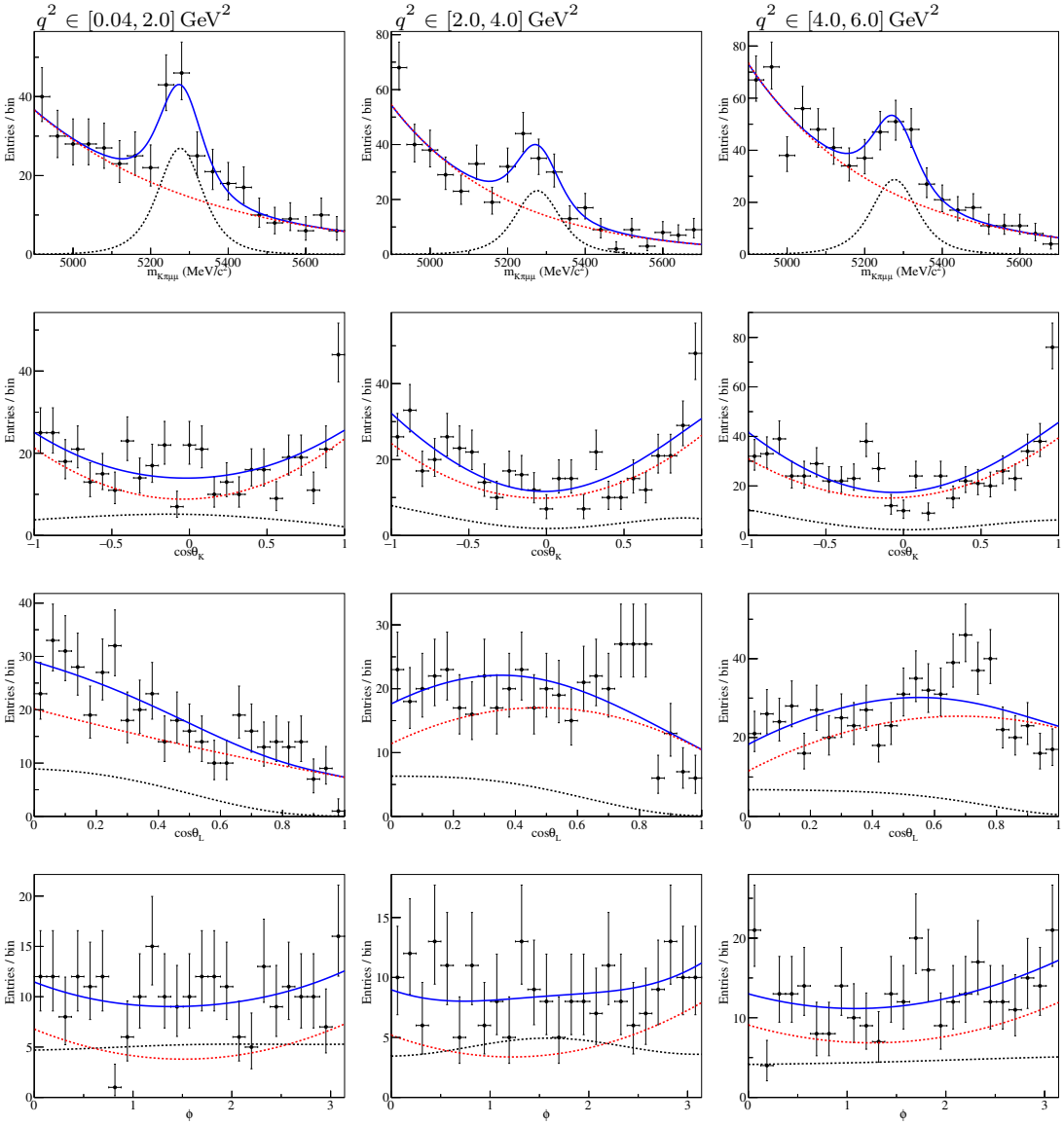

Figure 4.5: Distributions of observables $m_{K\pi\mu\mu}$, $\cos\theta_K$, $\cos\theta_L$ and ϕ in collision data found after unblinding the signal region: left to right are q^2 bins $[0.04, 2.0]$, $[2.0, 4.0]$ and $[4.0, 6.0]$ GeV^2. Plots show also projections of the fitted PDFs for signal (black) and background component (red) and total fit model (solid blue). The backgrounds at $\cos\theta_K \simeq 1$ and $|\cos\theta_L| \simeq 0.7$ are clearly visible, especially in the $[4.0, 6.0]$ GeV^2 bin.

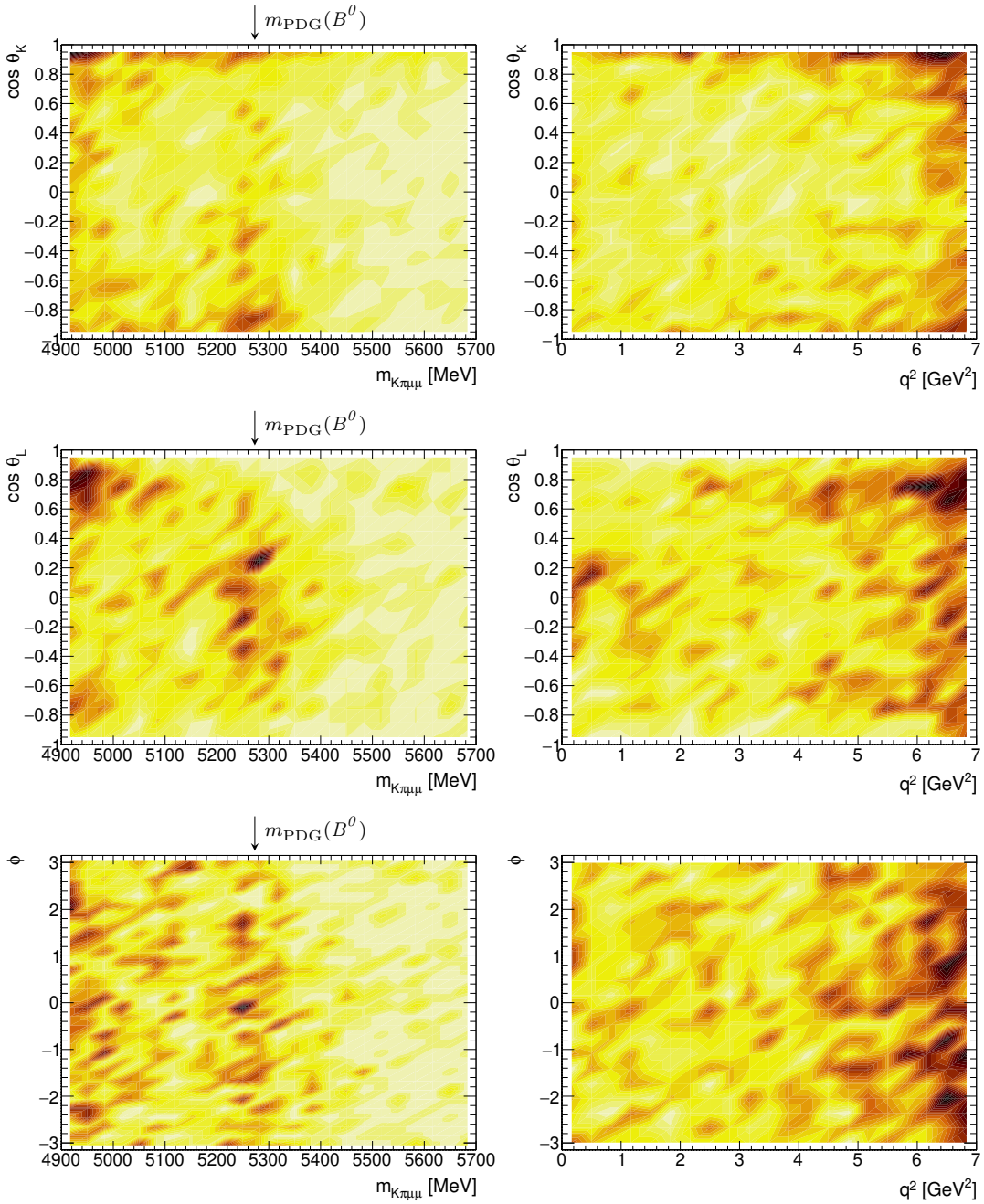

Figure 4.6: Distributions of observables $\cos\theta_K$, $\cos\theta_L$ and ϕ versus $m_{K\pi\mu\mu}$ (left) and q^2 (right) found after unblinding of data in the signal region. All left plots include candidates in q^2 range$[0.04, 6.0]\,\mathrm{GeV}^2$, while the q^2 range in the right plots is extended up to $7\,\mathrm{GeV}^2$ for better visibility.

4.5.1 Background peaking in the $\cos\theta_L$ distribution

The simulated samples of inclusive backgrounds $b\bar{b} \to \mu^+\mu^- X$ and $c\bar{c} \to \mu^+\mu^- X$ were scrutinised but only a small number of candidates (few tens) passed the full $B^0 \to K^*\mu^+\mu^-$ selection. Even by slightly relaxing some of the selection cuts (e.g. lifetime significance τ/σ_τ from 12.5 to 10) and by extending the K^* mass window, the sample contained only a few hundreds candidates. The MC-truth information was checked for candidates which contributed to the problematic $\cos\theta_K$ and $\cos\theta_L$ regions but no strong conclusion could be drawn due to low statistics. Yet, a few candidates from the $|\cos\theta_L| \simeq 0.7$ region had similar characteristics: they came from decays of B mesons via D mesons to a final state with multiple tracks. The B^0 candidate was formed from few of these tracks and one or more tracks from the underlying event or fake track. In many cases, one or both B and D decays were semi-leptonic.

Because the simulated samples of $B \to D \to X$ decays were not available, the hypothesis of partially reconstructed decays was tested on the collision data sample. The invariant mass of two, three and four tracks that form the signal candidate was computed with various mass hypotheses set. The invariant mass vs. $\cos\theta_L$ distributions for data were then compared to the same plots for $B^0 \to K^*\mu^+\mu^-$ and $\overline{B}^0 \to \overline{K}^*\mu^+\mu^-$ simulated samples. An example for the $D^+ \to K\pi\pi$ hypothesis is shown in Figure 4.7 for data and for the $B^0 \to K^*\mu^+\mu^-$ simulated sample. In addition to entries in the central region, a cluster of candidates is clearly visible in the data in the region of D meson masses (1900 to 2100 MeV) and $\cos\theta_L = -0.7$.[10] Similarly, for $D^- \to K\pi\pi$ hypothesis the observed background region is around $\cos\theta_L = +0.7$. The corresponding histograms of invariant mass are shown on the bottom plots and there is a clear structure on top of the distribution of the B^0 signal.

With this procedure, the contributions from $D^0 \to K^\pm\pi^\mp$, $D^+ \to K\pi\pi$ and $D_s^\pm \to KK\pi$ decays were found.

A set of vetoes was implemented to mitigate this background (referred to as D vetoes). Events are removed if the reconstructed two- or three-track invariant mass with hypotheses of partially reconstructed decays fits in a small window around the mass of a given D-meson. The width of this window was optimised with the simulated signal sample, together with the vetoes proposed in the next section. The D vetoes remove to larger extent candidates with values of $|\cos\theta_L| \simeq 0.7$ and with low reconstructed mass $m_{K\pi\mu\mu}$ and high q^2.[11]

However, only a few percents of the vetoed candidates have $\cos\theta_K \simeq 1$. This indicates that there is at least one additional source of background peaking in angular distributions.

[10] $m_{\rm PDG}(D^0) = 1864.8\,\text{MeV}$, $m_{\rm PDG}(D^+) = 1869.6\,\text{MeV}$, $m_{\rm PDG}(D_s^\pm) = 1968.3\,\text{MeV}$ [20]

[11] The value of $\cos\theta_L = \pm 0.7$ can be explained by kinematics: the $\cos\theta_L$ angle is defined (Section 1.4.1) as the angle between the μ^- (μ^+) and and the direction opposite to the B^0 ($\overline{B}^0$) in the dimuon rest frame. Thus, the distribution of angles between a random muon from the event and the reconstructed B^0 direction is sculpted significantly by the Lorentz boost into the dimuon rest frame. The minimum value of θ_L is then non-zero and the maximum value of $|\cos\theta_L|$ is less than 1.

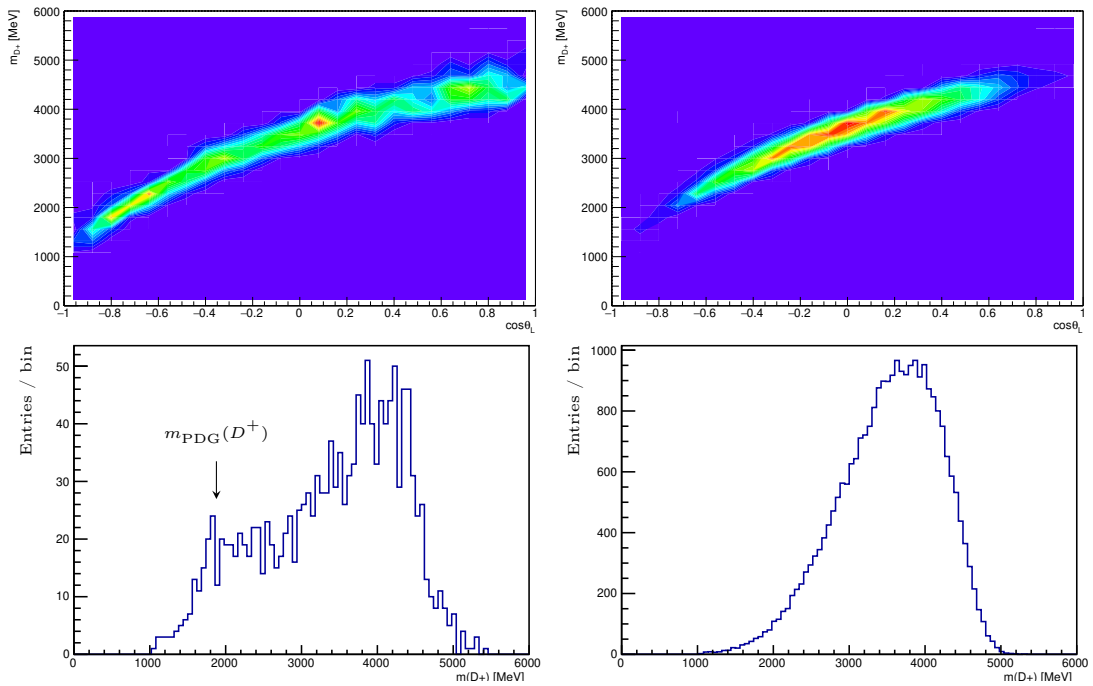

Figure 4.7: The invariant mass and $\cos\theta_L$ distributions computed for three-track combinations assuming the $D^+ \to K^{\pm}\pi^{\mp}\pi^+$ hypothesis for data (left) and $B^0 \to K^*\mu^+\mu^-$ signal MC, both in $q^2 \in [0.04, 6.0]\,\mathrm{GeV}^2$ range. The mass m_{D^+} is computed as the invariant mass of three particles forming the B^0 signal candidates: kaon track, pion track and the positive muon track with pion mass hypothesis. The bottom plots show projections of m_{D^+} for the same data.

4.5.2 Background peaking in the $\cos\theta_K$ distribution

The study of simulated samples showed that the decays $B^+ \to J/\psi\ K^+$, $B^+ \to J/\psi\ \pi^+$, $B^+ \to K^+\mu^+\mu^-$ and $B^+ \to \pi^+\mu^+\mu^-$ with an addition of a track from the underlying event could be a possible source of the background because they peak at $\cos\theta_K \simeq 1$.

- $B^+ \to J/\psi\ K^+$: Only 7 events from the simulated sample passed selection cuts for $q^2 \in [0.04, 6.0]\,\mathrm{GeV}^2$ but extrapolating from $[6.0, 7.0]\,\mathrm{GeV}^2$ plotted in Figure 4.8 shows that this decay might contribute to high-$\cos\theta_K$ region, especially if the simulation slightly underestimates the J/ψ radiative decays.
- $B^+ \to J/\psi\ \pi^+$: This is a similar case as the previous decay with only a few reconstructed candidates and a peaking distribution of $\cos\theta_K$. Moreover, this decay has even smaller branching fraction than $B^+ \to J/\psi\ K^+$ and is expected to contribute less than 1 event to the $q^2 < 6\,\mathrm{GeV}^2$ region.[12]
- $B^+ \to K^+\mu^+\mu^-$: Because of an addition of one track with pion hypothesis, the reconstructed mass $m_{K\pi\mu\mu}$ for this candidates is bigger than the B^0 mass. This decay is expected to contribute only about 7.5 events over the whole region $q^2 \in [0.04, 6.0]\mathrm{GeV}^2$ (Table 4.6 on page 64) but its contribution

[12] Although the available simulated samples for both decays had relatively small statistics: 10^6 events for $B^+ \to J/\psi\ \pi^+$ and 2.5×10^6 for $B^+ \to J/\psi\ K^+$.

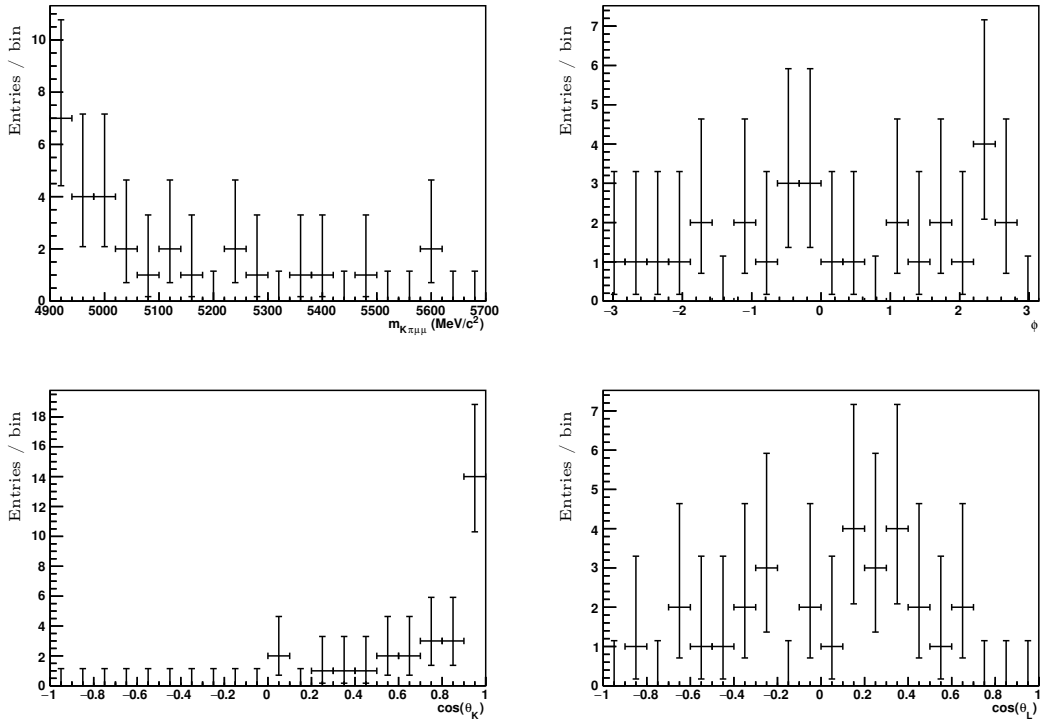

Figure 4.8: Mass and angular distributions for simulated $B^+ \to J/\psi\ K^+$ events (sample 208430) in q^2 bin [6.0, 7.0] GeV^2.

is already included in the estimation of systematic uncertainty (as described in the last paragraph of Section 4.6.1).

- $B^+ \to \pi^+\mu^+\mu^-$: This decay has about 30 times smaller branching fraction [20] than $B^+ \to K^+\mu^+\mu^-$ and it is also expected to contribute to the right $m_{K\pi\mu\mu}$ mass region.

As a check, a set of B-vetoes was implemented similar to the ones described in previous section. Candidates with the reconstructed invariant mass of the $K\mu\mu$ or $\pi\mu\mu$ triplet in a thin window around the $B^\pm$ mass are removed. In the collision-data sample from collisions this indeed removes some of the events with maximum value of $\cos\theta_K$.

Other decays were considered but they were not found to contribute to the observed backgrounds in $\cos\theta_K$ nor $\cos\theta_L$. These include:

- $B^0 \to J/\psi K^*$ with muon-hadron double swap has nearly flat angular distribution
- $B_s^0 \to J/\psi\ \phi$ has only 1 event satisfying this hypothesis
- $B^+ \to K^{*+}\mu^+\mu^-$ has a signal-like angular distribution
- $\Lambda_b \to \Lambda(pK^-)\mu^+\mu^-$ and $\Lambda_b \to pK^-\mu^+\mu^-$ have flat angular distributions
- $D \to K\pi\mu\nu_\mu$ overlaps with the D decays listed above
- $B \to \pi\mu\nu_\mu$, $B_s^0 \to K\mu\nu_\mu$ and $\Lambda_b \to p\mu\nu_\mu$ have only two particles in the final state

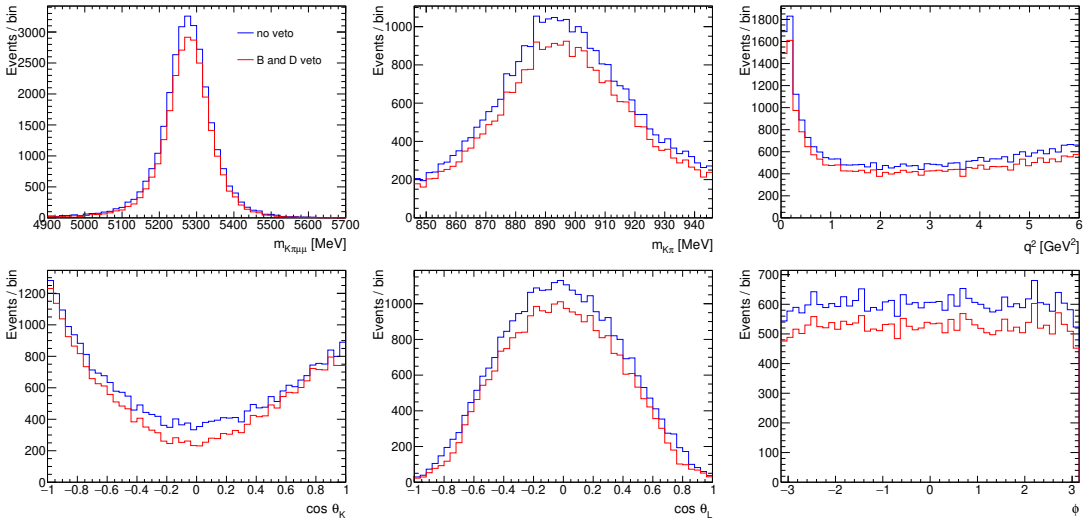

Figure 4.9: Simulated $B^0 \to K^*\mu^+\mu^-$ signal events (sample 208446) in q^2 range $[0.04, 6.0]\,\text{GeV}^2$ before and after applying the set of B and D vetoes described in text (30 MeV and 70 MeV around the D and B mas respectively).

4.5.3 Treatment of observed backgrounds

The D and B vetoes were optimised such that applying both sets to the simulated signal samples removes 2.8 % (2.7 %) of the candidates in the B^0 ($\overline{B}^0$) simulated sample for half-width of 30 MeV around the mass of D mesons and 70 MeV around the mass of $B^\pm$ mesons (masses are taken as world average from Ref. [20]). The same vetoes applied to the collision data sample cut away 11.5 % of the candidates. Figure 4.9 shows the mass, q^2 and angular distributions for the simulated signal sample before and after vetoes. The same plots are shown in Figure 4.10 for collision data.

However, by cutting away candidates in some regions of the helicity angle distributions, the vetoes sculpt significantly the angular acceptance maps. Figure 4.11 shows an example of acceptance function fits with vetoes applied. The order of polynomials was varied to achieve a better agreement but even fits with higher-order polynomials (e.g. seventh or eight order) fail to describe all features well, especially the dip at $\cos\theta_L = 0.7$.

Because these studies mostly depend on the data from signal region and lack a dedicated simulated samples, a conservative approach was proposed: the nominal fit was applied to data with a part of the left B^0 sideband cut off (the $m_{K\pi\mu\mu}$ range $[5150,\ 5700]\,\text{MeV}$ instead of $[4900,\ 5700]\,\text{MeV}$) and an additional fit of sample with vetoes was done (also in the restricted $m_{K\pi\mu\mu}$ range). The difference between results with and without vetoes was taken as a systematic uncertainty.

The described backgrounds peaking in $\cos\theta_K$ and $\cos\theta_L$ have the largest contribution to the total systematic uncertainty, especially for parameters F_L and S_8, as will be shown in Section 4.6.1. This motivates future studies of this background's sources, development of better selection procedure or addition of this component to the nominal fit PDF for analysis of Run 2 dataset. For a detailed study of the observed backgrounds, a simulated sample with inclusive $B \to DX$ decays would be necessary. This requires an additional effort because many of

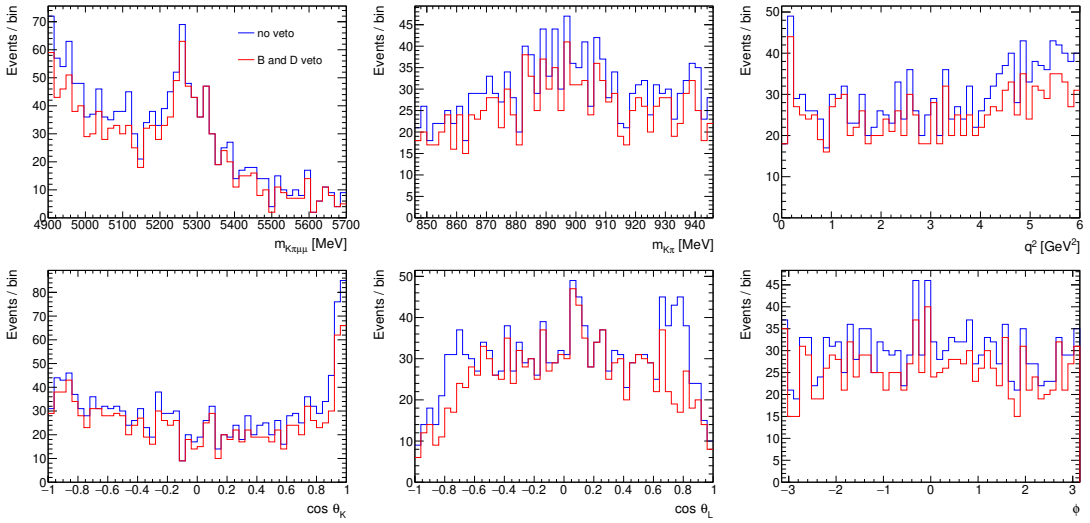

Figure 4.10: Events from signal region of collision data before and after applying the set of B and D vetoes described in text (30 MeV and 70 MeV around the D and B mass respectively).

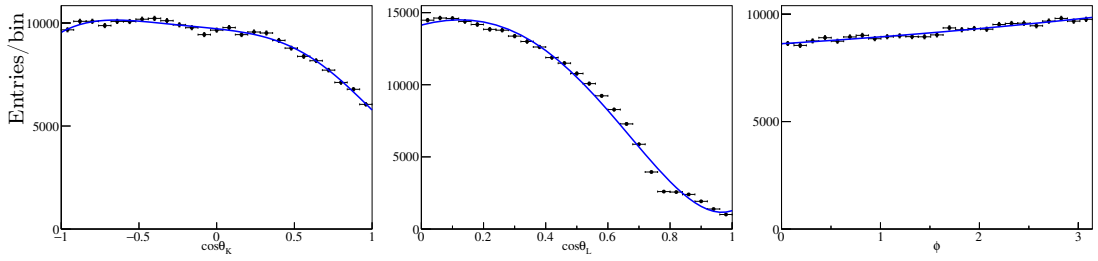

Figure 4.11: Acceptance functions extracted from the simulated sample with flat angular distributions for S_4 folding scheme and applying the D and B vetoes (30 MeV and 70 MeV around the D and B mass respectively). The $\cos\theta_K$ and $\cos\theta_L$ (ϕ) distributions are fitted with sixth (second) order polynomials.

these backgrounds are rare processes with not well measured decay rates and angular distributions. Moreover, the vetoes sculpt acceptance functions and the intrinsic bias of fitting procedure for acceptance maps by higher-order polynomials has to be checked and validated.

The presented findings are consistent with results presented by other experiments, e.g. both CDF [82] and LHCb [83] collaborations use the method of swapping mass hypotheses to remove backgrounds coming from partially-reconstructed decays from their dataset. The other approach is to extract the shape of mass and angular distributions from simulated samples of misreconstructed decays and add this component to the nominal fit.

4.6 Systematic uncertainties

The following text discusses the sources of systematic uncertainty that were considered. They were estimated either by comparison of the nominal and modified fit results or by the observed fit bias in modified pseudo-experiments (toy MC samples). The combination of uncertainties is presented in Section 4.6.12.

4.6.1 Peaking backgrounds

The background, which is observed at high values of $\cos\theta_K$ distribution as described in Section 4.5.2, is assumed to be of combinatorial origin. Because of an unknown angular distribution, this contribution is not included in the nominal fit and a systematic error is assigned to this source. The uncertainty is computed as the difference between the nominal fit results and those obtained from the fit of the dataset with imposed cut of $\cos\theta_K < 0.9$ which is removing a large part of this contribution. The largest uncertainty was found in S_8, up to 0.16 for the $q^2 \in [2.0, 4.0]$ bin. Other S_i parameters and F_L have smaller errors, up to 0.06.

To estimate the effect of background peaking in the $\cos\theta_L$ distribution around $|\cos\theta_L| = 0.7$, a set of cuts to remove the partially reconstructed decays of B and D mesons was developed, as described in Section 4.5.1. The vetoes are applied to the the collision dataset and also to the simulated sample which was used for extraction of the acceptance functions. The deviation of the nominal fit results and results of fit with vetoes is then considered to be the systematic uncertainty.

Uncertainties of up to 0.110 are observed for the F_L measurement in the $q^2 \in [0.04, 2.0]$ and $[4.0, 6.0]\,\mathrm{GeV}^2$ bins, for other parameters and bins the errors are smaller. However, backgrounds peaking in angular distributions are two largest contributions to the total systematic uncertainty.

The contributions from backgrounds listed in Table 4.6 that peak in $m_{K\pi\mu\mu}$ ($B^+ \to K^{*+}\mu^+\mu^-$, $B_s^0 \to \phi\mu^+\mu^-$, $B^+ \to K^+\mu^+\mu^-$, $\Lambda_b \to \Lambda(pK^-)\mu^+\mu^-$ and $\Lambda_b \to pK^-\mu^+\mu^-$) were neglected in the nominal fits. To study their effect on the fit results, sets of pseudo-datasets were prepared using the nominal PDF (signal and combinatorial background components only) and with embedded peaking background components. A systematic uncertainty is computed as the difference between the fitted angular parameters in nominal and embedded toys. The level of this error is small, less than 0.013 for F_L and less than 0.004 for all other parameters.

4.6.2 Combinatorial background PDF shape

The shape of combinatorial background PDF as defined by Equation (4.4) has an uncertainty arising from the model choice. The exponential function is assumed to be adequate for the mass distribution. However, the angular distributions are refitted using third-order Chebyshev polynomials and the deviation from the parameters obtained in nominal fits are taken as the uncertainties. The most significant bias is observed for F_L (up to 0.044 in $[4.0, 6.0]\,\mathrm{GeV}^2$ bin) and S_3 of up to 0.039 in the same q^2 bin.

The uncertainty coming from the parameter λ being fixed in the nominal fits is addressed together with other nuisance parameters in Section 4.6.9.

4.6.3 Acceptance functions

The angular acceptance function is assumed to factorise into three separate components according to Equation (4.5) and polynomials of sixth (second) order are used to model the $\cos\theta_K$ and $\cos\theta_L$ (ϕ) acceptance functions. To evaluate the uncertainty coming from these assumptions, the $B^0 \to K^*\mu^+\mu^-$ sample simulated with flat angular distributions is fitted with the acceptance functions obtained from this sample. The fit bias is then the difference between the generated and extracted values of angular parameters.

The most significant bias is observed for S_4 (0.051 to 0.070 in all q^2 bins) and for F_L (up to 0.014). All other biases are negligible.

4.6.4 Mass fit range

Setting the B^0 candidate mass window to [5150, 5700] MeV instead of a wider and more symmetric range of [4900, 5700] MeV suppresses the observed contribution from partially reconstructed B-meson decays that peak in the $\cos\theta_L$ distribution. However, possible residues of this background influence the angular background PDF under the B^0 peak.

To study these effects, fits are performed with the lower bound of the mass range varying from 5150 MeV to 5200 MeV. They show a good stability of results and a systematic uncertainty is computed as the difference of values extracted from fits with lower mass threshold of 5150 MeV and 5200 MeV.

The observed bias is small for F_L and S_4 (< 0.034 and < 0.022 for all bins) and slightly larger for the S_i parameters, especially in bins $[2.0, 4.0]\,\text{GeV}^2$ and $[4.0, 6.0]\,\text{GeV}^2$, up to 0.082 for S_5.

4.6.5 Tracking and ID alignment

The uncertainties of magnetic field and alignment influence the precision of the tracking detectors and manifest themselves as rapidity and momentum scale bias. The uncertainty in magnetic field strength results in momentum scale bias of 0.02 % to 0.12 % depending on track rapidity [84]. The alignment errors result in a radial uncertainty of 0.14 % in barrel and 0.55 % in the endcap regions [85].

To estimate the uncertainty from these sources, the momenta of four-track candidates in data are multiplied by a factor of $(1 \pm \delta_{p_\text{T}})$, where δ_{p_T} is the sum of biases above in quadrature. The B^0 invariant mass and helicity angles are then recalculated and both datasets are refitted. The larger of differences with respect to the nominal fit results is taken as a systematic uncertainty. Their values are in general small, with bias of up to 0.048 in few bins.

4.6.6 Intrinsic fit bias

The intrinsic bias of maximum-likelihood estimator is determined using the toy Monte Carlo studies as described in Section 4.4.4. The measured bias is assigned as a systematic uncertainty.

4.6.7 Data-MC agreement

Systematic uncertainties coming from differences between collision data and simulated MC samples were evaluated.

The shape of mass and angular PDF for peaking backgrounds included in the embedded toys is taken from the MC simulated samples. A systematic error coming from neglecting these backgrounds is very small (as discussed in Section 4.6.1) and as a result the effect of disagreements between data and simulated samples is considered negligible.

Comparison of distributions of kinematic variables in the $B^0 \to J/\psi K^*$ control region shows a small difference in the p_{T} spectrum of the B^0 candidates. To account for the possible bias, the p_{T} distribution of the simulated control-region sample is normalised to the distribution in background-subtracted data. The simulated sample of $B^0 \to K^*\mu^+\mu^-$ signal is then reweighted and refitted. The effect on the fitted values of angular variables was at most 0.020 for F_L, 0.019 for S_4 and negligible for all other variables.

4.6.8 Non-resonant $B^0 \to K^+\pi^-\mu^+\mu^-$ contribution

The non-resonant $B^0 \to K^+\pi^-\mu^+\mu^-$ event yield is expected to be approximately 5 % of the resonant P-wave contribution [12] and it was not included in the nominal fit. To account for the possible effect on the measured the angular parameters, ensembles of toy MC simulated events were prepared with 5 % of the signal sampled from the S-wave dataset and the remaining events from the signal dataset. The change of fit results with respect to the toy study with signal only is assigned as the systematic error from this source.

The measured bias is very small in most bins, the largest is 0.026 in S_8 in bin $[4.0, 6.0]\,\mathrm{GeV}^2$. Variations in the S-wave content as a function of q^2 are considered negligible.

4.6.9 Nuisance parameters

Other contributions come from the fixed parameters of PDF in the nominal angular fit. The nuisance parameters include the signal and background yields, m_0 and S parameters of the signal mass PDF, the shape parameter λ of the combinatorial background mass distribution and the parameters of signal acceptance functions. Values of these parameters are varied independently by $\pm 1\sigma$ from their nominal values and the angular fit is performed with both modified PDFs. The systematic uncertainty is computed as the deviation from the value obtained in the nominal fit.

The systematic uncertainties from all parameters are combined in a quadrature. They have a small effect and the dominant contribution comes from varying the signal and background yields.

4.6.10 Event migration due to wrong flavour tag

The systematic error resulting from event migration due to mistagging the B^0 flavour is estimated by fitting the simulated B^0 signal dataset with acceptance function extracted from the $\overline{B}^0$ dataset. The observed difference with respect to

the fit with the correct-tag acceptance functions is negligible in most of q^2 bins and up to 0.009 for F_L and S_3 in bins $q^2 \in [2.0, 4.0]$ and $[4.0, 6.0]\,\mathrm{GeV}^2$.

4.6.11 Dilution

The probabilities of reconstructing a B^0 or $\overline{B}^0$ candidate with the opposite flavour, ω and $\overline{\omega}$, are extracted from simulated MC samples and their error is limited by the sample statistics. The dilution D is then computed from the average mistag probability but this approximation is valid only if the difference $\Delta\omega = (\omega - \overline{\omega})$ is small. As shown in Table 4.5, the value of $\Delta\omega$ is consistent with zero. Hence, the uncertainties of ω and $\overline{\omega}$ are computed from the statistical uncertainty in simulated samples and the dilution uncertainty is computed by error propagation.

The dilution of measured values of angular parameters affects only S_5 and S_8 and the measured uncertainties are smaller than 0.003 in all q^2 bins.

4.6.12 Combined systematic uncertainty

For all systematic uncertainties, the errors obtained from the nominal fit and the varied fit were consistent. Therefore, the uncertainties are assumed to be additive and the errors are added in quadrature and symmetrised. The only exception is the dilution factor uncertainty which is multiplicative. The uncertainty of P_i parameters is computed from the F_L and S_i uncertainties using error propagation.

An overview of the largest values of systematic uncertainties from different sources is shown in Table 4.8. The systematic uncertainties are smaller than statistical uncertainties for all measured parameters.

Table 4.8: The largest value of systematic uncertainties across the q^2 bins for F_L and S_i from different sources considered. The systematic uncertainties vary from bin to bin in q^2 and some bins have smaller uncertainties than those presented here. Entries marked with − have no contribution from that systematic effect.

Source	$\boldsymbol{F_L}$	$\boldsymbol{S_3}$	$\boldsymbol{S_4}$	$\boldsymbol{S_5}$	$\boldsymbol{S_7}$	$\boldsymbol{S_8}$
Background peaking in $\cos\theta_K$	0.03	0.03	0.05	0.04	0.06	0.16
Background peaking in $\cos\theta_L$	0.11	0.04	0.05	0.04	0.01	0.06
Background from Λ_b, B^+ and B_s^0	0.01	0.01	0.01	0.01	0.01	0.01
Combinatorial background PDF shape	0.04	0.04	0.03	0.03	0.03	0.01
Acceptance functions	0.01	0.01	0.07	0.01	0.01	0.01
Mass fit range	0.03	0.05	0.02	0.08	0.05	0.06
Alignment and tracking (B field)	0.02	0.04	0.05	0.04	0.04	0.04
Intrinsic fit bias	0.01	0.01	0.02	0.03	0.01	0.05
Data/MC differences in p_{T}	0.02	0.02	0.01	0.01	0.01	0.01
Non-resonant $B^0 \to K^+\pi^-\mu^+\mu^-$	0.01	0.01	0.01	0.01	0.01	0.03
Nuisance parameters	0.01	0.01	0.01	0.01	0.01	0.01
Wrong flavour tag	0.01	0.01	0.01	0.01	0.01	0.01
Dilution	−	−	−	<0.01	−	<0.01

4.7 Results

Mass fits

The PDF of mass fits includes the signal and combinatorial background components described in Section 4.4.1: the signal $B^0 \to K^*\mu^+\mu^-$ mass distribution is defined as a Gaussian function with per-event mass error and the combinatorial background is a single exponential with a parameter λ. The signal parameters m_0 and S were fixed to values extracted from fits of the $B^0 \to J/\psi K^*$ region.

The fitted signal and combinatorial background yields are shown in Table 4.9, together with the background shape parameter λ. The mass distributions are shown in Figures A.1 and A.2 in Appendix A. Plots of the likelihood ratio (LR) are also included, where the LR is computed on an event-by-event basis as

$$\mathrm{LR} = \frac{\mathcal{L}_{\mathrm{sig}}}{\mathcal{L}_{\mathrm{sig}} + \mathcal{L}_{\mathrm{bkg}}}$$

and $\mathcal{L}_{\mathrm{sig}}$ and $\mathcal{L}_{\mathrm{bkg}}$ are likelihoods for a given event to be signal or background, respectively. In these LR plots, the green (red) component corresponds to the signal (combinatorial background) toy MC generated from the likelihood normalised to the extracted yields.

Table 4.9: The values of fitted signal and combinatorial background yields n_{sig} and n_{bkg} and the exponential parameter λ. The uncertainties are statistical only.

q^2 (GeV^2)	n_{sig}	n_{bkg}	λ
$[0.04, 2.0]$	128^{+22}_{-22}	122^{+22}_{-21}	$-0.0013^{+0.0010}_{-0.0008}$
$[2.0, 4.0]$	106^{+23}_{-22}	113^{+23}_{-22}	$-0.0021^{+0.0011}_{-0.0009}$
$[4.0, 6.0]$	114^{+24}_{-23}	204^{+26}_{-25}	$-0.0030^{+0.0006}_{-0.0006}$
$[0.04, 4.0]$	236 ± 31	233^{+32}_{-31}	$-0.0016^{+0.0007}_{-0.0006}$
$[1.1, 6.0]$	275^{+35}_{-34}	363^{+36}_{-35}	$-0.0024^{+0.0005}_{-0.0005}$
$[0.04, 6.0]$	342^{+39}_{-38}	445^{+40}_{-39}	$-0.0023^{+0.0004}_{-0.0004}$

Angular fits

Results are listed in Table 4.10 for F_L and S_i parameters and in Table 4.11 for the P_i parameters. The fitted mass, $\cos\theta_K$, $\cos\theta_L$ and ϕ distributions for the S_4 folding transformation are shown in Figures A.3–A.5 in Appendix A.

Because the F_L and S_i parameters are measured in four separate fits in each q^2 bin, it is not possible to extract a full correlation matrix. Therefore, ensembles of pseudo-experiments are simulated using the PDFs of the nominal angular distributions. For each ensemble, four folding schemes are applied and the resulting samples are fitted. The distributions obtained for pairs of parameters are used to compute the Pearson correlation coefficients for those pairs. A similar procedure is applied for the P_i parameters. Results are shown in Tables A.3 to A.8 in Appendix A.

Table 4.10: The values of F_L, S_3, S_4, S_5, S_7 and S_8 parameters obtained for different bins in q^2. The uncertainties indicated are statistical and systematic, respectively.

q^2 (GeV^2)	F_L	S_3	S_4	S_5	S_7	S_8
$[0.04, 2.0]$	$0.44 \pm 0.08 \pm 0.07$	$-0.02 \pm 0.09 \pm 0.02$	$0.15 \pm 0.20 \pm 0.10$	$0.33 \pm 0.13 \pm 0.08$	$-0.09 \pm 0.10 \pm 0.02$	$-0.14 \pm 0.24 \pm 0.09$
$[2.0, 4.0]$	$0.64 \pm 0.11 \pm 0.05$	$-0.15 \pm 0.10 \pm 0.07$	$-0.37 \pm 0.15 \pm 0.10$	$-0.16 \pm 0.15 \pm 0.06$	$0.15 \pm 0.14 \pm 0.09$	$0.52 \pm 0.20 \pm 0.19$
$[4.0, 6.0]$	$0.42 \pm 0.13 \pm 0.12$	$0.00 \pm 0.12 \pm 0.07$	$0.32 \pm 0.16 \pm 0.09$	$0.13 \pm 0.18 \pm 0.09$	$0.03 \pm 0.13 \pm 0.07$	$-0.12 \pm 0.21 \pm 0.05$
$[0.04, 4.0]$	$0.52 \pm 0.07 \pm 0.06$	$-0.05 \pm 0.06 \pm 0.04$	$-0.15 \pm 0.12 \pm 0.09$	$0.16 \pm 0.10 \pm 0.05$	$0.01 \pm 0.08 \pm 0.05$	$0.19 \pm 0.16 \pm 0.12$
$[1.1, 6.0]$	$0.56 \pm 0.07 \pm 0.06$	$-0.04 \pm 0.07 \pm 0.03$	$0.03 \pm 0.11 \pm 0.07$	$0.00 \pm 0.10 \pm 0.04$	$0.02 \pm 0.08 \pm 0.06$	$0.11 \pm 0.14 \pm 0.10$
$[0.04, 6.0]$	$0.50 \pm 0.06 \pm 0.04$	$-0.04 \pm 0.06 \pm 0.03$	$0.03 \pm 0.10 \pm 0.07$	$0.14 \pm 0.09 \pm 0.03$	$0.02 \pm 0.07 \pm 0.05$	$0.07 \pm 0.13 \pm 0.09$

Table 4.11: The values of P_1, P_4', P_5', P_6' and P_8' parameters obtained for different bins in q^2. The uncertainties indicated are statistical and systematic, respectively.

q^2 (GeV^2)	P_1	P_4'	P_5'	P_6'	P_8'
$[0.04, 2.0]$	$-0.05 \pm 0.30 \pm 0.08$	$0.31 \pm 0.40 \pm 0.20$	$0.67 \pm 0.26 \pm 0.16$	$-0.18 \pm 0.21 \pm 0.04$	$-0.29 \pm 0.48 \pm 0.18$
$[2.0, 4.0]$	$-0.78 \pm 0.51 \pm 0.34$	$-0.76 \pm 0.31 \pm 0.21$	$-0.33 \pm 0.31 \pm 0.13$	$0.31 \pm 0.28 \pm 0.19$	$1.07 \pm 0.41 \pm 0.39$
$[4.0, 6.0]$	$0.14 \pm 0.43 \pm 0.26$	$0.64 \pm 0.33 \pm 0.18$	$0.26 \pm 0.35 \pm 0.18$	$0.06 \pm 0.27 \pm 0.13$	$-0.24 \pm 0.42 \pm 0.09$
$[0.04, 4.0]$	$-0.22 \pm 0.26 \pm 0.16$	$-0.30 \pm 0.24 \pm 0.17$	$0.32 \pm 0.21 \pm 0.11$	$0.01 \pm 0.17 \pm 0.10$	$0.38 \pm 0.33 \pm 0.24$
$[1.1, 6.0]$	$-0.17 \pm 0.31 \pm 0.13$	$0.05 \pm 0.22 \pm 0.14$	$0.01 \pm 0.21 \pm 0.08$	$0.03 \pm 0.17 \pm 0.12$	$0.23 \pm 0.28 \pm 0.20$
$[0.04, 6.0]$	$-0.15 \pm 0.23 \pm 0.10$	$0.05 \pm 0.20 \pm 0.14$	$0.27 \pm 0.19 \pm 0.06$	$0.03 \pm 0.15 \pm 0.10$	$0.14 \pm 0.27 \pm 0.17$

4.8 Comparison with other experiments and with theoretical predictions

The results obtained by the analysis described in this thesis are compared to the results obtained by other collaborations:

- BaBar measurement of F_L from Ref. [40]
- Belle measurements of F_L [7] and P_4', P_5', P_6' and P_8' [10]
- CMS measurements of F_L [9], P_1 and P_5' [13]
- LHCb measurements of all variables published in Ref. [12].

The results for F_L and S_i parameters are shown in Figure 4.12 and the measured values of P_i parameters are in Figure 4.13. Theoretical predictions for the Standard Model from three collaborations are also overlaid, each of them is computed using a different approach:

- Descotes-Genon et al. (labelled DHMV) in Ref. [86] use QCD factorisation
- Jäger and Martin Camalich (JC) [87] also use QCD factorisation with a correction of long-distance effects by a helicity amplitude approach
- Ciuchini et al. (CFFMPSV) in Ref. [88] use the QCD factorisation framework to check the compatibility of the LHCb results [12, 89, 90] (angular parameters and branching fractions of $B^0 \to K^*\mu^+\mu^-$ and $B^0 \to K^*e^+e^-$) with the theoretical predictions. Their method takes into account correlations of angular variables by removing a given parameter from the fit and adding the experimental covariance matrix to the one obtained from the fit.

In general, there is a good agreement between the presented measurement and theoretical predictions and all obtained values are within three standard deviations from the different predictions, neglecting trial factors.

The most significant deviations are observed for parameters P_4', P_5' and P_8' in one q^2 bin each. The values of P_4' and P_5' in bin $q^2 \in [4.0, 6.0]\,\text{GeV}^2$ are for both parameters approximately 2.7 standard deviations away from the calculation of DHMV. The P_5' deviation is consistent with the one reported by the LHCb collaboration in Ref. [12]. Moreover, the P_4' and P_5' parameters have statistical correlations ranging from 0.37 to 0.78, depending on a bin. A deviation of $1.9\,\sigma$ from the DHMV prediction is also observed for P_8' in bin $q^2 \in [2.0, 4.0]\,\text{GeV}^2$. Here, a compatibility between values by ATLAS and LHCb is observed. The differences are less significant for the JC prediction and CFFMPSV fit.

S observables

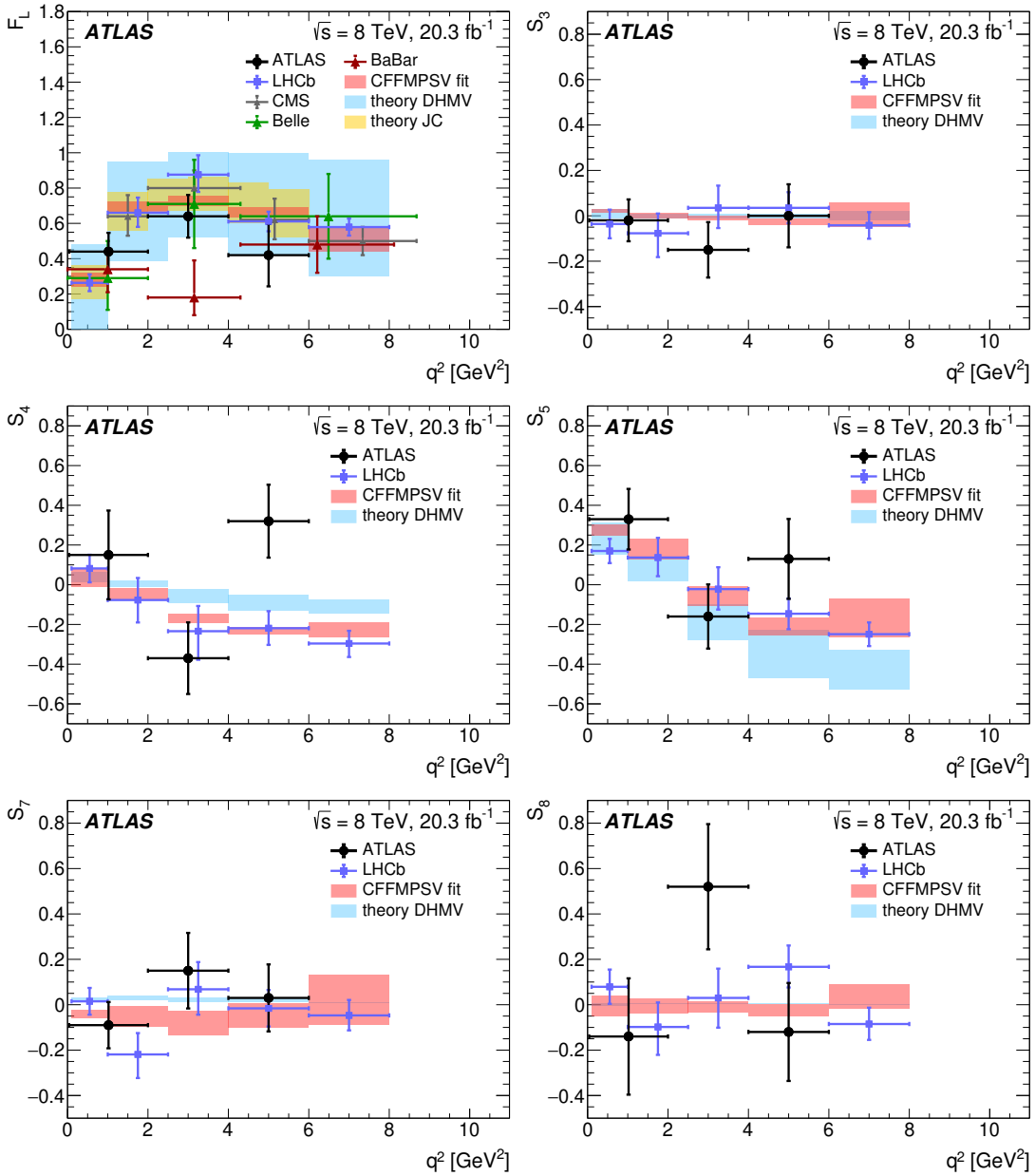

Figure 4.12: The measured values of F_L, S_3, S_4, S_5, S_7, S_8 compared with predictions from the theoretical calculations discussed in the text. Statistical and total uncertainties are shown for the data, i.e. the inner mark indicates the statistical uncertainty and the total error bar the total uncertainty.

P observables

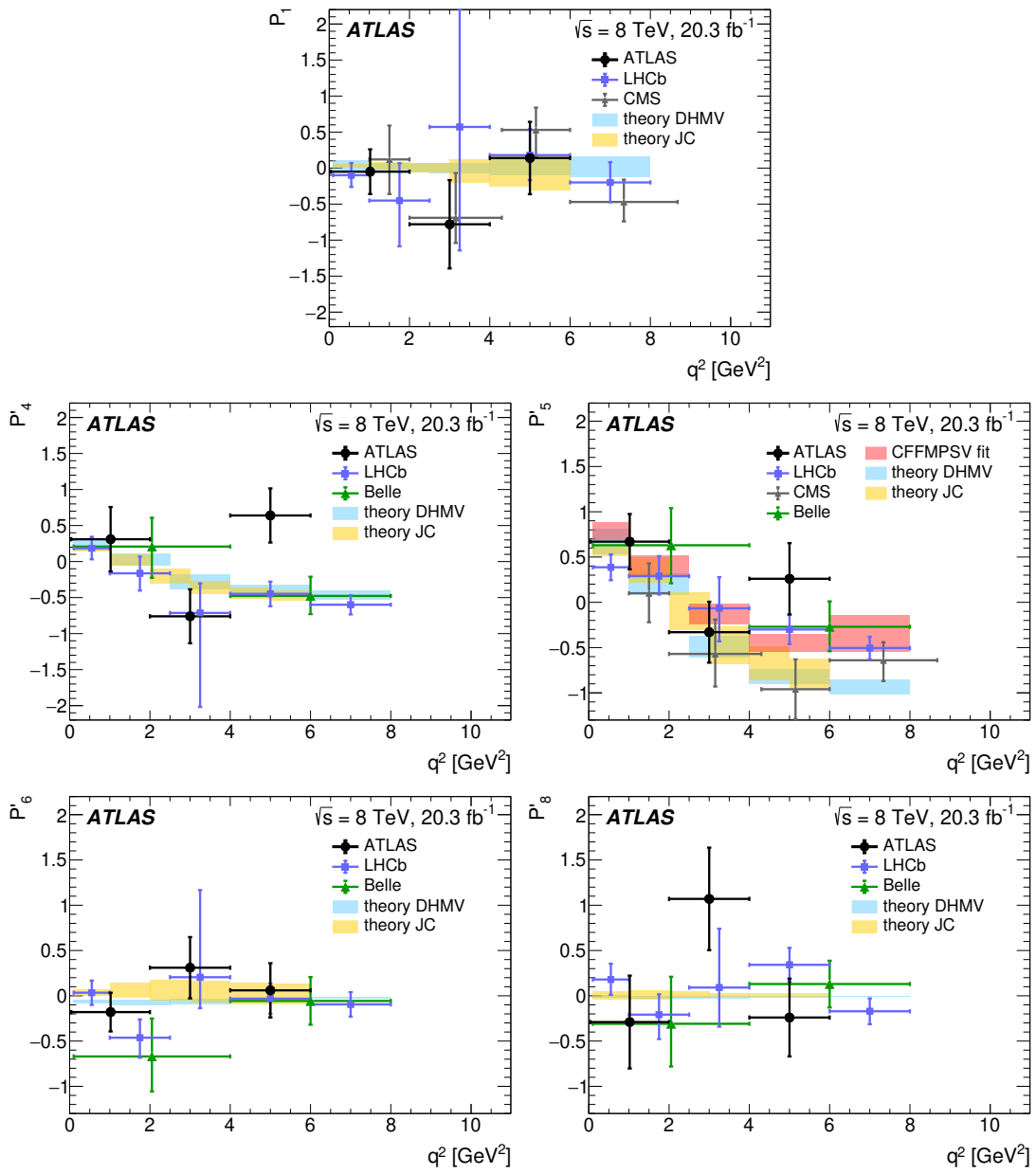

Figure 4.13: The measured values of P_1, P_4', P_5', P_6', P_8' compared with predictions from the theoretical calculations discussed in the text. Statistical and total uncertainties are shown for the data, i.e. the inner mark indicates the statistical uncertainty and the total error bar the total uncertainty.

4.9 Future prospects

The ATLAS experiment is expected to collect pp collisions with an integrated luminosity of more than $140\,\text{fb}^{-1}$ during the LHC Run 2 and the increase of centre-of-mass energy from 8 to 13 TeV also means about two times higher production cross-section of b-quarks and consequently larger number of produced B-mesons. Therefore, the whole Run 2 dataset is expected to contain a larger sample of $B^0 \to K^*\mu^+\mu^-$ candidates and the B-physics group is planning to provide updates based on whole Run 2 statistics.

The possible improvements of this analysis which are currently studied or planned include:

- selection partially or fully based on machine learning techniques
- fit of the full angular distribution, described by Eq. (1.4) and measure also S_6, S_9, A_{FB}, P_2 and P_3
- non-sequential mass and angular fit
- covering full q^2 range
- finer q^2 binning
- adding K^* mass in fit
- acceptance maps as 4D functions of $\cos\theta_K$, $\cos\theta_L$, ϕ and q^2 (no q^2 binning)
- correlation in acceptance functions (e.g. using spherical harmonic functions)
- for combinatorial background PDF including correlations in helicity angles
- studies of the observed partially-reconstructed background
- additional components in the nominal fit PDF:
  - candidates with a wrong flavour tag
  - non-resonant $B^0 \to K^+\pi^-\mu^+\mu^-$ (S-wave)
  - peaking backgrounds
- additional variables and decay modes:
  - CP asymmetries A_i
  - zero-crossing points of angular parameters
  - differential branching fraction
  - extend measurements to $B^0 \to K^* e^+ e^-$ (due to low statistics probably only folded angular analysis)
  - measurement of $R(K^*) = \mathcal{B}(B^0 \to K^*\mu^+\mu^-)/\mathcal{B}(B^0 \to K^* e^+ e^-)$
  - angular analysis of $B^0 \to J/\psi K^*$ and $B^0 \to \psi(2S)K^*$
  - angular analysis of $B_s^0 \to \phi\mu^+\mu^-$ (requires b-tagging)

For the future analyses, detectors and data acquisition upgrades will be instrumental in achieving the level of performance in tracking and vertexing which is needed for precision measurements of heavy-flavour decays. Developments of new trigger strategies, such as fast hardware tracker, should allow to keep relatively low p_{T} thresholds at the trigger level even at higher instantaneous luminosity during the LHC Run 3 and beyond.

5. ATLAS SCT and ITk strip detectors

5.1 Silicon strip detectors

Semiconductor detectors are solid state devices which use the electron-hole pair creation to detect ionising particles. ATLAS SCT and its proposed upgrade Inner Tracker (ITk) strip are planar silicon microstrip detectors used for tracking of charged particles.

The principle of operation of these devices is the p-n junction: a layer of n-type silicon with higher donor concentration which is in contact with p-type layer with higher acceptor concentration. The electrons from n-type diffuse to p-type and holes from p to n-type. This results in electron-hole recombination and ionised atoms in both layers. The charged regions create a difference of potential referred to as built-in voltage.

The region without charge carriers (depleted region) can be used for detection of ionising particles because they create electron-hole pairs that can be extracted by an applied bias voltage. Applying positive voltage to the n-type side increases the width of depletion region and is called reverse biasing. The current induced by the reverse bias voltage is termed the leakage current. A typical structure of silicon strip detectors is shown in Figure 5.1.

The passage of ionising particles can create stable defects in the silicon, such as dislocated atoms in interstitial positions or vacancies. These defects decrease the charge carrier mobility and reduce the energy resolution because they act as charge trapping centres. Because the majority of defects are acceptor-like, the n-type silicon undergoes a type inversion and become quasi p-type. Large displacements in crystal lattice can alter the energy levels in the band gap of the material and thermally excited electrons start creating electron-hole pairs. This rises the leakage current which increases the temperature and leakage current further, a process called thermal runaway. It can be mitigated by lowering the temperature of the sensor.

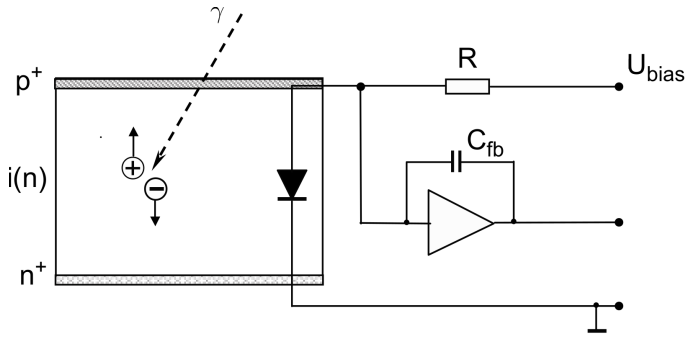

Figure 5.1: Principle of a silicon detector with a p^+-in-n^+ structure [91]. The pn junction is created on the p^+-i boarder and when reverse-biased, extends up to the n^+ layer.

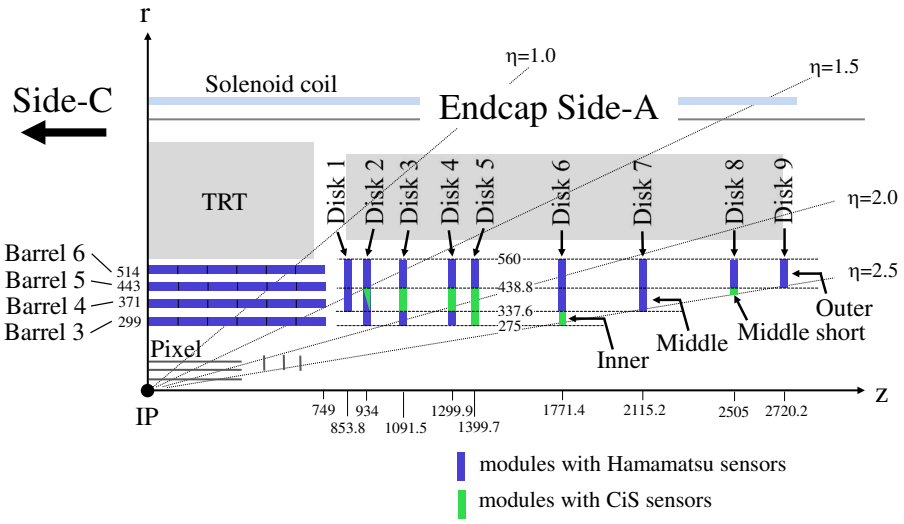

Figure 5.2: Structural elements of the SCT [92].

5.2 Semiconductor Tracker

This section describes the ATLAS Semiconductor Tracker (SCT) and its operation and performance during the LHC Run 1. It is largely based on Refs. [46] and [92] and where possible, the information is updated with results obtained during Run 2.

The SCT is one of three subsystems of the ATLAS Inner Detector. It consists of 4088 modules arranged into four concentric barrels in the central region and nine disks in each endcap, as shown in Figure 5.2.[1] All the 2112 barrel modules have the same geometry and are built from four rectangular sensors that are bonded in pairs to form 12.8 cm-long strips. Two sensors are placed on each side of the module with a stereo angle of 40 mrad. Each endcap is built from 988 modules placed on circular support structures called disks, which hold up to three rings of modules with trapezoidal sensors and strips running in the radial direction. Modules on the outer and middle rings have two daisy-chained sensors per side, while the inner rings have one sensor on each side.

Sensors use high-resistivity n-type bulk silicon with p^+-type implants on one side (p^+-*in*-n) and have a thickness of (285 ± 15) µm. The strip pitch is 80 µm in the barrel and 56.9 µm to 94.2 µm in the endcaps. Two vendors produced the sensors: Hamamatsu Photonics (all barrel and 75 % of endcap) and CiS(25 % of endcap).[2] Sensors are reverse biased with a voltage of 150 V [93].

The readout of approximately 6.3 million strips is done by front-end ABCD chips [94] mounted on flexible circuits referred to as hybrids. There are 6 chips per module side, each of them reading out 128 strips. The analog part of each chip contains preamplifiers, signal shapers and discriminators for binary readout (nominal threshold 1 fC, gate width 25 ns). The output from each channel is sampled with a frequency of 40 MHz and stored in a buffer for up to 3.3 µs. If a

[1] The endcaps are referred to as endcap A (positive z, towards the LHC Point 8) and endcap C (negative z, towards the LHC Point 2).

[2] Hamamatsu Photonics, K.K., Japan https://www.hamamatsu.com/, CiS Institut für Mikrosensorik, Germany https://cismst.org

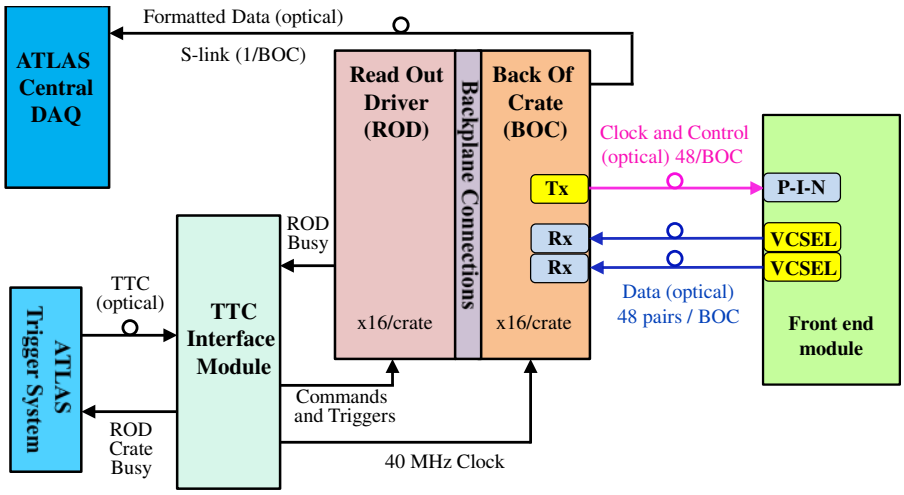

Figure 5.3: Schema of the SCT data acquisition [92].

trigger accept signal arrives, the buffered information from the chip is formatted and sent out via one optical link per side.

The architecture of the SCT readout system is shown in Figure 5.3. It is composed of eight VME crates which host the Readout-Driver Board (ROD) and Back-Of-Crate readout card (BOC) pairs. Each of the 90 ROD-BOC pairs reads out up to 48 modules, formats the data and sends them to the central Data Acquisition System (DAQ) chain via an optical fibre, the S-link. For each module, there is one transmitting optical link (TX) to send configuration and Trigger, Timing and Control (TTC) signals from BOC to the module, and two links for receiving data (RX). The transmission is based on Vertical-Cavity Surface-Emitting Laser (VCSEL) arrays and silicon *p-in-n* diodes. Redundancy in case of problems with optical fibre, VCSEL or diode is implemented for TX links by means of electrical links between neighbouring modules and for RX links by an option to read out whole module via one link.

The header of data fragments (at the module, ROD or SCT level) contains bits for byte-stream errors which can be set to signal problems during readout. The most common and SCT errors are:

- Timeout error - no data from module.
- Masked link error - set by ROD for links that were temporarily disabled from readout.
- BCID and L1ID mismatch errors signal timing problems.
- ROD errors, e.g. fragment error, masked ROD, ROD clock error.
- ABCD errors for invalid data from one chip.
- Data format errors, e.g. missing link header, formatter and trailer errors.

The byte-stream errors are monitored at ROD level during data taking so that modules with a high fraction of errors can be reset or masked promptly. For errors that flag invalid data, hits are not used for track reconstruction.

The SCT Detector Control System (DCS) is implemented as a part of the ATLAS DCS using commercial controls software PVSS/WinCC-OA.[3] It ensures that

[3] ETM professional control, Austria http://www.etm.at

the correct operation parameters are set to the detector hardware, provides monitoring (currents, gas flow, environmental parameters such as temperature and humidity), displays the values and handles alarms. It also archives the measured values and provides an interface to the readout system.

Each module is powered by two cables: one provides the sensor bias voltage (high-voltage, up to 450 V) and the other provides a set of low-voltage links to power the on-detector chips and optical transceivers (3.5–10 V).

To mitigate the impact of radiation damage, the SCT is cooled by an evaporative cooling system which is based on C_3F_8. A total of 204 independent cooling loops run through the detector support structure. The average temperature of hybrids is in the range of 2–7 °C and sensors are at –10 to 5 °C. The system is controlled by the DCS and a hardware interlock ensures that power is switched off in case of too high temperature on the cooling loop outlet or on modules.

5.2.1 Operation during LHC Run 1

The SCT was operated during the whole LHC Run 1 period (2009–2013) and recorded high-quality tracking data for >99 % of the delivered integrated luminosity. The operation and performance was reported in Ref. [92] and will be briefly summarised here. Some of the encountered issues will be described more in detail because their understanding is important for the long-term operation and future upgrades of the ATLAS strip tracker.

More than 99 % of modules were functional during Run 1. Typically around 30 modules were disabled, about half of them due to issues with on-detector electronics or optical links and half because of a disabled cooling loop which was not operated since the SCT installation.[4] In addition, some chips or strips were disabled from the readout due to issues such as high noise or unbonded strips. The fraction of disabled elements was stable at around 0.11 % of chips and 0.18 % of strips.

The infrastructure (cooling, flushing of the ID volume with nitrogen or dry air) was running smoothly during the LHC Run 1, with only a few instances of partial or complete shutdown of the cooling system.

Typical operation cycle and calibrations

The operation of ATLAS and SCT is driven by the LHC cycle and conditions. The SCT is continuously powered but the module bias voltage is set to a lower value during injection, ramp and beam adjust phase, typically 50 V (referred to as standby voltage). This is done to mitigate the impact of sudden beam instabilities and high hit rates of particles passing through SCT. The efficiency at 50 V is still high enough (in the range of 50–80% for non-irradiated sensors) to check the DAQ or to monitor the beam background rates.

After stable beams are declared, the voltage is automatically ramped up to the nominal value, 150 V for most of the modules. The DAQ and trigger are

[4] The disabled cooling loop covers one quarter of the outermost disk in endcap C and thus has a negligible impact on tracking.

switched to the physics mode and data is read out with higher rate.[5] The voltage is set back to standby in case of a scheduled or sudden beam dump.

In periods between LHC fills or during technical stop, calibrations and standalone testing of SCT can be performed. The tests include:

- Module probe to establish communication with modules.
- Optical tests to adjust parameters of the transmission links such as RX/TX thresholds and to check the timing and stability of communication.
- Electrical tests of the digital part of ABCD chips (checking dead or stuck bits, data pipelines on module).
- Electrical tests of the analog part of the chips to adjust discriminator thresholds and measure noise, gain and pulse timing.

Most of the electrical scans are based on injection of a calibration pulse with a known charge to strips from a dedicated circuit and subsequent readout of the response while varying parameters such as discriminator threshold and timing, more details are for example in Ref. [95].

If needed, fast calibration can be run on a subset of modules which are reported as problematic by the data quality checks (e.g. have low hit efficiency, high noise or high number of byte-stream errors). Additionally, scans can be done with colliding beams to finely adjust the timing on a per-module basis (using reconstructed tracks) or to monitor the depletion voltage (measuring the hit efficiency as a function of module bias voltage). This is typically done once per year, during the first collision runs.

Operational problems

Even with a long commissioning and testing period before the start of LHC, some unexpected issues were encountered in the operation of the SCT in collision conditions. Most of them were quickly addressed by the control room shift crew or experts and the system was constantly improved to mitigate future problems.

The largest loss of efficiency came from a DAQ busy flag which signalled problem with some of the readout elements, usually RODs, and inhibited all ATLAS triggers. This was often triggered by high hit occupancy and trigger rates so it was more common at the beginning of LHC fills.[6] ROD busy can also be provoked if the size of data fragments to be read out is large, for example because of noisy chips and optical links. The fraction of lost integrated luminosity because of ROD problems was 0.9 % in 2012 and less during other years.

Several procedures were implemented to minimise the frequency and impact of DAQ issues. These included:

- Online monitoring of byte-stream errors was implemented at ROD level and links which have errors for a certain period of time are automatically

[5] The procedure is referred to as warm start. During Run 1 it took typically 4 min from the declaration of stable beams, after improvements during Run 2 it lasts around 1 min.

[6] The design expected pile-up was routinely exceeded by the LHC, e.g. in 2012 it often reached 30 interactions per bunch crossing, while the expected value was 23.

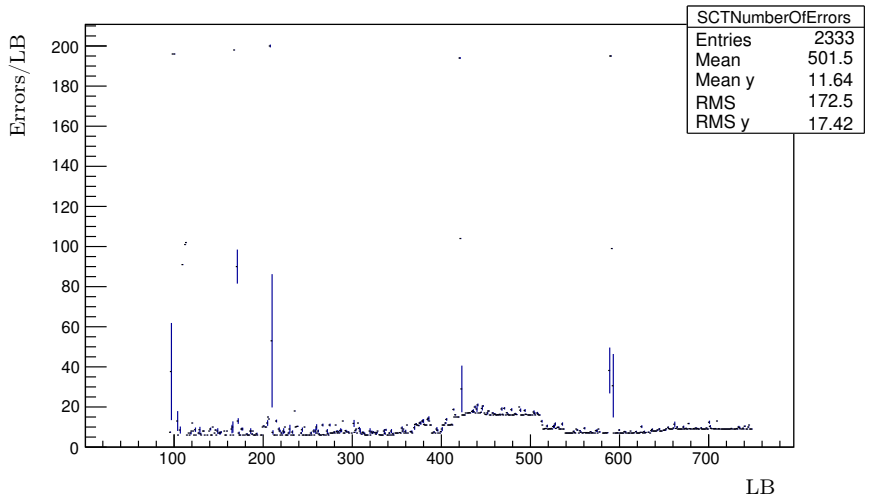

Figure 5.4: Average number of links with byte-stream errors vs. luminosity block number for run 214523 (LHC fill 3286, 14 November 2012, stable beams in LB 92–754). The number of errors is kept under 20, i.e. 0.25 % of links, by the automatic module reconfiguration. The increments of 96 or 192 link errors come from one or two RODs giving errors and being recovered after few LBs.

reconfigured. This is also efficient to recover chips that become temporarily noisy because of Single-Event Upset (SEU).[7]

- Global reconfiguration was added to send configuration to all modules at regular intervals, typically every 30 (90) minutes during Run 1 (Run 2). The process takes about 1.5 s and mitigates the impact of SEUs for chips which are not flagged by the automatic module recovery.
- Busy RODs can be removed, reconfigured and re-integrated. The procedure was automatised and currently takes only a few seconds.
- TTC restart was implemented. It pauses the triggers for all subdetectors and reconfigures only one of them. This procedure is done infrequently on request of experts in case of serious DAQ problems. It is faster than restarting the run (typically during Run 1 TTC restart took about 4 min while run restart lasted 10–20 min.)

Thanks to many improvements of the SCT DAQ, firmware and monitoring, the frequency of problems was kept at a manageable level and the data quality was affected minimally. Figure 5.4 shows an example of the evolution of the number of byte-stream errors vs. luminosity block from run in the end of 2012.

The only significant hardware issues during Run 1 were failures of the TX VCSEL arrays on BOC cards. If one channel of this 12-link array failed, the TX redundancy could be used. However, if the neighbouring channel deteriorated as well, the plug-in needed to be exchanged. From 2009 until 2012, the failures occurred at a rate of about 10 channels per week. Finally, it was found that the issue came from exposure of the VCSELs to humidity and during 2012 all arrays

[7] SEU is an error in the on-detector electronics caused by ionising particles passing through a chip and flipping a bit in some of the configuration registers. If the threshold setting is changed, chips become noisy, inefficient or dead (do not send any hits at all).

were replaced with new design that were more robust against humidity. Because the newly installed components were failing as well, though at smaller rates, all were replaced by more reliable commercial assemblies before the start of Run 2.[8]

SCT monitoring and data quality evaluation

The detector performance parameters are monitored by regular online calibrations (noise occupancy, gain, noisy strips) and during data taking and processing. The online monitoring of raw hit data at the ROD level provides a fast feedback on the beam and SCT conditions. A fraction of events is also fully reconstructed and monitoring histograms are produced to be used by the control-room shifters.[9]

For each recorded run, a subset of events is reconstructed promptly for the first data quality assessment and detector-specific analyses are run to extract calibration constants. This is referred to as calibration loop and takes 24–48 hours. For SCT, strips that became noisy since the previous run are flagged and excluded from the bulk reconstruction. All collected data are then reconstructed and ready to be used for physics analysis.

The variables used for offline data quality monitoring of the SCT include hit efficiency, noise occupancy, number of links with readout errors, number of problematic modules (disabled, noisy, inefficient), hit maps and tracking parameters such as track fit residual and pull. Detailed plots of parameters per module or per luminosity block are produced as well. The plots are reviewed by a shifter and the results are uploaded in a form of defect flags to a database which is used for the production of the good run list. Each defect corresponds to an issue that might impact the tracking quality and is set per run or per LB. Physics analysis groups can use defects to define luminosity blocks with good data according to their requirements.

5.2.2 Radiation damage

The SCT was designed to provide good-quality tracking in *pp* collisions up to a radiation dose corresponding to an integrated luminosity of $700\,\text{fb}^{-1}$ at centre-of-mass energy of 14 TeV [92]. During LHC Run 1, an integrated luminosity of $29\,\text{fb}^{-1}$ has been delivered. The total fluence was up to 1×10^{13} 1 MeV neutron equivalent particles per cm^2, depending on the sensor position. The total ionising dose was up to 4 kGy. During LHC Run 2 in 2018, around $140\,\text{fb}^{-1}$ are expected and the fluence will reach values of $5 \times 10^{13}\,\text{cm}^{-2}$. Additional $150\,\text{fb}^{-1}$ might be delivered during the Run 3.

The radiation dose received by the SCT is generated by particles directly produced in the *pp* collisions or from secondary particles produced by interactions of primary particles with detector materials, such as hadronic showers, e^+e^- pairs from photon conversion and neutrons. The radiation impacts both the silicon sensors and the readout electronics. Changes include leakage current increase,

[8] LightABLE arrays from Reflex Photonics, Canada http://reflexphotonics.com/

[9] The *express* trigger stream used for monitoring of physics variables contains events triggered by a mixture of triggers (muons, egamma, jets, tau, missing E_{T}, minimum-bias triggers). Typically it records at rates of 10–20 Hz. In addition, bunch-group aware monitoring is used for detector monitoring, e.g. noise measurements in empty BCIDs. The monitoring histograms are updated every few LBs, what allows a prompt action in case of detector or trigger issues.

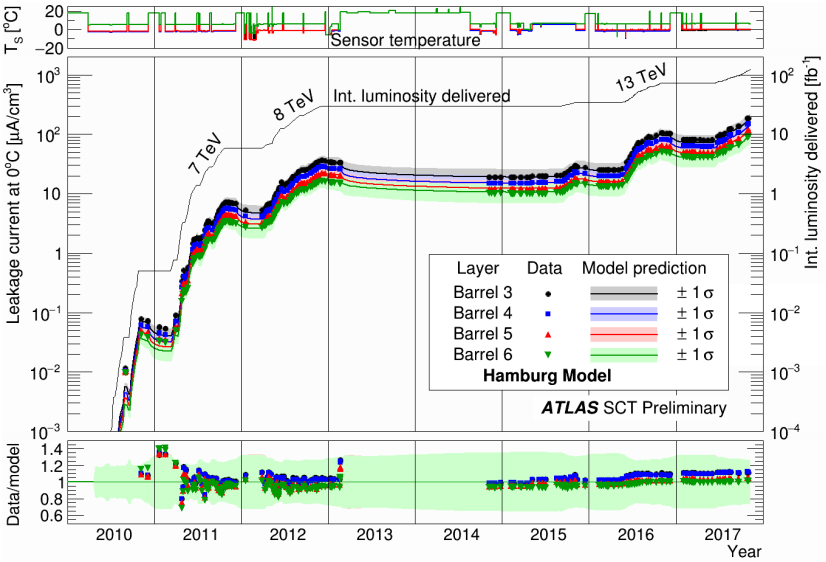

Figure 5.5: The values of the leakage current measured in the SCT barrel modules, together with the predictions of Hamburg-Dortmund model [96, 97]. The measured values have been corrected to a temperature of 0 °C and the uncertainties do not include error of conversion factors from luminosity to fluence at the sensor location [99].

depletion voltage variations, decrease of the signal-to-noise ratio, charge accumulation on the module surface or in the silicon oxide layers and SEUs.

The evolution of the leakage current with the delivered integrated luminosity up to December 2017 is shown in Figure 5.5. A decrease of the leakage current due to annealing during the long shutdown in 2013–14 is visible. The observations agree with theoretical predictions of the Hamburg-Dortmund model [96, 97] and with the Sheffield-Harper model [98] within uncertainties.

The model projections show that the majority of modules should have manageable leakage current and a depletion voltage around 200 V (the limit of the high-voltage power supplies is 450 V) even at the end of Run 3. Simulations of various cooling scenarios (temperature during LS2 and running during Run 3) show that even assuming no annealing during LS2 (sensors cooled to −2 °C), there will be a factor of 2 safety margin against the thermal runaway. However, decreasing the operating temperature (e.g. to −7 °C) during Run 2 might be necessary to mitigate unforeseen problems and to reduce the final value of leakage current in 2024.

Impact of radiation damage on SCT operation and performance

The measurements of noise and gain during Run 1 showed some unexpected behaviours which are illustrated in Figure 5.6. The noise decreased by about 7 % in late 2010 (at neutron-equivalent fluence of about $10^{10}\,\mathrm{cm}^{-2}$, dose of few Gy), while the gain remained stable. The drop appeared first in the innermost barrel modules and was not observed for sensors with crystal lattice orientation

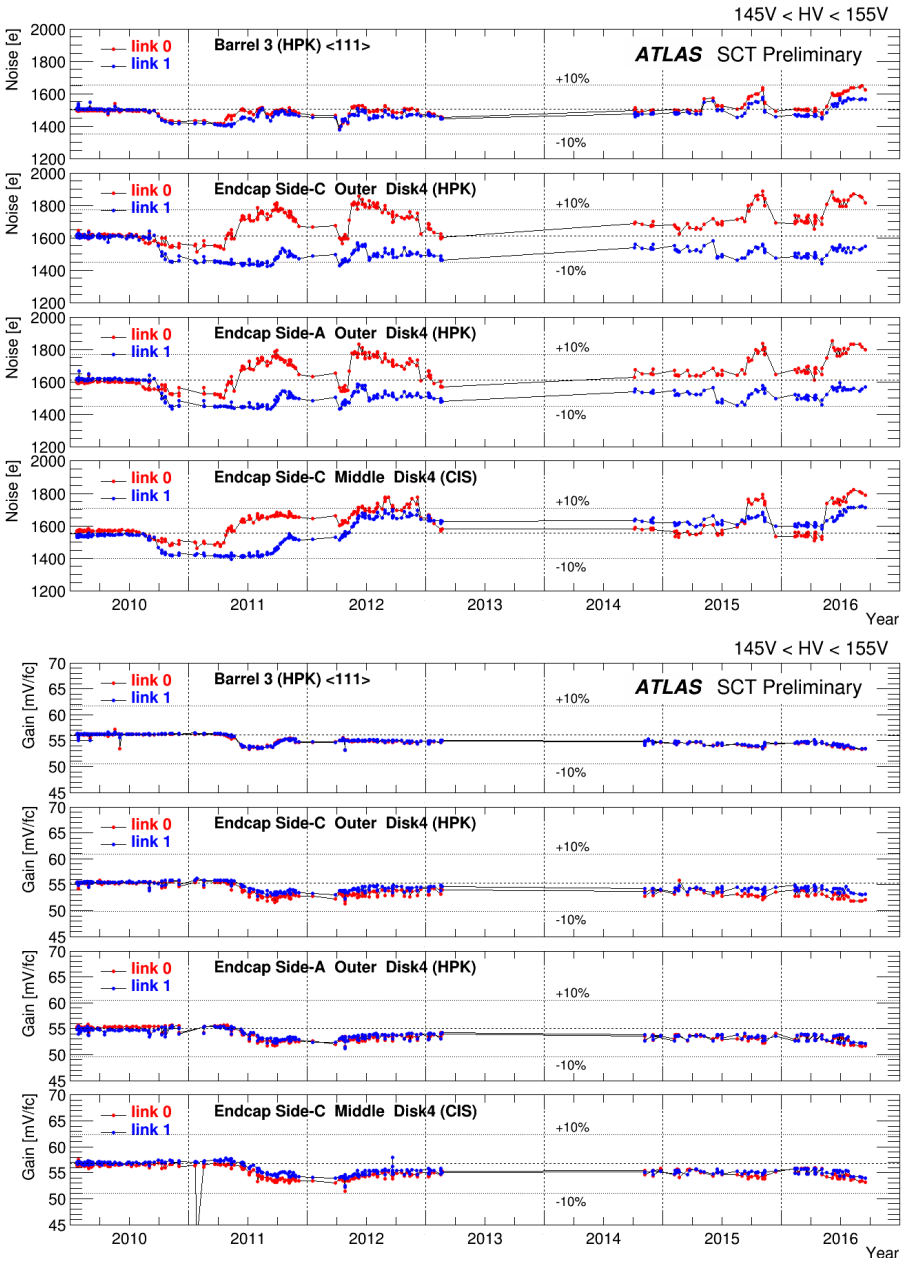

Figure 5.6: Evolution of chip-averaged noise (top) and gain (bottom plots) as a function of time for four types of SCT modules: module in the innermost barrel with Hamamatsu (HPK) sensor, two endcap modules with HPK sensors and an endcap module with CiS sensor. The two readout links (module sides) are plotted separately. For endcap, link 1 side is facing the support disk, link 0 faces the gas gap [100].

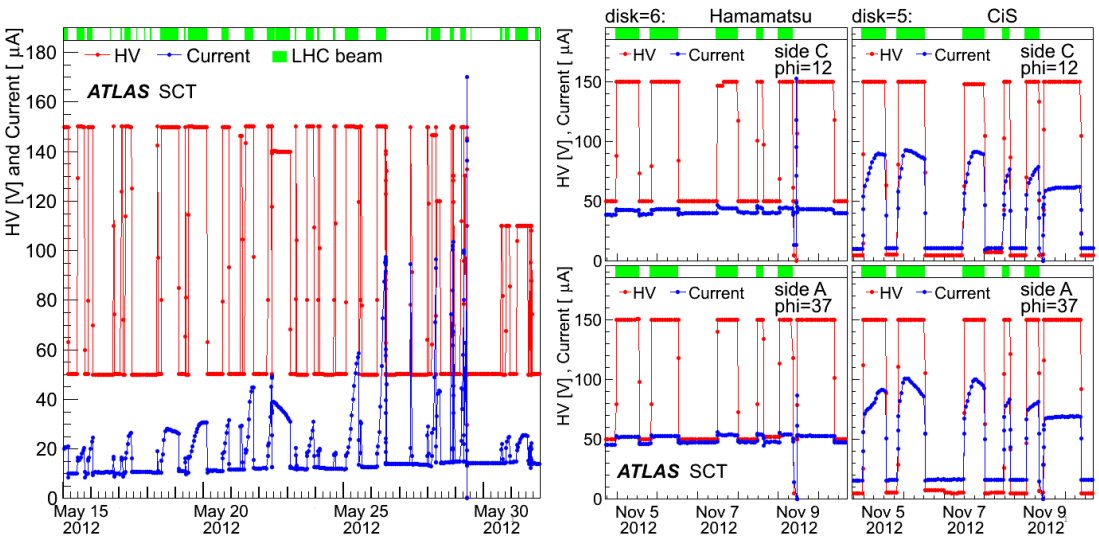

Figure 5.7: Leakage current and bias voltage for a module with CiS sensor in May 2012 (left) and a typical behaviour of modules using Hamamatsu and CiS sensors in November 2012. Green bands above plots show periods with stable beam conditions [92].

<100>.[10] It varied with the location of strip on modules (largest change was observed in the middle of each module side) and disappeared during 2011. Later it was reproduced in a beam test at the CERN Proton Synchrotron and attributed to radiation-induced changes of charge carrier mobility and a possible accumulation of charge on the sensor surface which changes the interstrip capacitance.

In 2011 and 2012 the noise increased back to the original values and gain dropped by ∼5 %. However, the behaviour of the module sides in the endcaps differed: noise from link 0 (facing the gap between disks) increased by about 10 % and noise from link 1 decreased with time. The difference was largest in the endcap modules with Hamamatsu sensors and persisted also in Run 2. The behaviour was suspected to be due to a flow of ionised air in the gap between disks during high-luminosity data taking. However, the values of noise (gain) remained within 13 % (8 %) of the values measured before the start of the SCT operation.

In the beginning of 2012, unrecoverable ROD busy instances occurred. These were linked to modules with CiS sensors which showed very high and varying leakage currents in the first few hours of high-luminosity *pp* runs. An examples of such behaviour is shown in the left plot of Figure 5.7. During the periods of high leakage current, a significant increase of noise was observed. This was sufficient to provoke a ROD busy and prevent data taking. It was found empirically that a change of bias voltage can mitigate the behaviour. The standby voltage was set to 5 V for all CiS modules and the ready voltage was decreased by 30–40 V for the problematic modules (still above depletion voltage). The cause of this behaviour is still unknown but observations from Run 2 show that the issue is decreasing with radiation.

[10] Most of SCT modules are built from silicon wafers with Miller indices <111> except of 93 barrel modules which are constructed from wafers with Miller indices <100>.

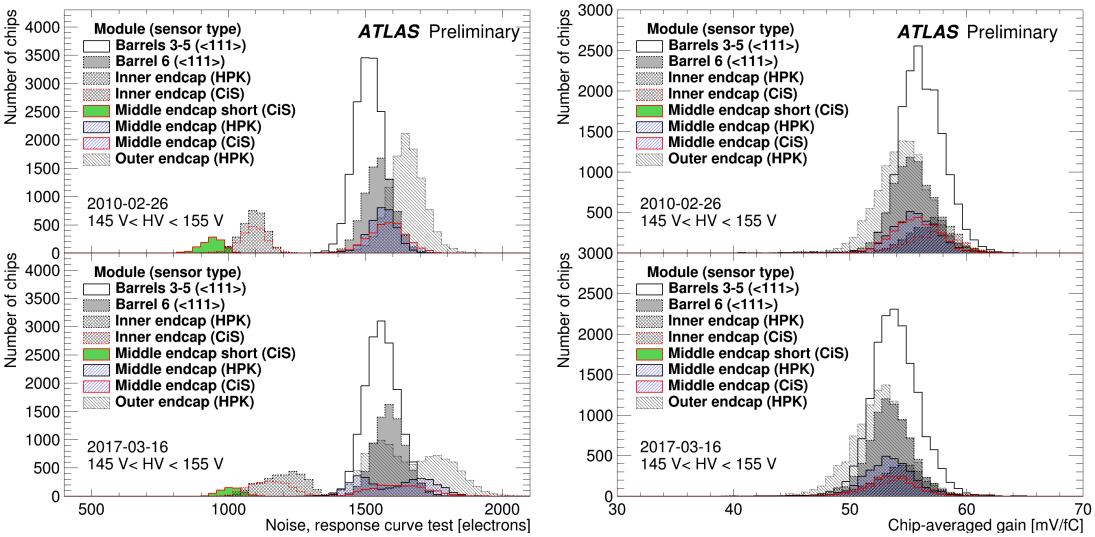

Figure 5.8: Chip-averaged values of noise (left) and gain (right) measured by the response-curve test in February 2010 (upper plots) and March 2017 (bottom, after an integrated luminosity of about 75 fb^{-1}) [102]. Different types of modules are plotted separately to illustrate that the noise changed only slightly for most of modules. For barrel, only modules with <100> sensors are plotted and barrel 6 is plotted separately as it has a higher temperature and thus higher noise.

5.2.3 Tracking performance

Even though the pile-up conditions in LHC collisions exceeded the expected values already during Run 1, the SCT tracking efficiency stayed above the design values (hit efficiency of >99 % and noise occupancy of $< 5 \times 10^{-4}$). The tracking performance in Run 1 is described in Ref. [92].

In Run 2, the average strip occupancy was less than 2 % in the innermost barrel and lower elsewhere. The hit efficiency for active strips was 99.7 % for the first BCID in bunch trains [101] (May 2016, measured from the presence of hits or holes on reconstructed tracks). The noise occupancy at a threshold of 1 fC was lower than the required value of 5×10^{-4} for almost all chips. The values of noise and gain measured in 2012 and 2017 are shown in Figure 5.8. The observed changes are consistent with the expected radiation damage, except for the small effects described in previous section (e.g. endcap modules facing the air gap). The number of noisy strips found in the calibration loop is shown in Figure 5.9; it scales with the instantaneous luminosity and with the length of runs (the probability of SEU is luminosity-dependent), the dips coincide with performed calibrations.

Currently, around 40 modules are disabled from readout due to various reasons and the number of active strips is 98.7 % (May 2018) [104]. The luminosity-weighted efficiency for good data from SCT is about 99.6 % in 2018 [105].

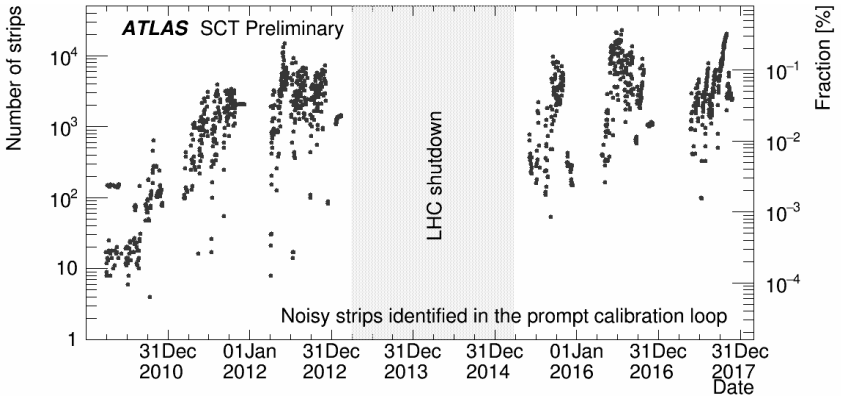

Figure 5.9: The number of noisy strips identified in the prompt calibration loop as a function of time [103]. Strips are considered noisy if they have an occupancy of >1.5 % in empty BCID and strips which have other problems identified in online calibration are not used for reconstruction and are excluded from this plot.

5.2.4 SCT upgrades

Only small changes of off-detector hardware were done during the LHC long shutdown in 2013–14. To increase the available readout bandwidth, the number of RODs was increased from 90 to 128 and the optical links were redistributed so each ROD reads out 24 or 36 channels instead of 48. The DAQ software and ROD firmware were also improved, together with BOC hardware modifications.

In 2017, TX and RX fibres of about 200 modules were shuffled in RODs to equalise the occupancy across S-links. An option to dynamically disable chips for a period of run with high pile-up was also added. This was applied typically in the beginning of high-luminosity runs in 2017, when the trigger rate and track occupancy were high and the readout rates were close to the bandwidth limitations. Already disabling 60 chips (0.12 % of all chips) on the modules with highest occupancy significantly decreased the frequency of ROD busy instances without a measurable impact on tracking.[11]

Changes for Run 3 that are under consideration include increasing the number of RODs by adding readout crates or implementing further data compression on RODs. However, these changes will require a significant effort (re-cabling of the optic fibres) and additional studies of their impact on tracking performance. A commissioning of new cooling system is also ongoing; it will be using the thermosiphon effect (gravity in pipes from the surface to the ATLAS cavern) instead of the current compressor system in the service cavern. This should allow a lower operating temperature and ensure a cold operation of SCT while performing maintenance of the compressor system during shutdown periods.

[11] Thanks to ROD firmware improvements, the chip masking did not have to be applied during 2018 data taking.

5.3 Inner Tracker upgrade for HL-LHC

By the end of the LHC Run 3, the current ATLAS Inner Detector will have accumulated an amount of radiation damage which will make it unsuitable for further use. A higher granularity and new on-detector electronics will also be needed for efficient tracking and triggering in the conditions expected at the High-Luminosity LHC (instantaneous luminosity of up to $7.5 \times 10^{34}\,\mathrm{cm}^{-2}\mathrm{s}^{-1}$, 200 interactions per bunch crossing and $3000\,\mathrm{fb}^{-1}$ delivered until ~2037).

The proposed ITk [65, 66] will be an all-silicon detector. The central region will be built from 5 concentric barrels of pixel modules with inclined modules at higher pseudorapidity and 4 strip barrels, as shown in Figure 3.15 (page 47). The forward regions will use pixel and strip sensors on disk support structures (42 rings of pixel modules and 6 strip disks). The active area of ITk will be 10 times larger that the current ID and extend the pseudorapidity coverage up to $|\eta| = 4$. The number of readout channels will increase from current 90 million to around 600 million for the pixel subsystem and from 6 million to 70 million for strips.

The pixel ITk will use a hybrid detector technology, similar to the current Pixel detector and IBL (described in section 3.1 on page 27). Studies are underway for the selection of sensors which would have the required radiation tolerance, intrinsic resolution and add a minimal amount of material. For the innermost layer, 3D sensors are being considered and planar sensors will be used for the rest. An effort is also focused on using some of the industrial technologies, such as CMOS monolithic pixel sensors.

The design of the strip part of ITk is highly modular. The basic mechanical element in barrel region will be a 1.3 m long stave, which provides support, power, readout and cooling to 14 modules on each side. There will be 392 staves with nearly 11 thousand barrel modules. The disks in forward regions will be built from 384 identical petals which overlap slightly to be hermetic for particles with momenta of 1 GeV. Each petal will hold 9 modules of different type per side organised in 6 rings. To cover the trapezoidal petal, six sensor types and 14 hybrid variations are required. In total, 6912 modules will be installed in the endcaps.

ITK strip module

The fluence in the inner layers of the strip detector in HL-LHC is expected to be around 2×10^{15} 1 MeV neutron equivalent particles per cm^2 (including a safety factor of 2). Because of this, the *p-in-n* technology is not suitable and the baseline option is single-sided n^+*-in-p* sensors with *p*-stop as strip isolation.

Components of a barrel module and the sensor structure are schematically shown in Figure 5.10. Each module will have multiple rows of strips with a pitch of 74.5 µm in barrel and from 69–85 µm in endcaps. All barrel modules will have the same dimensions, however, the strips in the inner two barrels will be 24 mm long and those in the outer barrels will have 48 mm. The inner barrel modules will have two hybrids and the outer modules will have one hybrid. Similarly, endcap modules will have one or two hybrids. Each hybrid circuit will carry a DC-DC converter, power board and readout and control chips. A part of the prototyping programme was done with the ABCN-25 front-end chips [106], the final version will use an improved design of the chip using 130 nm technology [107].

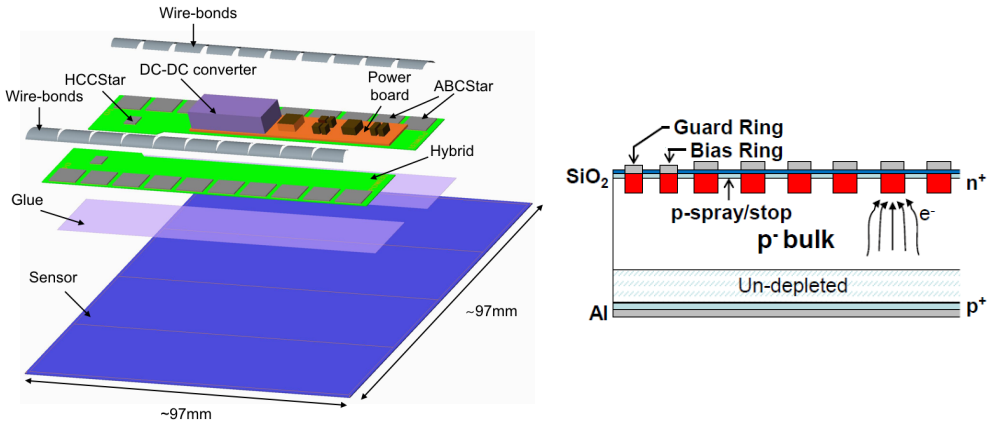

Figure 5.10: Components of the short-strip module for ITk (left [65]) and a cross-section of single-sided n^+-*in*-p sensor used for the ITk strip modules [108].

5.3.1 Electrical tests and calibration

As a part of preparations for module tests in laboratory at IPNP, Charles University (Prague, CR), a prototype of endcap module was tested in December 2015. The aim was to prepare the test infrastructure, verify the module and readout chain functionality, compare the performance parameters with values measured during module production and prepare the settings and configuration files for subsequent studies, such as laser tests.

The device under test was a prototype of endcap module `El_Petl_upmod_06` produced at Freiburg University (Germany) as a part of the ITk strip R&D effort. Its geometry was the same as upper modules used for the petalet, a fully functional structure with 3 modules on each side, described in Refs. [109]. The sensor had an embedded double metal layer which was connected to strips and has the same pitch as chips [110]. This reduced the wire-bonding angle but led to increased noise compared to standard sensors. A single hybrid flex was populated with two rows of ABCN-25 chips, six chips each, and each chip reads out 128 strips. Data was sent out via an adaptor board separately for each half of hybrid (referred to as link 0 and link 1) and the readout was done via the HSIO board [111] with a firmware revision 4129 and run from the SctDaq software.

The module was wire-bonded to a test frame, a PCB which provided powering and readout interface. The board was placed on top of a cooled aluminium block. A picture of the module is shown in Figure 5.11.

Chips were powered with V_{cc}= 2.85–3 V (analog voltage) and V_{dd}= 5 V (digital voltage). The analog current was around I_{cc}= 2 A (should not exceed 2.5 A). The sensor bias voltage ranged from 30 V to 160 V and cooling was set to 15 °C for most of the tests.[12]

Latency, strobe delay and timewalk scans

Because many of the electrical tests are done by injecting test charges into the chips, the timing has to be optimised to read out the correct signals. The latency scan measures the number of clock cycles for which the binary data in the chip

[12] These conditions were partially given by the equipment available for these tests (no humidity control inside the dark box, oil-based cooling).

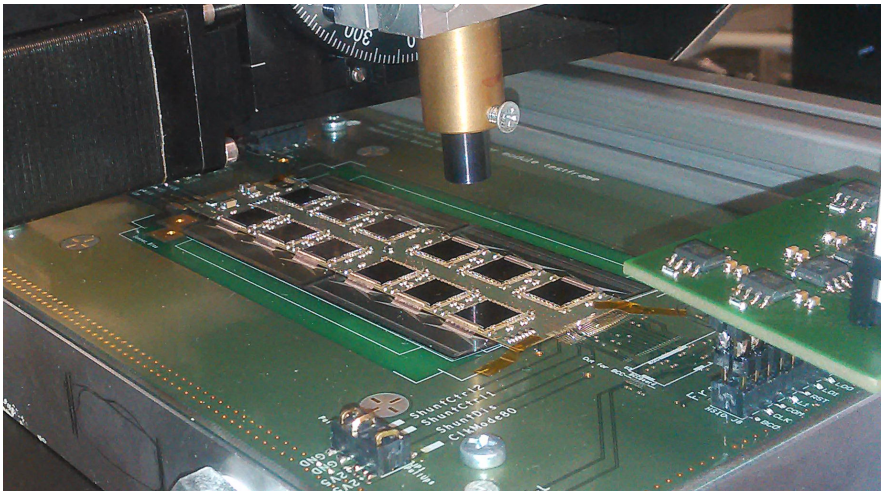

Figure 5.11: Photo of the ITk strip module ready for calibrations and laser testing.

pipeline should shift before transmitting it. The measured latency was 32 clock cycles.

The strobe delay scan fine-tunes the timing within one clock cycle. The delay is set to a 6-bit register with a Digital-to-Analog Converter (DAC) unit of ∼0.8 ns, i.e. the scanned range is around 50 ns. For each DAC value, 50 triggers are sent and the average hit efficiency per chip is computed. The measured value of delay is then used for subsequent scans (usually at 25 or 40 % of the working range).

Results of a scan for one half of hybrid are shown in Figure 5.12. The scan with V_{cc}= 2.85 V showed that some chips were not fully powered (signal was not amplified properly) because the efficiency was ∼60 % for most of the working range. The voltage was therefore increased to 3 V (I_{cc}= 1.96 A).

Because of non-linearity in the analog part of the chip, the signal shaper and discriminator response depend on the injected charge. The timewalk test evaluates a strobe delay for calibration pulses of 1.25–10 fC, the measured value of timewalk was 15 ns. For most of tests this is within the working range but for tests with too high or too low injected charge the timewalk has to be taken into account. The response of the analog circuit also depends on chip temperature and radiation damage, so the timing scans should be repeated after large temperature changes or irradiation.

N-point gain scan

The response curve or N-point gain test is a threshold scan with a known charge injected into each chip channel (SCT and ITk software uses N=3 and 10). The dependence of hit occupancy on the discriminator threshold, known as S-curve, is measured for each channel. The threshold at which the occupancy is 50 %, V_{t50}, corresponds to the median of the injected charge or noise. The width of the distribution is a measure of the output noise.

The gain is extracted from a fit to V_{t50} for multiple values of injected charge. The input noise is computed by dividing the output noise by the gain. The input noise is usually expressed as equivalent noise charge (ENC) in units of electrons, where 1 fC = 6242 e^-. Examples of S-curve and response curve (10-point gain) tests are illustrated in Figure 5.13.

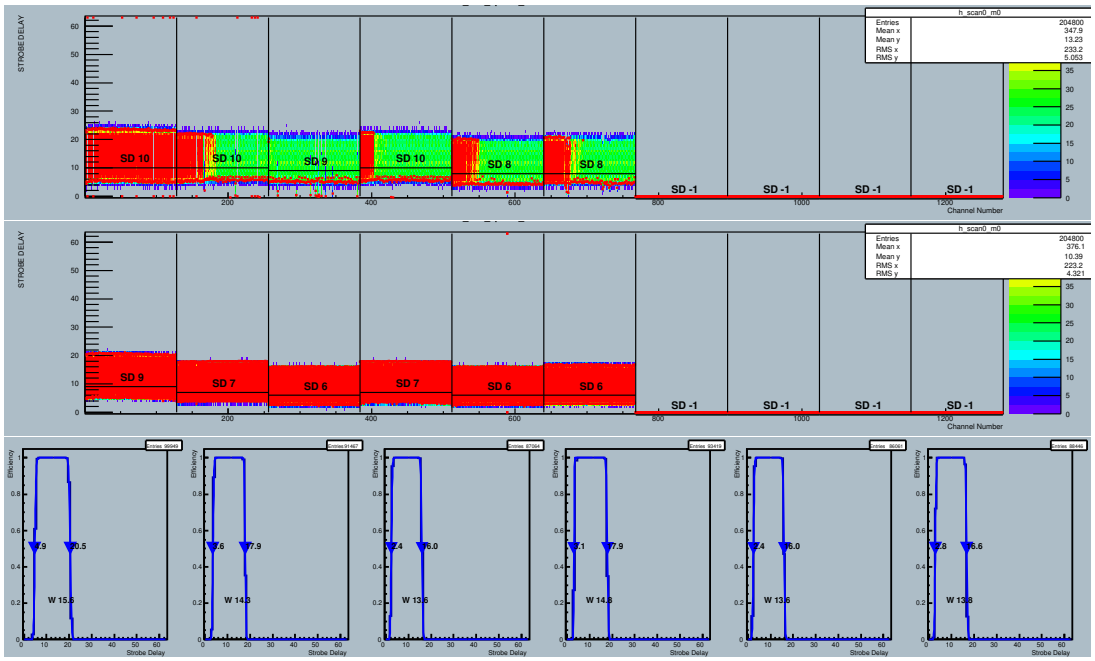

Figure 5.12: Results of the strobe delay scan for six chips on link 0 at V_{cc}= 2.85 V (top) and 3 V (middle) and fits to the per-chip average efficiency for the later scan (bottom).

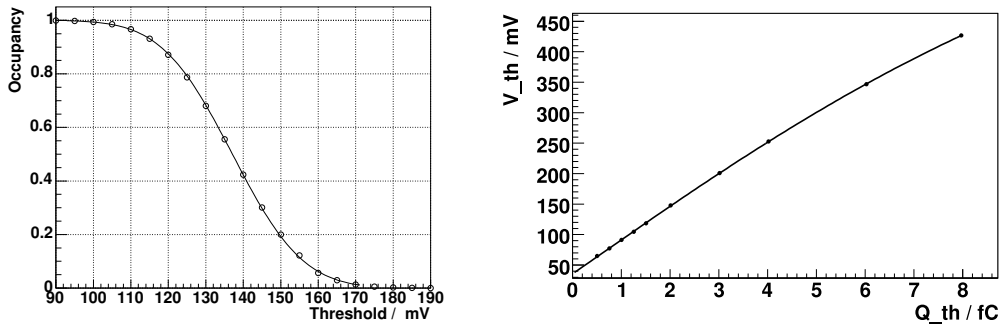

Figure 5.13: Occupancy as a function of the discriminator threshold with the S-curve fit by a complementary error function (left) and response curve scan with a quadratic fit (right) [95].

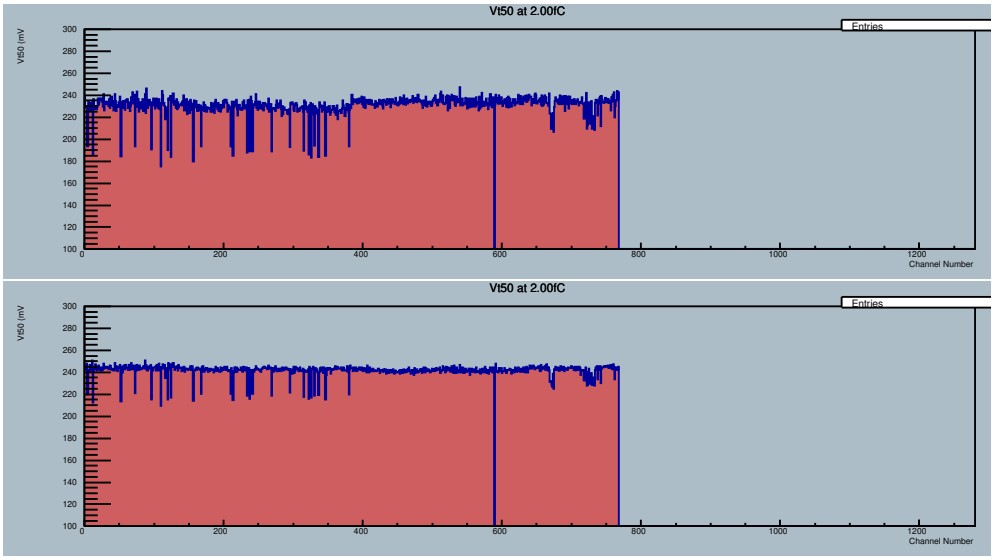

Figure 5.14: Values of V_{t50} measured in 3-point gain scan with default settings (trim range and DAC) and after calibration

Trim scan

It is important to set the discriminator threshold for binary readout very precisely so that the hit efficiency is uniform across readout channels. However, because the response of chip preamplifiers and discriminators varies, a trim calibration has to be done.

The trim range defines the limits and coarseness of the DAC for discriminator. For the ABCN-25 chips, there are eight trim ranges and the DAC value is set per channel by a 5-bit register (values 0-31). The trim range scan injects a 2 fC charge and performs threshold scans for different trim ranges and DAC values, and measures the discriminator threshold V_{t50}. The scan finds range (set per chip) and DAC settings (per channel) so that the number of channels with the same threshold is maximised, i.e. they have the same response. The results from all ranges are combined so that the threshold is uniform across the module.

For the tested module, the best trim ranges were 2 to 5 and the target threshold was 137.6 mV. For an irradiated module, usually a higher range has to be used and it becomes difficult to trim all channels to a common threshold as the response varies more significantly.

A comparison of threshold measured by the 3-point gain calibration before and after trim is shown in Figure 5.14. The response across channels is more uniform, however, there are still some problematic channels.

Noise occupancy scan

The noise can be measured from N-point gain scan as described above or in noise occupancy scan. The later is a threshold scan without charge injection and the input noise is obtained by fitting the dependence of logarithm of noise occupancy on threshold squared. An example of results is shown in Figure 5.15

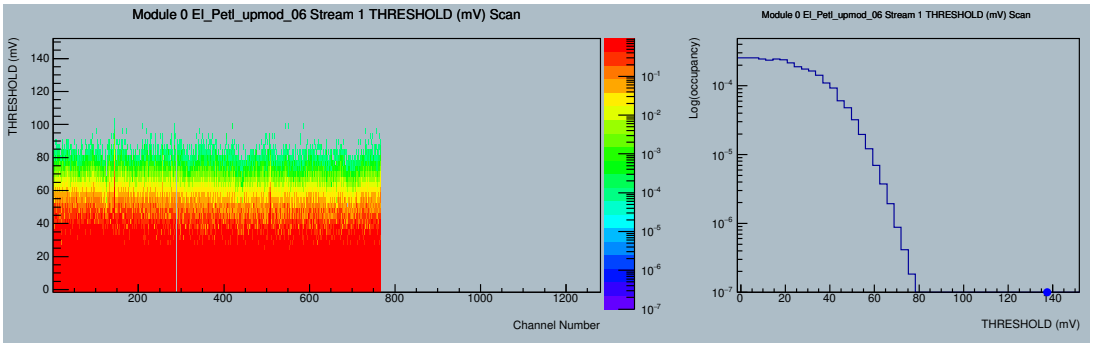

Figure 5.15: Noise occupancy scan for link 1 at bias voltage of 150 V, 10 °C: the threshold scan of link 1 (left) and logarithm of occupancy versus threshold (right).

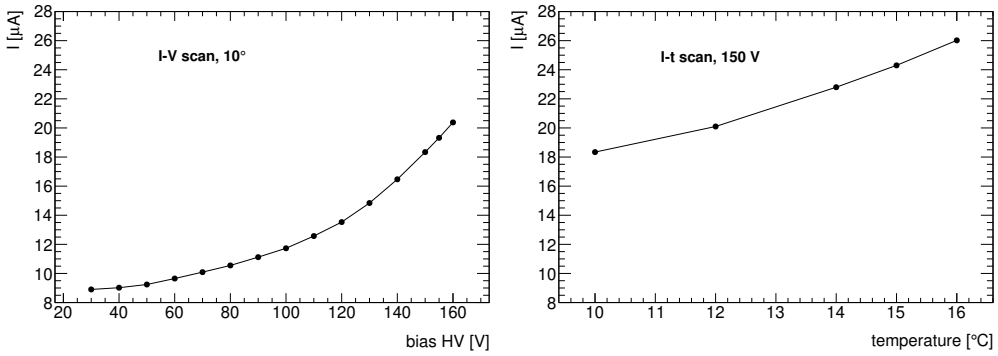

Figure 5.16: IV scan results for temperature of 10 °C (left) and the dependence of the leakage current on the sensor temperature for bias voltage of 150 V, both for chips powered on.

5.3.2 Results

Before the electrical scans with bias voltage, an I–V scan was done to check the sensor leakage current, depletion voltage and to set the maximum feasible bias voltage and avoid breakdown. The results of the I–V scan for values between 30 and 160 V are shown in Figure 5.16. The scan was repeated for different temperature (temperature of the cooling liquid) and with chips powered on, as the additional heat generated by chips increases the sensor temperature and consequently the leakage current.

The communication with chips was then probed and timing and trim were calibrated. In addition, about 60 channels were disabled due to various problems (high noise, low gain or unbonded channels).

The noise was measured by a response curve scan and results for link 1 are in Figure 5.17 (bias voltage 150 V, 10 °C). The module average gain is 104 mV/fC and the average input noise is 772 e^-. The value of gain is consistent with the one measured after production of the module, noise is slightly higher. Attempts to decrease the noise were done by checking and improving the grounding and noise shielding of the whole readout chain.

The dependence of noise on the sensor bias voltage was also measured and is plotted in Figure 5.18.

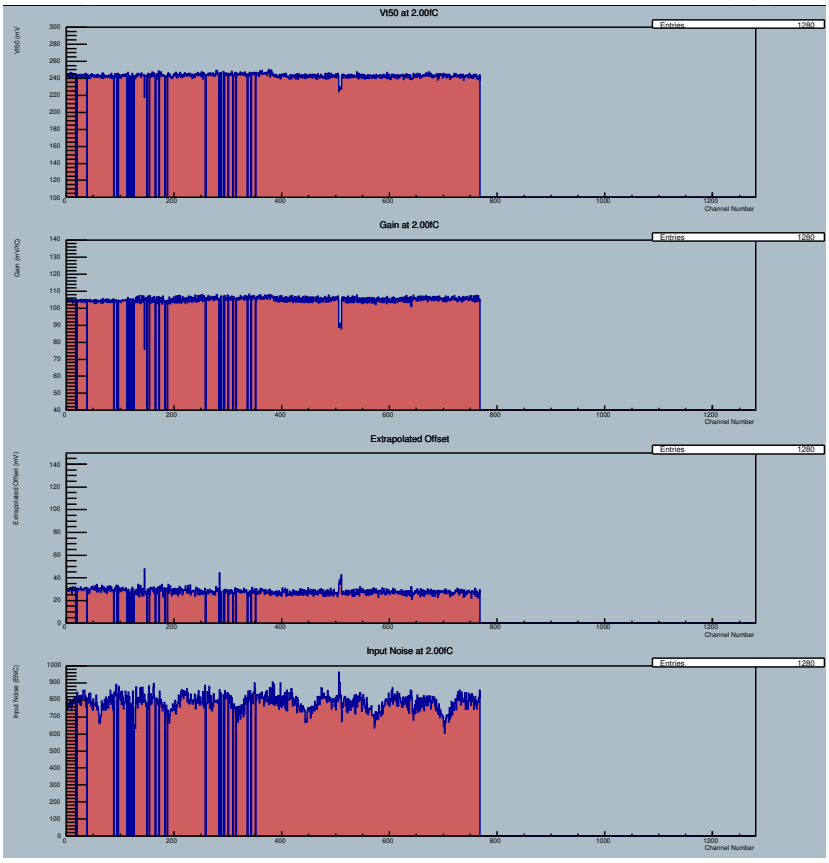

Figure 5.17: Response curve scan (10-point gain) results for link 1: from top to bottom are shown the V_{t50} threshold, gain, offset and input noise at 2 fC. This scan was done with bias voltage 150 V and 10 °C.

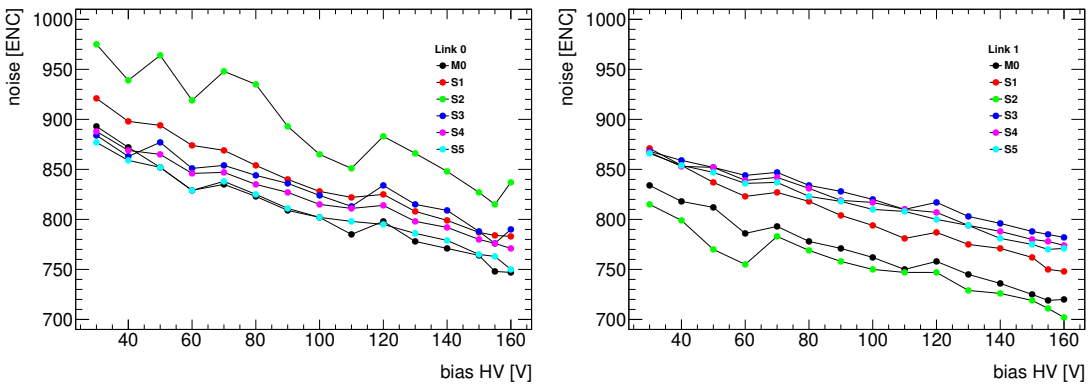

Figure 5.18: Dependence of the average input input noise per chip on the sensor bias voltage. The noise was measured by the 3-point gain scan, chips read out by link 0 and link 1 are shown separately.

6. Non-collision background monitoring

The understanding of backgrounds is important for detector safety and for many physics analyses, from luminosity measurements to studies of rare processes with signatures that can be faked by the backgrounds (e.g. BSM searches with high missing E_{T}, monojets or displaced tracks in the final state). The ATLAS Non-collision Background Task Force was established to study, recognise and monitor conditions which could have an impact on detector performance and quality of physics analyses. It also provides feedback to the LHC Background Study Group and recommends procedures to tag or remove events with high background contributions from collision datasets. Some of results of studies done during the LHC Run 1 were published in Refs. [112–114] and references listed therein.

This chapter provides a brief overview of non-collision background sources and of the LHC operational conditions that are relevant for background formation. It describes some of the used background detection and triggering methods, with more details about the monitoring with SCT that was implemented by the author of this thesis. The results produced by a background monitoring package which was implemented in Athena by the author while working in the Non-collision Background Task Force are shown as well.

6.1 Sources of non-collision background at LHC

The non-collision backgrounds in experiments at the LHC in general fall into two categories: Beam Induced Background (BIB) and non beam induced background. The BIB includes secondary particles produced in collisions of protons from beam with the accelerator instrumentation (beampipe, collimators) or with gas in the beampipe and background coming from delayed tails of particle cascades produced in the detector material, called afterglow. The non beam induced background includes cosmic rays and detector noise.

The protons in LHC bunches are lost from the beam by various processes. Beam cleaning, i.e. removing the off-momentum and off-orbit particles, is needed to protect the machine elements, especially the cryogenic superconducting magnets. Most of the cleaning instrumentation is localised in straight sections without superconducting magnets (Point 3 and Point 7 of the LHC ring) but a small fraction of the beam halo composed of secondary and tertiary particles reaches the experiments. A system of collimators and absorbers is installed around the LHC to mitigate the halo and there is a heavy shielding hermetically closing the entrances from the LHC tunnel to the ATLAS experimental cavern. However, the products of inelastic collisions of halo with collimators include high-energy pions and muons which can pass through the shielding and enter the detector areas.

Another source of BIB is the scattering of the primary beam on residual gas in the beampipe, especially in the vicinity of the experiments. The rate is proportional to the beam intensity and on the residual gas pressure in the vacuum chamber. The elastic beam-gas scattering often results in small deflection of protons which can be lost on the next collimator before reaching the cleaning

section. Inelastic beam-gas scattering produces showers of secondary particles, most of which are absorbed locally but high-energy muons can travel large distances and reach the ATLAS detector.

Background collisions can also come from protons that have the correct beam orbit but they are not in the nominal bunch. Protons can end up in the neighbouring radio-frequency buckets because of slight mistiming during injection to the LHC or if debunching happens in the pre-accelerators or in the LHC. These bunches are referred to as satellites (for protons in buckets within the 25 ns duration of one BCID) or ghost charge (for BCID which are designed to be empty).[1]

Background not directly induced by the LHC beam includes cosmic rays, mostly muons and muon showers, which are not totally absorbed by the overburden rock. The signals from these particles are not timed in with the collisions and can be tagged by cosmic muon reconstruction algorithms. Spurious noise hits also contribute to background and can fake hits in tracking detectors or clusters of deposited energy in calorimeters. These are partially removed during the data quality inspection (e.g. masking of noisy pixels, strips and calorimeter noise bursts) and their impact on physics is studied by performance and analysis groups.

For background from all sources, two types of signatures are of a high concern for the detector operation and physics analyses:

- Particles close to the beam orbit can cause large clusters of energy deposition, especially in the Pixel detector. This increases the detector occupancy and affects the track reconstruction by producing fake hits.
- High-energy muons which penetrate the shielding material can deposit part of their energy in the calorimeters. The resulting longitudinal clusters can potentially be reconstructed as fake high-energy jets.

6.2 Tools for background monitoring

In the ATLAS CTP, the bunches in each beam are flagged as filled or empty according to the actual LHC filling scheme. The collision BCIDs are then sorted into categories called bunch groups (BG). The BGs used in the background monitoring are defined as follows:

- Group 0 (BGRP0) - all BCIDs, except a few at the end of the abort gap.
- Paired - a bunch of protons in each beam.
- Unpaired isolated (UnpairedIso) - a bunch in only one beam with no bunch in the other beam within 7 BCIDs (150 ns).[2]
- Unpaired non-isolated (UnpairedNonIso) - a bunch in only one beam with a nearby bunch in the other beam.
- Empty - a BCID without any bunch and separated from by at least 5 BCIDs from any filled bunch.

[1] As is described in Section 2 on page 21, the LHC radio-frequency cavities operate at a frequency of 400 MHz creating buckets every 2.5 ns which can be be populated by protons. Nominally every tenth bucket has protons and is assigned a BCID with a duration of 25 ns.

[2] In 2012 it was changed from 3 empty BCIDs used during 2009-11 data taking.

The background measurements are based mainly on the unpaired or empty BGs. The trigger system can use this information so that some trigger items can fire only for a given BG or the prescales can be set different for each BG. The timing of the CTP is adjusted such that the collision time of two filled bunches falls in the middle of the BCID.

The data from beginning of the LHC cycle are very useful as well: LHC is filled by protons in bunch trains from the injector chain and the beams are then accelerated, squeezed (change of optics at the interaction points to decrease the beam emittance) and finally brought into collisions. The phases before start of collisions but at full energy allow monitoring of backgrounds without the overwhelming signal rate from pp collisions.

The LHC is equipped with few thousand beam loss monitors which can dump the beam in case of severe beam losses. Their time resolution is limited to about 40 µs so they cannot be used for per-bunch monitoring but they provide information about time development of losses on a given element such as a collimator. Signals from the LHC beam pickup stations [115] installed 175 m from the IP can also be used for bunch group check and for fine adjustments of the LHC bunch clock with collisions.

The residual gas pressure in the beampipe close to the experiment is monitored by several vacuum gauges. The ones considered for monitoring are closest to ATLAS, installed at 22 m, 58 m, 150 m and 250 m from the IP.

ATLAS has a dedicated subdetector used for beam-related monitoring, the Beam Conditions Monitor described on page 29 in Section 3.1. Its primary purpose is to detect beam conditions which could result in detector damage and to issue a beam interlock signal which dumps the LHC beams. The time resolution of BCM is 0.5 ns and the data recorded in one 25 ns event contain 64 bins, each approximately 390 ps wide. This allows to extract the arrival time and duration of signals very precisely and to monitor the luminosity and background levels.

Dedicated luminosity and forward detectors (LUCID, ZDC, ALFA and AFP) are rarely used for background studies, mainly because the collision activity masks the small background signals. They are however very useful in special low-luminosity runs.

Online and offline background monitoring code

A small fraction of events recorded by the ATLAS detector is promptly processed during data taking for monitoring purposes. This is usually referred to as online monitoring. A full event reconstruction is done and the results are available within few minutes after the data is recorded. The monitored variables include detector observables (byte stream errors, efficiency, noise, pulse shape) and physics observables (numbers of hits/clusters/tracks and angular, energy or time distributions of reconstructed objects such as electrons, muons, jets, J/ψ, Z candidates etc.). This serves as a first check of data quality and it speeds up the detection and fixing of problems with detector or data acquisition system.

A similar analysis is done in the first few days after a run is recorded to asses the data quality and flag luminosity blocks suited to be used for analysis. This is called offline data quality and it is based on similar tools as the online data quality.

While working in the ATLAS Non-collision Background Task Force, the author of this thesis implemented an Athena tool `DQTBackgroundMon`[3] which was added to the `DataQualityTools` package and used for both online an offline background monitoring. Several older runs that were flagged as having a high BIB content were reprocessed as well and the results were used to provide a feedback to the LHC operations group. Some of the plots produced by this package will be shown in the following section and will be flagged as online/offline monitoring.

6.3 Implementation of background monitoring

Some of the background monitoring algorithms developed during LHC Run 1 will be described here, mostly using data collected in 2012. The conditions during 2012 were stable, the LHC collided protons at $\sqrt{s}$ =8 TeV with bunch spacing of 50 ns and typically $1.1 - 1.7 \times 10^{11}$ protons/bunch at the start of a fill. The filling scheme changed slightly few times during the year and allowed up to 1377 colliding bunches. For major part of the year there were 3 isolated and 3 non-isolated unpaired bunches injected in each beam.

The algorithms described here are used also during LHC Run 2 but the code had to be altered slightly by other members of the Non-collision Background Task Force because ATLAS changed the analysis and computing model, including data formats.

Monitoring of trigger rates

Few types of L1 trigger chains can be used for background monitoring:

- `L1\_BCM\_AC\_CA` is a trigger which selects particles travelling parallel to the beam from side A to side C or opposite. It requires a coincidence of an early hit and an in-time hit on the other side of BCM. The time windows are defined as $\pm(6.25 \pm 2.73)$ ns where the nominal collision time is at $t = 0$.[4]
- `L1\_BCM\_Wide` trigger requires a collision-like coincidence of in-time hits on both sides. If this trigger is fired in UnpairedIso or UnpairedNonIso BG, it indicates ghost collisions.
- `L1\_Jxx` triggers require a calorimeter jet in a $\Delta\eta \times \Delta\phi = 0.8 \times 0.8$ region within $|\eta| < 3$. Thresholds of 10 or 30 GeV are used in the unpaired BGs to study fake jets, ghost collisions. Events recorded by this chain in empty BG often contain cosmic-ray induced fake jets.

Some of these triggers are used for online monitoring during data taking, together with luminosity values. Very useful are per-BCID rates averaged over time (e.g. 5 min) or per LB. The rates of BCM triggers are strongly correlated with the pressure measured in the beampipe at 22 m and at 58 m from the IP [114].

[3] https://gitlab.cern.ch/atlas/athena/blob/master/DataQuality/DataQualityTools/src/DQTBackgroundMon.cxx

[4] The BCM modules are placed at $z = \pm 1.84$ m, giving the time of propagation from the IP to BCM of z/c =6.14 ns.

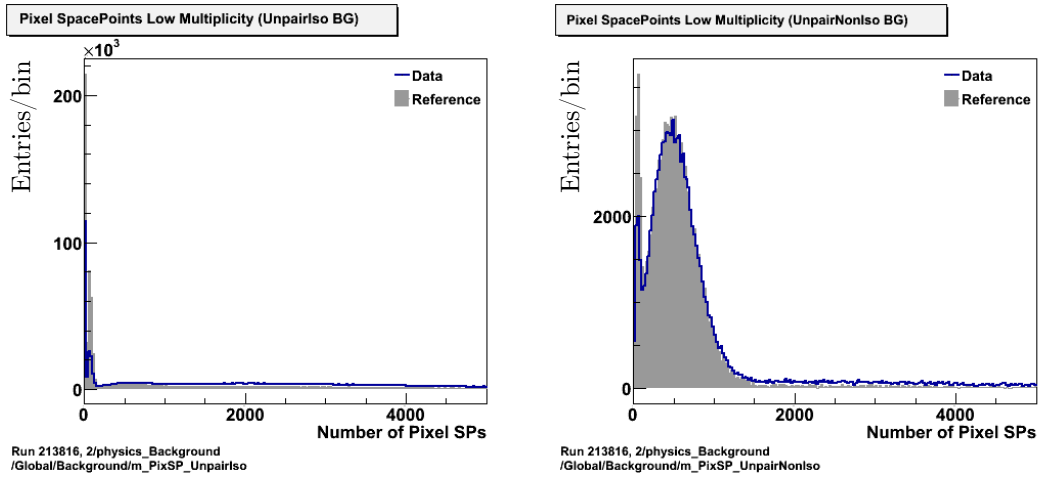

Figure 6.1: Offline monitoring plots for run 213816: number of Pixel space points in unpaired isolated BG (left) and in unpaired non-isolated BG (right). The distributions are compared to a reference run 207447.

BIB identification with the Pixel detector

The Pixel detector is very close to the beampipe thus it is sensitive to beam conditions and can both monitor the changes in background rates and tag single hit clusters or tracks of beam halo particles. It was also found that simply a higher number of pixel clusters and space points or the number of clusters not associated to tracks are good indicators of increased BIB [112]. Histograms of number of Pixel space points in unpaired (non-)isolated BG from high-background run 213816 are shown in Figure 6.1.

A more elaborated method is based on the presence of clusters elongated in the beam direction, caused by halo particles particles passing through the barrel modules nearly parallel with the beam. For each cluster, the probability that it originates from collision or from BIB is computed from cluster width and η. For a sufficient number of such clusters the event can be tagged as having high BIB content. However, because the clusters of particles originating in the IP also become long at high η, this tagging technique is most efficient in the central region below $|\eta| \sim 1.5$.

BIB identification with SCT

The signal from SCT strips is processed by the analog part of the readout chip and digitised by comparing the integrated charge to a given threshold (nominally 1 fC). The hit information from each strip is then stored in a buffer and if an L1 trigger accept signal arrives, the binary hit data is sent out. There are three time bins with a length of 25 ns for each hit: the central bin corresponds to the expected time of arrival of particle from the collision in IP and the early and late bins contain data from BCID before and after the time of collision.[5]

[5]The timing of readout chain is adjusted on module-by-module basis by a calibration algorithm in standalone SCT run. The fine tuning is done with tracks from collisions in a dedicated timing scan, usually at the beginning of each year. The time bin distribution is also checked during the data quality assessment and can be re-optimised if needed.

The resulting hit patterns can give limited information about timing, noise or background levels. To reduce the data size, some hit patterns can be suppressed, i.e. modules can be configured not to transfer them to the data acquisition. At the beginning of the LHC Run 1, the SCT readout chain was configured in the any-hit mode (accepting hits with pattern 1XX, X1X and XX1) and from 2011 in the level mode (X1X). Thanks to the available bandwidth and low occupancy, it was not necessary to switch to the edge mode (01X) during Run 1.[6]

Background tagging in SCT is based on the idea that when a particle from halo of the incoming bunch passes through a module in distance z from the IP, it gives a hit earlier than collision products from the IP. The time difference is roughly $\Delta t \simeq 2z/c$. The endcap position of $0.85\,\text{m} \leq z \leq 2.72\,\text{m}$ leads to a signal time difference of $6\,\text{ns} \leq \Delta t \leq 18\,\text{ns}$, with the largest difference in the outermost endcap disks. The number and distribution of these early hits in endcaps can then imply background conditions.

It is also useful to define an asymmetry of early hits in z as

$$A_z = \frac{N_{z+} - N_{z-}}{N_{z+} + N_{z-}},$$

where N_{z+} and N_{z-} are the numbers of early hits at positive and negative z, respectively. To flag events with higher background content, only the z asymmetry of early hits in disks 7 and 8 is used. The asymmetry in disks 9 cannot be used because a quarter of modules on disk 9, side C had to be disabled because of a cooling loop leak since the beginning of the SCT operation.

An example of early SCT hits in the UnpairedIso BG for a run with high background content is shown in Figure 6.2. The asymmetry of hits is clearly visible and the higher number of early hits on side A (positive z) can be explained by the halo of beam 1 (clockwise). This run (ATLAS run 213816, LHC fill 3252) from November 2$^{\text{nd}}$ 2012 had an unusually high levels of BIB and the background was later correlated with a quench of the triplet magnet on side A of ATLAS and a consequent increase of residual gas pressure in the beampipe [114].

The asymmetry of early hits for the same run is plotted in Figure 6.3. The rate of events with asymmetry $A_z > 0.9$ in disks 7 and 8 per LB is plotted in Figure 6.4 (left), together with run 214523 (from November 14$^{\text{th}}$, LHC fill 3286) which is an example of run with relatively low level of background with few short spikes.

[6] However, in the middle of 2016 it was necessary to reduce the amount of data read out and change to 01X mode because of higher link occupancy when running with 25 ns bunch spacing. Therefore, the algorithm described in this section cannot be used any more.

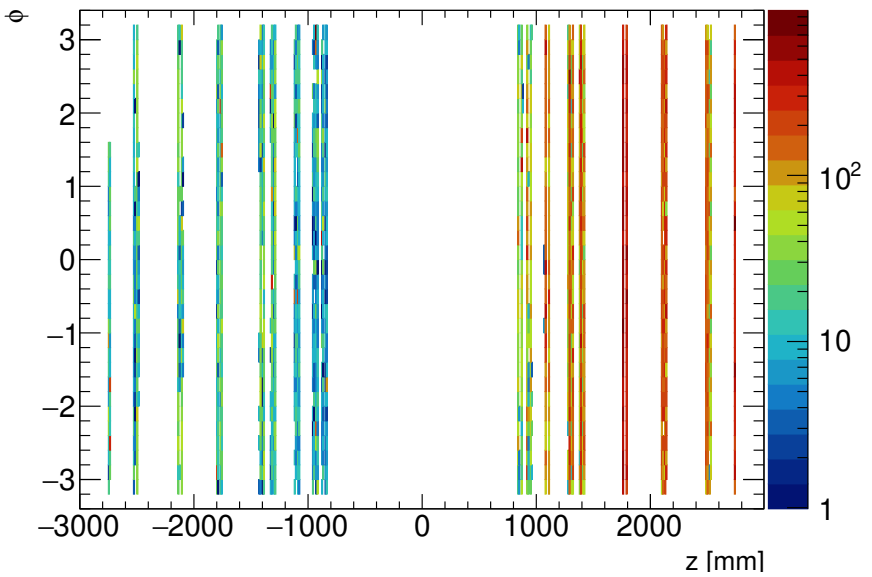

Figure 6.2: A map of SCT early hits in $z - \phi$ plane (run 213816, LB 217). The hits on a quarter of the leftmost endcap are missing because this modules are permanently disabled.

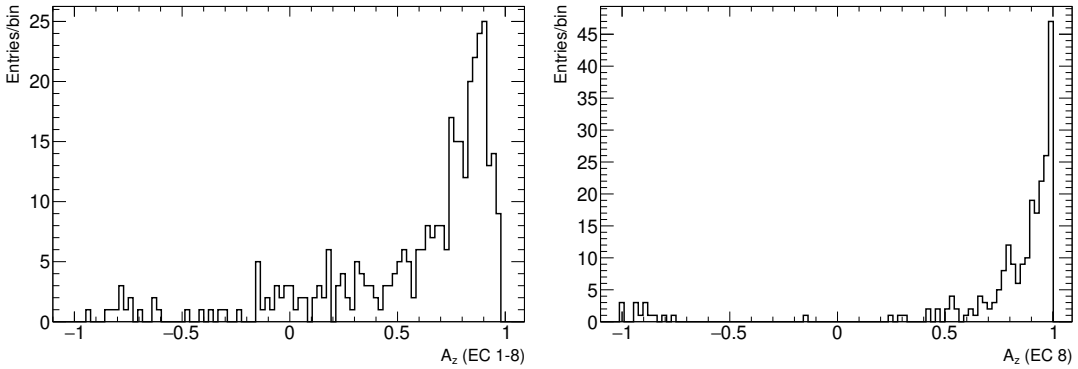

Figure 6.3: The asymmetry of SCT early hits in run 213816: hits in endcap disks 1-8 (left) and hits in disks 8 only (right).

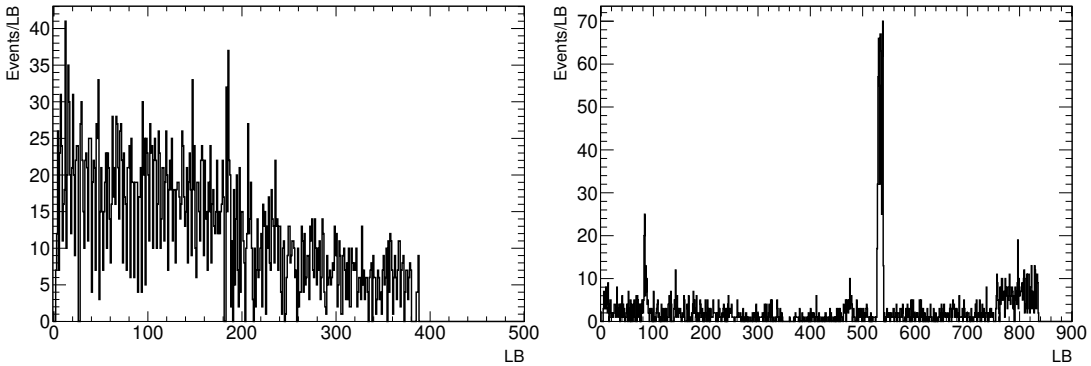

Figure 6.4: Rate of events with asymmetry $A_z > 0.9$ in disks 7 and 8 per LB in the high-background run 213816 (left), compared to run 214523 (right). The spikes in run 214523 coincide with beam optimisation done by the LHC operators before stable beams (LB 92) and with moving the beam to achieve higher luminosity during collisions (LB 520).

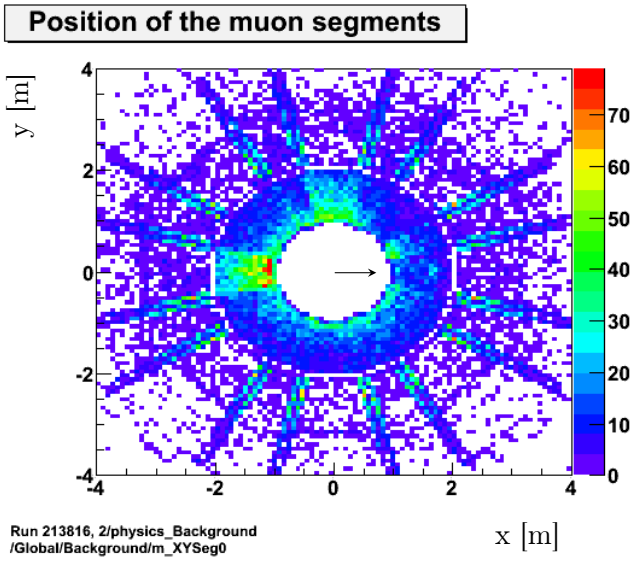

Figure 6.5: Position of the muon segments in CSC and MDT in unpaired bunches in high-background run 213816. The arrow shows a direction towards the centre of LHC ring.

BIB identification with muon chambers and calorimeters

The BIB at larger radii can be studied with calorimeters and the Muon Spectrometer. The LAr barrel covers a radial range of 1.5 to 2.0 m what corresponds to the CSC endcap wheels. The Tile calorimeter with radius 2.2 to 4.3 m overlaps with the inner endcap wheel of MDT. In addition, the MBTS wheels installed on the front plate of the calorimeter endcaps can be used for background monitoring.

The monitored muon observables include the time and position of the muon segments in CSC and MDT. An example of distribution of muon segments with a direction nearly parallel to the beampipe reconstructed in run 213816 is shown in Figure 6.5. The regions with more clusters are negative x (direction outside of the LHC ring) and positive y coordinates (upwards). This reflects the geometry of the LHC tunnel: the beampipe is installed about 95 cm from the bottom of the LHC tunnel which is 3 m high.

The timing of calorimeter clusters in LAr or Tile calorimeter was found to be useful for background monitoring as well. The halo muons passing nearly parallel to the beampipe give early signals, similar to those described in the SCT section above. The expected cluster time for background is

$$t_{\text{expected}} = -\frac{(\pm z + \sqrt{z^2 + r^2})}{c},$$

where z and r are the cluster coordinates. The $\pm$ sign depends on the direction of the background muon (incoming or outgoing) and can be reconstructed from the time and position of the muon segment matched with the cluster in ϕ. The jets from collisions in IP are expected at $t = 0$, while fake jets originating from background muons have a characteristic banana-shaped distribution in the $(\eta - t)$ plot. An example is shown in Figure 6.6 (top left), together with the same plot for jets tagged as fake based on their shape and missing associated tracks in the ID (top right). The curvature of the pattern depends on the calorimeter radius; the

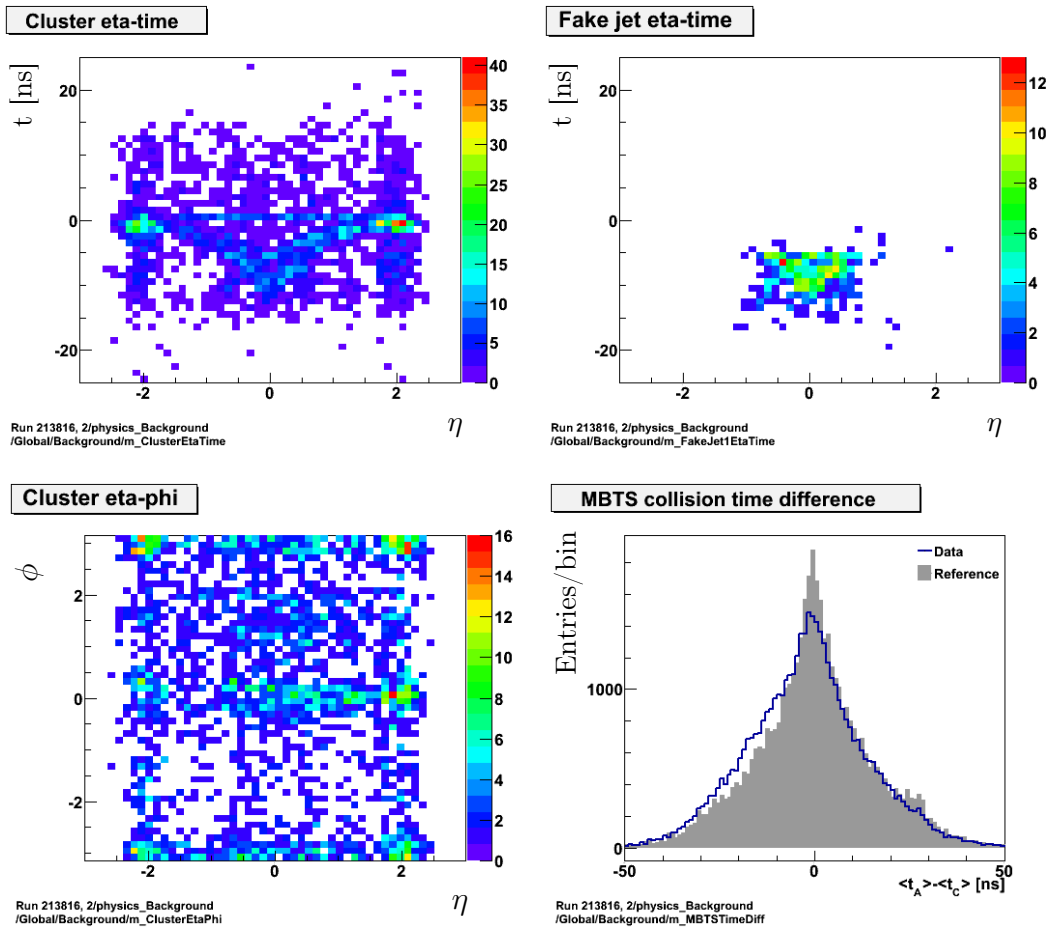

Figure 6.6: Background offline monitoring plots for run 213816: $\eta-$time of calorimeter clusters (top left) and of fake jets (top right), $\eta-\phi$ of calorimeter clusters (bottom left) and time difference of MBTS side A and side C hits.

larger curvature contains clusters in the Tile calorimeter and the smaller curvature is from LAr. Also shown in Figure 6.6 (bottom right) is the time difference of MBTS signals on side A and side C. For particles from IP this is expected to be close to zero, while hits with larger negative (positive) difference signals an incoming halo of beam 1 (beam 2). Other calorimeter observables include the calorimeter cluster shape, signal shape of of LAr cells or the number of cells with poor signal shape.

Conclusions

The flavour-changing neutral currents played an important role in the construction of the Standard Model of particle physics. They are forbidden at tree level and only proceed at loop level, hence the decays mediated by them are rare and sensitive to potential contributions from physics beyond the Standard Model. One group of such processes includes the decays of hadrons containing the b quark that can be described as $b \to s\ell^+\ell^-$ transitions at the quark level.

The angular analysis of one of these decays, $B^0 \to K^*(892)\mu^+\mu^-$, in the final state with $K^*(892) \to K^+\pi^-$, is described in this thesis. The study used a data sample from pp collisions at centre-of-mass energy of 8 TeV corresponding to an integrated luminosity of $20.3\,\text{fb}^{-1}$, which was recorded by the ATLAS detector in 2012. An extended unbinned maximum-likelihood fit was used to measure the CP-averaged angular observables F_L, S_3, S_4, S_5, S_7 and S_8 and the corresponding form-factor independent observables P_1, P_4', P_5', P_6' and P_8'. The measurements were done in six bins of the dimuon mass squared in the region $0.04 < q^2 < 6\,\text{GeV}^2$, where three bins overlapped.

In general, the results are in good agreement with the available theoretical predictions for Standard Model. The most significant deviations are observed for parameters P_4', P_5' and P_8' in one q^2 bin each. The measured values of P_4' and P_5' in bin $q^2 \in [4.0, 6.0]\,\text{GeV}^2$ are approximately 2.7 standard deviations away from the calculation by Descotes-Genon et al. [86] and a deviation of $1.9\,\sigma$ from the same prediction is observed for P_8' in bin $q^2 \in [2.0, 4.0]\,\text{GeV}^2$. The differences are less significant for all other bins and theoretical predictions. The measurements are compatible with those published by the BaBar [40], Belle [7, 10], CMS [9, 13] and LHCb [12] collaborations. The P_5' deviation in $q^2 \in [4.0, 6.0]\,\text{GeV}^2$ is consistent with the one reported by the LHCb collaboration in Ref. [12]. However, the presented results are statistically limited and measurements with a larger dataset collected during the LHC Run 2 are planned. Improvements of the analysis methods are foreseen as well, e.g. further studies of the observed background which has the highest contribution to the systematic uncertainty and use of machine learning techniques for selection of the signal candidates.

The quality of collected data relies on the high availability and efficiency of all ATLAS subdetectors, data acquisition and trigger. Two last chapters summarised author's contribution to these topics. The performance of the ATLAS Semiconductor Tracker during LHC Run 1 and changes induced by the radiation damage were outlined briefly. This section also included the results obtained during testing of prototypes for the ATLAS strip tracker upgrade, ITk. Finally, the monitoring of non-collision background which has been implemented as part of this work was described.

Bibliography

[1] HFLAV Collaboration, Y. Amhis et al., *Averages of b-hadron, c-hadron, and τ-lepton properties as of summer 2016*, Eur. Phys. J. C **77** (2017) 895, arXiv:1612.07233 [hep-ex].

[2] LHCb Collaboration, R. Aaij et al., *Test of lepton universality using $B^+ \to K^+\ell^+\ell^-$ decays*, Phys. Rev. Lett. **113** (2014) 151601, arXiv:1406.6482 [hep-ex].

[3] LHCb Collaboration, R. Aaij et al., *Test of lepton universality with $B^0 \to K^{*0}\ell^+\ell^-$ decays*, JHEP **08** (2017) 055, arXiv:1705.05802 [hep-ex].

[4] LHCb Collaboration, R. Aaij et al., *Measurement of the ratio of branching fractions $\mathcal{B}(B_c^+ \to J/\psi\tau^+\nu_\tau)/\mathcal{B}(B_c^+ \to J/\psi\mu^+\nu_\mu)$*, Phys. Rev. Lett. **120** (2018) 121801, arXiv:1711.05623 [hep-ex].

[5] LHCb Collaboration, R. Aaij et al., *Angular analysis and differential branching fraction of the decay $B_s^0 \to \phi\mu^+\mu^-$*, JHEP **09** (2015) 179, arXiv:1506.08777 [hep-ex].

[6] BaBar Collaboration, B. Aubert et al., *Angular Distributions in the Decays $B \to K^* l^+ l^-$*, Phys. Rev. D **79** (2009) 031102, arXiv:0804.4412 [hep-ex].

[7] Belle Collaboration, J.-T. Wei et al., *Measurement of the Differential Branching Fraction and Forward-Backward Asymmetry for $B \to K^{(*)} l^+ l^-$*, Phys. Rev. Lett. **103** (2009) 171801, arXiv:0904.0770 [hep-ex].

[8] CDF Collaboration, T. Aaltonen et al., *Measurements of the Angular Distributions in the Decays $B \to K^{(*)}\mu^+\mu^-$ at CDF*, Phys. Rev. Lett. **108** (2012) 081807, arXiv:1108.0695 [hep-ex].

[9] CMS Collaboration, V. Khachatryan et al., *Angular analysis of the decay $B^0 \to K^{*0}\mu\mu$ from pp collisions at $\sqrt{s} = 8$ TeV*, Phys. Lett. B **753** (2016) 424, arXiv:1507.08126 [hep-ex].

[10] Belle Collaboration, A. Abdesselam et al., *Angular analysis of $B^0 \to K^*(892)^0\ell^+\ell^-$*, arXiv:1604.04042 [hep-ex].

[11] Belle Collaboration, S. Wehle et al., *Lepton-Flavor-Dependent Angular Analysis of $B \to K^*\ell^+\ell^-$*, Phys. Rev. Lett. **118** (2017) 111801, arXiv:1612.05014 [hep-ex].

[12] LHCb Collaboration, R. Aaij et al., *Angular analysis of the $B^0 \to K^{*0}\mu^+\mu^-$ decay using 3 fb^{-1} of integrated luminosity*, JHEP **02** (2016) 104, arXiv:1512.04442 [hep-ex].

[13] CMS Collaboration, A. M. Sirunyan et al., *Measurement of angular parameters from the decay $\mathrm{B}^0 \to \mathrm{K}^{*0}\mu^+\mu^-$ in proton-proton collisions at $\sqrt{s} = 8$ TeV*, Phys. Lett. B **781** (2018) 517, arXiv:1710.02846 [hep-ex].

[14] W. Altmannshofer, P. Stangl and D. M. Straub, *Interpreting Hints for Lepton Flavor Universality Violation*, Phys. Rev. **D96** (2017) 055008, arXiv:1704.05435 [hep-ph].

[15] B. Capdevila, A. Crivellin, S. Descotes-Genon, J. Matias et al., *Patterns of New Physics in $b \to s\ell^+\ell^-$ transitions in the light of recent data*, *JHEP* **01** (2018) 093, arXiv:1704.05340 [hep-ph].

[16] ATLAS Collaboration, M. Aaboud et al., *Angular analysis of $B_d^0 \to K^*\mu^+\mu^-$ decays in pp collisions at $\sqrt{s} = 8$ TeV with the ATLAS detector*, *JHEP* **10** (2018) 047, arXiv:1805.04000 [hep-ex].

[17] J. Hořejší, *Fundamentals of Electroweak Theory*. Karolinum Press, 2002.

[18] F. Halzen and A. Martin, *Quarks and Leptons: An Introductory Course in Modern Particle Physics*. Wiley, 1984.

[19] Belle and BaBar Collaborations, A. J. Bevan et al., *The Physics of the B Factories*, *Eur. Phys. J. C* **74** (2014) 3026, arXiv:1406.6311 [hep-ex].

[20] Particle Data Group, C. Patrignani et al., *Review of Particle Physics*, *Chin. Phys. C* **40** (2016) 100001, http://pdg.lbl.gov.

[21] N. Cabibbo, *Unitary Symmetry and Leptonic Decays*, *Phys. Rev. Lett.* **10** (1963) 531–533.

[22] M. Kobayashi and T. Maskawa, *CP Violation in the Renormalizable Theory of Weak Interaction*, *Prog. Theor. Phys.* **49** (1973) 652–657.

[23] CKMfitter Group, J. Charles et al., *CP violation and the CKM matrix: assessing the impact of the asymmetric B factories*, *Eur. Phys. J. C* **41** (2005) 1–131, arXiv:hep-ph/0406184 [hep-ph], updated results and plots available at http://ckmfitter.in2p3.fr.

[24] G. Buchalla, A. J. Buras and M. E. Lautenbacher, *Weak decays beyond leading logarithms*, *Rev. Mod. Phys.* **68** (1996) 1125–1144, arXiv:hep-ph/9512380 [hep-ph].

[25] K. G. Chetyrkin, M. Misiak and M. Munz, *Weak radiative B meson decay beyond leading logarithms*, *Phys. Lett. B* **400** (1997) 206–219, arXiv:hep-ph/9612313 [hep-ph], erratum *Phys. Lett. B* **425** (1998) 414.

[26] T. Blake, T. Gershon and G. Hiller, *Rare b hadron decays at the LHC*, *Ann. Rev. Nucl. Part. Sci.* **65** (2015) 113–143, arXiv:1501.03309 [hep-ex].

[27] R. R. Horgan, Z. Liu, S. Meinel and M. Wingate, *Lattice QCD calculation of form factors describing the rare decays $B \to K^*\ell^+\ell^-$ and $B_s \to \phi\ell^+\ell^-$*, *Phys. Rev. D* **89** (2014) 094501, arXiv:1310.3722 [hep-lat].

[28] A. Bharucha, D. M. Straub and R. Zwicky, *$B \to V\ell^+\ell^-$ in the Standard Model from light-cone sum rules*, *JHEP* **08** (2016) 098, arXiv:1503.05534 [hep-ph].

[29] BaBar Collaboration, B. Aubert et al., *Evidence for the rare decay $B \to K^*\ell^+\ell^-$ and measurement of the $B \to K\ell^+\ell^-$ branching fraction*, *Phys. Rev. Lett.* **91** (2003) 221802, arXiv:hep-ex/0308042 [hep-ex].

[30] W. Altmannshofer et al., *Symmetries and Asymmetries of $B \to K^*\mu^+\mu^-$ Decays in the Standard Model and Beyond*, *JHEP* **01** (2009) 019, arXiv:0811.1214 [hep-ph].

[31] M. Beneke, T. Feldmann and D. Seidel, *Systematic approach to exclusive $B \to V\ell^+\ell^-$, $V\gamma$ decays*, Nucl. Phys. B **612** (2001) 25–58, arXiv:hep-ph/0106067 [hep-ph].

[32] A. Ali, P. Ball, L. T. Handoko and G. Hiller, *A Comparative study of the decays $B \to (K, K^*)\ell^+\ell^-$ in standard model and supersymmetric theories*, Phys. Rev. D **61** (2000) 074024, arXiv:hep-ph/9910221 [hep-ph].

[33] LHCb Collaboration, R. Aaij et al., *Observation of a resonance in $B^+ \to K^+\mu^+\mu^-$ decays at low recoil*, Phys. Rev. Lett. **111** (2013) 112003, arXiv:1307.7595 [hep-ex].

[34] LHCb Collaboration, R. Aaij et al., *Differential branching fraction and angular analysis of the decay $B^0 \to K^{*0}\mu^+\mu^-$*, JHEP **08** (2013) 131, arXiv:1304.6325 [hep-ex].

[35] LHCb Collaboration, R. Aaij et al., *Measurement of Form-Factor-Independent Observables in the Decay $B^0 \to K^{*0}\mu^+\mu^-$*, Phys. Rev. Lett. **111** (2013) 191801, arXiv:1308.1707 [hep-ex].

[36] J. Matias, F. Mescia, M. Ramon and J. Virto, *Complete Anatomy of $\bar{B}_d \to \bar{K}^{*0}(\to K\pi)l^+l^-$ and its angular distribution*, JHEP **04** (2012) 104, arXiv:1202.4266 [hep-ph].

[37] S. Descotes-Genon, J. Matias, M. Ramon and J. Virto, *Implications from clean observables for the binned analysis of $B \to K^*\mu^+\mu^-$ at large recoil*, JHEP **01** (2013) 048, arXiv:1207.2753 [hep-ph].

[38] M. De Cian, *Track reconstruction efficiency and analysis of $B^0 \to K^{*0}\mu^+\mu^-$ at the LHCb experiment*, Ph.D. thesis, University of Zurich, Faculty of Science, 2013. http://doi.org/10.5167/uzh-85745.

[39] CMS Collaboration, S. Chatrchyan et al., *Angular analysis and branching fraction measurement of the decay $B^0 \to K^{*0}\mu^+\mu^-$*, Phys. Lett. B **727** (2013) 77–100, arXiv:1308.3409 [hep-ex].

[40] BaBar Collaboration, J. P. Lees et al., *Measurement of angular asymmetries in the decays $B \to K^*\ell^+\ell^-$*, Phys. Rev. D **93** (2016) 052015, arXiv:1508.07960 [hep-ex].

[41] L.-S. Geng, B. Grinstein, S. Jäger, J. Martin Camalich et al., *Towards the discovery of new physics with lepton-universality ratios of $b \to s\ell\ell$ decays*, Phys. Rev. D **96** (2017) 093006, arXiv:1704.05446 [hep-ph].

[42] L. Evans and P. Bryant, eds., *LHC Machine*, JINST **3** (2008) S08001.

[43] M. Lamont, *Status of the LHC*, J. Phys. Conf. Ser. **455** (2013) 012001.

[44] R. Steerenberg, *Introduction, 8th LHC Operations Evian Workshop*, presentation slides retrieved from http://indico.cern.ch/event/663598/contributions/2740005/attachments/1573746/2484270/rs20171126_Intro_Evian-2017.pdf.

[45] G. Apollinari et al., eds., *High-Luminosity Large Hadron Collider (HL-LHC): Technical Design Report V. 0.1*. CERN Yellow Reports. CERN, Geneva, 2017, DOI: 10.23731/CYRM-2017-004.

[46] ATLAS Collaboration, G. Aad et al., *The ATLAS Experiment at the CERN Large Hadron Collider*, *JINST* **3** (2008) S08003.

[47] ATLAS Collaboration, G. Aad et al., *Track Reconstruction Performance of the ATLAS Inner Detector at* $\sqrt{s} = 13$ *TeV*, ATL-PHYS-PUB-2015-018, http://cds.cern.ch/record/2037683.

[48] ATLAS Collaboration, G. Aad et al., *Improved luminosity determination in pp collisions at* $\sqrt{s} = 7$ *TeV using the ATLAS detector at the LHC*, *Eur. Phys. J. C* **73** (2013) 2518, arXiv:1302.4393 [hep-ex].

[49] ATLAS Collaboration, G. Aad et al., *Performance of the ATLAS Trigger System in 2010*, *Eur. Phys. J. C* **72** (2012) 1849.

[50] ATLAS Collaboration, G. Aad et al., *Performance of the ATLAS muon trigger in pp collisions at* $\sqrt{s} = 8$ *TeV*, *Eur. Phys. J. C* **75** (2015) 120.

[51] ATLAS Collaboration, G. Aad et al., *ATLAS Computing: technical design report*, Tech. Rep. CERN-LHCC-2005-022, CERN, Geneva, 2005, http://cds.cern.ch/record/837738.

[52] R. Brun and F. Rademakers, *ROOT — An object oriented data analysis framework*, in *Proceedings AIHENP'96 Workshop, Lausanne, Sep. 1996*, *Nucl. Instrum. Meth. A* **389** (1997) 81–86. See also http://root.cern.ch/.

[53] C. Eck et al., eds., *LHC computing Grid: Technical Design Report*, tech. rep., CERN, Geneva, 2005, https://cds.cern.ch/record/840543.

[54] T. Maeno, *PanDA: distributed production and distributed analysis system for ATLAS*, *J. Phys. Conf. Ser.* **119** (2008) 062036.

[55] ATLAS Collaboration, G. Aad et al., *The ATLAS Simulation Infrastructure*, *Eur. Phys. J. C* **70** (2010) 823–874.

[56] T. Sjöstrand, S. Mrenna and P. Skands, *A Brief Introduction to PYTHIA 8.1*, *Comput. Phys. Commun.* **178** (2008) 852, arXiv:0710.3820 [hep-ph].

[57] M. Smizanska, *PythiaB, an interface to Pythia6 dedicated to simulation of beauty events*, Tech. Rep. ATL-COM-PHYS-2003-038, CERN, 2003, https://cds.cern.ch/record/681440. Available for ATLAS members only.

[58] D. J. Lange, *The EvtGen particle decay simulation package*, *Nucl. Instrum. Meth. A* **462** (2001) 152, See also http://evtgen.hepforge.org/.

[59] GEANT4 Collaboration, S. Agostinelli et al., *GEANT4: A simulation toolkit*, *Nucl. Instrum. Meth. A* **506** (2003) 250.

[60] ATLAS Collaboration, M. Aaboud et al., *Reconstruction of primary vertices at the ATLAS experiment in Run 1 proton-proton collisions at the LHC*, *Eur. Phys. J. C* **77** (2017) 332, arXiv:1611.10235 [physics.ins-det].

[61] ATLAS Collaboration, G. Aad et al., *Measurement of the muon reconstruction performance of the ATLAS detector using 2011 and 2012 LHC proton-proton collision data*, *Eur. Phys. J. C* **74** (2014) 3130.

[62] ATLAS Collaboration, G. Aad et al., *Letter of Intent for the Phase-I Upgrade of the ATLAS Experiment*, Tech. Rep. CERN-LHCC-2011-012, CERN, Geneva, 2011, http://cds.cern.ch/record/1402470.

[63] ATLAS Collaboration, G. Aad et al., *Letter of Intent for the Phase-II Upgrade of the ATLAS Experiment*, Tech. Rep. CERN-LHCC-2012-022, CERN, Geneva, 2012, http://cds.cern.ch/record/1502664.

[64] *ATLAS public results: Impact parameter resolution*, https://atlas.web.cern.ch/Atlas/GROUPS/PHYSICS/PLOTS/IDTR-2015-007/.

[65] ATLAS Collaboration, G. Aad et al., *Technical Design Report for the ATLAS Inner Tracker Strip Detector*, Tech. Rep. CERN-LHCC-2017-005, CERN, Geneva, 2017, http://cds.cern.ch/record/2257755.

[66] ATLAS Collaboration, G. Aad et al., *Technical Design Report for the ATLAS Inner Tracker Pixel Detector*, Tech. Rep. CERN-LHCC-2017-021, CERN, Geneva, 2017, https://cds.cern.ch/record/2285585.

[67] ATLAS Collaboration, M. Aaboud et al., *A High-Granularity Timing Detector for the ATLAS Phase-II Upgrade*, Tech. Rep. CERN-LHCC-2018-023, CERN, Geneva, 2018, http://cds.cern.ch/record/2623663.

[68] A. J. Bevan, M. Bona, I. Carli, P. Jussel et al., *Angular analysis of $B_d^0 \to K^{*0}\mu^+\mu^-$ decay with 2012 data (Backup note)*, Tech. Rep. ATL-COM-PHYS-2014-898, CERN, Geneva, Jul, 2014, https://cds.cern.ch/record/1745005. Available for ATLAS members only.

[69] A. J. Bevan, P. Reznicek, E. Kneringer, T. Nooney et al., *Backgrounds for the angular analysis of $B_d^0 \to K^{*0}\mu^+\mu^-$ using 2012 data from ATLAS*, Tech. Rep. ATL-COM-PHYS-2015-1368, CERN, Geneva, Nov, 2015, https://cds.cern.ch/record/2066759. Available for ATLAS members only.

[70] A. J. Bevan, P. Reznicek, T. Nooney and I. Carli, *Angular analysis of $B_d^0 \to K^{*0}\mu^+\mu^-$ (angle definition summary)*, Tech. Rep. ATL-COM-PHYS-2018-260, CERN, Geneva, Mar, 2018, https://cds.cern.ch/record/2309783. Available for ATLAS members only.

[71] ATLAS Collaboration, M. Aaboud et al., *Luminosity determination in pp collisions at $\sqrt{s} = 8$ TeV using the ATLAS detector at the LHC*, *Eur. Phys. J. C* **76** (2016) 653, arXiv:1608.03953 [hep-ex].

[72] ATLAS Collaboration, G. Aad et al., *ATLAS Run 1 Pythia8 tunes*, Tech. Rep. ATL-PHYS-PUB-2014-021, CERN, 2014, https://cds.cern.ch/record/1966419.

[73] E. Barberio and Z. Was, *PHOTOS: A Universal Monte Carlo for QED radiative corrections*, *Comput. Phys. Commun.* **79** (1994) 291–308.

[74] ATLAS Collaboration, M. Aaboud et al., *Study of the rare decays of B_s^0 and B^0 into muon pairs from data collected during the LHC Run 1 with the ATLAS detector*, *Eur. Phys. J. C* **76** (2016) 513.

[75] A. Usanova, *Analysis of $B_d^0 \to K^{*0}\mu^+\mu^-$ decay with the ATLAS experiment*, Ph.D. thesis, Innsbruck University, 2014. http://diglib.uibk.ac.at/ulbtirolhs/content/titleinfo/233516.

[76] C. Anastopoulos et al., *Physics analysis tools for beauty physics in ATLAS*, in *Proceedings, 16th International Conference on Computing in High Energy and Nuclear Physics*, *J. Phys. Conf. Ser.* **119** (2008) 032003.

[77] P. Bernat, *Architecture and Performance of the Inner Detector Trigger of the ATLAS detector*, Tech. Rep. ATL-DAQ-PROC-2012-032, CERN, Geneva, 2012, https://cds.cern.ch/record/1458060.

[78] ATLAS Collaboration, G. Aad et al., *Measurement of the CP-violating phase ϕ_s and the B_s^0 meson decay width difference with $B_s^0 \to J/\psi\phi$ decays in ATLAS*, *JHEP* **08** (2016) 147, arXiv:1601.03297 [hep-ex].

[79] A. E. Barton, *Looking for new physics in the $B_s^0 \to J/\psi\phi$ decay*, Ph.D. thesis, Lancaster University, 2013. https://cds.cern.ch/record/1956688.

[80] W. Verkerke and D. Kirkby, *The RooFit toolkit for data modeling*, in *Statistical Problems in Particle Physics, Astrophysics and Cosmology*, *eConf* **C0303241** (2003) 186–189, arXiv:physics/0306116 [physics.data-an].

[81] G. Punzi, *Comments on likelihood fits with variable resolution*, in *Statistical problems in particle physics, astrophysics and cosmology, eConf* **C030908** (2003) 235–237, arXiv:physics/0401045 [physics.data-an].

[82] CDF Collaboration, T. Aaltonen et al., *Measurement of the Forward-Backward Asymmetry in the $B \to K^{(*)}\mu^+\mu^-$ Decay and First Observation of the $B_s^0 \to \phi\mu^+\mu^-$ Decay*, *Phys. Rev. Lett.* **106** (2011) 161801, arXiv:1101.1028 [hep-ex].

[83] LHCb Collaboration, R. Aaij et al., *Measurement of the isospin asymmetry in $B \to K^{(*)}\mu^+\mu^-$ decays*, *JHEP* **07** (2012) 133, arXiv:1205.3422 [hep-ex].

[84] M. Aleksa, F. Bergsma, P. A. Giudici, A. Kehrli et al., *Measurement of the atlas solenoid magnetic field*, *JINST* **3** (2008) P04003.

[85] ATLAS Collaboration, *Alignment of the ATLAS Inner Detector and its Performance in 2012*, Tech. Rep. ATLAS-CONF-2014-047, CERN, Geneva, Jul, 2014, http://cds.cern.ch/record/1741021.

[86] S. Descotes-Genon, L. Hofer, J. Matias and J. Virto, *On the impact of power corrections in the prediction of $B \to K^*\mu^+\mu^-$ observables*, *JHEP* **12** (2014) 125, arXiv:1407.8526 [hep-ph].

[87] S. Jäger and J. Martin Camalich, *Reassessing the discovery potential of the $B \to K^*\ell^+\ell^-$ decays in the large-recoil region: SM challenges and BSM opportunities*, *Phys. Rev. D* **93** (2016) 014028, arXiv:1412.3183 [hep-ph].

[88] M. Ciuchini et al., *$B \to K^*\ell^+\ell^-$ decays at large recoil in the Standard Model: a theoretical reappraisal*, *JHEP* **06** (2016) 116, arXiv:1512.07157 [hep-ph].

[89] LHCb Collaboration, R. Aaij et al., *Measurement of the $B^0 \to K^{*0}e^+e^-$ branching fraction at low dilepton mass*, *JHEP* **05** (2013) 159, arXiv:1304.3035 [hep-ex].

[90] LHCb Collaboration, R. Aaij et al., *Angular analysis of the $B^0 \to K^{*0}e^+e^-$ decay in the low-q^2 region*, *JHEP* **04** (2015) 064, arXiv:1501.03038 [hep-ex].

[91] C. Grupen and B. Shwartz, *Particle detectors*. Cambridge University Press, 2008.

[92] ATLAS Collaboration, G. Aad et al., *Operation and performance of the ATLAS semiconductor tracker*, *JINST* **9** (2014) P08009.

[93] A. Abdesselam et al., *The barrel modules of the ATLAS semiconductor tracker*, *Nucl. Instrum. Meth. A* **568** (2006) 642–671, https://cds.cern.ch/record/974073.

[94] F. Campabadal et al., *Design and performance of the ABCD3TA ASIC for readout of silicon strip detectors in the ATLAS semiconductor tracker*, *Nucl. Instrum. Meth. A* **552** (2005) 292–328.

[95] B. M. Demirkoz, *Construction and Performance of the ATLAS SCT Barrels and Cosmic Tests*, Ph.D. thesis, Oxford University, 2007. https://cds.cern.ch/record/1078223.

[96] M. Moll, *Radiation damage in silicon particle detectors*, Ph.D. thesis, University of Hamburg, 1999. https://mmoll.web.cern.ch/mmoll/thesis.

[97] O. Krasel, *Charge collection in irradiated silicon detectors*, Ph.D. thesis, University of Dortmund, 2004. http://doi.org/10.17877/DE290R-14839.

[98] R. Harper, *Radiation Damage studies of the silicon microstrip detectors and finding an intermediate mass Higgs Boson at ATLAS*, Ph.D. thesis, University of Sheffield, 2001.

[99] *SCT public results*, https://atlas.web.cern.ch/Atlas/GROUPS/PHYSICS/PLOTS/SCT-2018-002/.

[100] *SCT public results*, https://atlas.web.cern.ch/Atlas/GROUPS/PHYSICS/PLOTS/SCT-2016-002/.

[101] *SCT public results*, https://atlas.web.cern.ch/Atlas/GROUPS/PHYSICS/PLOTS/SCT-2016-001/.

[102] *SCT public results*, https://atlas.web.cern.ch/Atlas/GROUPS/PHYSICS/PLOTS/SCT-2017-004/.

[103] *SCT public results*, https://atlas.web.cern.ch/Atlas/GROUPS/PHYSICS/PLOTS/SCT-2018-001/.

[104] *ATLAS Run-2 Detector Status*, https://twiki.cern.ch/twiki/bin/view/AtlasPublic/ApprovedPlotsATLASDetector.

[105] *ATLAS Data Quality Information*, https://twiki.cern.ch/twiki/bin/view/AtlasPublic/RunStatsPublicResults2010.

[106] F. Anghinolfi, Dabrowski, N. Dressnandt, J. Kaplon et al., *Performance of the ABCN-25 readout chip for the ATLAS Inner Detector Upgrade*, in *Topical Workshop on Electronics for Particle Physics,*

[107] W. Lu, F. Anghinolfi, L. Cheng, J. De Witt et al., *Development of the ABCStar front-end chip for the ATLAS silicon strip upgrade*, in *Topical Workshop on Electronics for Particle Physics, JINST* **12** (2017) C04017.

[108] C. David, *A new strips tracker for the upgraded ATLAS ITk detector*, in *11th International Conference on Position Sensitive Detectors, JINST* **13** (2018) C01003.

[109] S. Kuehn et al., *Prototyping of petalets for the Phase-II Upgrade of the silicon strip tracking detector of the ATLAS Experiment*, *JINST* **13** (2018) T03004, arXiv:1711.01594 [physics.ins-det].

[110] M. Ullan et al., *Embedded pitch adapters: A high-yield interconnection solution for strip sensors*, in *10th International 'Hiroshima' Symposium on the Development and Application of Semiconductor Tracking Detectors*, *Nucl. Instrum. Meth.* **A831** (2016) 221–228.

[111] D. Nelson, *HSIO Development Platform User Guide - Version C02*, http://www.slac.stanford.edu/∼djn/Atlas/hsio/.

[112] ATLAS Collaboration, *Non-collision backgrounds as measured by the ATLAS detector during the 2010 proton-proton run*, ATLAS-CONF-2011-137, https://cds.cern.ch/record/1383840.

[113] ATLAS Collaboration, G. Aad et al., *Characterisation and mitigation of beam-induced backgrounds observed in the ATLAS detector during the 2011 proton-proton run*, *JINST* **8** (2013) P07004, arXiv:1303.0223 [hep-ex].

[114] ATLAS Collaboration, G. Aad et al., *Beam-induced and cosmic-ray backgrounds observed in the ATLAS detector during the LHC 2012 proton-proton running period*, *JINST* **11** (2016) P05013.

[115] C. Ohm and T. Pauly, *The ATLAS beam pick-up based timing system*, in *Technology and instrumentation in particle physics 2009*, *Nucl. Instrum. Meth. A* **623** (2010) 558–560, arXiv:0905.3648 [physics.ins-det].

List of Figures

List of Tables

List of Abbreviations

AFP ATLAS Forward Protons 45, 109

ALFA Absolute Luminosity For ATLAS 38, 109

BCID Bunch Crossing IDentifier 22, 93, 97, 98, 108, 109, 111

BCM Beam Conditions Monitor 29, 109, 110

BG bunch group 108–110

BIB Beam Induced Background 107, 110–112, 114

BOC Back-Of-Crate readout card 89, 92

BSM Beyond Standard Model 3, 10, 11, 20, 107

CSC Cathode Strip Chambers 33, 35, 114

CTP Central Trigger Processor 39, 41, 108, 109

DAC Digital-to-Analog Converter 101, 103

DAQ Data Acquisition System 89–92, 98

EF Event Filter 39–42, 57

FCal Forward Calorimeter 30, 32, 33

FCNC Flavour-Changing Neutral Currents 8, 9, 11

HEC Hadronic Endcap Calorimeter 30, 32

HLT High-Level Trigger 39, 40

IBL Insertable B-Layer 45, 99

ID Inner Detector 25, 26, 29, 31, 39, 41, 42, 45–47, 52, 57, 63, 66, 69, 99, 114

IP Interaction Point 25, 26, 33, 35–38, 41, 109

ITk Inner Tracker 46, 99

L1 Level 1 trigger 39, 41, 46, 47, 57, 58, 110, 111

L2 Level 2 trigger 39–41, 46, 57

LAr Liquid Argon Calorimeter 30, 31, 46, 114, 115

LUCID LUminosity Cerenkov Integrating Detector 37, 109

MBTS Minimum Bias Trigger Scintillators 38, 114, 115

MC Monte Carlo 43, 49–51, 57, 59, 60, 63, 65–67, 72, 133

MDT Monitored Drift Tubes 33–35, 41, 47, 114

MS Muon Spectrometer 25, 33, 34, 36, 41, 42, 45, 52, 57

PCB Printed-Circuit Board 27, 28, 100

PMT photomultiplier tube 32, 37, 38

QCD Quantum Chromodynamics 6, 9

ROD Readout-Driver Board 89, 91–93, 96, 98

RoI Region of Interest 39–41, 46, 47

RPC Resistive Plate Chambers 34, 35, 41

SCT SemiConductor Tracker 26, 28, 46, 87, 88, 107, 111, 112

SEU Single-Event Upset 92, 94, 97

SM Standard Model 3, 5, 6, 8–11, 20, 21, 25, 49, 50

TGC Thin Gap Chambers 34, 36, 41

TRT Transition Radiation Tracker 26, 28, 29, 46

TTC Trigger, Timing and Control 89, 92

VCSEL Vertical-Cavity Surface-Emitting Laser 89, 92

ZDC Zero Degree Calorimeter 37, 38, 109

A. Additional material for the $B^0 \to K^* \mu^+ \mu^-$ analysis

A.1 Datasets

The dataset included all runs in 2012 which had stable beams and a good run list was prepared by the detector and combined performance groups. This contains list of luminosity blocks for given runs that contain data without any major problems which would influence detector performance. The good run list used here is `data12_8TeV.periodAllYear_DetStatus-v61-pro14-02_DQDefects-00-01-00_PHYS_StandardGRL_All_Good.xml`
available at http://atlasdqm.web.cern.ch/atlasdqm/grlgen/

Both *Muons* and *Bphysics* trigger streams were processed, with the *Bphysics* stream present from run 202712 (during period B1, beginning of May 2012).

The following containers were processed:

- Muons stream:

data12_8TeV.periodA.physics_Muons.PhysCont.AOD.repro14_v02/
data12_8TeV.periodB.physics_Muons.PhysCont.AOD.repro14_v01/
data12_8TeV.periodC.physics_Muons.PhysCont.AOD.repro14_v01/
data12_8TeV.periodD.physics_Muons.PhysCont.AOD.repro14_v01/
data12_8TeV.periodE.physics_Muons.PhysCont.AOD.repro14_v01/
data12_8TeV.periodG.physics_Muons.PhysCont.AOD.repro14_v01/
data12_8TeV.periodH.physics_Muons.PhysCont.AOD.repro14_v01/
data12_8TeV.periodI.physics_Muons.PhysCont.AOD.t0pro14_v01/
data12_8TeV.periodJ.physics_Muons.PhysCont.AOD.t0pro14_v01/
data12_8TeV.periodL.physics_Muons.PhysCont.AOD.t0pro14_v01/

- Bphysics stream:

data12_8TeV.periodB.physics_Bphysics.PhysCont.AOD.repro14_v01/
data12_8TeV.periodC.physics_Bphysics.PhysCont.AOD.repro14_v01/
data12_8TeV.periodD.physics_Bphysics.PhysCont.AOD.repro14_v01/
data12_8TeV.periodE.physics_Bphysics.PhysCont.AOD.repro14_v01/
data12_8TeV.periodG.physics_Bphysics.PhysCont.AOD.repro14_v01/
data12_8TeV.periodH.physics_Bphysics.PhysCont.AOD.repro14_v01/
data12_8TeV.periodI.physics_Bphysics.PhysCont.AOD.repro14_v01/
data12_8TeV.periodJ.physics_Bphysics.PhysCont.AOD.repro14_v01/
data12_8TeV.periodL.physics_Bphysics.PhysCont.AOD.repro14_v01/

The MC simulated samples are listed in Tables A.1 and A.2.

Table A.1: MC simulated samples for signal and inclusive backgrounds $b\bar{b}$ and $c\bar{c}$. The table lists dataset numbers, used generator, numbers of requested and simulated events and the number of candidates passing the selection cuts described in Section 4.2, without trigger selection applied.

Process	Generator	Dataset	Size	Generated	Candidates	Events	Cand/Ev.	Note
$B_d \to K^*\mu^+\mu^-$	EvtGen, flat	208445	50M	49937978	5939872	5062537	1.173	
$B_d \to K^*\mu^+\mu^-$	EvtGen, SM	208446	5M	4992493	599041	510868	1.173	
$\overline{B_d} \to K^*\mu^+\mu^-$	EvtGen	208447	5M	4994494	594125	506593	1.173	
$B^0 \to K^+\pi^-\mu^+\mu^-$	EvtGen	208451	50M	19960379	216073	195251	1.107	
$b\bar{b} \to \mu^+\mu^- X$	Pythia	208301	20M	19980978	16604	14536	1.142	
$b\bar{b} \to \mu^+\mu^- X$	EvtGen	208303	1M	998500	73	63	1.159	
$b\bar{b} \to \mu^+\mu^- X$	Pythia	208308	40M	39811573	302	247	1.223	AA
$b\bar{b} \to \mu^+\mu^- X$	Pythia	208309	48M	47916460	1317	1086	1.213	AB
$b\bar{b} \to \mu^+\mu^- X$	Pythia	208310	48M	47933451	1303	1078	1.209	BA
$b\bar{b} \to \mu^+\mu^- X$	Pythia	208311	135M	134413380	1789	1411	1.268	BB, 1.3G events in sample
$c\bar{c} \to \mu^+\mu^- X$	Pythia	208312	50M	31842479	7608	6638	1.146	

Table A.2: MC simulated samples for exclusive backgrounds expected to contribute to the $B^0 \to K^*\mu^+\mu^-$ signal region. The table lists dataset numbers, used generator, numbers of requested and simulated events and the number of candidates passing the selection cuts described in Section 4.2, without trigger selection applied.

Process	Generator	Dataset	Size	Generated	Candidates	Events	Cand/Ev.	Note
$B_s^0 \to J/\psi\ \phi$	Pythia	208400	5M	4996495	10432	9949	1.049	40M events in sample
$\Lambda_b \to \Lambda J/\psi$	Pythia	208404	5M	4993998	598	571	1.047	
$\overline{\Lambda_b} \to \Lambda J/\psi$	Pythia	208405	5M	4961995	618	596	1.037	
$B^0 \to J/\psi\ K_S^0$	Pythia	208412	5M	4994000	1011	963	1.050	20M events in sample
$B \to K_s\psi(2S)$	Pythia	208423	4M	3997994	1032	952	1.084	
$\Lambda_b \to \Lambda\psi(2S)$	Pythia	208424	1M	999999	191	169	1.130	
$\overline{\Lambda_b} \to \Lambda\psi(2S)$	Pythia	208425	1M	998999	210	192	1.094	
$B^+ \to J/\psi\ K^+$	Pythia	208430	2.5M	2499598	7491	7386	1.014	
$B^+ \to J/\psi\ \pi^+$	Pythia	208432	1M	999999	2219	2197	1.010	
$B^- \to J/\psi\ K^-$	Pythia	208436	2.5M	2499597	7350	7232	1.016	
$B^+ \to K^{*+}(K^0\pi^+)\mu^+\mu^-$	EvtGen	208440	5M	4996392	5906	5299	1.115	
$B_s^0 \to \phi\mu^+\mu^-$	EvtGen	208441	5M	4997488	38870	36979	1.051	
$B^0 \to J/\psi K^*$	EvtGen	208448	5M	4813995	613757	529206	1.160	
$B^0 \to \psi(2S)K^*$	EvtGen	208449	5M	4990992	630888	535692	1.178	
$B^+ \to K^+\mu^+\mu^-$	EvtGen	208450	5M	4983998	14851	14462	1.027	
$B_s^0 \to J/\psi\ K^*$	EvtGen	208452	5M	4993595	717309	612775	1.171	
$B^0 \to K^*\phi$	EvtGen	208455	5M	4997395	587768	512648	1.147	
$\Lambda_b \to \Lambda(pK^-)\mu^+\mu^-$	EvtGen	208456	5M	4992591	190689	174440	1.093	
$\Lambda_b \to pK^-\mu^+\mu^-$	EvtGen	208457	5M	4995797	38074	33853	1.125	

A.2 Mass fits

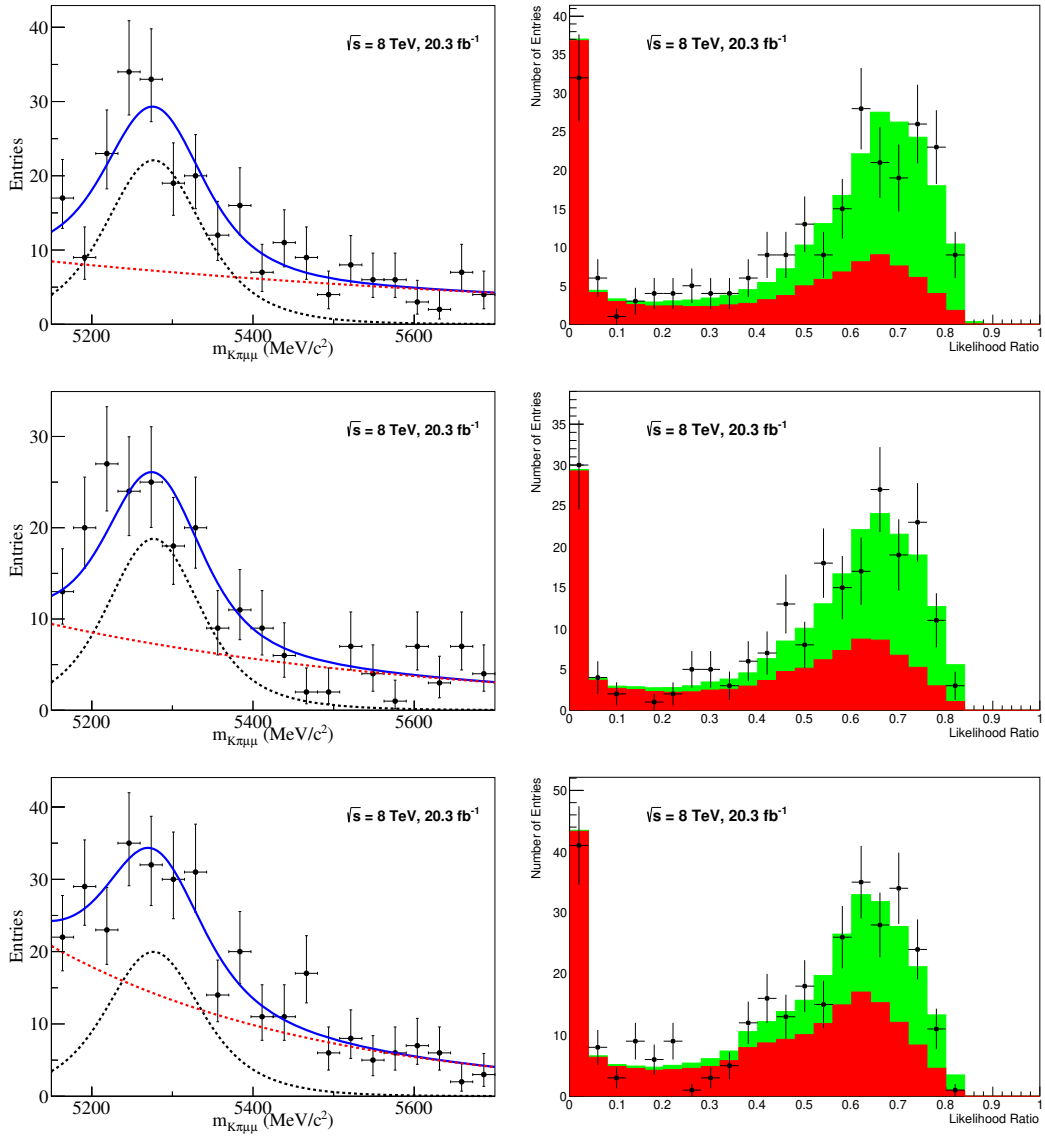

Figure A.1: Mass fits for q^2 bins $[0.04, 2.0]\,\mathrm{GeV}^2$ (top), $[2.0, 4.0]\,\mathrm{GeV}^2$ (middle) and $[4.0, 6.0]\,\mathrm{GeV}^2$ (bottom). In the mass fit projections on the left, the blue solid line is a projection of the total PDF, the red dot-dashed line represents the background, and the black dashed line represents the signal component. In the likelihood ratio distributions on the right, the green component corresponds to the signal toy MC and the red to the combinatorial background toy MC.

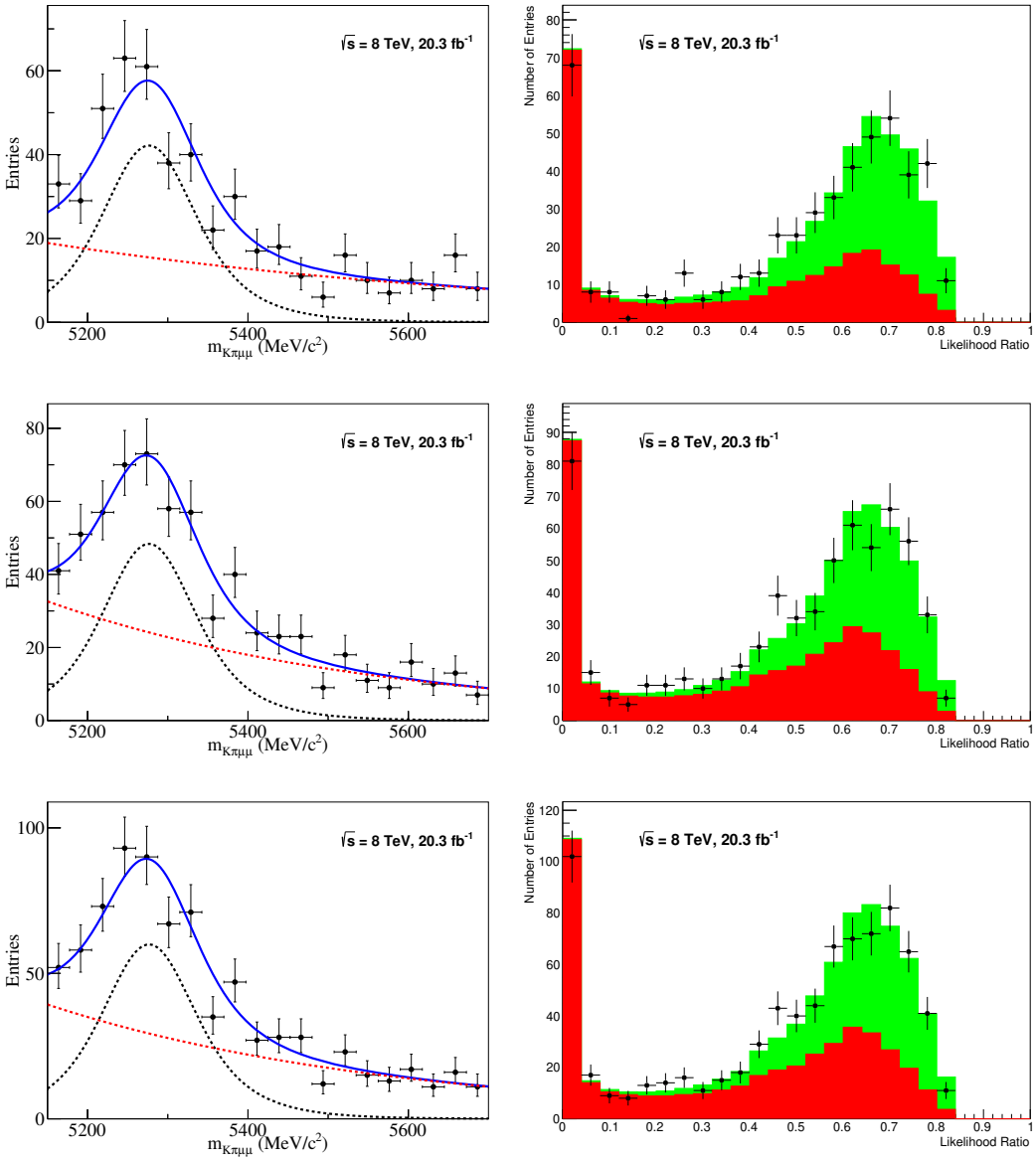

Figure A.2: Mass fits for q^2 bins $[0.04, 4.0]\,\mathrm{GeV}^2$ (top), $[1.1, 6.0]\,\mathrm{GeV}^2$ (middle) and $[0.04, 6.0]\,\mathrm{GeV}^2$ (bottom). In the mass fit projections on the left, the blue solid line is a projection of the total PDF, the red dot-dashed line represents the background, and the black dashed line represents the signal component. In the likelihood ratio distributions on the right, the green component corresponds to the signal toy MC and the red to the combinatorial background toy MC.

A.3 Angular fits

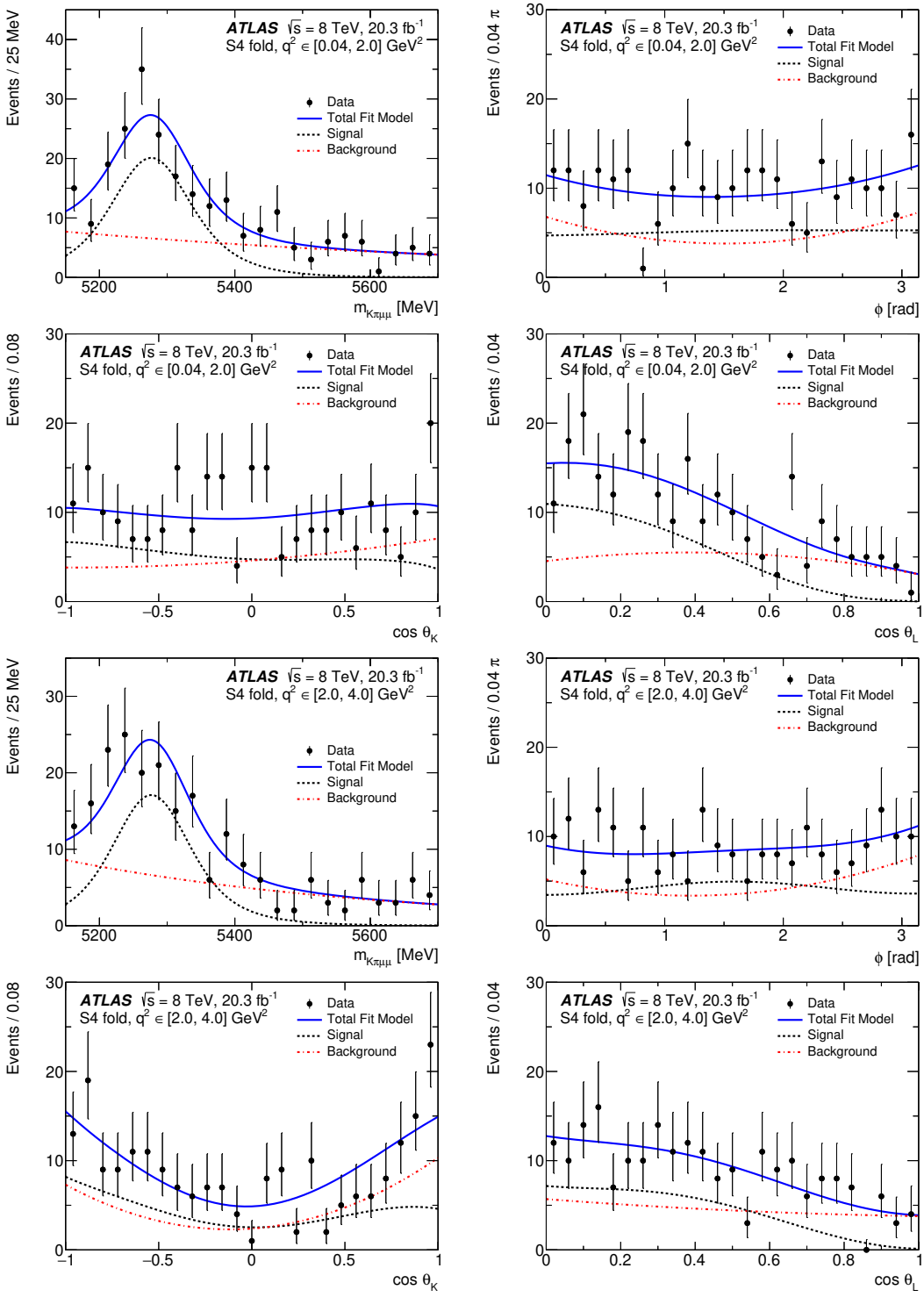

Figure A.3: The distributions of $m_{K\pi\mu\mu}$, ϕ, $\cos\theta_K$, and $\cos\theta_L$ obtained for $q^2 \in [0.04, 2.0]\,\mathrm{GeV}^2$ (top 4 plots) and $q^2 \in [2.0, 4.0]\,\mathrm{GeV}^2$ (bottom). The solid line is a projection of the total pdf, the dashed line represents the background, and the dashed line represents the signal component. These plots are obtained from a fit using the S_5 folding scheme.

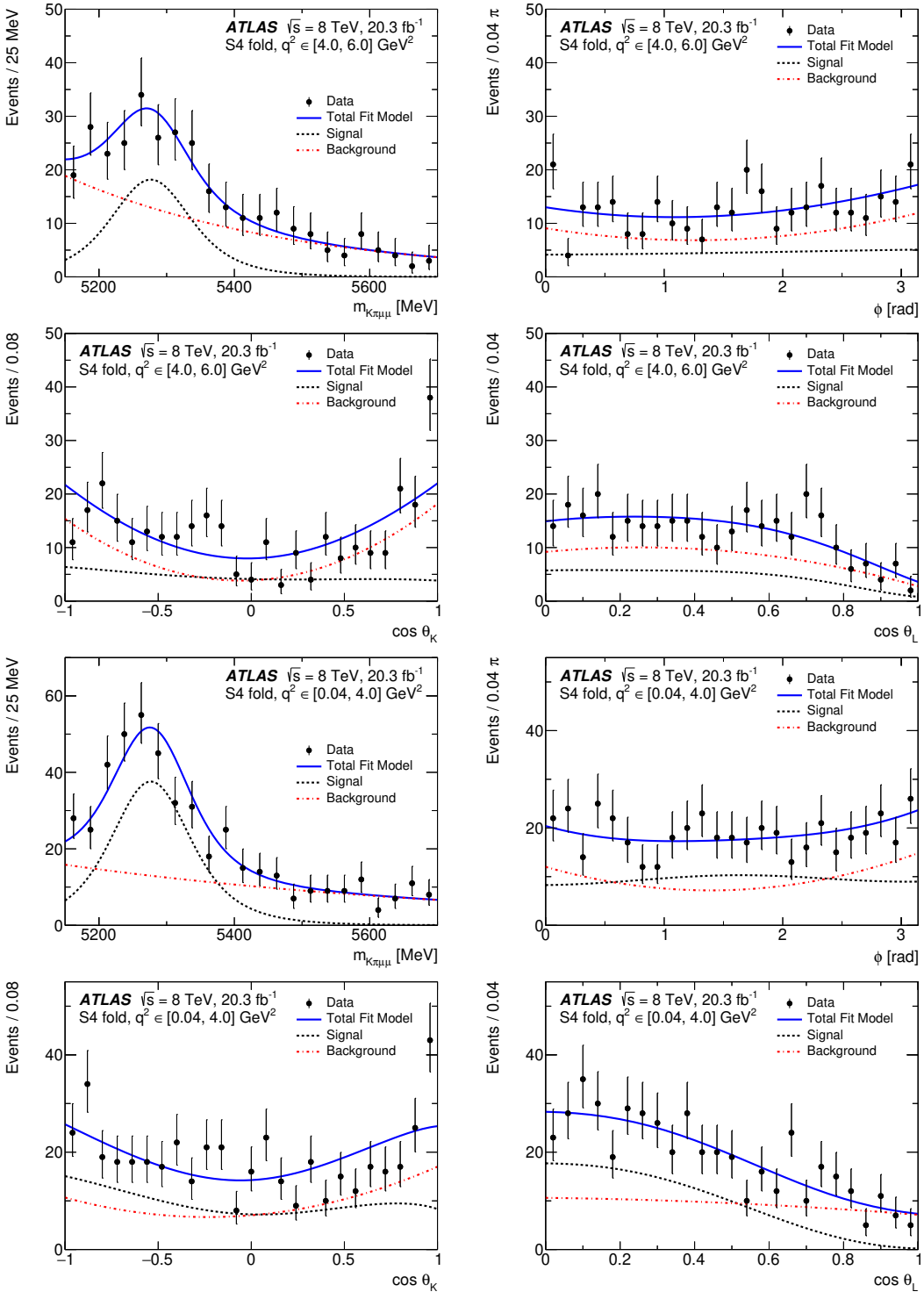

Figure A.4: The distributions of $m_{K\pi\mu\mu}$, ϕ, $\cos\theta_K$, and $\cos\theta_L$ obtained for $q^2 \in [4.0, 6.0]\,\mathrm{GeV}^2$ (top 4 plots) and $q^2 \in [0.04, 4.0]\,\mathrm{GeV}^2$ (bottom). The solid line is a projection of the total pdf, the dashed line represents the background, and the dashed line represents the signal component. These plots are obtained from a fit using the S_5 folding scheme.

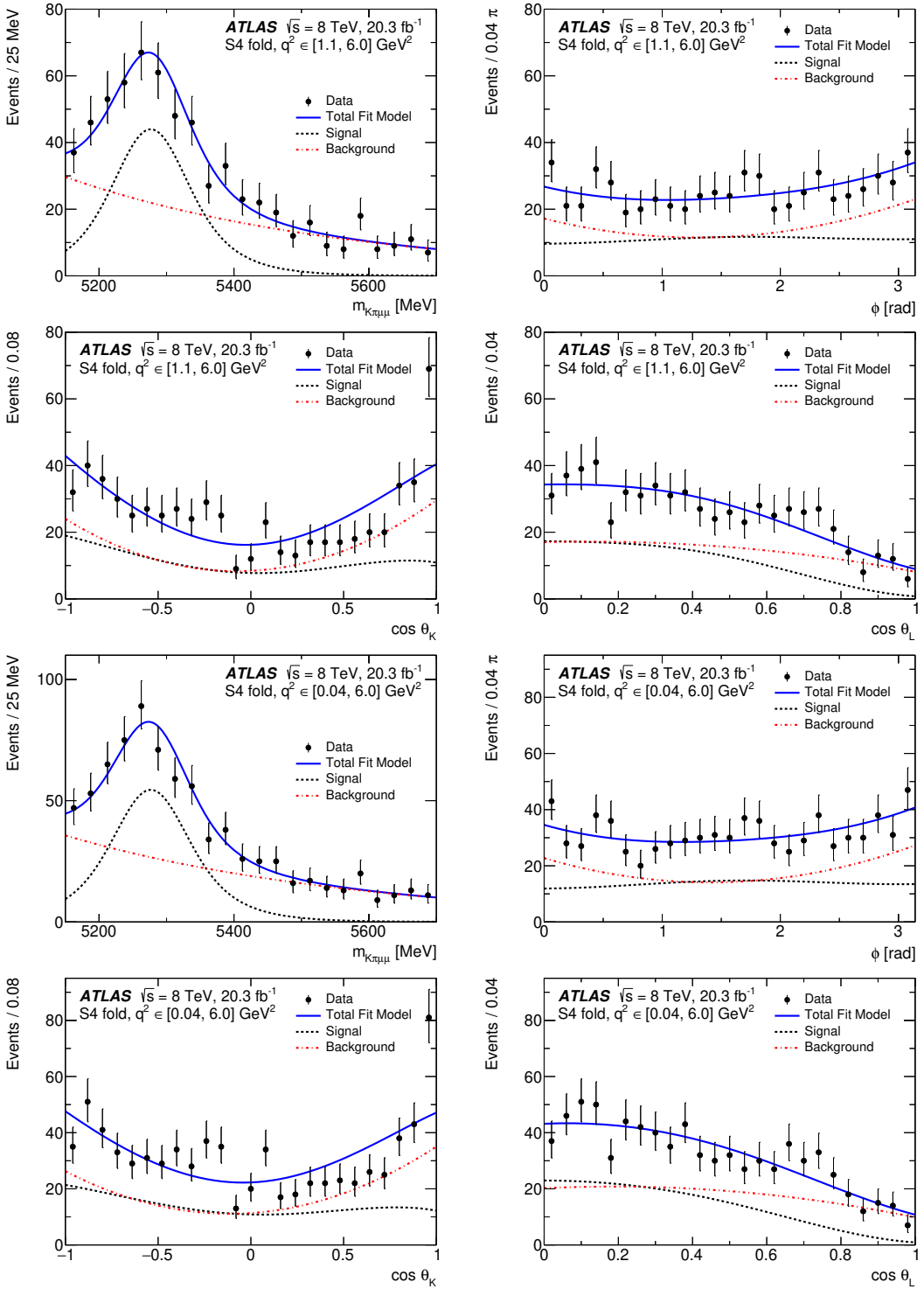

Figure A.5: The distributions of $m_{K\pi\mu\mu}$, ϕ, $\cos\theta_K$, and $\cos\theta_L$ obtained for $q^2 \in [1.1, 6.0]\,\mathrm{GeV}^2$ (top 4 plots) and $q^2 \in [0.04, 6.0]\,\mathrm{GeV}^2$ (bottom). The solid line is a projection of the total pdf, the dashed line represents the background, and the dashed line represents the signal component. These plots are obtained from a fit using the S_5 folding scheme.

A.4 Correlation matrices

Table A.3: Statistical correlation matrices for the F_L and S parameters (left) and $P^{(\prime)}$ parameters (right) obtained for $q^2 \in [0.04, 2.0]$ GeV^2.

	F_L	S_3	S_4	S_5	S_7	S_8
F_L	1.00	0.11	−0.13	0.03	0.16	0.24
S_3		1.00	0.31	0.28	0.73	0.45
S_4			1.00	0.58	0.19	0.22
S_5				1.00	0.14	0.28
S_7					1.00	0.59
S_8						1.00

	P_1	P_4'	P_5'	P_6'	P_8'
P_1	1.00	0.04	0.05	0.62	0.32
P_4'		1.00	0.53	−0.08	−0.06
P_5'			1.00	0.00	0.22
P_6'				1.00	0.55
P_8'					1.00

Table A.4: Statistical correlation matrices for the F_L and S parameters (left) and $P^{(\prime)}$ parameters (right) obtained for $q^2 \in [2.0, 4.0]$ GeV^2.

	F_L	S_3	S_4	S_5	S_7	S_8
F_L	1.00	0.27	0.35	−0.04	−0.15	−0.37
S_3		1.00	−0.08	−0.44	−0.09	−0.20
S_4			1.00	0.60	−0.02	−0.12
S_5				1.00	−0.11	−0.20
S_7					1.00	0.63
S_8						1.00

	P_1	P_4'	P_5'	P_6'	P_8'
P_1	1.00	−0.12	−0.21	0.05	0.05
P_4'		1.00	0.51	0.08	0.03
P_5'			1.00	−0.23	0.22
P_6'				1.00	0.66
P_8'					1.00

Table A.5: Statistical correlation matrices for the F_L and S parameters (left) and $P^{(\prime)}$ parameters (right) obtained for $q^2 \in [4.0, 6.0]$ GeV^2.

	F_L	S_3	S_4	S_5	S_7	S_8
F_L	1.00	0.33	−0.18	0.04	0.22	0.28
S_3		1.00	0.15	0.23	0.60	0.05
S_4			1.00	0.52	0.03	0.01
S_5				1.00	0.28	0.27
S_7					1.00	0.60
S_8						1.00

	P_1	P_4'	P_5'	P_6'	P_8'
P_1	1.00	0.11	0.34	0.41	0.16
P_4'		1.00	0.37	0.06	0.04
P_5'			1.00	0.39	0.33
P_6'				1.00	0.62
P_8'					1.00

Table A.6: Statistical correlation matrices for the F_L and S parameters (left) and $P^{(\prime)}$ parameters (right) obtained for $q^2 \in [0.04, 4.0]$ GeV^2.

	F_L	S_3	S_4	S_5	S_7	S_8
F_L	1.00	0.08	0.05	0.01	0.18	0.14
S_3		1.00	−0.04	0.03	0.29	−0.16
S_4			1.00	0.79	0.08	0.03
S_5				1.00	0.03	−0.02
S_7					1.00	0.60
S_8						1.00

	P_1	P_4'	P_5'	P_6'	P_8'
P_1	1.00	−0.07	0.00	0.21	0.12
P_4'		1.00	0.78	0.08	0.02
P_5'			1.00	0.03	−0.04
P_6'				1.00	0.59
P_8'					1.00

Table A.7: Statistical correlation matrices for the F_L and S parameters (left) and $P^{(\prime)}$ parameters (right) obtained for $q^2 \in [1.1, 6.0]$ GeV^2.

	F_L	S_3	S_4	S_5	S_7	S_8
F_L	1.00	0.05	0.00	0.07	0.18	−0.03
S_3		1.00	0.41	0.46	0.32	−0.01
S_4			1.00	0.60	0.09	0.03
S_5				1.00	0.17	0.24
S_7					1.00	0.67
S_8						1.00

	P_1	P_4'	P_5'	P_6'	P_8'
P_1	1.00	0.23	−0.09	0.08	−0.07
P_4'		1.00	0.53	0.15	0.08
P_5'			1.00	0.28	0.24
P_6'				1.00	0.67
P_8'					1.00

Table A.8: Statistical correlation matrices for the F_L and S parameters (left) and $P^{(\prime)}$ parameters (right) obtained for $q^2 \in [0.04, 6.0]$ GeV^2.

	F_L	S_3	S_4	S_5	S_7	S_8
F_L	1.00	0.03	0.01	−0.10	0.13	0.06
S_3		1.00	−0.02	−0.09	0.32	−0.01
S_4			1.00	0.68	0.00	0.04
S_5				1.00	−0.05	0.03
S_7					1.00	0.65
S_8						1.00

	P_1	P_4'	P_5'	P_6'	P_8'
P_1	1.00	−0.02	−0.14	0.17	0.04
P_4'		1.00	0.65	0.00	0.05
P_5'			1.00	−0.06	0.09
P_6'				1.00	0.61
P_8'					1.00